



HAL
open science

One-pot synthesis of bio-inspired apatite nanoparticles stabilized with new bioactive peptide-based stabilizing agents: toward wound healing applications

Mathilde Guerin

► To cite this version:

Mathilde Guerin. One-pot synthesis of bio-inspired apatite nanoparticles stabilized with new bioactive peptide-based stabilizing agents: toward wound healing applications. Material chemistry. Montpellier, Ecole nationale supérieure de chimie, 2022. English. NNT : 2022ENCM0027 . tel-04217092

HAL Id: tel-04217092

<https://theses.hal.science/tel-04217092v1>

Submitted on 25 Sep 2023

HAL is a multi-disciplinary open access archive for the deposit and dissemination of scientific research documents, whether they are published or not. The documents may come from teaching and research institutions in France or abroad, or from public or private research centers.

L'archive ouverte pluridisciplinaire **HAL**, est destinée au dépôt et à la diffusion de documents scientifiques de niveau recherche, publiés ou non, émanant des établissements d'enseignement et de recherche français ou étrangers, des laboratoires publics ou privés.

THESE POUR OBTENIR LE GRADE DE DOCTEUR DE
L'ÉCOLE NATIONALE SUPÉRIEURE DE CHIMIE DE MONTPELLIER

En Ingénierie Biomoléculaire

École doctorale ED 459 Sciences Chimiques Balard

Institut des Biomolécules Max Mousseron (IBMM) – UMR 5247
et Centre Inter-universitaire de Recherche et d'Ingénierie des Matériaux (CIRIMAT) – UMR 5085

**Synthèse one-pot de nanoparticules d'apatite bio-
inspirées entourées par de nouveaux agents
stabilisants bioactifs à base de peptides:
vers une application pour la cicatrisation des plaies**

**One-pot synthesis of bio-inspired apatite
nanoparticles stabilized with new bioactive peptide-
based stabilizing agents:
toward wound healing applications**

Présentée par **Mathilde Guérin**

le 15 décembre 2022

Sous la direction de Gilles Subra et Christophe Drouet

Devant le jury composé de

Lucie Sancey	Directrice de Recherche, IAB UMR 5309, Grenoble, France	Présidente du jury, Examinatrice
Paula Gomes	Professeure, FCUP, Porto, Portugal	Rapportrice
Michele Iafisco	Chercheur Habilité, ISTE, Faenza, Italy	Rapporteur
Liisa Kuhn	Professeure, UConn Health, Farmington (Connecticut), USA	Membre invité
Gilles Subra	Professeur, IBMM, Montpellier	Directeur de thèse
Christophe Drouet	Directeur de Recherche CNRS, CIRIMAT, Toulouse	Directeur de thèse



**UNIVERSITÉ DE
MONTPELLIER**

A mes grands-parents,
A mes parents,
A mon frère, ma belle-soeur et mon neveu

Special thanks

This PhD is the result of a collaboration between two teams : the team "Acids, peptides and proteins" of the Institut des Biomolécules Max Mousseron (IBMM) in Montpellier and the team "Phosphates, Pharmacotechnics and Biomaterials" (PPB) of the Centre Inter-universitaire de Recherche et d'Ingénierie des Matériaux (CIRIMAT) in Toulouse.

I thank first of all, the Carnot Institute Chimie Balard CIRIMAT which financed this PhD project and gave me the opportunity to present my work during the Carnot days in particular.

I warmly thank Pr. Paula Gomes and Pr. Michele Iafisco for having accepted to be the reviewers of this manuscript. I also thank Dr. Lucie Sancey for having accepted to be an examiner during my PhD defense.

I would also like to thank Dr. Muriel Amblard and Dr. David Grossin for having welcomed me in both teams.

My thanks go of course to my PhD supervisors. I thank Pr. Gilles Subra first of all for his unlimited supervision, his scientific advice but also for his optimism and his perpetual good mood. I also thank Dr. Christophe Drouet for his patience and his pedagogy during our discussions about calcium phosphate but also for his constant good mood and his availability. Thank you both for supporting me and for the freedom you gave me during this project so that I could participate in popularization competitions, congresses or even go to the USA. I am very grateful for these enriching three years in every way.

I would like to thank Pr. Liisa Kuhn for having welcomed me in her laboratory during my PhD internship in order to carry out in vitro biological tests for wound healing but also within her family (including dogs!). This internship would not have been possible without you and it was for me a first experience in biology rich in teaching. My thanks also to David Bertrand for all the formulation experiments performed. I would like to thank Olivier Marsan for all the RAMAN analyses you performed for my project. I also thank Ofélia Maniti and Thierry Granjon, from the ICBMS laboratory in Lyon, for the preliminary tests on the mobility of fibroblast membranes. I also thank Thierry Azaïs and Guillaume Laurent from the LCMCP laboratory of the Sorbonne University in Paris for the solid state NMR analyses performed. I would also like to thank Karine Parra and Aurélien Lebrun for helping me to understand all NMR analyses and Pierre Sanchez for the LC-MS analyses performed during my PhD project. I would also like to thank Patricia Licznar-fajardo and Agnes Masnou for allowing me to work in their laboratory and for teaching me the antibacterial experiments.

Thanks to all the IBMM team who shared and brightened up my day life during 3 years: Luc, Pascal, Elodie, Youssef, Veronique, Sonia, JAF, Bruno, Anthony M., Cécile, Baptiste, Lubomir, Nicolas, Severine, Ludovic, Laurent, Jean-François, Sylvie, Karine A., Emmanuelle, Lyne-Rose. Special dedication to Ahmad for his kindness and the opportunities that you gave me to present my PhD work. A special thanks for all PhD students and post docs Mylène, Anthony, Laurianne, Pauline, Raquel, Anna, Aline, Nicole, Fabien, Quentin, Célia, Titouan, Alexandre, Myanou, Samantha, Hélène, Audrey, for all the good times we had together. Thanks also to the CIRIMAT team for having warmly welcomed me during my visits. You have brightened up my stay in Toulouse with your kindness and your good mood.

My thanks go especially to my colleagues/friends of labs. A huge thank you to Laurine and Margaux with whom I shared my three years. Thank you for your unfailing support (even when 6 000 km separated us) but also for all the good moments spent together in the lab or outside. Without you, these three years of PhD would have been much less beautiful. A big thank to Aïcha for her good mood, kindness in the laboratory and for her advices in sciences and to Chloé and Jules.

Special thanks for my parents who have always believed in me, have supported me in all my projects and for their unconditional love. A huge thank to my brother Christophe and my sister-in-law Chloé for their support and the time spent together skiing and hiking. A little thought to my nephew Wandrille, new family member for having brightened up my end of PhD with his little smiles. You are a golden family.

Scientific productions

1. Accepted publication

Review paper in “Techniques de l’Ingénieur” (accepted) 2023 pagination in progress

« Particules minerals-organiques à base d’apatite pour applications biomédicales »
Mathilde Guérin, Gilles Subra, Christophe Drouet

2. Oral communications

1. Journée Méditerranéenne des Jeunes Chercheurs (JMJC) – October 28th, 2021 – Montpellier (France)

« First colloidal hybrid nanoparticles apatite/peptide for the treatment of wound healing »
Mathilde Guérin, Gilles Subra, Christophe Drouet
2. Journées Annuelles du GdR CNRS “BIOMIM – Biomimétisme et bio-inspiration” – November 16th, 2021 – Videoconference

« Peptide-decorated bio-inspired apatite nanoparticles: Towards wound healing applications »
Mathilde Guérin, Gilles Subra, David Bertrand, Audrey Tourette, Christophe Drouet
➔ Winner of the 2nd Best Oral Presentation Award
3. Groupe Français des Peptides et des Protéines (GFPP) – June 2nd, 2022 – Port Leucate (France)

« Hybrid apatite/peptide colloidal nanoparticles for the treatment of complex wounds »
Mathilde Guérin, Christophe Drouet, David Bertrand, Audrey Tourette, Liisa Kuhn, Fatma Elshishiny, Gilles Subra
4. Franco-Quebecoise Scientific day around Nanomaterials – June 9th, 2022 – Montpellier (France)

« One-pot synthesis of a new hybrid colloidal nanoparticles of hydroxyapatite/peptide »

Mathilde Guérin, David Bertrand, Audrey Tourette, Liisa Kuhn, Fatma Elshishiny, Christophe Drouet, Gilles Subra

5. European Peptide Symposium (EPS) – August 30th, 2022 – Sitges (Spain)

« Peptide-decorated colloidal apatite NPs for the treatment of complex wounds »

Mathilde Guérin, Christophe Drouet, David Bertrand, Audrey Tourette, Liisa Kuhn, Fatma Elshishiny, Gilles Subra

6. Bioceramics32 – September 23rd, 2022 – Venezia (Italy)

« Hybrid particles for the local treatment of complex wounds with high risk of infection »

Mathilde Guérin, Christophe Drouet, David Bertrand, Audrey Tourette, Liisa Kuhn, Fatma Elshishiny, Gilles Subra

7. MATERIAUX 2022 – October 25th, 2022 – Lille (France)

« Hybrid apatite/peptide nanoparticles: toward the treatment of complex wounds »
Mathilde Guérin, Gilles Subra, David Bertrand, Jérémy Soulié, Olivier Marsan, Thierry Azaïs, Guillaume Laurent, Audrey Tourette, Liisa Kuhn, Fatma Elshishiny, Christophe Drouet

3. Miscellaneous

1. « My Thesis in 180 seconds » competition – From January to June 2021
➔ Winner of the 1st Regional Award and selected for the National Finale – France
2. « My Thesis in 400 words » - 7 November 2022 – Perpignan (France) – 1st Price
3. Participation in CHIMAES projects (online platform for students)
4. PhD internship at the University of Connecticut, USA, from January to March 2022 in the laboratory of Prof. Liisa Kuhn (UConn Health), Scholarships obtained from the *Fondation de la maison de la Chimie* and from *Toulouse INP*.

Summary

Special thanks	5
Scientific productions	7
Summary	9
List of figures	19
Tables index	25
Equations index	27
List of abbreviations	29
Extended summary (in French) of the PhD	31
I. Etat de l'art	31
II. Synthèse de nanoparticules stabilisées avec les nouveaux agents stabilisants P(Peptide)	34
A. Synthèse des P(Peptide) sur support solide	34
B. Synthèse et caractérisation des NPs d'apatite stabilisées avec différents ratios AEP/P(Peptide).....	34
III. Synthèse des NPs stabilisées avec les nouveaux agents stabilisants P(PEG3K)-Peptide	36
A. Synthèse des nouveaux agents stabilisants P(PEG3K)-Peptide.....	36
B. Synthèse et caractérisation des NPs d'apatite stabilisées avec une couronne organique de P(PEG3K)-NEt ₂ / P(PEG3K)-Peptide	37
1. Détermination du rapport R-PO ₃ H ₂ /Ca	37
2. Synthèse et caractérisation des NPs stabilisées par différents ratios de P(PEG3K)-NEt ₂ /P(PEG3K)-Peptide	38
IV. Evaluation biologique des NPs d'apatite colloïdale stabilisées par P(PEG3K)-Peptide et tests préliminaires de formulation	39
V. Conclusion	40
Introduction	43
Chapter I- State of art:	47
Applications of hybrid apatite-based NPs in nanomedicine	47
I. Apatite: structure and synthesis	49
A. Apatite structure.....	49
B. Characterization of nanocrystalline bio-inspired apatites.....	55

1. X-Ray Diffraction.....	55
2. Fourier transform infrared spectroscopy (FTIR)	57
II. State of the art: synthesis of nano-sized apatite particles.....	60
A. Solid state methods	60
B. Wet state methods	61
1. Co-precipitation synthesis.....	62
2. Stabilizing agents used to control the particles size: toward colloidal suspensions	63
a. Nanoparticles stabilized by electrostatic repulsion induced by AEP, PhCol or Citrate corona	64
Case of citrate	64
Case of PhCol.....	64
Case of AEP.....	65
b. Nanoparticles stabilized by steric hindrance induced by a P(PEG)-OCH ₃ corona .	66
III. Functionalization of nano-apatite surfaces – hybrid nanoparticles	68
A. Different types of interactions between organic molecules and apatite surfaces	68
1. Interactions by “covalent” bonding	68
2. Electrostatic interactions.....	69
B. Applications of nano-sized particles of apatite in nanomedicine	71
1. Importance of the size of particles in medical applications.....	71
2. Applications of hybrid apatite NPs in nanomedicine	73
a. Oncology	73
b. Hematology	75
c. Dermatology.....	77
d. Genetic disease – Cystic Fibrosis	79
e. Application in medical imaging.....	79
Description of the PhD thesis objectives.....	85
Chapter 2 - One-pot co-precipitation synthesis and characterization of peptide-decorated colloidal hybrid apatite nanoparticles	87
I. Generalities about peptide synthesis and apatite co-precipitation synthesis	90
A. Proteogenic amino acids - Solid phase synthesis – Fmoc/tBu Strategy.....	90
1. Proteogenic amino acids	90
2. Principe of SPPS synthesis	90
3. Choice of Fmoc/tBu strategy.....	92
4. Notion of orthogonality.....	93

5. List of commercial AAs for the Fmoc/tBu strategy	94
6. Description of each step of the SPPS peptide synthesis with the Fmoc/tBu strategy	96
a. Loading of the first AA on the linker of the resin bead	96
Choice of the resin	96
Loading of the first AA on the linker	97
b. Temporary protective group Fmoc removal	97
c. Carboxylic acid activation with HATU – coupling step.....	99
d. Linker cleavage and side chain protection removal	100
B. Synthesis of colloidal nanoparticles of apatite stabilized by an organic corona.....	101
II. Synthesis and characterization of hybrid peptide-apatite nanoparticles obtained from 2-aminoethylphosphonate-analog, P(Peptide).....	102
A. Synthesis of new peptide-based stabilizing agent from 2-aminoethylphosphonate-analog, P(Peptide) 6 and 7	103
1. Peptidyl resin 1 and 2 synthesis on solid support with Fmoc-tBu strategy	104
2. Functionalization of the peptidyl resin 1 and 2 with 3-phosphonopropanoic acid 3 on solid support.....	105
3. Functionalization of the peptidyl resin 1 and 2 with the (diethoxyphosphoryl)propionic acid 9 on solid support.....	107
4. Dealkylation of compound 10 and 11 to obtain the new peptide-based stabilizing agents 6 and 7	108
B. Synthesis of apatite particles surrounded with a mixture of P(Peptide) and AEP	110
C. Results and characterizations of apatite particles surrounded with a mixture of P(Peptide) and AEP	111
1. Observations of the suspensions obtained after maturation.....	111
2. Physicochemical characterizations of the particles surrounded by a mixture of P(Peptide) and AEP.....	113
a. XRD analysis	113
b. FTIR analysis.....	115
c. RAMAN analysis	116
d. Determination of particles size thanks to DLS analysis and TEM imaging	118
TEM imaging.....	118
DLS analysis	119
e. Liquid-state NMR	121
³¹ P NMR ERETIC.....	121
¹ H quantitative liquid-state NMR.....	122

D. Conclusion	122
III. Synthesis and characterization of hybrid peptide-apatite nanoparticles surrounded by new peptide-based stabilizing agents P(PEG3K)-Peptide	123
A. Synthesis of new peptide-based stabilizing agents, P(PEG3K)-Peptide and synthesis of the simple stabilizing agent P(PEG3K)-NEt ₂	124
1. Functionalization of peptidyl resin 2 with the P(PEG5K)-COOH 12 on solid support with Fmoc-tBu strategy	125
a. Peptidyl-resin 2 synthesis	125
b. Functionalization of the N-terminal of the peptidyl resin 2' with a P(PEG5K)-COOH 12	125
2. Functionalization of the N-terminal amine of the peptidyl resin 2 with a FmocNH-PEG3K-COOH 15 on solid support	127
3. Synthesis of P(PEG3K)-Peptide 27, 28, 29 and P(PEG3K)-NEt ₂ 30 with a multi-steps synthesis in solution	128
a. Synthesis of the PO ₃ Et ₂ (PEG3K) 21	128
b. SPPS peptides synthesis 1', 2' and 22	133
c. Functionalization of the primary amine of peptides 1', 2' and 22 with the PO ₃ Et ₂ (PEG3K) 21 and synthesis of PO ₃ Et ₂ (PEG3K)-NEt ₂ 26	133
d. Dealkylation of the PO ₃ Et ₂ (PEG3K)-Peptide 23, 24, 25 and PO ₃ Et ₂ (PEG3K)-NEt ₂ 26	136
4. Conclusion	137
B. Synthesis of apatite particles surrounded with a mixture of P(PEG3K)-Peptide 27, 28, 29 and P(PEG3K)-NEt ₂ 30	137
1. Optimization of R-PO ₃ H ₂ /Ca ratio	138
a. Co-precipitation synthesis of the NPs with different R-PO ₃ H ₂ /Ca ratios	138
b. Results and characterizations of apatite particles synthesized with several R-PO ₃ H ₂ /Ca ratios.....	139
Observations of the suspensions obtained after maturation	139
XRD analyses of NPs 12 to 17	140
DLS analyses of NPs 12 to 17	140
TEM imaging of NPs 12 to 17	141
Determination of the concentrations of the P(PEG3K)-NEt ₂ 30 grafted around the NPs 12-17 during the synthesis.....	143
Calculation of grafting density from liquid-state NMR analyses of NPs 12-17 ...	144
c. Conclusion.....	147
2. Synthesis of apatite nanoparticles surrounded with P(PEG3K)-NEt ₂ 30 and P(PEG3K)-Peptide 27, 28 and 29	147

3. Results and characterization of apatite particles surrounded with a mixture of P(PEG3K)-NEt ₂ 30 and P(PEG3K)-Peptide 27, 28, 29	148
a. Observations of the apatite particles obtained after the maturation time	148
b. XRD analyses.....	149
c. FTIR analyses.....	152
d. RAMAN Spectroscopy.....	154
e. Solid-state NMR analyses	155
f. Determination of the NPs size thanks to DLS analysis and TEM imaging	158
g. Liquid-state NMR analyses to determine (i) the grafting density (ii) the conformation of the stabilizing agents around the NPs and (iii) the peptide concentrations.....	159
Determination of the stabilizing agent concentration of the NPs 18-29	161
Determination of the grafting density of NPs 18-29	161
Determination of the stabilizing agent conformation around the NPs 18-29.....	161
Determination of the peptide concentration in 1 mL of colloidal suspension by using ¹ H quantitative liquid state NMR.....	162
Conclusion.....	165
IV. Conclusion.....	165
Chapter 3 - Toward the treatment of complex wounds.....	167
I. Wounds and healing process of complex wounds.....	169
A. Skin composition – Wound definition – Healing process.....	169
1. Skin structure	169
a. Hypodermis.....	169
b. Dermis.....	169
c. Epidermis	170
2. Definition of acute wounds and healing process	170
a. Acute wound defintion	170
b. Healing process.....	170
Hemostasis.....	171
Inflammation.....	171
Proliferation	172
Remodeling	172
3. From acuete wound to chronic wound	172
4. Current treatment of chronic wounds	173
II. Our objective: apatite nanoparticles surrounded by P(PEG3K)-Peptide for the treatment of complex wounds.....	174

A. Apatite NPs surrounded by pro-adhesion peptides-based stabilizing agents 27 and 28 to promote wound healing	174
1. Pro-adhesion peptides	175
2. General considerations for biocompatibility and proliferation experiments on NIH/3T3 fibroblast cells	175
a. Choice of cells studied	175
b. Experiments design	176
Determination of the initial concentrations	176
Sample preparation	176
Compounds and controls tested for biocompatibility experiments.....	177
Evaluation methods	177
3. Biocompatibility and proliferation results	178
4. Preliminary scratch assays.....	179
III. Other preliminary experiments.....	182
A. Antibacterial experiments	182
B. Fibroblast membrane mobility experiments	183
C. Preliminary formulation assays	184
1. Impregnation on commercial dressings.....	185
2. Direct fabrication of alginate dressings loaded with apatite NPs by freeze-casting	187
3. Spray.....	189
IV. Conclusion.....	191
General conclusions	193
Perspectives	197
Chapter 4 – Experimental section for Chapters 2 and 3.....	199
I. Experimental section for chapter 2	201
A. Commercial products and solvents	201
B. Equipment.....	201
1. High performance Liquid Chromatography coupled with Mass Spectrometry (LC-MS)	201
2. Purification by HPLC-preparative	202
3. Liquid Nuclear Magnetic Resonance (NMR)	202
a. Instrumentations	202
b. Carbon	202
c. Phosphorus	202

d. 2D NMR experiments	203
e. Quantitative experiments.....	203
NMR tube preparation.....	203
NMR Spectra Calibration.....	203
Quantitative ¹ H NMR.....	203
ERETIC ³¹ P NMR.....	203
4. Solid-state Nuclear Magnetic Resonance	204
5. Dynamic Light Scattering analysis (DLS).....	204
6. Transmission Electron Microscopy (TEM) imaging	204
7. X-Ray Diffraction.....	205
8. Fourier Transform Infrared (FTIR)	205
9. RAMAN Spectroscopy.....	205
C. Synthesis of hybrid peptide-apatite nanoparticles obtained from 2-aminoethylphosphonate-analog, P(Peptide).....	205
1. Synthesis of 3-(diethoxyphosphoryl)propanoic acid 9	205
2. Peptidyl resin 1 and 2 synthesis	207
a. Peptidyl resin 1 (precursor of Ac-LRGDNK-NH ₂ 1' peptide).....	207
b. Peptidyl resin 2 (precursor of H-GDPGYIGSR-NH ₂ 2' peptide)	207
3. Functionalization of the peptidyl resin 1 and 2 with the (diethoxyphosphoryl)propionic acid 9 on solid support	208
4. Dealkylation of compound 10 and 11 by using the McKenna reaction to obtain the new peptide-based stabilizing agents 6 and 7	210
D. Synthesis of novel bioactive peptide-based stabilizing agents P(PEG3K)-Peptide 27 , 28 , 29 and P(PEG3K)-NEt ₂ 30	213
1. Synthesis of peptides 1' , 2' and 22	213
a. Synthesis of Ac-LRGDNK-NH ₂ 1'	213
b. Synthesis of H-GDPGYIGSR-NH ₂ 2'	218
c. Synthesis of H-AhXRR-NH ₂ 22	223
2. Synthesis of PO ₃ Et ₂ (PEG3K)-COOH 21	227
a. Synthesis of compound 18 : Activation of carboxylic acid via the N-acyl benzotriazole formation	227
b. Boc deprotection of BocNH-PEG3K-COOH 19	230
c. N-acyl benzotriazole 18 coupling with the free primary amine of NH ₂ -PEG3K-COOH 20	230
3. Synthesis of P(PEG3K)-Peptide 27 , 28 , 29 and P(PEG3K)-NEt ₂ 30	233

a. Synthesis of PO ₃ Et ₂ (PEG3K)-Peptide 23, 24, 25 and synthesis of PO ₃ Et ₂ (PEG3K)-NEt ₂ 26	233
Characterization of PO ₃ Et ₂ (PEG3K)-NEt ₂ 26	234
Characterization of PO ₃ Et ₂ (PEG3K)-RGD 23	238
Characterization of PO ₃ Et ₂ (PEG3K)-YIGSR 24	241
Characterization of PO ₃ Et ₂ (PEG3K)-AhXRR 25	244
4. Dealkylation of compounds 23, 24, 25, 26 by using the McKenna reaction in solution.....	245
E. Synthesis of colloidal nanoparticles surrounded by a mixture of AEP/P(Peptide) 6 and 7	246
F. Synthesis of colloidal nanoparticles surrounded by P(PEG3K)-NEt ₂ 30/P(PEG3K)-Peptide 27, 28, 29.....	247
II. Experimental section of the Chapter 3	248
A. Commercial products.....	248
B. Biocompatibility experiments	248
1. Peptides synthesis for the biological experiments	248
a. Ac-LRGDNK(Ac)-NH ₂ 1''	248
b. Ac-GDPGYIGSR-NH ₂ 2''	249
2. In vitro Biocompatibility Assay with MC3T3-E1 Osteoblast Cells	250
a. Preparation of the cell culture plate.....	251
b. Preparation of the drug master plate.....	251
c. Addition of compounds to the cell culture plate.....	251
d. Assessing Cell Viability with the CellTiterBlue assay	251
3. In vitro Biocompatibility Assay using NIH/3T3 Fibroblast Cells	252
a. Preparation of the cell culture plate.....	252
b. Preparation of the drug master plate.....	252
c. Addition of compounds to the cells culture plate	252
d. Cell Viability Assay	253
C. In vitro CellTiter Blue method Proliferation Assay with NIH/3T3 Fibroblast Cells	253
1. Preparation of the cell culture plate	253
2. Preparation of the drug master plate	253
3. Addition of compounds in the cell culture plate.....	254
4. Proliferation Assay using CellTiterBlue	254
D. <i>In vitro</i> Scratch Assay against NIH/3T3 Fibroblast Cells	254
1. Preparation of the cells culture plate.....	254

2. In Vitro Scratch Assay Procedure	254
3. Scratch observations on the microscope	255
E. Antibacterial experiments.....	255
1. MIC determination	255
a. Preparation of the inoculum (<i>S. aureus</i> and <i>P. aeruginosa</i>)	255
b. Plate preparation.....	255
c. Plate reading	255
E. Fibroblast membrane mobility experiments	255
References.....	258

List of figures

Figure 1 : Synthèse one-pot par co-précipitation de NPs d'apatite colloïdale grâce à l'utilisation d'agent stabilisant	33
Figure 2 : Synthèse par co-précipitation des NPs d'apatite avec différents ratios entre AEP et P(Peptide).....	35
Figure 3 : Synthèse multi-étapes des nouveaux agents stabilisants P(PEG3K)-Peptide.....	37
Figure 4 : Synthèse des NPs d'apatite stabilisées par un mélange de P(PEG3K)-NEt ₂ et P(PEG3K)-Peptide	38
Figure 5: Crystal structure of stoichiometric hydroxyapatite	50
Figure 6 : Representation of biomimetic apatite nanocrystals (inspired by ⁶)	54
Figure 7: XRD pattern of stoichiometric hydroxyapatite (relative to the copper K α anticathode) and a typical biomimetic nanocrystalline apatite ⁹	55
Figure 8: FTIR spectrum of a partially carbonated biomimetic nanocrystalline apatite ⁹	58
Figure 9 : Spectral decomposition around the ν_4 adsorption band of phosphate ions. ap. = apatitic ⁹	59
Figure 10: Pechini method to synthesize hydroxyapatite nanoparticles ¹⁶	61
Figure 11: Example of colloidal suspension of apatite nanoparticles stabilized with AEP (Al-Kattan et al.) ³⁷	64
Figure 12: Principle of stabilizing agents via an electrostatic repulsion (AEP, PhCol, Citrate) or steric hindrance (P(PEG)-OCH ₃)	65
Figure 13: Typical XRD and FTIR features for colloidal apatite particles stabilized with AEP ³⁵	66
Figure 14 : XRD analysis of colloidal apatite NPs stabilized by a P(PEG)-OCH ₃ corona compared with a non-colloidal apatite reference and the P(PEG)-OCH ₃ molecule alone ⁴⁴	67
Figure 15 : FTIR analysis of colloidal apatite stabilized by a P(PEG)-OCH ₃ corona compared with the FTIR features of a non-colloidal apatite reference and P(PEG)-OCH ₃ alone ⁴⁴	67
Figure 16 : Covalent interaction between apatite and APTES (inspired by ref ⁴⁶).....	69
Figure 17: Two main mechanisms involving electrostatic interactions between different organic groups and an apatite surface.....	70
Figure 18: DOX release from DOX-loaded apatite particles thanks to a pH stimulus ⁵⁹	75
Figure 19: Use of hybrid apatite NPs to facilitate membrane permeability of trehalose in red blood cells in view of enhanced cryoprotection (inspired by ref ⁷⁵).....	77
Figure 20: Ex vivo permeation study for FA solution and FA-functionalized colloidal particles, in dynamic conditions ⁴⁴	78
Figure 21: Example of APIs adsorbed via electrostatic interaction onto the apatite surface .	79
Figure 22 : General structure of an Amino Acid (AA) and N-ter and side-chain protected Amino acid. The stereochemistry is noted L when using Fisher's representation or (S), except for Cys which is (R)	90
Figure 23 : Solid support synthesis of peptide (SPPS).....	91
Figure 24: General principle of SPPS by Fmoc/tBu strategy for the preparation of C-terminal amidated peptide on a resin carrying a Rink Amide linker. P represents permanent, acid-labile protections.....	93
Figure 25: Principe of resin bead strategy for SPPS peptide synthesis.....	96
Figure 26: Formation of oxazolone, a side reaction of AAs coupling.....	98
Figure 27 : Fmoc deprotection process.....	98
Figure 28 : Mechanism of HATU activation of carboxylic acid.....	99

Figure 29 : Reaction of Ninhydrin with amines: Kaiser test.....	100
Figure 30: Reference synthesis protocol to obtain colloidal NPs in the presence of stabilizing agents	102
Figure 31: Principe of dialysis purification	102
Figure 32 : Strategy to functionalize the peptidyl resin 1 and 2 with an acidic analogue of AEP in view of obtaining the new peptide-based stabilizing agents P(RGD) 6 and P(YIGSR) 7	104
Figure 33 : Functionalization of the peptidyl resins 1 and 2 with the 3-phosphonopropanoic 3 acid	106
Figure 34 : Amide formation in the presence of a phosphonic acid.....	107
Figure 35 : Mechanism of the McKenna reaction to deprotect the diethylphosphonate on solid support.....	108
Figure 36 : General synthesis of peptide-based stabilizing agents P(RGD) 6 and P(YIGSR) 7 on solid support.....	109
Figure 37 : NPs synthesis with different ratios between AEP and P(RGD) 6 or P(YIGSR) 7 ...	110
Figure 38 : Picture of stable colloidal (NPs 1), unstable (NPs 3) and non-colloidal (without stabilizing agent) suspensions.....	111
Figure 39 : XRD patterns of particles surrounded by a mixture of AEP / P(RGD) 6	114
Figure 40 : XRD patterns of NPs 5 (ratio AEP / P(RGD) 6 = 25/75)) after background subtraction	114
Figure 41 : XRD patterns of natural bone, NPs 1 (100% AEP) and stoichiometric HA	115
Figure 42 : XRD patterns of particles surrounded by a mixture of AEP / P(YIGSR) 7	115
Figure 43 : FTIR Spectra of particles surrounded by AEP / P(RGD) 6 25/75 (NPs 5)	116
Figure 44 : RAMAN spectra of NPs stabilized with a mixture of a) AEP/P(RGD) 6 and b) AEP/P(YIGSR) 7	117
Figure 45 : Difference and complementarity between size parameters obtained by DLS, DRX and TEM.....	118
Figure 46 : TEM imaging of NPs stabilized with 100% of AEP (NPs 1), with a mixture of AEP/P(RGD) 6 90/10 (NPs 2) and with a mixture of AEP/P(YIGSR) 7 90/10 (NPs 7).....	119
Figure 47 : Principe of Dynamic Light Scattering (DLS)	119
Figure 48 : DLS analysis of NPs surrounded with a mixture of AEP/P(RGD) 6 90/10 (NPs 2) and with a mixture of AEP/P(YIGSR) 7 90/10 (NPs 7) (Table 14)	120
Figure 49 : Functionalization of the peptidyl resin 2 with the commercial P(PEG5K)-COOH 12 by using a SPPS synthesis	125
Figure 50 : PEGylation of peptidyl resin 2 with FmocNH-PEG3K-COOH 15 and different initial loadings of 0.94, 0.47 and 0.3 mmol.g ⁻¹	127
Figure 51 : First attempt for the synthesis of PO ₃ Et ₂ (PEG3K) 21	129
Figure 52 : Multi-step synthesis of the P(PEG3K)-Peptide 27 , 28 , 29 and P(PEG3K)-NEt ₂ 30	130
Figure 53 : ¹ H NMR of the N-acyl benzotriazole 18	131
Figure 54 : ¹³ C- ¹ H HMBC NMR of PO ₃ Et ₂ (PEG3K) 21 ; calibrated with the PEG signal (e.g. PEG : 3.74 ppm - ¹ H / 69.6 ppm - ¹³ C)	132
Figure 55 : Superposition of the ¹ H NMR spectra of the desired product 21 and the two reagents 18 and 20	132
Figure 56 : Observation the amide carbonyle formed during the coupling between peptides or NEt ₂ with the carboxylic acid of the PO ₃ Et ₂ (PEG3K) 21	135
Figure 57 : Evolution of the dialkylphosphonate with McKenna reaction	137

Figure 58 : Picture of colloidal suspensions obtained for different R-PO ₃ H ₂ /Ca starting ratios: (0.005, 0.008, 0.01, 0.016, 0.032, 0.128) giving rise to NPs 12 to 17	139
Figure 59 : XRD patterns of NPs 12-17 (the NPs 14 sample was not analyzed due to too little product remaining).....	140
Figure 60: TEM imaging of NPs 15 before and after the dilution	142
Figure 61 : TEM imaging of the P(PEG3K)-NEt ₂ 30 /apatite NPs 12-17 prepared with different R-PO ₃ H ₂ /Ca ratios.....	143
Figure 62 : Curve representing the grafting density as a function of the R-PO ₃ H ₂ /Ca ratio..	145
Figure 63 : Conformation of organic molecule around a particle thanks to Flory's equation	146
Figure 64 : Synthesis of colloidal NPs of apatite stabilized with P(PEG3K)-Peptide 27, 28, 29 and P(PEG3K)-NEt ₂ 30	148
Figure 65 : X-Ray Diffraction pattern of NPs functionalized with different ratios of P(PEG3K)-NEt ₂ 30 /P(PEG3K)-RGD 27	149
Figure 66 : XRD patterns of NPs surrounded with a mixture of P(PEG3K)-NEt ₂ 30 /P(PEG3K)-RGD 27 – a) 0/100 - NPs 18 and b) 25/75 – NPs 19). The tabulated data report the mean crystallite dimensions as drawn from Scherrer's equation as well as the Ca/P ratio estimated from heating the samples at 1000°C for 15 h	150
Figure 67: XRD patterns of apatite NPs surrounded with a mixture of P(PEG3K)-YIGSR 28 and P(PEG3K)-NEt ₂ 30 (NPs 22-25).....	151
Figure 68: XRD patterns of apatite NPs surrounded with a mixture of P(PEG3K)-AhXRR 29 and P(PEG3K)-NEt ₂ 30 (NPs 26, 28 and 29)	152
Figure 69 : FTIR analyses of NPs surrounded with 100% P(PEG3K)-RGD 27 (NPs 18) as well as with 100% P(PEG3K)-NEt ₂ 30 (NPs 15). For comparison purposes, the FTIR spectra of the molecule P(PEG3K)-RGD 27 alone and a typical biomimetic apatite (matured 7 days at RT) have been added.....	153
Figure 70 : Zoomed-in view around the ν ₄ (PO ₄) domain of the FTIR spectra of NPs 18 and the reference biomimetic apatite sample	154
Figure 71 : RAMAN spectra for apatite NPs surrounded with 100% P(PEG3K)-RGD 27 (NPs 18) or with 100% P(PEG3K)-NEt ₂ 30 (NPs 15) and for the pure P(PEG3K)-RGD molecule 27	155
Figure 72 :Solid-state NMR analyses of apatite NPs surrounded with 100% P(PEG3K)-RGD 27 (NPs 18)	157
Figure 73 : TEM imaging of apatite NPs surrounded by different ratios of P(PEG3K)-Peptide 27, 28, 29 / P(PEG3K)-NEt ₂ 30 (NPs 18 to 29)	159
Figure 74 : General procedure to obtain (i) stabilizing concentration in 1 mL of colloidal suspension, ii) grafting density, iii) conformation of the stabilizing agents around the NPs and iv) peptide concentration in 1 mL of colloidal suspension	160
Figure 75 : ¹ H quantitative NMR spectra of NPs 19 surrounded by P(PEG3K)-NEt ₂ / P(PEG3K)-RGD 25/75	163
Figure 76 : Skin layers.....	169
Figure 77 : Healing process of an acute wound	171
Figure 78 : Resazurin reduction induced by live cells leads to the fluorescent product Resorufin	177
Figure 79 : Relative metabolic activity of i) NPs 15, 18, peptide 1'' and P(PEG3K)-RGD with a range of RGD peptide concentration from 0.07 to 2.25 mM and ii) NPs 15, 22, peptide 2'' and P(PEG3K)-YIGSR with a range of YIGSR peptide concentration from 0.06 to 1.91 mM	179

Figure 80 : Evolution of notch closure on the NIH/3T3 fibroblast monolayer over time in the presence of NPs 18 (1.13 mM) and NPs 22 (0.96 mM).....	181
Figure 81 : Antibacterial peptide PalmRR-NH ₂ and its analog H-AhXRR-NH ₂	182
Figure 82 : Experiments of membrane rigidity on primary human fibroblasts with or without apatite NPs and P(RDG) or P(YIGSR) peptide functionalization.....	184
Figure 83: Custom-built set-up for the determination of the absorption at saturation of a colloidal suspension of apatite NPs (stabilized here with AEP) on different commercial dressings.....	185
Figure 84 : SEM image before and after impregnation of dressings with colloidal suspension	186
Figure 85 : RAMAN analyses: left: typical photoluminescence spectrum of Eu ³⁺ ions (solution of europium nitrate) and right: 3D mapping on a fiber of alginate dressing (Algo steril) covered by dried colloidal apatite NPs	187
Figure 86 : Illustration of the freeze-casting approach to directly fabricate 3D dressings (here in alginate) loaded with hybrid apatite NPs. a) type of porous network obtained; b), c) and d) alginate dressings fabricated here by freeze-casting in the presence of Eu-doped apatite NPs, under UV light (254nm). In image d) two different types of homogenizing methods have been tested, namely the Ultra Turrax homogenizer (UT) and regular ultrasound (US)	188
Figure 87 : Spraying test of colloidal NPs (stabilized by AEP and doped with Eu ³⁺ ions)	190
Figure 88 : Preliminary spray test using a suspension of 60% colloidal NPs in water, sprayed on filter paper, and reference (sprayed with pure water).....	190
Figure 89 : ¹ H NMR Spectrum of 3-(diethoxyphosphoryl)propanoic acid 9 (CDCl ₃ , 600 MHz)	206
Figure 90: ³¹ P NMR Spectra of 3-(diethoxyphosphoryl)propanoic acid 9 (CDCl ₃ , 600 MHz, 31.0ppm)	206
Figure 91 : LC-MS Spectra of compound 10	209
Figure 92 : LC-MS Spectra of compound 11	210
Figure 93 : ¹ H NMR Spectrum of P(RGD) 6 (D ₂ O, 600 MHz).....	211
Figure 94 : ³¹ P NMR Spectrum of P(RGD) 6 (D ₂ O, 600 MHz, 36.32ppm)	211
Figure 95 : ¹ H NMR Spectrum of P(YIGSR) 7 (D ₂ O, 600 MHz)	212
Figure 96 : ³¹ P NMR Spectrum of P(RGD) 6 (D ₂ O, 600 MHz, 26.76ppm)	212
Figure 97: LC-MS Spectra of Ac-LRGDNK-NH ₂ peptide 1'	214
Figure 98: ¹ H NMR Spectrum of Ac-LRGDNK-NH ₂ peptide 1' (D ₂ O, 600 MHz)	215
Figure 99: ¹³ C NMR Spectrum of Ac-LRGDNK-NH ₂ peptide 1' (D ₂ O, 600 MHz)	215
Figure 100 : ¹ H- ¹ H COSY NMR Spectrum of Ac-LRGDNK-NH ₂ peptide 1' (D ₂ O, 600 MHz).....	216
Figure 101: ¹³ C- ¹ H HSQC NMR Spectrum of Ac-LRGDNK-NH ₂ peptide 1' (D ₂ O, 600 MHz)	217
Figure 102 : LC-MS Spectra of H-GDPGYIGSR-NH ₂ peptide 2'	219
Figure 103: ¹ H NMR Spectrum of H-GDPGYIGSR-NH ₂ peptide 2' (D ₂ O, 600 MHz)	220
Figure 104: ¹³ C NMR Spectrum of H-GDPGYIGSR-NH ₂ peptide 2' (D ₂ O, 600 MHz)	220
Figure 105 : ¹ H- ¹ H COSY NMR Spectrum of H-GDPGYIGSR-NH ₂ peptide 2' (D ₂ O, 600 MHz). 221	
Figure 106: ¹³ C- ¹ H HSQC NMR Spectrum of H-GDPGYIGSR-NH ₂ peptide 2' (D ₂ O, 600 MHz) 222	
Figure 107 : LC-MS Spectra of H-AhXRR-NH ₂ peptide 22	224
Figure 108: ¹ H NMR Spectrum of H-AhXRR-NH ₂ peptide 22 (D ₂ O, 600 MHz)	225
Figure 109: ¹ H- ¹ H COSY NMR Spectrum of H-AhXRR-NH ₂ peptide 22 (D ₂ O, 600 MHz).....	226
Figure 110: ¹³ C- ¹ H HSQC NMR Spectrum of H-AhXRR-NH ₂ peptide 22 (D ₂ O, 600 MHz)	226
Figure 111: ¹³ C- ¹ H HMBC NMR Spectrum of H-AhXRR-NH ₂ peptide 22 (D ₂ O, 600 MHz)	227
Figure 112 : LC-MS Spectra of N-acyl benzotriazole 18	228

Figure 113: ^1H NMR Spectra of the N-acyl benzotriazole 18 (D_2O , 600 MHz)	229
Figure 114: ^{31}P Spectra of the N-acyl benzotriazole 18 (D_2O , 600 MHz, 34.2ppm).....	229
Figure 115 : ^1H NMR Spectra of NH_2 -PEG3K-COOH 20 (D_2O , 600 MHz)	230
Figure 116 : ^1H NMR Spectrum of $\text{PO}_3\text{Et}_2(\text{PEG3K})\text{-COOH}$ 21 (D_2O , 600 MHz)	231
Figure 117: ^{13}C NMR Spectrum of $\text{PO}_3\text{Et}_2(\text{PEG3K})\text{-COOH}$ 21 (D_2O , 600 MHz)	231
Figure 118 : $^{13}\text{C}\text{-}^1\text{H}$ HMBC NMR Spectrum of $\text{PO}_3\text{Et}_2(\text{PEG3K})\text{-COOH}$ 21 (D_2O , 600 MHz)	232
Figure 119 : $^{13}\text{C}\text{-}^1\text{H}$ HSQC NMR Spectrum of $\text{PO}_3\text{Et}_2(\text{PEG3K})\text{-COOH}$ 21 (D_2O , 600 MHz)	232
Figure 120: ^{31}P NMR Spectra of $\text{PO}_3\text{Et}_2(\text{PEG3K})\text{-COOH}$ 21 (D_2O , 600 MHz).....	233
Figure 121 : ^1H NMR Spectrum of $\text{PO}_3\text{Et}_2(\text{PEG3K})\text{-NEt}_2$ 26 (D_2O , 600 MHz).....	234
Figure 122: ^{13}C NMR Spectrum of $\text{PO}_3\text{Et}_2(\text{PEG3K})\text{-NEt}_2$ 26 (D_2O , 600 MHz).....	235
Figure 123: $^{13}\text{C}\text{-}^1\text{H}$ HMBC NMR Spectrum of $\text{PO}_3\text{Et}_2(\text{PEG3K})\text{-NEt}_2$ 26 (D_2O , 600 MHz).....	235
Figure 124: $^1\text{H}\text{-}^1\text{H}$ COSY NMR Spectrum of $\text{PO}_3\text{Et}_2(\text{PEG3K})\text{-NEt}_2$ 26 (D_2O , 600 MHz)	236
Figure 125: $^{13}\text{C}\text{-}^1\text{H}$ HSQC NMR Spectrum of $\text{PO}_3\text{Et}_2(\text{PEG3K})\text{-NEt}_2$ 26 (D_2O , 600 MHz)	236
Figure 126: ^{31}P NMR Spectra of $\text{PO}_3\text{Et}_2(\text{PEG3K})\text{-NEt}_2$ 26 (D_2O , 600 MHz, 33.2ppm).....	237
Figure 127 : ^1H NMR Spectrum of $\text{PO}_3\text{Et}_2(\text{PEG3K})\text{-RGD}$ 23 (D_2O , 600 MHz)	238
Figure 128 : ^{13}C NMR Spectrum of $\text{PO}_3\text{Et}_2(\text{PEG3K})\text{-RGD}$ 23 (D_2O , 600 MHz).....	239
Figure 129: $^{13}\text{C}\text{-}^1\text{H}$ HMBC NMR Spectrum of $\text{PO}_3\text{Et}_2(\text{PEG3K})\text{-RGD}$ 23 (D_2O , 600 MHz).....	239
Figure 130: $^1\text{H}\text{-}^1\text{H}$ COSY NMR Spectrum of $\text{PO}_3\text{Et}_2(\text{PEG3K})\text{-RGD}$ 23 (D_2O , 600 MHz)	240
Figure 131: $^{13}\text{C}\text{-}^1\text{H}$ HSQC NMR Spectrum of $\text{PO}_3\text{Et}_2(\text{PEG3K})\text{-RGD}$ 23 (D_2O , 600 MHz).....	240
Figure 132: ^{31}P NMR Spectra of $\text{PO}_3\text{Et}_2(\text{PEG3K})\text{-RGD}$ 23 (D_2O , 600 MHz, 33.8ppm).....	241
Figure 133 : ^1H NMR Spectrum of $\text{PO}_3\text{Et}_2(\text{PEG3K})\text{-YIGSR}$ 24 (D_2O , 600 MHz).....	242
Figure 134: $^{13}\text{C}\text{-}^1\text{H}$ HSQC NMR Spectrum of $\text{PO}_3\text{Et}_2(\text{PEG3K})\text{-YIGSR}$ 24 (D_2O , 600 MHz)	242
Figure 135: $^{13}\text{C}\text{-}^1\text{H}$ HMBC NMR Spectrum of $\text{PO}_3\text{Et}_2(\text{PEG3K})\text{-YIGSR}$ 24 (D_2O , 600 MHz)	243
Figure 136: ^{31}P NMR Spectra of $\text{PO}_3\text{Et}_2(\text{PEG3K})\text{-YIGSR}$ 24 (D_2O , 600 MHz, 34.0ppm).....	243
Figure 137: ^1H NMR Spectra of $\text{PO}_3\text{Et}_2(\text{PEG3K})\text{-AhXRR}$ 24 (D_2O , 600 MHz).....	244
Figure 138 : $^{13}\text{C}\text{-}^1\text{H}$ NMR Spectra of $\text{PO}_3\text{Et}_2(\text{PEG3K})\text{-AhXRR}$ 24 (D_2O , 600 MHz).....	245
Figure 139: ^{31}P NMR Spectra of $\text{PO}_3\text{Et}_2(\text{PEG3K})\text{-AhXRR}$ 24 (D_2O , 600 MHz, 33.8ppm)	245
Figure 140 : ^{31}P NMR of peptide-based stabilizing agents P(PEG3K)-Peptide 27, 28, 29 and of P(PEG3K)- NEt_2 30 (D_2O , 600 MHz)	246
Figure 141 : LC-MS Spectra of peptide Ac-LRGDNK(Ac)- NH_2 . 1''	249
Figure 142 : LC-MS Spectra of peptide Ac-GDPGYIGSR- NH_2 . 2''	250

Tables index

Table 1: Summary of the main members of apatite-group minerals ²	51
Table 2: Main compounds of the calcium phosphate (CaPs) family of minerals.....	52
Table 3: FTIR band positions of nanocrystalline hydroxyapatite in the 400-4000 cm ⁻¹ range	58
Table 4: Position and allocation of FTIR bands around the $\nu_4(\text{PO}_4)$ domain ⁹	60
Table 5: Synthesis methods to generate (hydroxy)apatite nanoparticles	62
Table 6: Summary of the contributions of nanoparticles compared to active agents used alone (adapted from ref ⁵⁶)	72
Table 7: Summary of apatite NPs-based strategies	83
Table 8 : List of proteogenic AAs and their protections for the Fmoc/tBu strategy.....	95
Table 9 : Resins used during the PhD project	97
Table 10 : Sequences and pHi of peptide-based P(Peptide) stabilizing agents	103
Table 11 : Microcleavage LC-MS analysis of peptidyl resin 1 and 2	105
Table 12 : Microcleavage and cleavage LC-MS analyses of the intermediate 10 and 11 and of the final P(RGD) 6	108
Table 13 : Observations of suspension after maturation time for NPs 1 to 11	112
Table 14 : DLS analyses of NPs 1, 2 and 7	120
Table 15 : Concentration of stabilizing agents AEP/P(Peptide) present in 1mL of colloidal suspension (NPs 1 to 11) estimated by ³¹ P ERETIC NMR (ND: Not Dtermine)	122
Table 16 : Sequences of the new family of peptide-based stabilizing agents P(PEG3K)-Peptide	124
Table 17 : Pegylation of peptidyl resin: the influence en PEG length (adapted from ¹¹⁷)	126
Table 18 : Results of a Fmoc dosage after the terN functionalization of the peptidyl resin 2 with a FmocNH-PEG3K-COOH 15 on solid support	127
Table 19: Sequences of the peptides 1' , 2' and 22	133
Table 20 : Reference number, name and sequence of compounds obtained during the multi- steps synthesis (Figure 52)	134
Table 21 : ¹³ C- ¹ H HMBC NMR Correlation between the PO ₃ Et ₂ (PEG3K) 21 and the peptides or NEt ₂	135
Table 22 : PEGylation rate, yield and masse obtained of compounds 23 , 24 , 25 and 26	136
Table 23 DLS and TEM characterizations of hybrid P(PEG3K)-NEt ₂ 30 /apatite NPs 12-17 with different R-PO ₃ H ₂ /Ca	141
Table 24 : ³¹ P ERETIC NMR characterizations of P(PEG3K)-NEt ₂ 30 /apatite hybrid NPs obtained with different R-PO ₃ H ₂ /Ca ratios	144
Table 25 : DLS and TEM characterizations of NPs 18 to 29.....	158
Table 26 : Liquid-state NMR characterizations of NPs 18 to 2.....	164
Table 27: Maximum volume of colloidal apatite NPs at saturation (in mL) by dressing samples (m \cong 0.06 g) and mean absorption rate in wt. %	186
Table 28 : Protons and carbons chemical shift assignments of the peptide Ac-LRGDNK-NH ₂ 1' (D ₂ O, 600 MHz)	216
Table 29 : Protons and carbons chemical shift assignments of the peptide H-GDPGYIGSR-NH ₂ 2' (D ₂ O, 600 MHz).....	221
Table 30 : Proton and carbons chemical shift assignments of the peptide H-AhXRR-NH ₂ 22 (D ₂ O, 600 MHz).....	225

Table 31 : Yield and mass obtained (mg) for PO ₃ Et ₂ (PEG3K)-NEt ₂ 26 and PO ₃ Et ₂ (PEG3K)-Peptide 23, 24, 25	233
Table 32 : Summary of the stabilizing agents quantities P(Peptide) 6 or 7 used for the synthesis of NPs 1-11	247
Table 33 : Summary of the stabilizing agents quantities P(PEG3K)-NEt ₂ and P(PEG3K)-Peptide used for the synthesis of NPs 12-29.....	248

Equations index

Équation 1 : Determination of the volume of NPs cylinder NPs 15 with a R-PO ₃ H ₂ /Ca equal to 0.016 (Table 23).....	144
Équation 2 : Determination of the number of NPs obtained in 1mL of colloidal suspension NPs 15.....	144
Équation 3 : Determination of the number of stabilizing agents P(PEG3K)-NEt ₂ 30 in 1mL of colloidal suspension (Table 23)	145
Équation 4 : Determination of the surface of a cylindrical NPs 15 with r the radius of the particle obtained by TEM (Table 23)	145
Équation 5 : Determination of the number of P(PEG3K)-NEt ₂ 30 per nm ² on NPs 15.....	145

List of abbreviations

APTES	3-Aminopropyltriethoxysilane
AA	Amino Acid
ACN	Acetonitrile
AEP	2-Aminoethylphosphate
APIs	Pharmaceutical active agents
ATP	Adenosine Triphosphate
BCS	Calf Bovine Serum
Boc	tert-Butoxycarbonyl
BOP	Benzotriazol-1-yloxytris(dimethylamino)phosphonium hexafluorophosphate
CaP	Calcium phosphate
COSY	Correlated spectroscopy
DBF	Dibenzofulvene
DCC	Dicyclohexylcarbodiimide
DCM	Dichloromethane
DIC	N,N'-diisopropylcarbodiimide
DIEA	N,N-Diisopropylethylamine
DLS	Dynamic light scattering
DMEM	Dulbecco's Modified Eagle Medium
DMF	N,N-dimethylformamide
DNA	Deoxyribonucleic acid
DOX	Doxorubicine
ECM	Extracellular matrix
EDC	1-Ethyl-3-(3-dimethylaminopropyl)carbodiimide
EPR	Enhanced permeability and retention effect
ERETIC	Electronic reference to access in vivo concentration
ESXY	Exchange spectroscopy
Et ₂ O	Diethylether
EtOAc	Ethyl Acetate
FA	Folic Acid
FBS	Fetal Bovine Serum
Fmoc	Fluorenylmethyloxycarbonyl
FTIR	Fourier Transform Infrared Spectroscopy
HA	Hydroxyapatite
HATU	N,N-dimethylmethaniminium Hexafluorophosphate
HBTU	2-(1H-benzotriazole-1-yl)-1,1,3,3-tetramethyluronium hexafluorophosphate
HMBC	Heteronuclear multiple bond correlation
HMBC	Heteronuclear multiple bond correlation
HOAt	1-Hydroxy-7-azabenzotriazole

HOBt	Hydroxybenzotriazole
HPLC	High performance liquid chromatography
HSQC	Heteronuclear single quantum coherence
LC-MS	Liquid Chromatography -Mass Spectroscopy
LPS	Lipopolysaccharide
MEAlpha	Minimum Essential Medium Alpha
MIC	Minimum inhibitory concentration
MTX	Methotrexate
MW	Molecular weight
NHS	N-hydrosuccinimide
NMR	Nuclear magnetic resonance
NOESY	Nuclear Overhauser effect spectroscopy
NPs	Nanoparticles
PA	Polyamide
PBS	Phosphate Buffer Saline
PdI	Polydispersity index
PEG	Poly(ethylene)glycol
PhCol	Phosphocoline chloride
PS	Polystyrene
PyAOP	Benzotriazol-1-yloxytripyrrolidinophosphonium hexafluorophosphate
RNA	Ribonucleic acid
siRNA	Small Interfering RNA
SPPS	Solid Support Synthesis
TCP	Tricalcium phosphate
TEM	Transmission electron microscopy
TFA	Trifluoroacetic acid
TIS	Triisopropylsilane
TMSBr	Bromotrimethylsilane
UV	Ultraviolet
XRD	X-Ray Diffraction

Extended summary (in French) of the PhD

La recherche biomédicale s'intéresse de plus en plus à l'utilisation de matériaux biofonctionnels. C'est notamment le cas pour la vectorisation de principes actifs pour des traitements locaux – moins invasifs et plus ciblés que les traitements systémiques – où le développement et l'utilisation de (nano)vecteurs de médicaments sont de plus en plus explorés, par exemple en oncologie et en imagerie médicale, mais aussi plus récemment en hématologie ou en dermatologie. Parmi l'arsenal de « biotechnologies » développé qui comprend les (nano)vecteurs d'agents biologiquement actifs, les particules organiques ou inorganiques sont particulièrement attrayantes. Outre une éventuelle protection du principe actif via son association avec des particules, l'utilisation de ces dernières présente également d'autres avantages tels que la possibilité de cumuler plusieurs agents biologiquement actifs (ioniques ou moléculaires) pour une complémentarité d'actions voire des effets synergiques, ou la possibilité de permettre la libération "intelligente" de principes actifs, par exemple via l'hydrolyse d'un fragment moléculaire ou par la dissolution sélective des vecteurs en fonction de stimuli tels que le pH local ou une activité enzymatique. Les vecteurs étudiés au cours des années, qu'ils soient organiques ou inorganiques, présentent en effet des avantages dans leur capacité à agir comme vecteurs de médicaments et pour leur stabilisation. Toutefois, ils présentent aussi généralement des inconvénients comme une certaine toxicité, une faible stabilité ou encore une absence de biodégradabilité. Dans cette optique, la recherche de (nano)vecteurs hautement biocompatibles et (multi)fonctionnalisables constitue plus que jamais un défi majeur en biomédecine, notamment compte-tenu du vieillissement des populations.

Dans ce contexte, le caractère bio-inspiré des phosphates de calcium à structure "apatite" très proches du minéral osseux naturel, leur grande réactivité de surface et leur modularité, en font d'excellents candidats pour des applications biomédicales, et ce non seulement en lien avec des applications comme substituts osseux, mais aussi en « (nano)médecine » comme vecteurs d'agents thérapeutiques. D'autre part, les peptides peuvent présenter de très nombreux effets biologiques comme des propriétés pro-cicatrisantes ou antibactériennes. Associer dans un même (nano)objet des apatites nanocristallines avec des peptides bioactifs peut ainsi constituer une approche résolument bio-inspirée et pertinente, et à ce jour quasiment inexplorée dans le domaine de la nanomédecine, par exemple pour le traitement de plaies complexes. Il s'agit là du principal objectif de ce travail de thèse.

I. Etat de l'art

Les phosphates de calcium à structure « apatite » sont présents naturellement dans la constitution du squelette de tous les vertébrés, depuis leur apparition sur Terre il y a plusieurs millions d'années. Il s'agit donc de composés que le corps humain, notamment, a appris à produire, utiliser puis éliminer en fonction de ses besoins. Il est désormais possible de

préparer des analogues de synthèse inspirés de ces apatites naturelles, en vue d'applications biomédicales.

Grâce à sa structure accueillante, l'apatite peut être dopée par de nombreux ions biologiquement actifs (par exemple Cu^{2+} , Zn^{2+} , Sr^{2+} , Mg^{2+} ...) pour leur conférer des propriétés biologiques additionnelles, ou encore des ions luminescents (Eu^{3+} , Tb^{3+} ...) pour des applications en diagnostic médical. De plus, la forte réactivité de surface des cristaux d'apatites nanocristallines biomimétiques (analogues au minéral osseux) permet d'envisager l'adsorption de divers types de composés moléculaires tels que des agents dispersants/stabilisants ou encore des agents thérapeutiques variés (antibiotiques, anticancéreux, hémostatiques, anti-ostéoporotiques, enzymes, facteurs de croissance, agents de ciblage cellulaire, etc.). De telles (nano)particules minérales-organiques sont alors dites hybrides car impliquant une interaction entre les composantes organiques et inorganiques à l'échelle moléculaire (à l'opposé d'un "simple" système composite). Pour pouvoir interagir de manière reproductible à une échelle cellulaire ou tissulaire, il est par ailleurs pertinent de disposer de (nano)particules présentant une taille submicronique, relativement monodisperse et si possible une stabilité colloïdale. Ceci a été rendu possible dans l'état de l'art par l'adsorption d'agents stabilisants tels que le 2-aminoéthylphosph(on)ate (AEP), la phosphocholine, les ions citrates, ou encore le poly(éthylène glycol) phosphonaté (P(PEG)-OCH₃) qui agissent par répulsion électrostatique et/ou par gêne stérique (Tableau 1). Les molécules pouvant être adsorbées de manière relativement stable à la surface de l'apatite présentent en général un groupement anionique avec une affinité (électrostatique) notable pour les ions calcium de surface, tels que les groupements phosphates, phosphonates, voire carboxylates, sulfonates et alcoolates.

Tableau 1 : Diamètre hydrodynamique et indice de polydispersité des NPs d'apatite obtenues dans la littérature par co-précipitation stabilisées par des agents stabilisants (AEP, PhCol, Citrate et P(PEG)-OCH₃)

	Diamètre hydrodynamique (nm)	Indice de Polydispersité (Pdl)
AEP	25	0,07
PhCol	70	0,11
Citrate	200	0,26
P(PEG)-OCH ₃	130 (530 g.mol ⁻¹)	0,33
	350 (5800 g.mol ⁻¹)	0,4

Jusqu'à ce jour, l'ajout de propriétés biologiques additionnelles (autre via une substitution ionique de l'apatite) n'a cependant été possible que par la co-adsorption, après synthèse des particules colloïdales d'apatite, d'une molécule thérapeutique ou de ciblage cellulaire. Il s'agit donc systématiquement à ce jour de synthèses multi-étapes passant d'abord par la cristallisation de l'apatite et sa stabilisation colloïdale, puis par une étape subséquente d'adsorption de l'agent biologiquement actif. Cependant, cette co-adsorption peut mener à des problèmes d'adsorption compétitive car le nombre de sites présents en surface des

particules reste limité. De plus, il apparaîtrait pertinent de mettre au point des composés moléculaires qui puissent à la fois stabiliser les (nano)particules d'apatite et simultanément leur conférer des propriétés biologiques. Enfin, la force de la liaison entre l'apatite et la surface est fortement dépendante des fonctions présentes sur chaque molécule à adsorber. Ainsi, disposer de nanoparticules (NPs) d'apatite "plateforme" permettant une modulation aisée de la nature de l'agent actif associé présenterait un avantage conséquent sur les systèmes existant à ce jour.

Certaines applications biomédicales requièrent des particules d'apatite de taille nanométrique, notamment pour agir à l'échelle cellulaire voire subcellulaire. Pour ce faire, différentes méthodes de synthèse par voie solide ou par voie humide ont été élaborées. Celle que nous retiendrons ici est la méthode par co-précipitation avec ajout d'agent stabilisant (fonctionnalisé dans notre cas par un peptide) pendant la synthèse (Figure 1).

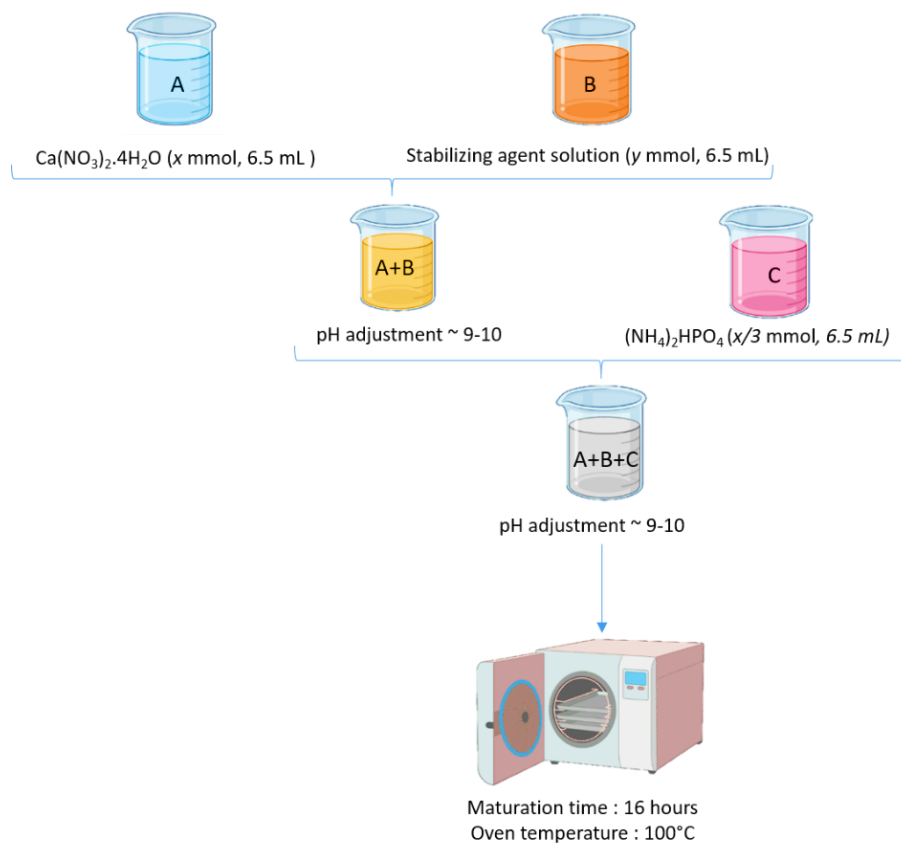


Figure 1 : Synthèse one-pot par co-précipitation de NPs d'apatite colloïdale grâce à l'utilisation d'agent stabilisant

L'objectif de ce projet de thèse est d'établir la preuve de concept de la synthèse one-pot de particules d'apatite bio-inspirées colloïdales de taille nanométrique stabilisées par de nouveaux agents stabilisants bioactifs à base de peptides. Ces nouveaux agents stabilisants pourront ainsi jouer un double rôle : (i) stabiliser les particules de taille nanométrique en une suspension colloïdale stable et (ii) conférer des propriétés biologiques supplémentaires aux

particules d'apatite grâce aux peptides dont la nature pourra être variées pour des propriétés "à la carte" dans une approche de NPs "plateforme". Dans ce travail, nous avons sélectionné trois séquences peptidiques possédant des propriétés physico-chimiques et biologiques différentes : Ac-LRGDNK-NH₂, H-GDGPYIGSR-NH₂ (peptides d'adhésion cellulaire) et H-AhXRR-NH₂ (peptide antibactérien). Deux familles d'agents stabilisants à base de peptide, inspirées d'agents stabilisants connus et simples, ont alors été synthétisées : P(Peptide) et P(PEG3K)-Peptide.

II. Synthèse de nanoparticules stabilisées avec les nouveaux agents stabilisants P(Peptide)

A. Synthèse des P(Peptide) sur support solide

Les nouveaux agents stabilisants bioactifs P(Peptide) ont été synthétisés sur support solide via une stratégie Fmoc/tBu sur une résine Rink Amide PS pour obtenir une terminaison C-terminal amide. Un analogue acide de l'AEP, l'acide 3-(diéthoxyphosphoryl)propionique a été couplé sur support solide sur le N-terminal de la H-GDGPYIGSR-NH₂ et sur la chaîne latérale de la Lysine dans le cas de la séquence Ac-LRGDNK-NH₂. Afin d'activer l'acide carboxylique de l'acide 3-(diéthoxyphosphoryl)propionique en présence du groupement phosphonate, il était nécessaire de protéger ce dernier sous forme dialkyle. La dealkylation du phosphonate a été réalisée grâce à la réaction de McKenna adaptée sur support solide. Après clivage et purification par HPLC préparative, les nouveaux agents stabilisants P(RGD) et P(YIGSR) ont été obtenus avec respectivement 56% de rendement (93% de pureté) et 41% de rendement (94% de pureté).

B. Synthèse et caractérisation des NPs d'apatite stabilisées avec différents ratios AEP/P(Peptide)

Afin d'obtenir une suspension colloïdale par répulsion électrostatique et d'observer l'influence des peptides sur la précipitation de l'apatite, une étude de co-adsorption d'AEP et de P(Peptide) a été réalisée avec différentes proportions de départ de ces deux agents stabilisants (100/0, 90/10, 75/25, 50/50, 25/75 et 0/100 (Figure 2)).

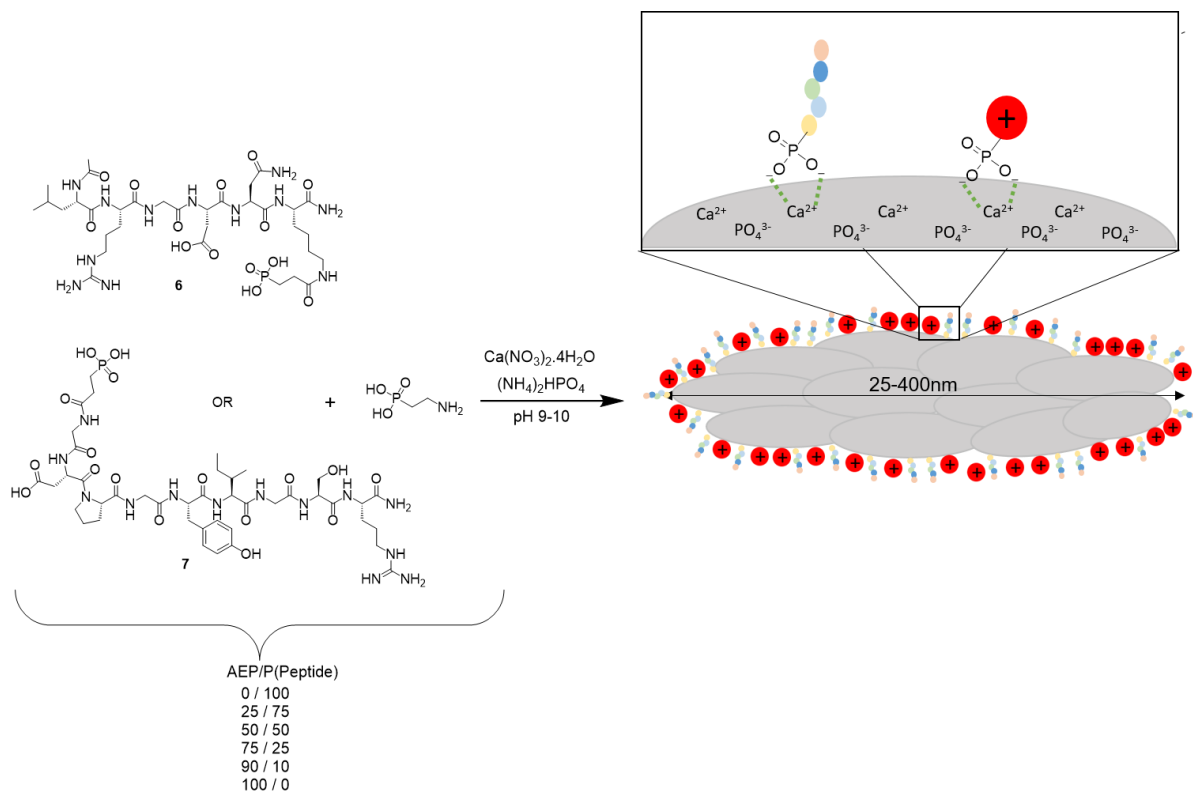


Figure 2 : Synthèse par co-précipitation des NPs d'apatite avec différents ratios entre AEP et P(Peptide)

Quel que soit le peptide, une suspension colloïdale n'a pu être obtenue que lorsque la quantité d'AEP était largement majoritaire, typiquement de l'ordre de AEP/P(Peptide) = 90/10. Les résultats ont ainsi montré que les P(Peptide) présents autour des particules ne permettaient pas de limiter efficacement l'agglomération de particules adjacentes d'apatite par répulsion électrostatique ou stérique entre les P(Peptide) adsorbés à leur surface. Aucune particule nanométrique de taille contrôlée n'a pu être obtenue par cette approche, comme démontré par DLS. Dans certains cas, la quantité de molécules organiques greffées autour des particules a été déterminée par spectroscopie RMN liquide ERETIC ^{31}P lorsque la sensibilité de l'appareil le permettait. Les résultats ont montré que le rendement de greffage n'était pas reproductible. De plus, la spectroscopie RAMAN a confirmé que la proportion de composante organique associée aux particules ne suivait en effet pas une tendance claire, probablement à cause d'interactions additionnelles non contrôlées entre les groupements chargés exposés en surface des peptides et des ions de surface de l'apatite. La présence de P(Peptide) ne semblait pas, en revanche, modifier notablement les paramètres structuraux de l'apatite formée, puisqu'une phase apatitique modérément cristallisée a été obtenue dans tous les cas étudiés, ce dont ont témoigné des analyses par DRX et FTIR.

Ces conclusions suggèrent qu'il peut être pertinent d'éloigner les entités peptidiques de la surface de l'apatite afin de viser une stabilité colloïdale. Dans la partie suivante de l'étude, un linker PEG a été utilisé dans ce but.

III. Synthèse des NPs stabilisées avec les nouveaux agents stabilisants P(PEG3K)-Peptide

A. Synthèse des nouveaux agents stabilisants P(PEG3K)-Peptide

Après des tentatives infructueuses de synthèse des nouveaux agents stabilisants P(PEG3K)-Peptide sur support solide, une synthèse multi-étape en solution a été mise au point (Figure 3). Pour éviter les purifications par HPLC préparative ou sur colonne qui conduiraient à des pertes de produits trop importantes, une stratégie a été développée pour obtenir quantitativement les produits sans nécessité d'étape de purification additionnelle.

Les peptides Ac-LRGDNK-NH₂ **1'**, H-GDPGYIGSR-NH₂ **2'** et H-AhXRR-NH₂ **22** ont été synthétisés sur support solide et obtenus après purification avec respectivement 32%, 41% et 48% de rendement et 98%, 95% et 89% de pureté. Ensuite, le même analogue de l'AEP, l'acide 3-(diethoxyphosphoryl)propionique **9** utilisé pour la synthèse des P(Peptide) a été utilisé. La formation du N-acyl benzotriazole **18** a permis d'activer la fonction acide carboxylique de l'acide 3-(diethoxyphosphoryl)propionique **9** et de procéder à la réaction d'amidation quantitativement avec l'amine primaire libre du NH₂-PEG3K-COOH **20**. La séparation par une simple étape de lavage du N-acyl benzotriazole **18** introduit en excès et du produit désiré PO₃Et₂(PEG3K)-COOH **21** est également rendue possible grâce au groupement benzotriazole. La pré-activation de l'acide carboxylique du PO₃Et₂(PEG3K)-COOH **21** par l'HATU et la DIEA a permis le couplage avec les amines primaires en N-ter des peptides H-AhXRR-NH₂ **22** et H-GDPGYIGSR-NH₂ **2'** et sur la chaîne latérale de la lysine du peptide Ac-LRGDNK-NH₂ **1'**.

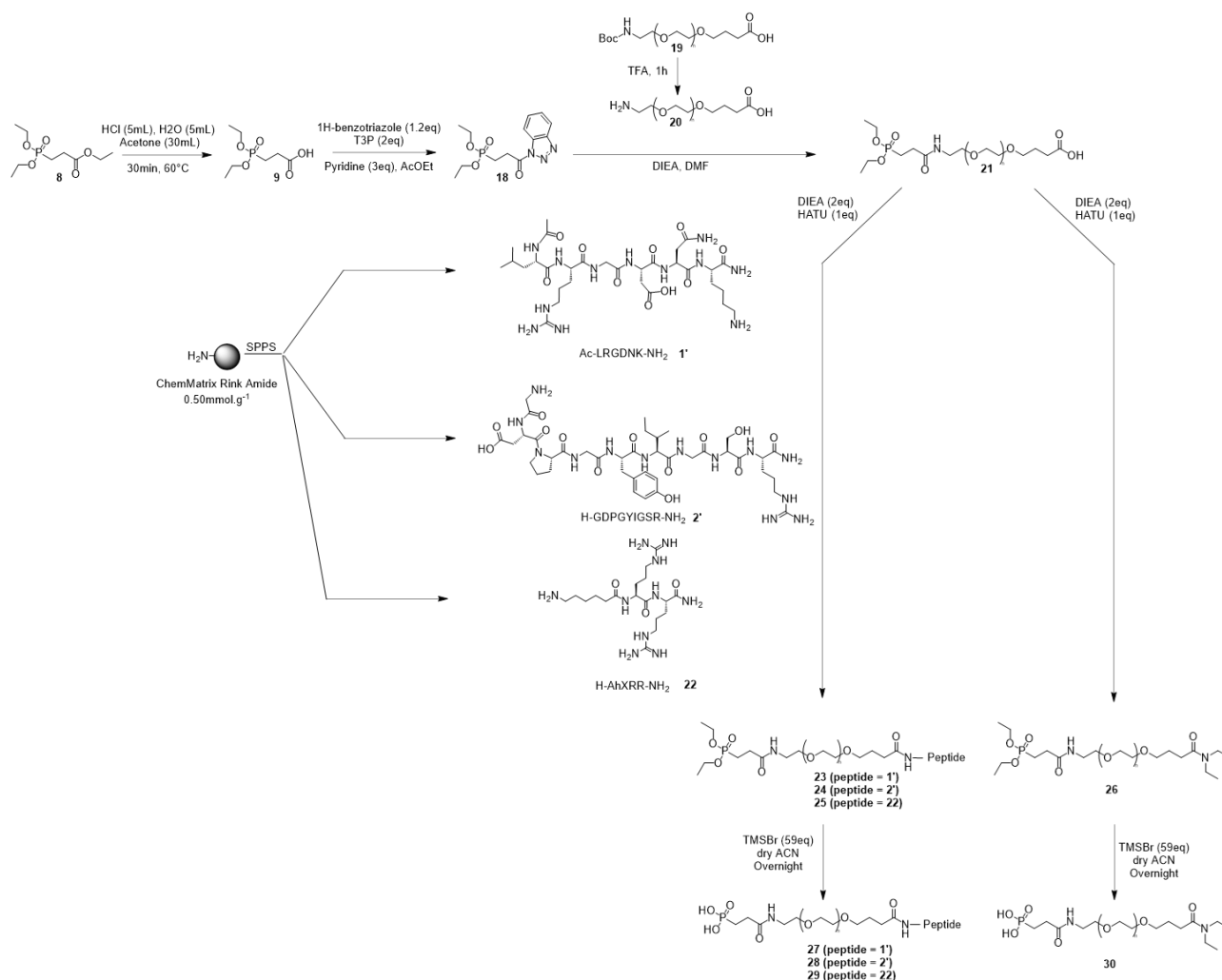


Figure 3 : Synthèse multi-étapes des nouveaux agents stabilisants P(PEG3K)-Peptide

Des suivis par RMN liquide ¹H et ¹³C-¹H HMBC ont permis de confirmer la structure des conjugués PEGylés obtenus et de quantifier le taux de phosphorylation et de PEGylation. Enfin, la dealkylation des phosphonates a été réalisée en solution grâce à la réaction de McKenna.

B. Synthèse et caractérisation des NPs d'apatite stabilisées avec une couronne organique de P(PEG3K)-NEt₂/ P(PEG3K)-Peptide

1. Détermination du rapport R-PO₃H₂/Ca

Des expériences préliminaires ont été réalisées afin de déterminer le ratio R-PO₃H₂/Ca approprié pour la synthèse des NPs avec les nouveaux agents stabilisants P(PEG3K)-Peptide **27**, **28** et **29**. Ces expériences ont été réalisées avec l'agent stabilisant P(PEG3K)-NEt₂. Parmi les valeurs du rapport R-PO₃H₂/Ca testées, le rapport égal à 0,016 s'est avéré être le meilleur compromis pour obtenir à la fois des particules colloïdales de taille nanométrique, une phase apatitique biomimétique (proche du minéral osseux) et une densité de greffage suffisamment importante pour les analyses subséquentes et les expériences biologiques. De plus, la

conformation en peigne ou « régime en brosse » des molécules organiques autour des particules a été démontrée par application de l'équation de Flory sur la base de divers résultats expérimentaux (MET, RMN). Cela est de bon augure car nous pouvons attendre des résultats similaires avec l'agent stabilisant complet, P(PEG3K)-Peptide, et ainsi disposer de nanoparticules qui exposent le peptide bioactif à la surface externe des particules (et non pas recroquevillé en conformation de pelote) en vue d'interactions externes. C'est pourquoi ce rapport a été choisi pour le reste des expériences.

2. Synthèse et caractérisation des NPs stabilisées par différents ratios de P(PEG3K)-NET₂/P(PEG3K)-Peptide

Différents rapports entre les conjugués P(PEG3K)-Peptide **27**, **28** et **29** et P(PEG3K)-NET₂ **30** ont été évalués (100/0, 25/75, 50/50, 75/25 et 0/100) (Figure 4) afin d'observer l'influence des peptides et de tester la co-présentation possible de deux molécules à la surface des particules.

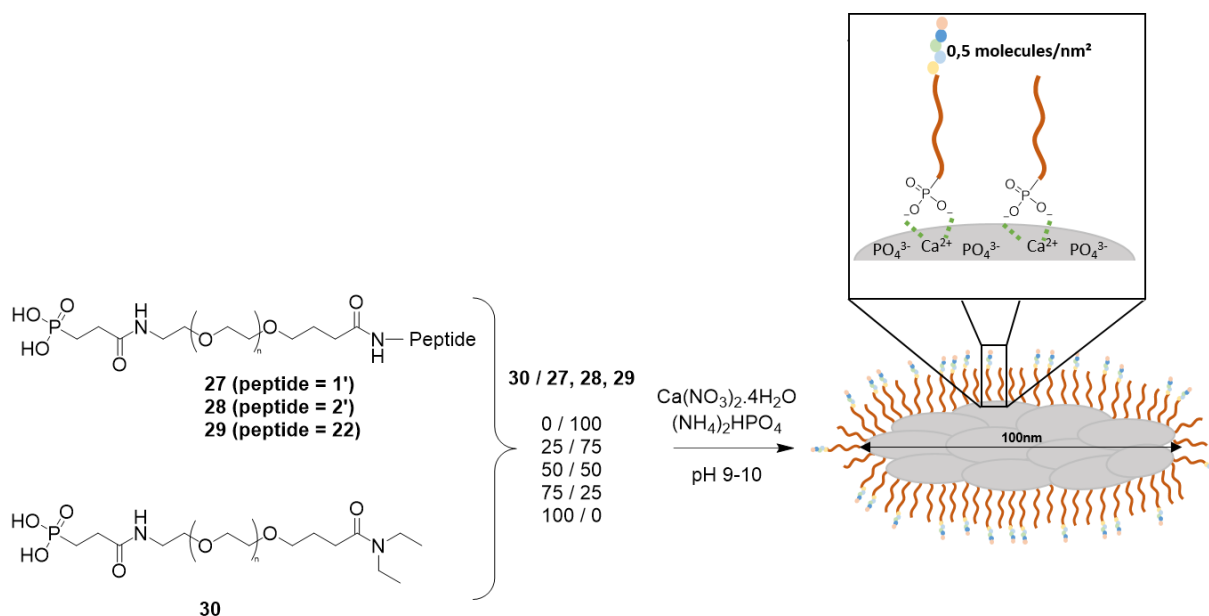


Figure 4 : Synthèse des NPs d'apatite stabilisées par un mélange de P(PEG3K)-NET₂ et P(PEG3K)-Peptide

L'incorporation d'agents stabilisants à base de peptides P(PEG3K)-Peptide ou d'un mélange de P(PEG3K)-Peptide et P(PEG3K)-NET₂ dans la synthèse d'apatites a permis d'obtenir dans tous les cas des suspensions colloïdales, quel que soit le peptide; et ces suspensions se sont avérées être constituées de NPs d'apatite sous-stœchiométriques assez proches du minéral osseux, comme démontré par DRX, FTIR et RAMAN. Notre hypothèse selon laquelle l'ajout d'une petite molécule à l'extrémité d'une longue chaîne PEGylée ne perturberait pas le rôle stabilisant du PEG a ainsi été confirmée. Les analyses par MET et DLS ont montré des particules de taille nanométrique (~100 nm – Pdl < 0.3) en cohérence avec une forme ellipsoïdale/de bâtonnets quelles que soient les NPs synthétisées. La présence de peptides autour de l'apatite

n'a pas non plus eu d'influence sur la densité de greffage (évaluée à $\sim 0,5$ molécules/nm² d'après les données de MET et RMN) ni sur la conformation en brosse de la couronne organique autour des NPs. Une étude par RMN du solide ¹H et ³¹P a permis par ailleurs de confirmer la proximité spatiale du phosphonate des conjugués organiques et de la surface de l'apatite, démontrant donc que le greffage de la molécule se faisait bien par le biais de la fonction phosphonate terminale des conjugués et non par le squelette peptidique. Deux types de mode de greffage ont pu alors être identifiés : monodentate et bidentate.

IV. Evaluation biologique des NPs d'apatite colloïdale stabilisées par P(PEG3K)-Peptide et tests préliminaires de formulation

Le potentiel d'application biomédical pour le traitement des plaies complexes des NPs 18 et 22 d'apatite entourées respectivement par les nouveaux agents stabilisants bioactifs P(PEG3K)-Peptide **27** et **28** a été évalué par des essais biologiques préliminaires.

Nous avons d'abord démontré la bonne biocompatibilité des NPs 18 et 22 sur des fibroblastes murins NIH/3T3. Nous avons pu mettre en évidence un phénomène synergique de chaque composante (organique et inorganique) des NPs sur la prolifération des fibroblastes. Par ailleurs, des tests de rayure de films 2D de fibroblastes ont été réalisés en présence ou en absence des NPs exposant les P(PEG3K)-Peptides pro-adhésifs, et une fermeture plus rapide du tapis cellulaire a été observée lorsque les NPs hybrides mises au point dans ce travail étaient utilisées.

En revanche, les tests antibactériens préliminaires réalisés à ce jour avec uniquement l'agent stabilisant P(PEG3K)-AhXRR seul n'ont pas mené à des résultats positifs contrairement aux attentes initiales. Cependant, ceci pourrait être lié au fait que l'agent stabilisant P(PEG3K)-AhXRR soit terminé par un groupement phosphonate qui rend la molécule beaucoup plus hydrophile que l'acide palmitique initial présentant les propriétés antibactériennes connues de la littérature. De nouveaux tests pour déterminer la concentration minimale inhibitrice (CMI) seront donc à prévoir avec l'agent stabilisant P(PEG3K)-AhXRR greffé sur les NPs. En effet, dans ce cas, comme le groupement phosphonate chélate les ions Ca²⁺ apatitiques, nous espérons alors trouver des propriétés antibactériennes similaires à celles de l'acide palmitique.

Enfin, des premiers essais de formulation intégrant ces nouvelles NPs hybrides apatite/peptide ont été initiés, dans le but d'illustrer divers types de dispositifs médicaux qui pourraient être mis au point pour les délivrer. Nous avons notamment exploré l'imprégnation de pansements commerciaux de 5 types différents, dont des pansements à base d'alginate ayant présenté un très fort taux de recouvrement des fibres par les NPs comme mis en évidence par MEB. Par un marquage des NPs via la substitution d'une partie des ions calcium de l'apatite par des ions europium Eu³⁺ luminescents, nous avons pu suivre la localisation des NPs après imprégnation, par cartographie 3D sous un microscope RAMAN confocal,

permettant de confirmer le fort recouvrement des fibres précédemment mentionné. Dans une seconde approche, nous nous sommes attachés à fabriquer des pansements/mousses poreuses par congélation-sublimation (« freeze-casting » en anglaise) directement en présence de NPs colloïdales d'apatite, et avons là encore démontré par la luminescence de l'euporium la bonne dissémination des NPs dans toute la matrice poreuse fabriquée. Qu'il s'agisse d'une imprégnation *a posteriori* de pansements commerciaux, ou au contraire de la synthèse de pansements *in situ* en présence de NPs, nous avons ainsi illustré la possibilité d'enrichir/d'élaborer des dispositifs médicaux (ici à base d'alginate) de manière possiblement modulable (nature et dose des peptides...) pour s'adapter au mieux aux besoins cliniques de traitement de plaies. La possibilité de détenir des pansements/mousses relativement épaisses (comme obtenues ici par freeze-casting) peut par exemple permettre de combler des plaies profondes comme dans le cas du pied du diabétique. Une troisième méthodologie a enfin été explorée de manière très préliminaire : la voie des pansements en spray. Nous avons là encore démontré que – sauf pour une concentration trop importante en NPs dans la suspension à pulvériser – les suspensions diluées pouvaient être « sprayées » sur une surface cible, ce qui peut présenter un intérêt pour le traitement de plaies de type plaie du grand brûlé où l'application de formulations de type crèmes voire de compresses peut être délicate.

V. Conclusion

L'objectif principal de ce projet de thèse était d'obtenir des suspensions colloïdales de particules d'apatite bio-inspirées de taille nanométrique décorées en surface par des peptides bioactifs. Ce défi a été atteint, grâce à la synthèse et l'utilisation des nouveaux agents stabilisants bioactifs de type P(PEG3K)-Peptide. De tels composés permettent en effet de générer d'une part une stabilisation colloïdale aux particules en contrôlant leur état d'agglomération, et d'autre part de leur conférer directement des propriétés biologiques sans la nécessité d'étapes subséquentes de co-adsorptions. En ce sens, nous avons donc réussi à mettre au point une synthèse en une étape ou « one-pot » pendant laquelle les particules d'apatites sont précipitées directement en présence des agents bioactifs P(PEG3K)-Peptide. Ces résultats indiquent aussi que de telles NPs stabilisées par des P(PEG3K)-Peptide peuvent être utilisées comme « plateforme » pour un large éventail de stratégies liées au choix du ou des peptides à exposer en surface des particules. Bien que nos résultats sur les NPs indiquent le greffage effectif des P(PEG3K)-Peptide, et ce via leur groupement terminal phosphonate, il serait intéressant aussi de mener une étude visant à déterminer si une partie de la couronne organique peut être désorbées dans certaines conditions. A ce jour, les colloïdes se sont cependant avérés stables sur plusieurs semaines, suggérant la présence continue d'un nombre important de molécules organiques greffées évitant la sédimentation des particules.

De nouveaux agents stabilisants bioactifs « déclenchables » pourraient encore être conçus spécifiquement pour certaines applications, par exemple si la délivrance locale du peptide est plus souhaitable. Pour cela, l'ajout d'un espaceur (linker) sensible au pH ou à une activité

enzymatique entre le PEG et le peptide paraîtrait être une voie pertinente afin de contrôler la libération du peptide. Par ailleurs, la co-adsorption entre deux agents stabilisants différents à base de peptides différents devrait être testée. En effet, on peut imaginer que les NPs soient porteuses de plusieurs peptides bioactifs différents, eux-mêmes délivrés de manière contrôlée. Il serait également judicieux d'essayer d'introduire des ions biologiquement actifs dans le milieu de précipitation lors de la synthèse des apatites afin d'obtenir à la fois un cœur d'apatite bioactif et une couronne organique biologiquement active. On peut imaginer que les peptides pourraient interagir avec le milieu extérieur (cellules, bactéries...) et qu'ensuite les ions actifs soient libérés par la résorption progressive des NPs d'apatite grâce à un effet pH. Notons par ailleurs que ces NPs pourraient aussi être de bons candidats pour la vectorisation intracellulaire de peptides bioactifs en vue d'autres applications en nanomédecine, par exemple en oncologie. Disposer de telles nanoparticules hybrides d'apatites bio-inspirées décorées de peptides bioactifs pourrait ainsi ouvrir de nombreuses perspectives pour applications en biomédecine, pour le traitement des plaies complexes et au-delà.

Introduction

Research in the biomedical field is increasingly interested in the use of biofunctional materials. This is particularly the case for the vectorization of active agents for local treatments – less invasive and more targeted than systemic treatments – where the development and use of drug (nano)vectors is increasingly explored, for example in oncology and medical imaging, but also more recently in hematology or dermatology. Among the armamentarium that is being developed as (nano)vectors, organic or inorganic particles are particularly appealing. In addition to a possible protection of the active ingredient via its association with particles, the use of these particles may also present other advantages such as the possibility of cumulating several biologically active agents for a complementarity of effects or even a synergy, or a possible “smart” release of active ingredients, for example through the hydrolysis of a molecular fragment or by the selective dissolution of the vectors according to stimuli such as the local pH or an enzymatic activity. The vectors studied over the years, whether organic or inorganic, present advantages in their ability to act as drug carriers and for drug stabilization; however, they also usually have drawbacks such as toxicity, poor stability or non-biodegradability. In this view, the search for bioactive, highly biocompatible, biodegradable and functionalizable (nano)carriers/(nano)particles is more than ever a key challenge in biomedicine, especially taking into account the aging of populations.

In this context, the bio-inspired character of biomimetic “bone-like” apatites and their high surface reactivity make them excellent candidates for biomedical applications and in particular as (nano)carriers of therapeutic agents. Several synthesis methods, by wet or dry process, have been tested and some of them have been developed in order to obtain particles of micron/submicron size and in some cases of nanometric size. However, the size of the particles obtained with these synthesis methods generally remained poorly controlled, especially for nanometer-scale particles. This is why the CIRIMAT of Toulouse has been developing apatite-based submicron particles for nanomedicine since the 2000s, taking advantage of the “intrinsic” biocompatibility and biodegradability of these bio-inspired compounds and their high surface reactivity. These particles are made of a calcium phosphate mineral core close to the chemical composition of bone mineral – thus intrinsically biocompatible – coated with an organic corona capable of stabilizing the particles as colloidal suspensions by electrostatic repulsion or steric hindrance upon controlling their agglomeration state. These molecules (typically 2-aminoethylphosph(on)ate “AEP” or phosphonated poly(ethyleneglycol)), called stabilizing agents, have allowed obtaining homogeneous submicron to nanometric size particles ranging from 25 to 350 nm with a monomodal distribution.

However, none of these methods – also tested by other research groups e.g. using citrate or DNA molecules as stabilizing agents – allowed directly conferring additional biological

properties to the apatite (nano)particles, as the organic moieties forming the corona only acted as stabilizers to control/hinder nanocrystals agglomeration. Such additional properties could then only be provided by the subsequent co-adsorption of therapeutic (e.g. methotrexate) or cell-targeting (e.g. folic acid or antibodies) agents, involving an electrostatic interaction between selected end-groups exposed on the active agents and the surface of the calcium phosphate apatite.

Based on these considerations, the essential objective of this PhD project was to develop new bioactive peptide-based stabilizing agents able to not only stabilize bio-inspired apatite particles as colloidal suspensions, with a controlled nanometric size, but also to confer *simultaneously* added biological properties. In the frame of this work, we have especially focused our research toward conferring pro-healing and antibacterial activity in view of the treatment of complex wounds with high infectious risks.

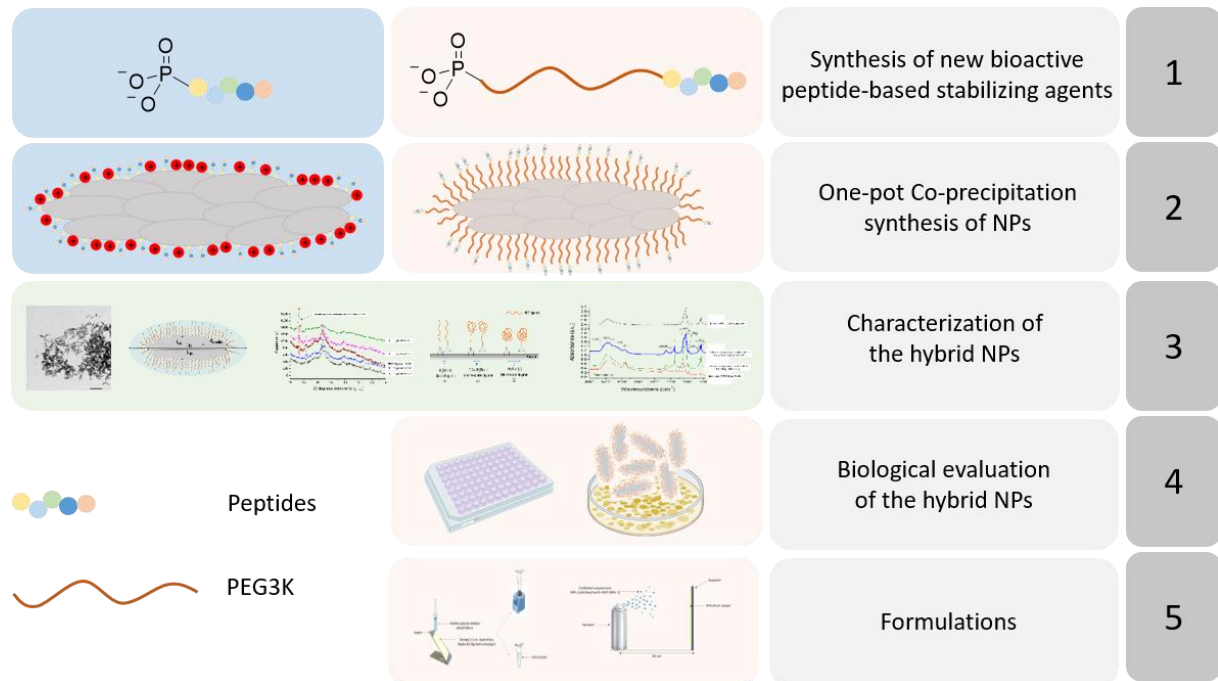
The first chapter of this manuscript presents, as a bibliographic overview, the structure, physicochemical characterization and synthesis methods developed to obtain apatite-based (nano)particles. The different existing means to control the particle size are presented and a particular attention is given to the use of stabilizing agents. Moreover, a review is made on the use of hybrid apatite (nano)particles in nanomedicine.

The second chapter of this manuscript is dedicated to the synthesis of two new peptide-based stabilizing agents that can stabilize (nano)particles as colloidal suspensions, via steric hindrance or electrostatic repulsion. This part of the study was deeply investigated, and several potential ways to provide final colloidal stabilization were envisioned and tested. We ultimately aim in this work the *one-pot synthesis* of peptide-decorated apatite (nano)particles by precipitating the apatite *in situ* in the presence of our newly engineered peptide-bearing stabilizing agents. The thorough characterization of the (nano)objects obtained is also described in this chapter, on the basis of a series of complementary techniques.

The third chapter of this manuscript is then dedicated to address more specifically wound healing applications. To this aim, a preliminary biological evaluation of the most relevant apatite-peptide hybrid nanoparticles generated was undergone. The pro-healing aspect was tackled by selecting cell-adhesion peptides. *In vitro* cell biocompatibility, proliferation and scratch tests were carried out on murine fibroblast cells and discussed. Preliminary results obtained on primary human fibroblasts were also obtained, showing the direct interaction of a peptide from apatite NPs surface and cell membranes. Providing antibacterial properties to such (nano)particles stabilized and functionalized by an antibacterial peptide was also addressed, and discussed in this section of the manuscript. The end of this chapter is devoted to galenic formulation of apatite-based hybrid nanoparticles in link with the treatment of wounds, whether by impregnation of commercial bandages or by generating our own wound dressings by freeze-casting in the presence of apatite NPs, or else by a spray methodology.

The conclusion will highlight the main results obtained in this PhD work, and the on-going and future directions opened by such novel apatite-peptide hybrid particles.

The following figure is a minimap representation of the manuscript, and of the main chapters that will be developed.



Chapter I- State of art:
Applications of hybrid apatite-based NPs in
nanomedicine

I. Apatite: structure and synthesis

A. Apatite structure

The word apatite comes from the Greek “απαταν” (to deceive), and was given about a century and a half ago, to a group of minerals often confused with aquamarine, amethyst or olivine because of their similar optical properties. These compounds can be of mineral or biological origins, and display a variety of compositional and crystalline features.

The stoichiometric apatite composition can be described by the following general formula:



In this formula, Me represents a divalent metal cation (e.g. Ca^{2+}), XO_4 a trivalent anion (e.g. PO_4^{3-}) and Y a monovalent anion (e.g. OH^-), but a very large variety of ions can substitute Me, XO_4 and Y, including with different charges, thus generating modifications of this generic formula provided that the overall electroneutrality of the crystal is retained.

The apatite structure can be described as a compact stacking of XO_4 ions, completed by the filling of some sites by Me cations, generating "tunnels" or channels in which Y ions are lodged axially. Figure 5 represents the structure of stoichiometric hydroxyapatite « HA » $\text{Ca}_{10}(\text{PO}_4)_6(\text{OH})_2$ (hexagonal system, space group $\text{P6}_3/\text{m}$), whose lattice parameters are generally considered to be $a = b = 9.432 \text{ \AA}$ and $c = 6.881 \text{ \AA}$.¹ This figure highlights the existence of two types of cationic crystallographic sites, denoted Me(I) and Me(II). While Me(I) sites form parallel columns to the c-axis, with an estimated column width of $\sim 2.5 \text{ \AA}$, Me(II) sites form equilateral triangles parallel to the ab-plane (two triangles being rotated with respect to each other by an angle of 60° around the c-axis). These Me(II) sites thus form the interior of apatite tunnels whose average diameter is estimated to be $\sim 3.5 \text{ \AA}$. The Y ions are then positioned with respect to these Me(II)_3 triangles. Depending on the Y ions and their volume, they can be at the center of gravity of the triangles (case of the small F^- ions) or more or less offset from this position (cases of OH^- and Cl^-) and thus lie above or below the plane of each triangle (Figure 5).¹

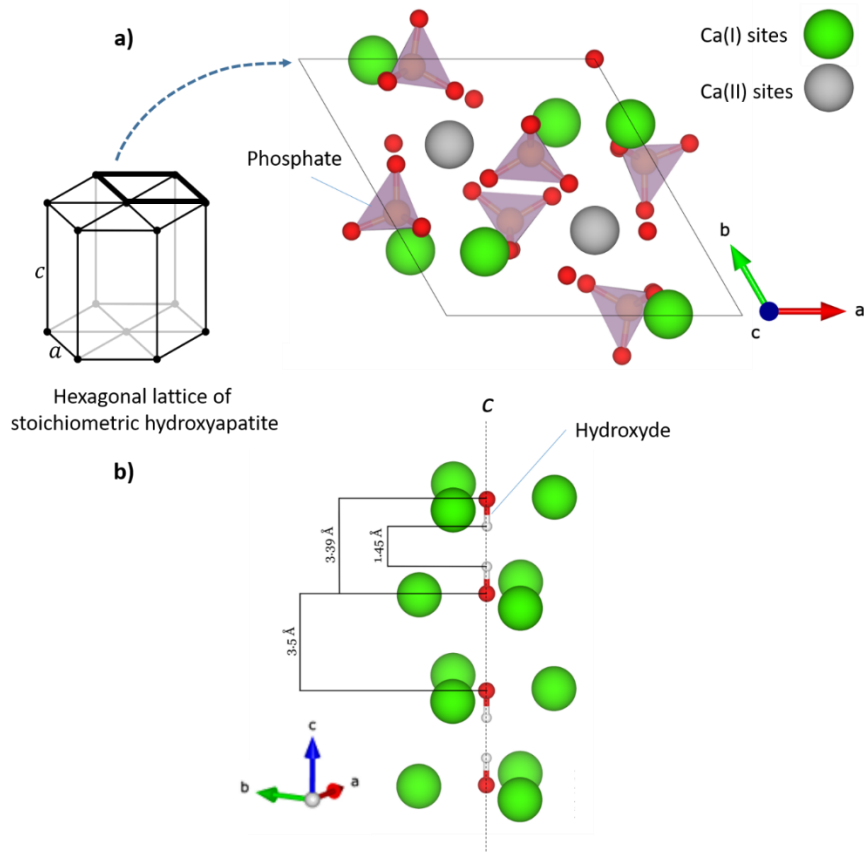


Figure 5: Crystal structure of stoichiometric hydroxyapatite

Due to the relative flexibility of the apatite structure, in part linked to the presence of the above-mentioned apatitic channels, various types of ionic substituents can be encountered in apatitic compounds, thus generating a large family of materials. Some of the most frequent components of the apatite family are listed in Table 1.

Mineral name	Formula	Reference
Fluorapatite	$\text{Ca}_{10}(\text{PO}_4)_6\text{F}_2$	Hughes et al. (1989)
Hydroxyapatite	$\text{Ca}_{10}(\text{PO}_4)_6(\text{OH})_2$	Ikoma et al. (1999)
Chlorapatite	$\text{Ca}_{10}(\text{PO}_4)_6\text{Cl}_2$	Mackie et al. (1972)
Fermorite	$\text{Ca}_{10}(\text{PO}_4)_3(\text{AsO}_4)_3(\text{OH})_2$	Hughes & Drexler (1991)
Alforsite	$\text{Ba}_{10}(\text{PO}_4)_6\text{Cl}_2$	Newberry et al. (1981)
Pyromorphite	$\text{Pb}_{10}(\text{PO}_4)_6\text{Cl}_2$	Dai & Hughes (1989)
Strontium-apatite	$\text{Sr}_{10}(\text{PO}_4)_6(\text{OH})_2$	Pushcharovskii et al. (1987)
Belovite-(La)	$\text{Sr}_6(\text{Na}_2\text{La}_2)(\text{PO}_4)_6(\text{OH})_2$	Pekov et al. (1996)
Belovite-(Ce)	$\text{Sr}_6(\text{Na}_2\text{Ce}_2)(\text{PO}_4)_6(\text{OH})_2$	Rakovan & Hughes (2000)
Deloneite-(Ce)	$\text{NaCa}_2\text{SrCe}(\text{PO}_4)_3\text{F P}_3$	Khomyakov et al. (1996)
Svabite	$\text{Ca}_{10}(\text{AsO}_4)_3\text{F}_2$	Welin (1968)
Johnbaumite	$\text{Ca}_{10}(\text{AsO}_4)_6(\text{OH})_2$	Dunn et al. (1980)
Clinomimetite	$\text{Pb}_{10}(\text{AsO}_4)_6\text{Cl}_2$	Dai et al. (1991)
Hedyphane	$\text{Pb}_6\text{Ca}_4(\text{AsO}_4)_6\text{Cl}_2$	Rouse et al. (1984)
Mimetite	$\text{Pb}_{10}(\text{AsO}_4)_3\text{Cl}_2$	Dai et al. (1991)

Morelandite	$Ba_{10}(AsO_4)_3Cl_2$	Dunn & Rouse (1978)
Turneaureite	$Ca_{10}(AsO_4)_3Cl_2$	Dunn et al. (1985b)
Britholite-(Ce)	$Ce_6Ca_4(SiO_4)_6(OH)_2$	Oberti et al. (2001)
Britholite-(Y)	$Y_6Ca_4(SiO_4)_6(OH)_2P_2$	Zhang et al. (1992)
Chlorellestadite	$Ca_{10}(SiO_4)_3(SO_3)_3Cl_2$	Rouse et al. (1982)
Fuorellestadite	$Ca_{10}(SiO_4)_3(SO_3)_3F_2$	Chesnokov et al. (1987)
Hydroxyllestadite	$Ca_{10}(SiO_4)_3(SO_3)_3(OH)_2$	Hughes & Drexler (1991)
Mattheddleite	$Pb_{10}(SiO_4)_3(SO_4)_3Cl_2$	Steele et al. (2000)
Cesanite	$Na_6Ca_4(SO_4)_6(OH)_2$	Deganello (1983)
Caracolite	$Na_6Pb_4(SO_4)_6Cl_2$	Schneider (1967)
Vanadinite	$Pb_{10}(VO_4)_6Cl_2$	Dai & Hughes (1989)

Table 1: Summary of the main members of apatite-group minerals²

It is sometimes considered that almost the entire periodic table of elements can be accommodated, at least to some extent, in the apatite structure – with some adjustments of the lattice parameters and distortions of the original crystallographic sites.¹ These ionic substitutions may sometimes lead to a complete solid solution as in the case of Sr^{2+} ions for example, $Ca_{10-x}Sr_x(PO_4)_6(OH)_2$, but are generally only partial. All of these ionic substitutions can take place as long as the overall electroneutrality of the whole crystal is maintained. When ions of different charges share the same sites and/or for non-stoichiometric apatites, vacancies (noted \square) may exist as is customary in "Me sites" and "Y sites".²⁻⁴ An illustrative example can be given with the oxy-hydroxyapatite compound $Ca_{10}(PO_4)_6(O_{1/2} OH_1 \square_{1/2})$. It may be noted that the possibility to have vacancies in the "XO₄ sites" has never been demonstrated, and this can most probably be explained by the large size of the XO₄ tetrahedral, which stabilize the crystal lattice, and whose absence would lead to too much instability. However, the XO₄ ions (normally trivalent) can be replaced by other ions with similar or different charges, provided that the whole crystal remains neutral. Thus, PO_4^{3-} ions can for example be substituted, at least in part, by SiO_4^{4-} or HPO_4^{2-} or CO_3^{2-} ions. A wide range of compositions thus exists due to the creation of vacancies and/or to the presence of many elements entering the chemical formula.

In this work dedicated to biomedical applications, we will focus on hydroxyapatite (in orange in Table 1) which belongs to the calcium phosphate family of minerals (CaPs). Indeed, the mineral part of bones and teeth in all vertebrates (including humans) is composed of a calcium phosphate apatitic phase close to hydroxyapatite. Therefore, CaPs materials are considered as bio-inspired and are thus particularly relevant for biomedical applications such as bone regeneration.⁵ CaPs however not only encompass hydroxyapatite (or their non-stoichiometric counterparts), but also a series of other calcium phosphate phases that can present different acido-basic properties. This series of CaPs corresponds in fact to the calcium salts of phosphoric acid H_3PO_4 at different stages of the neutralization of its 3 acidities, therefore

leading for example to the monocalcic, dicalcic, tricalcic, etc. series of compounds. From a practical point of view, CaPs are often described by their Ca/P molar ratio (Table 2).

Name	Chemical composition	Ca/P
Anhydrous monocalcium phosphate	$\text{Ca}(\text{H}_2\text{PO}_4)_2$	0,50
Monocalcium phosphate monohydrate	$\text{Ca}(\text{H}_2\text{PO}_4)_2, \text{H}_2\text{O}$	0,50
Anhydrous dicalcium phosphate (monetite)*	CaHPO_4	1,00
Dicalcium phosphate dihydrate (brushite)	$\text{CaHPO}_4, 2\text{H}_2\text{O}$	1,00
Octacalcium phosphate (OCP)	$\text{Ca}_8(\text{PO}_4)_4(\text{HPO}_4)_2, 5\text{H}_2\text{O}$	1,33
Apatitic octacalcium phosphate	$\text{Ca}_8(\text{PO}_4)_{3,5}(\text{HPO}_4)_{2,5}(\text{OH})_{0,5}$	1,33
Amorphous octacalcium phosphate	$\text{Ca}_8(\text{PO}_4)_4(\text{HPO}_4)_2, n\text{H}_2\text{O}$	1,33
α or β Tricalcium phosphates (α - or β -TCP)	$\text{Ca}_3(\text{PO}_4)_2$	1,50
Apatitic tricalcium phosphate (apTCP)	$\text{Ca}_9(\text{PO}_4)_5(\text{HPO}_4)(\text{OH})$	1,50
Amorphous tricalcium phosphate (amTCP)	$\text{Ca}_9(\text{PO}_4)_6, n\text{H}_2\text{O}$	1,50
Non-stoichiometric biomimetic apatites	$\text{Ca}_{10-x}(\text{PO}_4)_{6-x}(\text{HPO}_4)_x(\text{OH})_{2-x}$	1,33 - 1,67
Stoichiometric hydroxyapatite	$\text{Ca}_{10}(\text{PO}_4)_6(\text{OH})_2$	1,67
Oxyapatite	$\text{Ca}_{10}(\text{PO}_4)_6\text{O}$	1,67
Tetracalcium phosphate	$\text{Ca}_4(\text{PO}_4)_2\text{O}$	2,00

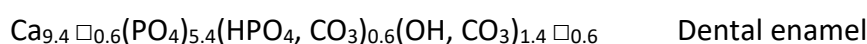
*note that the "dicalcium" terminology historically referred to the $2\text{CaO} \cdot 1\text{P}_2\text{O}_5 \cdot \text{H}_2\text{O}$ notation from simple constituting oxides as used in mineralogy to describe mineral compounds. Upon simplification, this leads to $\text{Ca}_2\text{H}_2\text{P}_2\text{O}_8$ that can further be simplified to CaHPO_4 .

Table 2: Main compounds of the calcium phosphate (CaPs) family of minerals

Stoichiometric (i.e. without vacancies) hydroxyapatite is usually cited as a reference CaP compounds in the literature. It responds to the following chemical formula:

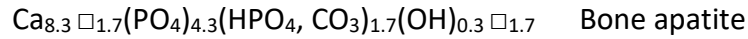


From this model formula, a large panel of hydroxyapatite-derived compounds can exist through ionic substitutions and/or vacancies creation. In particular, biological apatites are in most cases carbonated and non-stoichiometric. The composition of dental enamel, for example, refers to the mean chemical formula:



It may be remarked that it is close, in first approximation, to the composition of stoichiometric hydroxyapatite.

In contrast, in the case of bone mineral – which represents nearly 70% by mass of the composition of an average long bone such as the femur – the apatite chemical composition is farther from stoichiometry by a greater number of ion vacancies, and was reported as follows⁶:



As may be seen, in bone there is only a very small amount of hydroxide ions in Y sites; therefore, bone mineral is generally called « apatite » rather than « hydroxyapatite » since it is almost totally depleted in OH⁻ ions. The refinement of the composition of bone is still subject to investigations, especially because older studies were carried out on chemically-treated bone specimens which may have undergone some degree of alteration. A recent work revisited recently the composition of a rather mature bone specimen without any chemical treatment, and led to the following composition.⁷

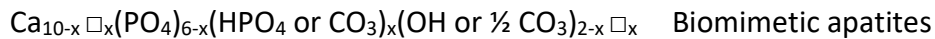


We may also note that most calcified tissues additionally incorporate minor/trace elements such as Mg²⁺, Sr²⁺, Na⁺ and F⁻, which slightly modify their physicochemical (and thermodynamic) properties, as pointed out in the literature.⁸

The two above examples reflect well the adaptability of phosphocalcic apatites to the biological function that they have to fulfill *in vivo*. Dental enamel should indeed resist the acidic attacks of oral bacteria and arising from food/drink degradation products. It is thus relevant to exhibit an apatite composition close to stoichiometry to present a high thermodynamic stability (the highest the number of cations and anions attracting each other, the greater the stability and the lower the solubility in acidic conditions). In contrast, bone apatite should be able to rather easily undergo bone remodeling (via the osteoclast/osteoblast cell activity), which necessitates greater sensitivity to the local acidic conditions generated by osteoclast cells, thus requiring the lacunar structure (i.e. containing ionic vacancies) of non-stoichiometric apatite. These two examples demonstrate the adaptability of the apatite structure to the function they have to play *in vivo*, thus probably explaining their ubiquitous presence within many biomineralizations.

These types of apatite compounds are not only encountered in Nature, but they can also be synthesized. Wet chemical routes are particularly well suited, especially for non-stoichiometric compositions that are sensitive to heat. In particular, the preparation of bone-biomimetic apatites in close-to-physiological conditions (i.e. neutral pH, temperature significantly below the boiling point of water) is appealing as they exhibit a high surface reactivity and their resorption *in vivo* can be controlled⁸ by their degree of non-stoichiometry: the more vacancies in the apatitic lattice, the more resorbable the apatite compound since its

thermodynamic stability decreases. Such biomimetic apatites may, in a first approximation, be described by the following general formula (with $0 \leq x < 2$):



It may be noted that, often, such apatite compounds are prepared without carbonate ions to simplify their composition.

Biomimetic apatites are composed of nanosized crystals that associate to form *polycrystalline* particles. The nanocrystals exhibit a platelet or elongated morphology that differs significantly from the hexagonal shape of sintered stoichiometric hydroxyapatite. By X-ray diffraction (XRD), the size of the smallest domains that diffract light in a coherent way (i.e. the *crystallites*) is considered to correspond to the individual nanocrystals. In an apatite specimen, whether as a powder or suspension, each particle is thus composed of several nanocrystals. Depending on the conditions of preparation, the nanocrystals can be covered by a more or less extended ionic and hydrated amorphous layer called “non-apatitic”, where the ions (Ca^{2+} , HPO_4^{2-} essentially) are located in chemical environments that differ from the regular crystallographic sites observed in hydroxyapatite (Figure 5). Such surface ions are particularly mobile or “labile” and can be easily exchanged with many types of ions contained in the surrounding liquid medium. Each nanocrystal or *crystallite* can then be seen as constituted by an “apatitic core” surrounded by a “non-apatitic ionic hydrated layer” (Figure 6).⁹ The high mobility of surface ions is one relevant feature of biomimetic apatites as this property may be exploited for surface ion exchanges with bioactive ions or for adsorption processes to confer additional biological functionalities. In addition, the nanoscale dimensions of the crystallites generate a high developed surface area which also contributes to their high surface reactivity.

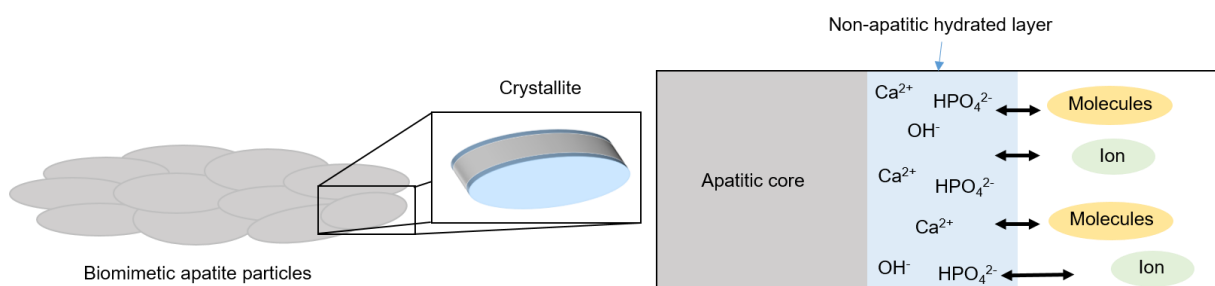


Figure 6 : Representation of biomimetic apatite nanocrystals (inspired by ⁶)

In this PhD work, we will study the preparation of such bio-inspired nanocrystalline apatite in conjunction with bioactive peptides.

B. Characterization of nanocrystalline bio-inspired apatites

All the apatites presented above, with various properties, can be synthesized in the laboratory and be isolated. In order to determine their composition, structure, crystallinity state, particle size and size of constituting crystallites, a variety of physicochemical analyses can be carried out. In this section, the essential analytical methodologies based on X-Ray Diffraction (XRD) and infrared spectroscopy (FTIR) will be detailed. These analyses will indeed be considered later as references to characterize the apatite phase constituting the hybrid apatite-peptide particles and to compare the results obtained with different strategies.

1. X-Ray Diffraction

X-Ray Diffraction is a technique aiming at characterizing crystallized materials (i.e. exhibiting long-range atomic order), often inorganic, with the view to determine their structural features at the atomic scale. A diffraction pattern is generated by recording the intensity of active (hkl) diffraction lines (h , k and l representing the Miller indices relative to the orientation of diffracting planes of atoms in the 3D crystal structure) as a function of the angle of diffraction θ (by convention, the plot is made versus 2θ to take into account both the incident and diffracted beams). While amorphous compounds will only lead to wide halos on the XRD pattern, crystallized substances will lead to well-defined lines corresponding to the (hkl) diffracting atomic planes. In the case of sintered stoichiometric hydroxyapatite, with a high degree of crystallinity, a characteristic pattern is obtained as depicted in Figure 7. In particular, the typical (002), (211), (112), (300), (310), (222), (213) and (004) peaks can be identified.¹⁰

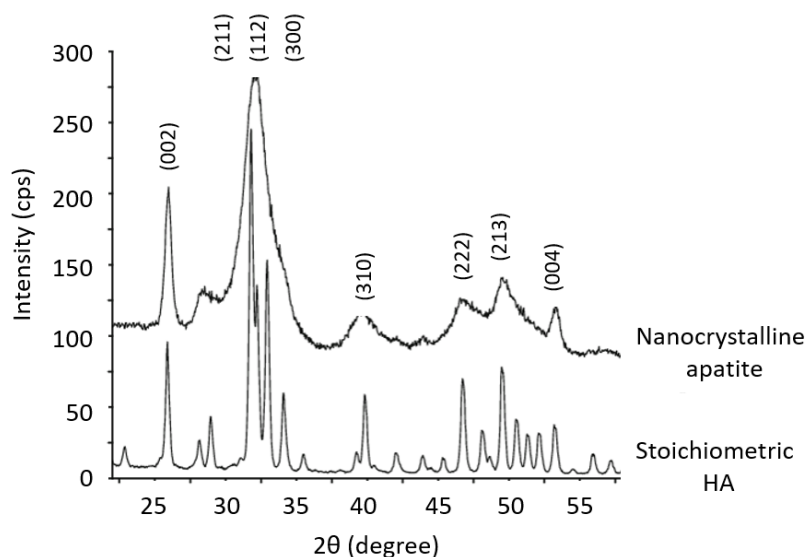


Figure 7: XRD pattern of stoichiometric hydroxyapatite (relative to the copper $K\alpha$ anticathode) and a typical biomimetic nanocrystalline apatite⁹

The XRD analysis also allows to explore the crystallinity state of the sample by observing the width of the peaks. The thinner the peaks, the larger the crystallinity: indeed, nanoscale dimensions (meaning smaller domains with a coherent diffraction behavior) as well as local constraints within the crystal (e.g. due to non-stoichiometry or to ionic substitutions) can be considered as “defects” and will lead to wider, less-resolved peaks indicative of a lower degree of crystallinity. Figure 7 shows the difference between a stoichiometric hydroxyapatite, very well crystallized with fine and well-resolved peaks, and a reference biomimetic nanocrystalline apatite compound, more weakly crystallized with broader peaks.^{10,11}

As mentioned above, the width of the peaks is directly linked (in a reverse relationship) to the size of the crystallites composing a particle. This property is interesting with the view to estimate, in a first approximation, the mean dimensions of the crystallites. For apatites, which crystallizes in a hexagonal system (space group $P6_3/m$, see Figure 5), it is relevant to seek indications along the c axis (to access the mean *length* of the crystallites) and in perpendicular directions (to estimate a *width/depth* of the crystallites). Taking into account the XRD pattern of hydroxyapatite as reference (Figure 7), two lines are particularly relevant to examine in this regard: lines (002) and (310). Line (002) is generally well visible in apatite XRD patterns even for lower crystallinity specimens, and it is of the form (hkl) with $h = k = 0$. It thus gives information along the c axis which relates to the l Miller index. Line (310) is in contrast of the form (hkl) with $l = 0$ and thus gives information on perpendicular directions to evaluate an order of magnitude in the $\sim(ab)$ dimensionality. Other peaks of the type $(h00)$ and $(0k0)$ would have been more adequate to distinguish the a from the b directions, however such lines are not clearly visible in apatite patterns.

The mean length and width/depth of the crystallites can be estimated from the full width at half maximum (FWHM) of the peaks (002) and (310) using Scherrer’s equation:

$$L_{hkl} = \frac{K\lambda}{\cos\theta_{hkl} \sqrt{\beta_{hkl}^2 - \beta_0^2}}$$

with:

- L_{hkl} , the apparent size of the crystallites in the direction perpendicular to the plane (hkl) (Å)
- K , Scherrer’s constant (generally considered as $K = 0.94$)
- λ , the wavelength of the X-ray beam (for example: $\lambda_{Cu\ K\alpha} = 1.54056$ Å)
- θ_{hkl} , the diffraction angle corresponding to the line (hkl) considered (radians)
- β_{hkl} , the FWHM of the diffraction line of the experimental diagram (radians)
- β_0 , the FWHM of the diffraction line due to the contribution of the diffractometer and reached using a well-crystallized compound, here sintered stoichiometric hydroxyapatite (radians)

In the present thesis work, this formula will be used to determine a first order of magnitude of the size of the crystallites constituting the bio-inspired apatite particles prepared.

2. Fourier transform infrared spectroscopy (FTIR)

Chemical bonds within a molecule or molecular ion can selectively absorb radiations at specific wavelengths, which changes the vibrational energy of the bond. Covalent bonds in particular can typically lead to absorption in the mid-infrared (mid-IR) range, which is experimentally accessed between 400 and 4000 cm^{-1} . The type of vibration (stretching or bending) induced by the infrared radiation depends on the nature of the atoms in the bond and on the organization of the atoms in the sample. In a solid, the local symmetry around a chemical bond also has an effect on IR absorption. For a given vibrating system, $3N-6$ vibration modes can be identified depending on the number of atoms N considered. This arises from the fact that each atom can be described in space by 3 parameters (its spatial x , y , z coordinates relative to a given reference), hence $3N$ degrees of freedom, to which should be subtracted the 3 degrees of freedom relative to any translation (which does not impact the vibration) and similarly also subtracting the 3 degrees of freedom relevant to any rotation. This leads to $3N-6$ possible modes of vibration in total. Note that, in the case of linear vibrating systems, the degree of freedom relative to the axis of the molecule should not be subtracted, leading to $3N-5$ vibration modes. Taking for illustration the tetrahedral PO_4^{3-} ion, it comes that $N = 5$ atoms thus leading to $3N-6 = 9$ vibration modes. To be active in infrared spectroscopy, a vibration mode should vary the dipolar moment of the bond; thus only selected vibrations may lead to actual IR spectral signatures. Also, it may be noted that some modes can relate to the same vibrational energy thus leading to degenerate energy states. For PO_4^{3-} , the most active modes are the $\nu_3(\text{PO}_4)$ and the $\nu_4(\text{PO}_4)$, respectively assignable to the asymmetrical stretching of P-O bonds within the PO_4 tetrahedron and to the angular deformation of P-O bonds. Note that, for instance, the totally symmetrical P-O stretching mode denoted $\nu_1(\text{PO}_4)$ should not be active in IR as it should not generate any change in dipole moment; it is however somewhat active (but with a very low intensity) due to local distortions of the PO_4 tetrahedron in link with anisotropy of nearest neighbors in the solid state. In contrast, it may be noted that RAMAN spectroscopy is another vibrational spectroscopy technique to explore materials composition, where the activity of Raman bands is related to the polarizability of the bonds and thus to the deformability of the electronic cloud upon vibration. In this context, the $\nu_1(\text{PO}_4)$ which relates to the symmetrical respiration of the P-O bonds in PO_4 mentioned above becomes the most active in RAMAN (as opposed to IR).

Figure 8 shows the typical FTIR spectrum of a biomimetic nanocrystalline apatite. The main band assignments have been added in Table 3.¹² In practice, thanks to vibrational spectroscopies and in particular to FTIR, phosphate, hydroxyl (and carbonate) ions present in the apatite composition can be identified, and some information on the local chemical

environment of these ions (apatitic or non-apatitic, hydroxylation rate...) within the apatite particles can be deduced from this analysis.

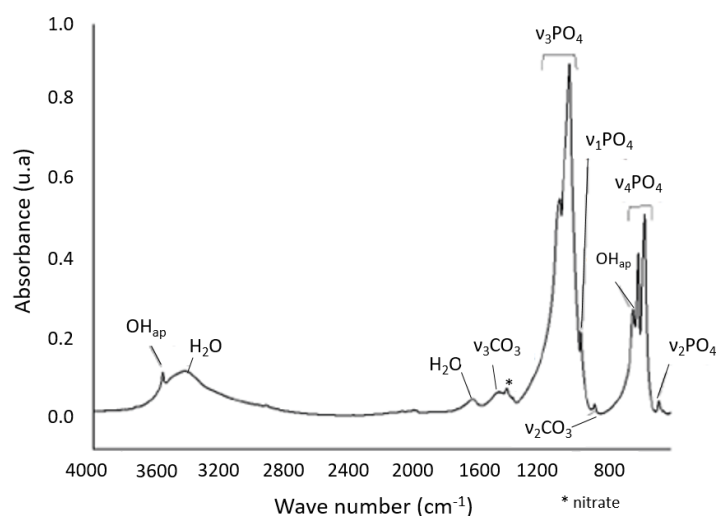


Figure 8: FTIR spectrum of a partially carbonated biomimetic nanocrystalline apatite⁹

Band assignments	Positions of the band	Vibration mode
PO ₄ ³⁻	470	v ₂ : Angular distortion
	560, 575, 601, 617	v ₄ : Angular distortion
	961	v ₁ : Symmetric elongation
	1040, 1090	v ₃ : Antisymmetric elongation
HPO ₄ ²⁻	534, 550, 870-875	v: Elongation
CO ₃ ²⁻	871-878	v ₂ : Out-of-plane vibration
	1415, 1450-1475, 1540	v ₃ : Elongation
OH ⁻	630-632	v _L : Vibration
	3570	v _S : Elongation

Table 3: FTIR band positions of nanocrystalline hydroxyapatite in the 400-4000 cm⁻¹ range

Apatitic OH⁻ ions are characterized by two bands around 3572 and 632 cm⁻¹. For water-containing apatites like biomimetic ones, the O-H stretching of water molecules gets partly superimposed with the 3572 cm⁻¹ band; then the 632 cm⁻¹ band becomes the most reliable spectral signature for apatitic OH⁻ by FTIR. Several bands can be attributed to phosphate groups present in the sample, either in apatitic or non-apatitic environment (Figure 9).¹¹ For example, two shoulders not present for stoichiometric hydroxyapatite are observed at 534 and 617 cm⁻¹ around the v₄(PO₄) vibrational domain, which have been attributed respectively to non-apatitic HPO₄²⁻ (major) and PO₄³⁻ (minor) present in the surface hydrated layer on the crystallites (Figure 9), their intensities are also reported in Table 4). In contrast, apatitic HPO₄²⁻ ions give rise to a band around 550 cm⁻¹. The presence of the hydrated layer is also observable to some extent via the broad and intense absorption band in the 3700 - 2700 cm⁻¹ range of

the O-H stretching of water as well as the H-O-H bending deformation of water at 1640 cm^{-1} which testify to the presence of water; however, care should be taken here as some of the water may be simply adsorbed on the surface of the particles.

Such FTIR analyses can thus provide information about the stoichiometry of the apatite particles. Depending on the conditions of formation of the apatite phase, and in particular to its “maturation” state (linked to its degree of crystallinity and amount of surface non-apatitic hydrated layer), more mature apatites will give rise to FTIR spectral features closer to those of hydroxyapatite while less mature samples will significantly depart from the “reference” spectrum of HA, with a decreased intensity of the band at 632 cm^{-1} characteristic of apatitic OH^- and an increase in HPO_4^{2-} -related absorption at 550 and 534 cm^{-1} . It was shown that upon increasing the temperature of apatite precipitation and/or the pH and/or the time of maturation prior to filtration, the apatite age or “mature” which can be linked to the progressive development of the apatitic core of the crystallites at the expense of the hydrated layer. The presence of organic moieties in the precipitation medium can also modify the maturity of the precipitated apatite phase, as some organic compounds may act as apatite crystallization inhibitors.¹³

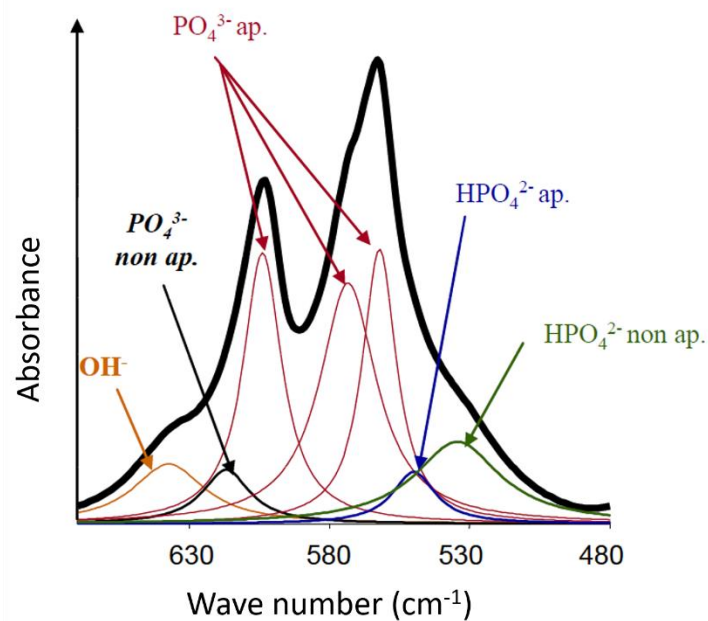


Figure 9 : Spectral decomposition around the ν_4 adsorption band of phosphate ions. ap. = apatitic⁹

Wavenumber	Attributions	Intensity
632	OH ⁻	Low
617	PO ₄ ³⁻ non apatitic	Shoulder
603	(<i>v</i> ₄) PO ₄ ³⁻	Medium
575	(<i>v</i> ₄) PO ₄ ³⁻	Medium
562	(<i>v</i> ₄) PO ₄ ³⁻	Medium
551	HPO ₄ ²⁻ apatitic	Shoulder
533	HPO ₄ ²⁻ non apatitic	Shoulder

Table 4: Position and allocation of FTIR bands around the *v*₄(PO₄) domain⁹

The above section on FTIR spectroscopy (and RAMAN by extension) and the previous one relating to XRD have pointed out the possibility to assess several compositional and structural features of apatite compounds. These techniques will thus be used as first line of characterization of the particles that will be obtained in this work. We also highlighted the fact that there does not exist only one single type of apatite but a large range of apatites which may present different characteristics. Different synthesis routes were developed in the literature to prepare apatitic compounds which may exhibit different features.^{13–16} Parameters such as pH, maturation time and temperature, concentration of starting materials and others were shown to allow obtaining apatites with different compositions, particle shapes or sizes.¹⁰ The control of particle size is in particular very relevant to the present PhD work aiming dermatological applications. Therefore, the following section will describe more specifically synthesis methodologies targeting the preparation of apatite nanoparticles.

II. State of the art: synthesis of nano-sized apatite particles

Nano-sized particles are defined as particles with at least one dimension in the nanometric scale (100 nm or less).¹⁴ They can typically offer improved properties due to their high specific surface area compared to conventionally sized materials. Moreover, compared to micro-scale materials, nano-sized objects may address several challenges in nanomedicine for drug delivery and targeting purpose, typically at the cellular or tissular level. For these reasons, scientists have tried to decipher the main parameters to prepare apatite nanoparticles, either via solid state or wet state synthesis routes.

A. Solid state methods

Solid state methods consist of mixing raw materials as dry powders to proceed the reaction at high temperature (generally higher than 700°C) for long treatment times. Since non-stoichiometric apatites are not stable in these conditions, it is necessary to start from stoichiometric proportions, and these methods can thus only lead to well-crystallized hydroxyapatite. Materials obtained via solid state methods are thus in the form of a sintered bulk. To obtain nano-sized particles, a post-synthesis treatment is needed, which can typically

be carried out through a physical process (by milling or grinding).¹⁴ After such post-treatments, variable sizes are obtained but, as far as we know, no detailed information on the size distribution was reported and polydispersity information is very rarely given (Table 5).¹⁵

The modified Pechini-method¹⁶ is another way to obtain NPs via a solid state synthesis. This method consists in preparing hydroxyapatite nanocrystals under non-stoichiometric conditions directly in CaO matrix. This matrix is then removed by several washing steps to get hydroxyapatite nanoparticles (Figure 10).

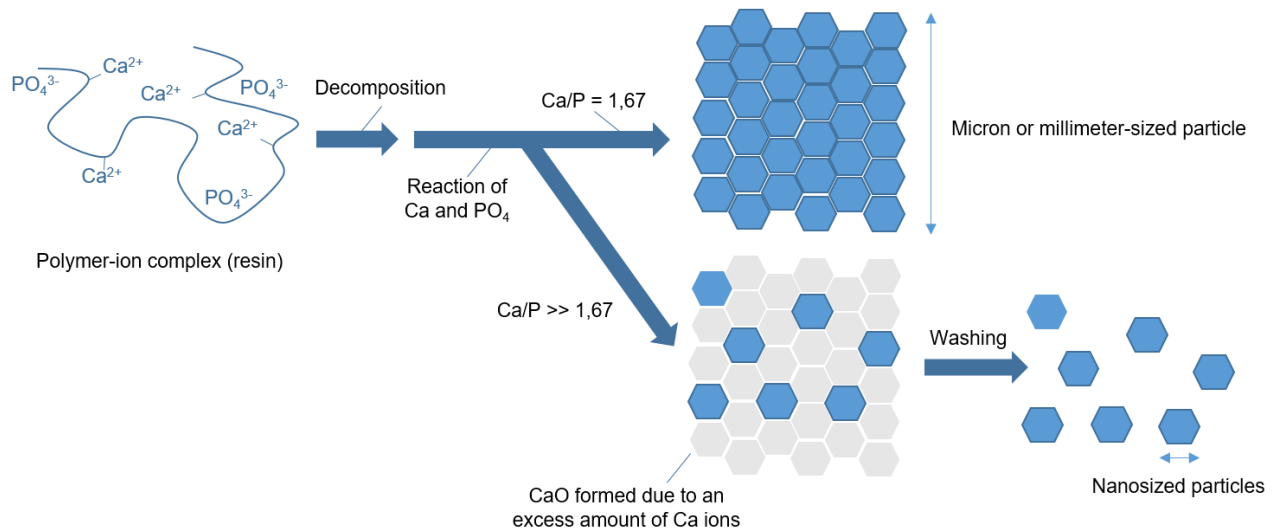


Figure 10: Pechini method to synthesize hydroxyapatite nanoparticles¹⁶

In the plasma technique, the raw material is melted (totally or partially) or in some case evaporated with a high temperature flame. The melted/evaporated materials are then cooled or condensed into nanoparticles.^{17,18} This technique can also be performed thanks to a radiofrequency plasma spray process and nanoparticles were also claimed to be obtained (10-100 nm) which contained both amorphous and crystalline phases.¹⁹ It is worth noting that high temperature during the synthesis or post-synthesis treatment, drives the obtainment of a hydroxyapatite phase with high crystallinity, and thus farther from natural bone mineral crystallites. Although effective to obtain nanosized particles, these techniques require high temperature, long synthesis times and specific equipment, and do not seem to allow obtaining well-determined particle sizes nor non-stoichiometric apatites. This is why wet state synthesis routes are often preferred.

B. Wet state methods

Requiring relatively low temperatures, wet state methods are the simplest way to synthesize apatite NPs. Without any post-synthesis thermal treatment, these methods allow obtaining non-stoichiometric and weakly-crystallized apatite compounds like in bone. Several procedures were developed to prepare nano-sized apatite particles, including co-

precipitation^{19–21}, hydrothermal synthesis^{22–24}, microwave irradiation²⁵, sol-gel synthesis^{26,27}, micelle-templated precipitation^{28,29}, emulsion method^{30,31}, citrate adsorption^{32,33}, stabilizing agents adsorption^{9,34,35} and others. Different sizes ranging from the nano to the micro scale were reported to be obtained, depending on the physicochemical conditions used (Table 5).

		Typical particle size	Pdl
Solid state	Solid-state reaction	-	/
	Ball milling	200-500 nm	/
	Selective dissolution of binary phase	70-500 nm	/
	Calcination with anti-sintering agents	50-300 nm	/
	Mechanochemical methods	Micron order	/
	Plasma spraying	100 nm	/
Wet state	Wet chemical precipitation	50-500 nm	/
	Micelle-templated precipitation	30-500 nm	/
	Emulsion method	30-100 nm	/
	Hydrothermal conversion	Micron order	/
	Hydrothermal crystal growth	30-100 nm	/
	Sol-gel method	-	/
	Calcium concentration	-	/
	Stabilizing agents	25-400nm	< 1
	Bicarbonate agent	-	/

Table 5: Synthesis methods to generate (hydroxy)apatite nanoparticles

By varying several parameters at the synthesis level (e.g. maturation time in solution, maturation temperature, pH, type of phosphate precursor) and post-synthesis treatments (e.g. drying and redispersion processes), it is possible to tune the properties of apatites.^{10,36} The most important parameters to take into account at the synthesis level are the maturation time in solution, the maturation temperature and the pH. For example, by increasing the temperature, it is possible to increase the crystallinity of the material as it favors diffusion processes. Also, since hydroxyapatite is a hydroxide, increasing the pH favors apatite crystallization. Below 80°C and at pH values close to neutrality, apatites are often moderately crystallized. This can be observed also for higher temperature, e.g. up to 100°C, in the co-presence of organic moieties that may exhibit a growth inhibition effect on apatite crystals.³⁷ For post-synthesis treatments, a “high” drying temperature (~80°C) allows obtaining a better crystallinity of the material. Depending on the properties targeted for the apatite particles, it may be relevant to aim the preparation of more or less matured nanocrystals.

1. Co-precipitation synthesis

The most common wet state approach to synthesize apatite is co-precipitation. It consists in mixing two aqueous solutions of calcium ions on the one hand and orthophosphate ions on the other hand, in more or less basic conditions and at a temperature between 25 to 100°C

for a maturation time ranging from few minutes to several days depending on the targeted apatite features. It results in the precipitation of apatite particles according to the following equation.¹⁴



The main issue with this method is the important number of parameters to be precisely controlled (addition rate, pH, mixing temperature, time, stirring speed...) which may hamper the reproducibility of stoichiometry. However, this drawback can also be seen as a way to obtain a multitude of properties by varying only one parameter at a time and to understand the impact of each parameter on the formation of apatite phases that are more or less crystallized.

In this PhD work, the co-precipitation method was selected because it has already allowed obtaining non-stoichiometric, weakly crystallized apatites close to the bone mineral composition and structure. In addition, we decided to use novel stabilizing agents not only to control the size and limit the agglomeration of nanoparticles, but also to confer biological properties via the direct involvement of bioactive peptides in the stabilizing conjugates prepared.

2. Stabilizing agents used to control the particles size: toward colloidal suspensions

A colloid is a dispersion of one or more substances suspended in a liquid, forming a system with two separate phases, in a stable way. It is considered that the weight of the individualized particles in suspension does not overcome the Brownian movement that particles undergo upon interparticle shocks (except at 0 K), and that the particles thus remain in suspension and avoid sedimentation. This may be favored by a surface charge (generally given by the zeta potential measurement) high enough – e.g. more than 30 mV in absolute value – but this is not a necessary requirement as far as the particles are capable of repulsing each other, which may be provided by sterical hindrance of adsorbed molecules. Colloidal suspensions are thus heterogeneous mixtures of particles, that may range in size from the nanometer to the micrometer scale (depending also on the density of the particles themselves).

Prior to this PhD work, four stabilizing agents have been particularly studied at the CIRIMAT lab and in the literature: 2-aminoethyl phosph(on)ate (AEP)^{34,35,38}, phosphocholine chloride (PhCol)³⁹, citrate^{33,40,41} and phosphonated poly(ethyleneglycol), noted P(PEG)-OCH₃⁹, in order to prevent/control the apatite particles agglomeration. These molecules were added directly in the precipitation medium during apatite formation to form an organic corona around the apatite particles that are generated. These molecules were grafted electrostatically thanks to a surface chelation mechanism between the phosph(on)ate group (AEP, PhCol and P(PEG)-

OCH₃) or carboxylate group (citrate) and the calcium ions present on the particles surface (as explained in section III.A).

Here, we will describe the particles obtained with the four stabilizing agents taken as reference for the present work, but we will especially focus on the characteristics of the NPs surrounded by AEP and P(PEG)-OCH₃ coronas. Both were indeed studied in this PhD project (see for example Figure 11).



Figure 11: Example of colloidal suspension of apatite nanoparticles stabilized with AEP (Al-Kattan et al.)³⁷

a. Nanoparticles stabilized by electrostatic repulsion induced by AEP, PhCol or Citrate corona

Case of citrate

In the literature, the addition of citrate in the co-precipitation synthesis of apatite allowed controlling apatite particle size by limiting the agglomeration of adjacent particles by electrostatic repulsion. During the synthesis, some carboxylates groups from the citrate molecular ion chelate with the apatitic calcium surface.³³ The other carboxylate group creates a negative charge screen (zeta potential = -33 mV⁴⁰) around the particle allowing to electrostatically repel the particles and to yield nanometric size particles (~200 nm, polydispersity index PDI = 0.26). Citrate ions also inhibit the crystal growth of apatite and a poorly crystallized hydroxyapatite phase was obtained with this method, especially for a short crystallization time. Moreover, the nanometric size of the crystallites that composed the NPs (48 nm relative to the L(002) peak and 8.6 nm relative to the L(310) peak) were estimated from XRD data via Scherrer's equation.

Case of PhCol

The adsorption of phosphocholine (PhCol) onto apatite particles may avoid the particles agglomeration via an electrostatic repulsion effect induced by the protonated tertiary amine (Figure 12). This phenomenon was confirmed by zeta potential measurements which pointed out a global positive surface charge (typically +12 mV) induced by the protonated amine.

Nanosized monodispersed particles (70 nm, Pdl = 0.11) were obtained with these two first stabilizing agents according to Dynamic Light Scattering (DLS) analyses.³⁹

Case of AEP

The adsorption of AEP was studied in several works. It also avoids particles agglomeration via electrostatic repulsion induced by the protonated primary amine (pK_a 10.5) for example at pH \sim 9-10 where the syntheses were carried out (Figure 12). This phenomenon was confirmed by zeta potential measurements which showed a global positive surface charge (typically +12mV) induced by the protonated amine. Smaller particles than with PhCol were obtained, with even smaller nanoscale dimensions (down to \sim 25 nm) and with a monodispersed size distribution (Pdl = 0.07) as indicated by DLS analyses.³⁹

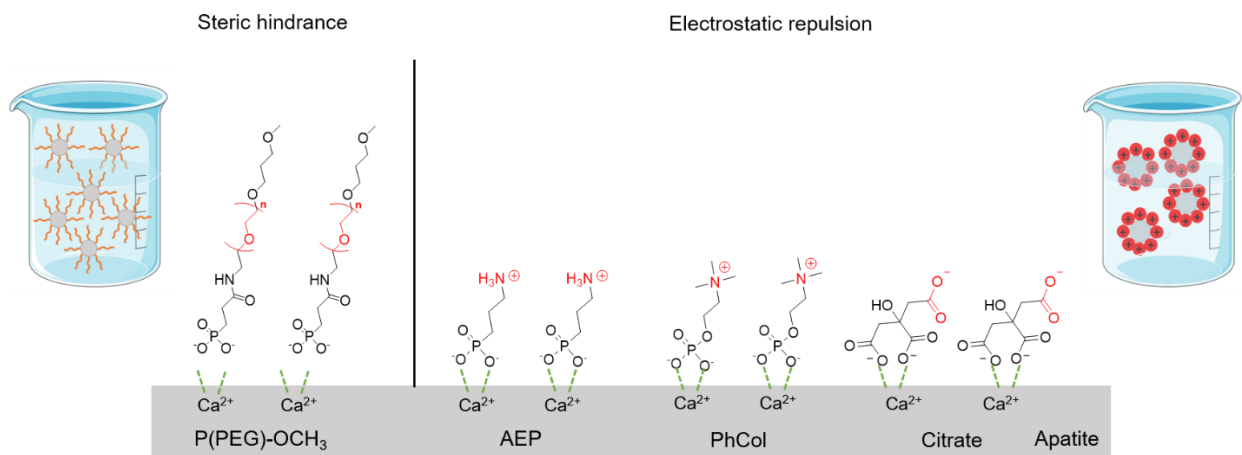


Figure 12: Principle of stabilizing agents via an electrostatic repulsion (AEP, PhCol, Citrate) or steric hindrance (P(PEG)-OCH₃)

The bone-like apatitic nature of the colloidal suspension was confirmed with AEP as stabilizing agent, as shown by XRD and FTIR (Figure 13).⁴² Moreover, the nanometric size of the crystallites (27 nm for the L(002) peak and 10 nm for the L(310) peak) were calculated from XRD data using Scherrer's equation. The dimensions are smaller than for a reference biomimetic apatite showing, in this case, that AEP plays a crystal growth inhibition role on the precipitated apatite crystals.

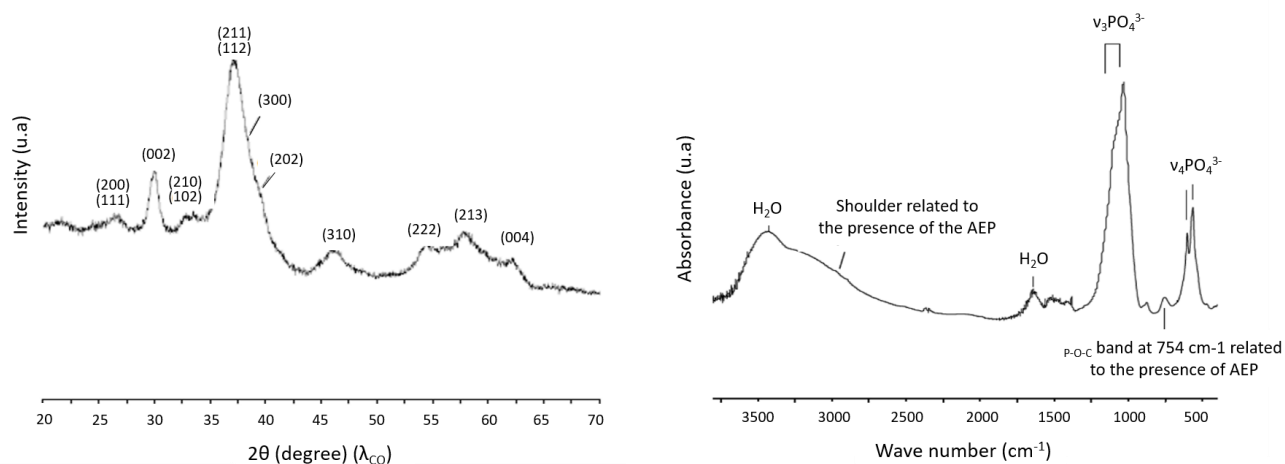


Figure 13: Typical XRD and FTIR features for colloidal apatite particles stabilized with AEP³⁵

b. Nanoparticles stabilized by steric hindrance induced by a P(PEG)-OCH₃ corona

Phosphonated PEG chains as in P(PEG)-OCH₃ were found in a previous work to act efficiently as a stabilizing agent, which may be explained by a steric hindrance around the particles to control agglomeration during apatite precipitation and reach an equilibrated state (Figure 12).⁹ The size of the particles was found to depend on the length of the PEGylated chain. Indeed, the smaller the length of the PEG, the lower the steric hindrance and the larger the size of the particles. Particles of homogeneous size were obtained, ranging from 350 nm for a PEG with a molecular weight mass of 530 g.mol⁻¹ down to 130 nm for a PEG with a molecular weight of 5 800 g.mol⁻¹.^{43,44}

The XRD (Figure 14) and FTIR (Figure 15) analyses showed a weakly crystallized apatite phase (but less obvious than with AEP – (Figure 13) with less resolved peaks and nano-sized crystallites than for regular biomimetic apatites prepared in the absence of stabilizing agent. The FTIR investigation allowed highlighting the sub-stoichiometric character of the apatite phase precipitated in the presence of P(PEG)-OCH₃, with a lower hydroxylation rate than for stoichiometric hydroxyapatite.

As demonstrated by the above examples using AEP, PhCol, Citrate and P(PEG)-OCH₃, the adsorption of such organic molecules allowed controlling, in previous works, the size of the apatite particles and to stabilize them as colloidal suspensions. Other molecules (e.g. small molecule drugs, antibodies) may be co-adsorbed on the surface of the particles to confer additional biological properties: in this case, apatite particles can be used in medicine as drug carriers. In the upcoming section, we focused our attention on applications in nanomedicine.

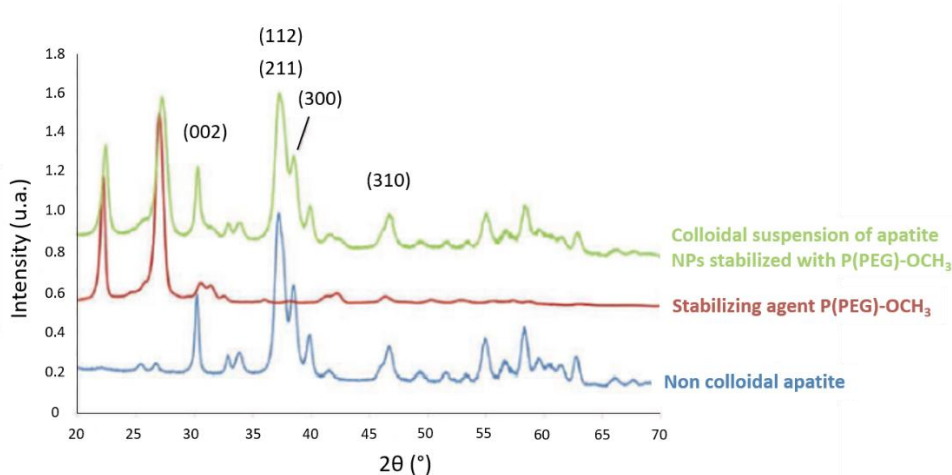


Figure 14 : XRD analysis of colloidal apatite NPs stabilized by a P(PEG)-OCH₃ corona compared with a non-colloidal apatite reference and the P(PEG)-OCH₃ molecule alone⁴⁴

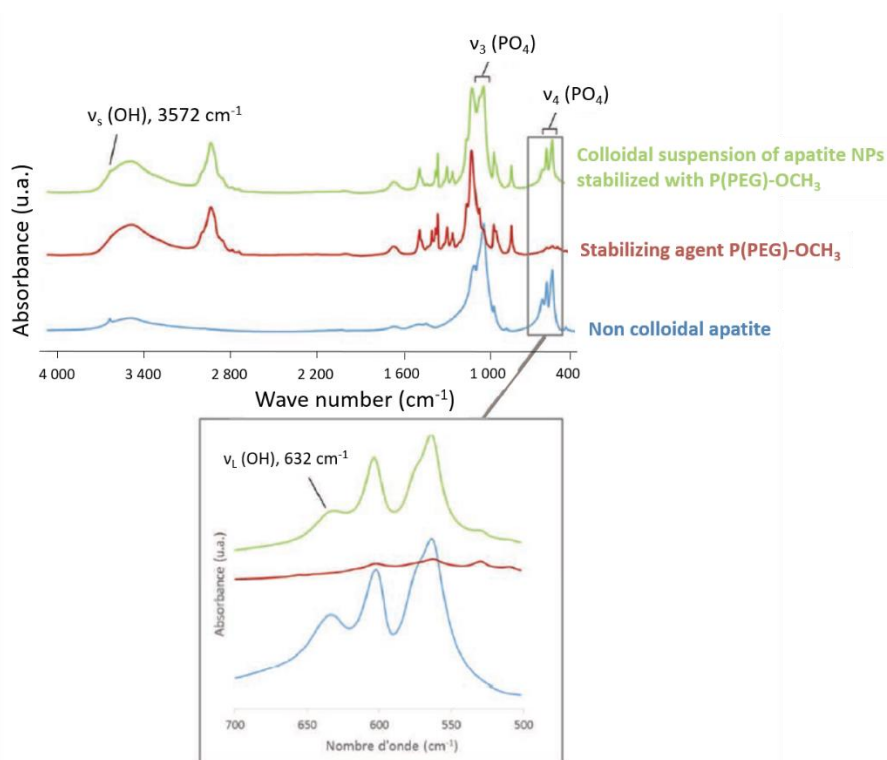


Figure 15 : FTIR analysis of colloidal apatite stabilized by a P(PEG)-OCH₃ corona compared with the FTIR features of a non-colloidal apatite reference and P(PEG)-OCH₃ alone⁴⁴

As seen previously, several synthesis routes (solid or liquid) were proposed to obtain nanometric apatite particles, and several studies have been conducted to obtain hybrid organic/inorganic apatite-based nanoparticles for different applications, typically in oncology, hematology or dermatology.

III. Functionalization of nano-apatite surfaces – hybrid nanoparticles

As described above, the apatite structure facilitates the exchange with the external environment, especially for nano-sized particles, thus allowing for the incorporation of biologically active ions and/or the adsorption of organic molecules/drugs. The latter opens the way to design hybrid organic/inorganic nanoparticles with different properties, in particular biological properties, in view of different biomedical applications. In this PhD project, the molecular adsorption aspects were particularly relevant, and this will thus be discussed below in more details.

In order to synthesize and manipulate apatite hybrid nanoparticles, it is essential to understand the different types of interaction that may exist or be expected between the surface of apatite crystals and organic (bio)molecules. Depending on the physicochemical properties of the apatite component itself (particle shape, stoichiometry...) and more importantly, on the chemical functions presented by the organic part, the affinity of the molecules for the apatite surface can widely vary.⁴⁵ Two essential types of mineral-organic interactions may be outlined: “covalent” bonds and electrostatic interactions.

A. Different types of interactions between organic molecules and apatite surfaces

1. Interactions by “covalent” bonding

Michelot *et al.*⁴ demonstrated that even if the apatitic structure by itself exists only via electrostatic interactions (i.e. cations attracting anions and vice-versa), it was not the only type of interaction that could involve apatite surfaces.⁶ Here, it is assumed that a covalent bond exists when an ion from the apatite surface creates a “covalent” bond with an external organic molecule, although the final interaction through the ion itself remains an electrostatic interaction with the rest of the apatite ionic network. “Covalent” bonds of this kind can in particular be created between silanol derivatives and calcium ions present at the surface of apatite crystals. A mechanism involving (3-aminopropyl)triethoxysilane (APTES) and the hydroxide ions of the apatite surface has been proposed for well-crystallized apatites.⁴⁶ In this mechanism, the hydroxide ions and APTES created a covalent bond forming silanolates which could chelate with apatitic Ca^{2+} ions (Figure 16). However, premature hydrolysis of the alkoxy silane can occur because of the residual water associated with the apatite, and thus initiate the polycondensation of APTES. In fact, silanol may form siloxane (Si-O-Si) bonds and an organosilane multilayer. It may however be remarked that, unfortunately, the formation of Ca-O-Si bonds can most probably not occur on the surface of *biomimetic* apatites that are free of surface OH^- ions (hydrogen atoms are still present on the surface, but belong to HPO_4^{2-} ions or to water molecules loosely bound to the surface).

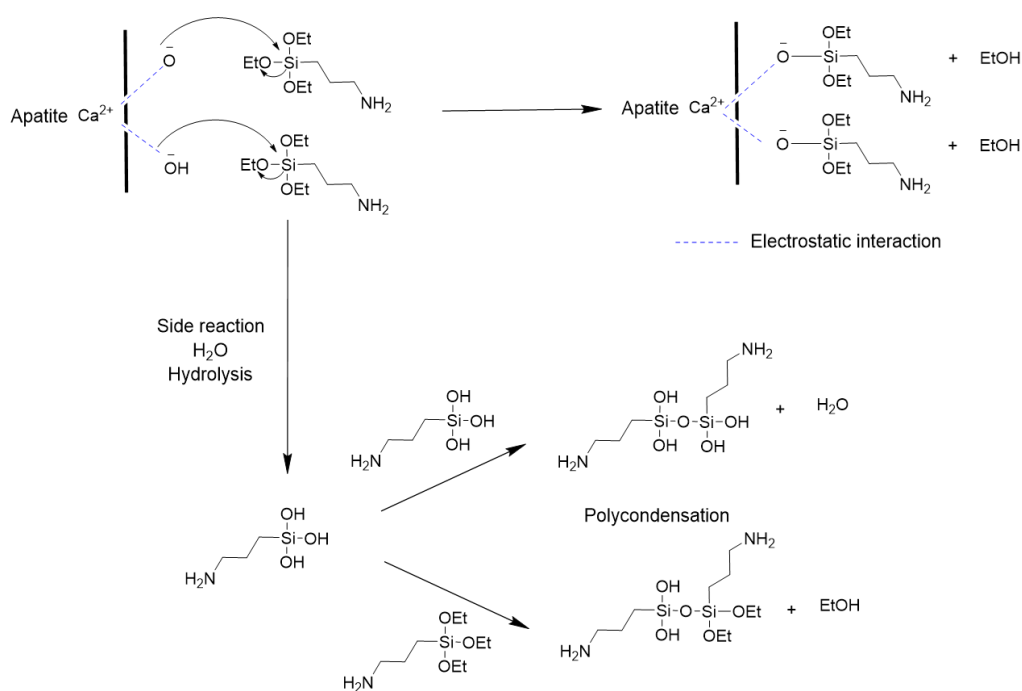


Figure 16 : Covalent interaction between apatite and APTES (inspired by ref⁴⁶)

2. Electrostatic interactions

The main type of interaction which was described when involving apatite surfaces was through electrostatic forces between ions exposed on the crystal surface and some chemical functions exposed by the molecule to be adsorbed. It seems that anionic groups have a significant affinity for apatitic calcium ions. Positively-charged functions (e.g. ammonium $R-NH_3^+$) or *a fortiori* neutral functions (e.g. alcohol $-OH$) have, in contrast, only a limited affinity for the surface of apatites.

In the literature, four organic functions have been especially reported to interact with apatite surfaces via electrostatic interaction: organophosph(on)ates, sulfonates, carboxylates and alcoholates. These groups appear to rather easily interact with the apatitic calcium ions and form an organic coating or corona around the apatite surface. For example, phosphate ($R-O-PO_3^{2-}$) or phosphonate ($R-PO_3^{2-}$) functions interact with surface Ca^{2+} cations of apatite crystals (or substituting cations). This is the case of AEP, PhCol or P(PEG)- OCH_3 described in the previous section.³⁹ Carboxylate ($R-COO^-$) or other negatively-charged functions such as sulfonates⁴⁷ or alcoholates⁴⁵ may also interact with apatitic Ca^{2+} , although less strongly than phosphate or phosphonate. Two main mechanisms may be highlighted, depending on the type of apatite and organic molecule (Figure 17)⁴⁵ :

1. Mechanism A: Direct coordination between negatively-charged organic groups and Ca^{2+} ions from the apatite surface. This is the most frequent case where the molecule

lays down on the surface. In this case, there is no physical anchoring, and the interaction is ensured by electrostatic forces. Desorption may be facilitated.

2. Mechanism B: Substitution of an inorganic phosphate ions from the apatite surface (PO_4^{3-} or HPO_4^{2-}) by an organic phosphate or phosphonate group, associated to their coordination with adjacent Ca^{2+} ions from the surface. In this case, there is a “physical” anchoring of the molecule, because the organic phosph(on)ate becomes part of the structure of the apatite. Desorption can then only be undergone by a reverse exchange mechanism (replacement of the anchored molecule by an inorganic ion or another molecule present in the medium) or by the dissolution of the apatitic support itself.

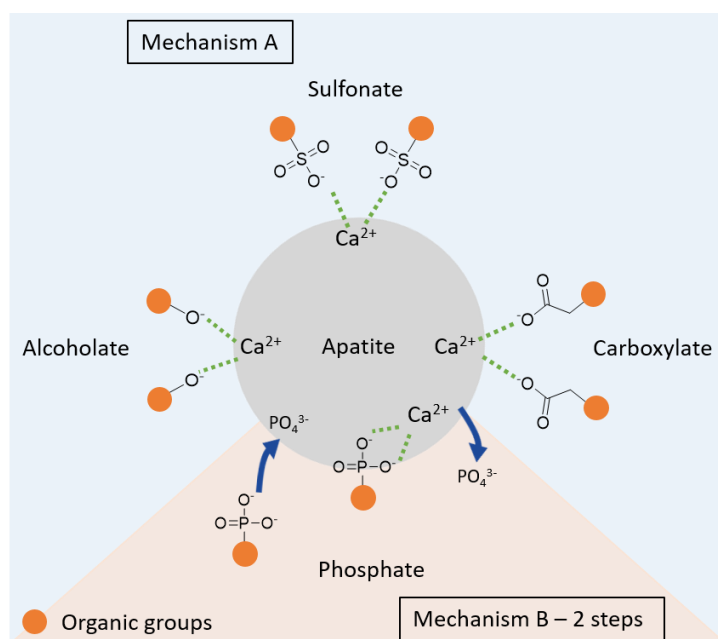


Figure 17: Two main mechanisms involving electrostatic interactions between different organic groups and an apatite surface

A study was conducted in the literature to compare the affinity for apatite of the organic groups mentioned above, namely alcoholates, phosphonates, carboxylates and sulfonates. To this aim, a borate, phenylphosphate and benzoic acid were chosen with an inert phenyl group toward the apatite to ensure that the interaction with the apatite crystals surface occurred only via the oxoanionic functions forming in solution. It was shown that alcoholates⁴⁵, carboxylates^{48,49} as well as sulfonates⁴⁷ adsorbed on the surface of apatite via mechanism A. Indeed, after adsorption of these molecules, the concentrations in solution of calcium and phosphate ions remained unchanged. On the contrary, the concentration of phosphate ions significantly increased during the adsorption of phenylphosphate, demonstrating that this organophosphate binds to the surface of apatite according to mechanism B which releases phosphate ions. It may also be noted that mechanism B was also reported in the case of the adsorption of bisphosphonate molecules (used in the treatment of osteoporosis) on

biomimetic nanocrystalline apatite.^{50,51} It is possible that this behavior is also related to the high surface reactivity and the high mobility of ions on the surface of biomimetic apatites, in contrast to stoichiometric hydroxyapatite. However, it should be noted that mechanism B is not systematically observed for all phosph(on)ate molecules. It probably requires an adapted molecular configuration and has not been observed for the adsorption of monophosphate nucleotides, for example, which were found to adsorb via mechanism A.^{52–54} Therefore, the affinity of an organic end-group/molecule for the apatite surface depends on different physicochemical factors as the organic groups exposed, the molecular configuration and the stoichiometry and shape of the particles.⁴⁵ Studies are still being conducted, including through atomic and molecular modeling, to better understand how the chemical composition and/or conformation of the molecule can direct adsorption to either mechanism A or B. However, it may be assumed that when the apatite crystals are precipitated in the direct presence of adsorbable molecules (thus not in a situation involving already formed apatite crystals), this mechanism may potentially come into play even in conditions leading to non-stoichiometric apatites, which are conditions considered in this work.

B. Applications of nano-sized particles of apatite in nanomedicine

Thanks to the previously developed synthesis methods to obtain nanosized particles and to better understanding the interactions between organic molecules and apatite surfaces, hybrid NPs (i.e. composed of both an organic and an inorganic component) have been developed in the literature in view of different applications in (nano)medicine. In all of the following examples listed, it may be highlighted that the particles were prepared by wet synthesis and the adsorption of the therapeutic agents was systematically carried out in a subsequent step.

1. Importance of the size of particles in medical applications

The "classical" galenic forms (tablet, suppository, cream, etc.), although widely used, present a certain number of limitations (Table 6).

First, active pharmaceutical ingredients (APIs) are distributed to different tissues and cells according to their physicochemical properties (pKa, hydrophilic/hydrophobic character, molecular weight...), without any particular specificity within the body. The dose administered must therefore be much higher than the dose that actually reaches its target, which may cause undesirable side effects. Then, therapeutic agents may encounter natural barriers that limit their efficacy. Molecules that are too hydrophilic or whose molecular weight is too high cannot cross cell membranes, which is a problem when the target is inside the cell.

In order to overcome these drawbacks, the development of (nano)particulate "carriers" for the transport of active ingredients can be envisaged. The (nano)particles can indeed advantageously modify the pharmacological and pharmacokinetic properties of the active

ingredients in comparison with their free form, and allow for example improving the solubility of hydrophobic agents, decreasing the toxicity of APIs, better controlling their release and metabolization and thus increasing the lifetime of APIs in the organism, but also improving their distribution to a specific site or target.^{55,56} The transport of APIs inside the cell proceeds through internalization mechanisms (such as endocytosis or macropinocytosis) which are themselves conditioned by the physicochemical characteristics of the particles, including their size and surface features.

Particles used as carriers can be classified into two main categories: organic or inorganic.⁵⁷ Organic vectors include in particular liposomal or lipidic nanoparticles or polymer and PEGylated polypeptide-based nanoparticles. Several of these systems have reached the market, in particular liposome-based systems (e.g. Doxil[®], Myocet[®], Caelyx[®] by Janssen Cilag, Daunoxome[®], Johnson & Johnson, Onxeo, or Celator Pharmaceuticals).⁵⁸ Inorganic carriers include in particular silica nanoparticles, gold nanoparticles, magnetic particles based on iron oxides, carbon nanotubes and apatite (nano)particles, the latter being bio-inspired and the subject of this PhD project.

Problems with active ingredients used alone	Contribution of nanoparticles
Poor solubility	Nanoparticles can provide a hydrophilic or hydrophobic environment to improve the solubility of the active ingredient
Destruction of healthy tissues and organs	Controlled release of APIs from the nanoparticles, which reduces or eliminates its extravasation into healthy tissues
Rapid degradation <i>in vivo</i>	Protection of active ingredients from metabolism. Reduction of the doses of therapeutic agents administered
Poor biodistribution	The nanoparticulate form reduces the volume of distribution and decreases adverse effects in non-target tissues
Low selectivity for targeted tissues	Nanoparticles allow the delivery or targeting of the drug in diseased tissues/cells. In addition, targeting agents, such as receptor ligands, can be added to their surface to further increase their specificity
One therapeutic effect	Several molecules and/or ions can be combined on the same particle for a synergic effect

Table 6: Summary of the contributions of nanoparticles compared to active agents used alone (adapted from ref ⁵⁶)

Thanks to their properties and great versatility, mineral-organic hybrid particles based on apatite were investigated for applications in (nano)medicine, in particular in oncology, hematology and dermatology, which are developed below.

2. Applications of hybrid apatite NPs in nanomedicine

a. Oncology

Cancer is the most common disease in the world. Current therapies continue to progress but have some limitations. Surgery is only suitable for well-localized tumors and remains a very invasive procedure. Conventional radiation and chemotherapy cause side effects due to the lack of selectivity of radiation or APIs that affect both cancer cells and healthy cells. Indeed, anticancer drugs are cytotoxic. Their administration via a classical galenic formulation only allows a delivery in the cells of the order of 2 to 5%, which implies a high systemic toxicity.

To overcome the lack of selectivity of chemotherapeutic agents, several strategies are deployed such as the use of vectors, the adsorption of targeting agents or the implementation of release systems controlled by external stimuli. The aim is to take advantage of specific characteristics of the tumor tissues and/or environment and/or cancer cells (e.g. overexpressed biomolecules on their surface), to specifically affect the diseased cells.

One of the proposed means is based on the association of the APIs with a nanoparticle vector of well-controlled size. Cancer cells secrete molecules that promote angiogenesis, the creation of new blood vessels to deliver oxygen and nutrients to the tumor. This rapid hypervascularization results in larger spaces (defects) in the walls of the newly formed vessels compared to healthy tissue, allowing particles injected into the circulatory system to cross these gaps and accumulate more easily in the cancerous tissue. This Enhanced Permeability and Retention (EPR) effect is still controversial but has been used to develop new vectors. Doxorubicin (DOX - Figure 21), a cytotoxic anticancer drug, has been adsorbed on the surface of biomimetic carbonated apatite particles previously synthesized by co-precipitation.⁵⁹ DOX can interact with the apatite surface through the presence of the primary amine (protonated with the basic environment caused by the co-precipitation synthesis) and several hydroxyl groups that can create an electrostatic interaction with the surface of the apatite particle (Table 7). DOX is an anthracyclinic drug (chemotherapy drug that aims at preventing cancer cells from dividing by interfering with their DNA chain) but must enter cells to exert its toxic effects. Apatite-DOX particles with an optimal size (e.g. ~70 nm) that facilitates cell penetration by endocytosis was compared to free DOX, and resulted in increased cytotoxicity in several human cancer cell lines *in vitro* and *in vivo* in mice for colorectal cancer.⁵⁹

Beyond their use as nanovectors, apatite particles may limit the degradation of some anticancer drugs, improve their pharmacokinetics and thus reduce their toxicity. For example, according to S.Hossain, as long as it is associated with the surface of carbonated apatite particles, DOX does not generate the free radicals responsible for serious side effects such as cardiomyopathy.⁵⁹ The association with particles also allows improving the administration of

poorly soluble molecules such as Docetaxel® and Paclitaxel® (Figure 21) which can interact via an electrostatic interaction between the alcoholate groups and the apatitic Ca²⁺ present onto the particle surface (Table 7). Both are commonly used in the treatment of breast cancer, and are usually associated with castor oil or polysorbate-ethanol 80 adjuvants that are not without side effects.⁵⁵

In addition to these cytotoxic molecules, or even as an alternative to them, it is now possible to have recourse to cancer gene therapy, via the approach using small interfering RNA molecules (siRNA). These oligonucleotides make it possible to selectively attenuate or extinguish the expression of a defective and/or overexpressed gene by cancer cells (e.g. linked to cell proliferation or angiogenesis), by matching with the mRNAs that code for the proteins whose expression is to be limited. In doing so, they cause the destruction of the mRNA and thus prevent the production of an oncogenic protein. SiRNAs are small molecules of so-called "interfering" RNA. The suffix "si" stands for "small interfering RNA". They are RNAs that can bind to a specific sequence of messenger RNA to prevent gene expression. However, siRNAs cannot easily cross the plasma membrane of cells and are very sensitive to nuclease enzymes that destroy them. These two drawbacks hinder the use of siRNAs in the treatment of cancers. Carbonated apatite NPs have been studied *in vitro* and *in vivo* for the transport and protection of siRNAs against their degradation by nucleases.^{60,61} These particles suppressed the expression of tumor growth limiting proteins in a mouse model (ER/BCL2 and ER/ERBB2/EGFR)⁶² and induced apoptosis *in vitro* in cervical and breast cancer cells.^{63,64} The effect of siRNAs was also found to synergize with anticancer drugs such as DOX, Cisplatin or Paclitaxel®.^{62,65}

Another way to affect cancer cells is to use targeting agents, i.e. molecules that recognize receptors or proteins overexpressed on the surface of cancer cells. Antibodies such as human immunoglobulin and DO-24 monoclonal antibody have been adsorbed onto the surface of apatite NPs.⁶⁶⁻⁶⁸ Antibodies both exhibit a targeting effect and block certain oncogenic mechanisms, and thus exert a toxic effect to the cancer cells. Other targeting agents have been studied. Folic acid (FA - Figure 21) for instance was adsorbed onto the apatite surface by an electrostatic interaction thanks to the two carboxylates which can interact with surface Ca²⁺ ions (Table 7). FA indeed targets certain cancer cells that overexpress folate receptors on their surface. Methotrexate (MTX - Figure 21) antagonizes FA ; it also adsorbs *via* an electrostatic interaction with Ca²⁺ and its carboxylate groups (Table 7) and thus has a dual effect of targeting and inhibiting proliferation once it enters the cell.⁶⁹

The final method discussed here is drug delivery controlled by an external stimulus such as local pH. In order to release therapeutic agents at the right place, another method is indeed to use the more acidic extracellular microenvironment of tumor cells (pH = 6.8). This is due to the secretion of lactate by anaerobic glycolysis. In the absence of oxygen, glycolysis (metabolization of glucose to pyruvate by the Krebs cycle and the respiratory chain ideally)

takes place in the cytoplasm. Glucose is then transformed into pyruvate and then into two 2H^+ lactate molecules, two H_2O molecules and two adenosine triphosphate (ATP) molecules. The massive production of lactic acid and carbonic acid leads the tumor cell to overexpress proteins involved in the export of these metabolic wastes. The accumulation of these wastes leads to a decrease of the extracellular pH of the tumor cells. As apatite dissolves at acidic pH, apatite nanoparticles seem to be a good choice to deliver therapeutic agents specifically in the vicinity of tumors (or other local environments exerting an acidic pH like inflammatory conditions). Moreover, the particles can be internalized into cells by different mechanisms, and are expected to enter endosomes and endolysosomes. These endosomal compartments have a lower pH than the cytosol (pH ~ 6.5) especially in cancer cells whose metabolism leads to the accumulation of intracellular acid waste. This phenomenon allows for an increased delivery of APIs as for DOX adsorbed on apatite particles (Figure 18).

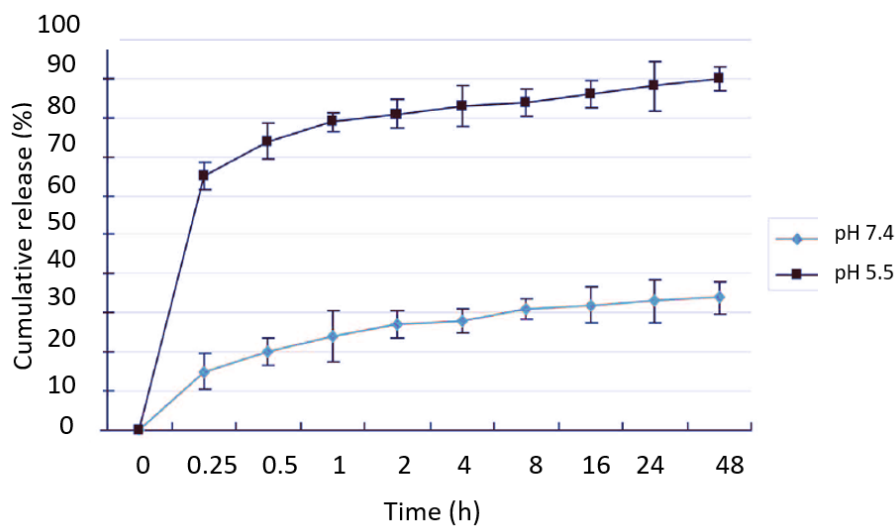


Figure 18: DOX release from DOX-loaded apatite particles thanks to a pH stimulus⁵⁹

b. Hematology

To increase the capacity of hospitals for blood transfusions, the cryopreservation of red blood cells is an interesting method. Unlike most other cells, mature red blood cells cannot multiply, which implies the need for regular blood donors. However, in the absence of a cryoprotective agent, cells that undergo a freeze-thaw cycle have a very low viability of about 20%. Cryoprotection or cryopreservation of cells is a process that consists of adding a cryoprotective agent that prevents the outer membrane of the cell from being damaged during the freezing step by ice crystal formation. This process very noticeably improves cell survival following the freeze-thaw cycle. Nevertheless, to be effective, a cryoprotective agent must generally be present on both sides of the plasma membrane, so this agent should ideally have good membrane permeability. Current cryopreservation methods use a high concentration of glycerol. However, this compound is toxic and can cause intravascular hemolysis or a change in the shape of red blood cells. Therefore, deglycerolization processes

are required before transfusion. These techniques are complex, costly and time-consuming and residual glycerol may remain inside the cells and cause complications in some patients. These drawbacks prevent large-scale cryopreservation and it is nowadays limited to rare blood phenotypes.⁷⁰ New non-toxic cryoprotective additives are proposed, in particular biopolymers such as polyvinyl alcohol⁷¹ or sugars such as trehalose.^{72–74} Unfortunately, their low membrane permeability limits their cryoprotective effect on red blood cells. Colloidal bio-inspired apatite nanoparticles possessing an organic corona with surface charged groups (i.e. AEP) facilitated the transmembrane diffusion of trehalose – a dimer of glucose that exerts cryoprotective properties – in these cells (Figure 19). Further analysis on model lipid bilayers mimicking the cell membranes of red blood cells showed that the NPs did not cross these membranes. Indeed, the latter are not capable of carrying out an active process of endocytosis to incorporate the NPs. The NPs however were shown to transiently modify the electrical properties of the membrane and momentarily alter the three-dimensional organization of the phospholipids, which allowed a greater passage of trehalose molecules into the cell. With this new method, the survival of red blood cells after freeze-thaw cycle increased to 91%, thus similar to the results obtained with glycerol and approved by FDA, but via a totally bio-inspired pathway involving bone-like apatites particles and a sugar molecule.⁷⁵ It is also necessary to note that blood is supersaturated with respect to apatite, which limits the dissolution of particles (unless acidic pHs are encountered or a specific cell activity) and may thus allow for a prolonged lifetime of the drug in the circulatory system prior to elimination by the natural pathways of the organism (then generating natural metabolites like Ca^{2+} and phosphates ions used all over the skeletal system). Opsonization of the particles (i.e. coverage by opsonin proteins to favor recognition by macrophages and subsequent elimination) may happen *in vivo* as for most foreign entity; however, a previous study⁴⁴ showed that the degree of interaction of the apatite NPs tested with plasma proteins was only moderate, and in fact of the same order as for some already-used nanosystems like citrate-coated Au NPs or flavonoids. It may thus be expected to have some non negligible circulation lifetime in the blood stream prior to elimination. One relevant characteristic may nonetheless be the particles size and surface features that remain important parameters to control.

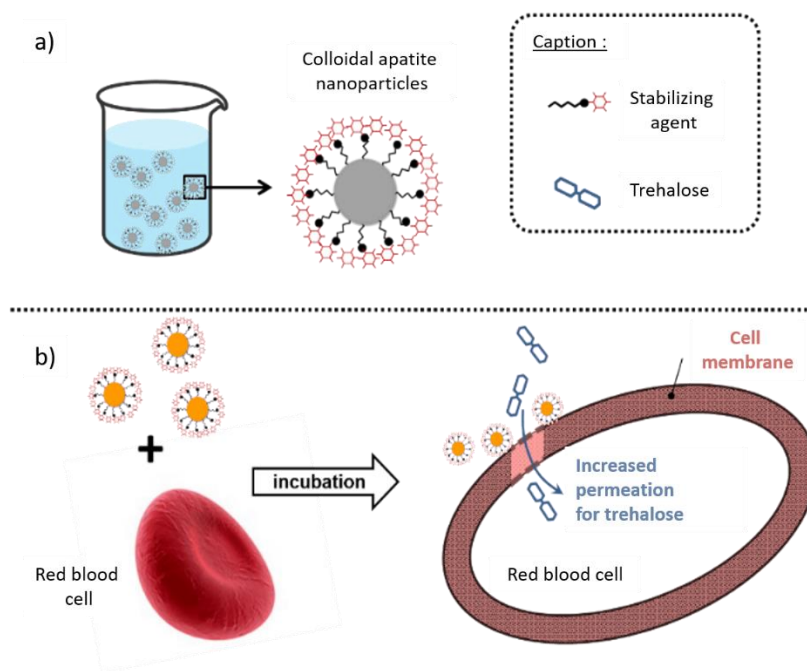


Figure 19: Use of hybrid apatite NPs to facilitate membrane permeability of trehalose in red blood cells in view of enhanced cryoprotection (inspired by ref ⁷⁵)

c. Dermatology

Skin is the largest organ of the human body. It protects the internal organs from the external environment. The presence of wounds or diseases such as acne or eczema affects the integrity of the skin barrier and facilitates the development of pathogenic microorganisms. In this view, it is thus relevant to engineer (nano)systems to fight against infections. The potential spreading of infectious pathogens is especially problematic in patients with chronic wounds as in the case of the diabetic foot, or else for burns patients, etc. where the continuity of the barrier created by the skin is obviously disrupted. This is in link with this PhD project.

To this date, the use of apatite-based NPs was only seldom reported for dermatological applications. A rather recent study initiated at CIRIMAT addressed the development of an anti-acne formulation based on P(PEG)-OCH₃ stabilized apatite NPs of around 180 nm in size and associated with an anti-acne antibiotic agent, clindamycin.⁹ The underlying idea was to retain as far as possible the NPs at the surface of the skin and at the opening of the hair follicles where acne is to be developed (upon the action of pathogens like the bacterium *Propionibacterium acnes*). To this aim, the clindamycin was adsorbed in its phosphate form, prone to interact efficiently with the Ca²⁺ ions from the surface of apatite (Table 7). Indeed, current treatments for mild to moderate acne, either orally or by local administration, have shown certain drawbacks including the possible transcutaneous passage of the drug into the bloodstream causing notable side effects. By adsorbing the active agent directly on particles too large to cross the skin barrier, the study showed a clear tropism of the particles and its

associated drug on the top of the skin and at the entrance of hair follicles: this approach thus limits the transcutaneous passage of the drug into the bloodstream due to the size of the particles. Clindamycin (Figure 21) has demonstrated its therapeutic efficacy against *P. acnes* involved in acne pathology, and is thus the “active” form of the molecule. A study on porcine ear skin showed that the adsorption of a model drug (folic acid) mimicking clindamycin (Figure 21) on apatite particles could indeed control the release (and therefore the action) of the drugs opposed to the free drug (Figure 20).⁹

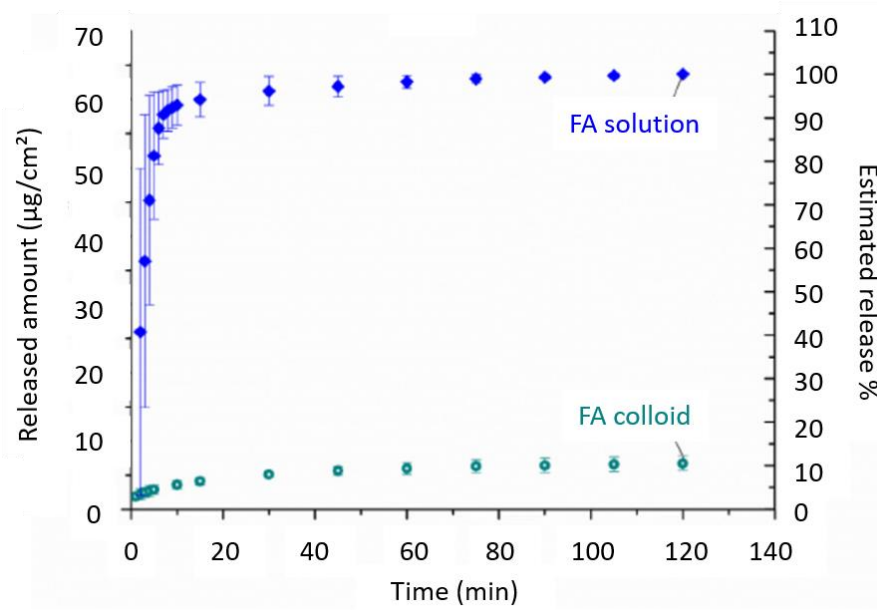


Figure 20: Ex vivo permeation study for FA solution and FA-functionalized colloidal particles, in dynamic conditions⁴⁴

In this context, during this current PhD, we aimed at exploring the potential of such particles for the treatment of cutaneous wounds, via the modularity of their peripheral organic coronas allowing us to envisage complementary actions such as antimicrobial, anti-inflammatory or pro-healing upon peptide functionalization.

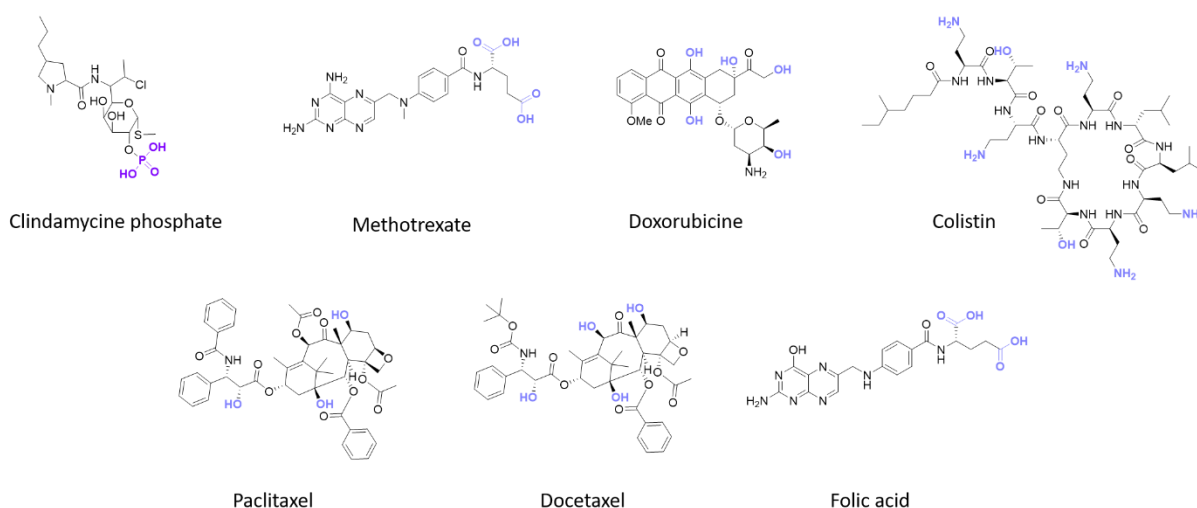


Figure 21: Example of APIs adsorbed via electrostatic interaction onto the apatite surface

d. Genetic disease – Cystic Fibrosis

In 2022, M. Iafisco *et al.* functionalized apatite NPs with a cyclic antibacterial peptide, Colistin, for the treatment of cystic fibrosis by inhalation.⁴⁰ For this purpose, nanosized particles (50-100 nm, PDI 0.26) were obtained thanks to the addition of sodium citrate tribasic dihydrate during the synthesis, playing the role of stabilizing agent thanks to negatively charged carboxylates (electrostatic repulsion – described part III.A.2). In this study, the negative charges also allowed for the adsorption at pH 7 of Colistin thanks to an electrostatic interaction between the primary amine (protonated at physiological pH) of the peptide and the negative charges of the particle. The electrostatic repulsion being no longer possible, an agglomeration of the NPs was observed giving particles of micrometric size and a neutral zeta potential. The particles stabilized by citrate and functionalized with Colistin were suspended in an 8 mM citrate buffer solution. Finally, particles of nanometric size (210 nm, PDI 0.26) sufficient to pass the mucus barrier (max size 250-300 nm) were obtained. These NPs showed no *in vitro* cytotoxicity on A549 lung cells and microbiological experiments on a clinical APIs strain isolated from a cystic fibrosis patient revealed that Colistin adsorbed on the NPs does not lose its therapeutic effect and presents an antimicrobial and anti-film efficacy comparable to that of Colistin alone. These results recall those of Weber *et al.* on enzyme-functionalized apatite where the biological activity of the enzyme was not altered due to the adsorption process.⁷⁶ *In vivo* tests have also shown promising results in a cystic fibrosis mouse model.^{40,41}

e. Application in medical imaging

Among the first imagined domains of application of apatite-based particles is medical imaging. Luminescent particles can indeed be helpful in this domain in several ways. This is especially true if the particles may have a specific interaction with some cells or tissues. For example, cancer cell targeting agents can be grafted on the particles, and luminescence (upon adapted

excitation) can then help visualizing the particles biodistribution after their administration in view of deciphering adapted therapeutic plans or to follow the evolution of cancer (e.g. from biopsies) with or without treatment.

Luminescence can be provided to apatites by substitution of part of the Ca^{2+} ions by lanthanide ions.^{34,38,77,78} This arises from the fact that the apatite structure, as mentioned previously, is very accommodative for a large variety of ions including lanthanide ions such as europium (Eu^{3+}) or terbium (Tb^{3+}), that exhibit luminescence properties respectively in the red and green domains. Lanthanide ions present several advantages such as a long luminescence lifetime (of the order of the millisecond, thus much longer than the self-fluorescence of biological tissues) and the absence of photo bleaching phenomena often encountered with organic dyes.⁷⁹ In this view, apatite particles doped with lanthanide ions (few molar % of substitution of calcium) have been prepared by several ways, and their luminescence features have been explored. Different organic coronas have then been used with the view to stabilize the particles, more or less efficiently, such as DNA⁷⁸, AEP^{34,38,77} or citrate^{80,81} ions. One difficulty remains the relatively strong absorption of exciting/emitted photons from water and hemoglobin contained in biological tissues, that may limit the use of lanthanide-doped particles. It may be noted that the DNA-covered particles cited above (not necessarily doped with luminescent ions) were also considered for transfection applications, e.g. in view of gene/RNA delivery or gene silencing.⁸²⁻⁸⁵

Reference	Types of apatite	Synthesis	Particles size	Parameters which control the size	Types of molecules	Types of interaction	Applications
59	Carbonate apatite	Co-precipitation	One particle ~70-80nm but agglomeration ~200-300nm	Calcium concentration	Drug (Doxorubicin)	Electrostatic interaction (OH ⁻ and NH ₃ ⁺)	Oncology
55	Carbonate apatite	Co-precipitation	Maximum 170nm	Bicarbonate buffered medium	Drugs (Docetaxel and Paclitaxel)	Electrostatic interaction (OH ⁻)	Oncology
61	Carbonate apatite	Co-precipitation in DMEM/DMB	350nm (7mM Ca ²⁺) in DMEM 1 500nm (4mM) in DMB	Calcium concentration, medium, bicarbonate buffered medium	SiARN	/	Oncology
	Hydroxyapatite	Co-precipitation	Maximum 1 200nm				
67	Biomimetic nanocrystalline apatite	Co-precipitation	~44nm	/	Antibody (DO-24 monoclonal antibody) Drug (Doxorubicin)	Electrostatic interaction (OH ⁻ and NH ₃ ⁺)	Oncology
75	Colloidal suspension of apatite	Co-precipitation in water	~40nm (AEP dependent)	Stabilizing agent (AEP)	Stabilizing agent (AEP)	Electrostatic interaction Mechanism B (R-PO ₃ ²⁻)	Hematology
34	Colloidal suspension of biomimetic apatite doped with Eu ³⁺	Co-precipitation in water	30-40nm	Stabilizing agent (AEP)	Stabilizing agent (AEP) and Drug (Acid folic)	Electrostatic interaction Mechanism B (R-PO ₃ ²⁻) and Electrostatic interaction (COO ⁻)	Oncology
38	Colloidal suspension of biomimetic apatite doped with Eu ³⁺ , Tb ³⁺	Co-precipitation in water	30-40nm	Stabilizing agent (AEP)	Stabilizing agent (AEP)	Electrostatic interaction Mechanism B (R-PO ₃ ²⁻)	Medical imaging
	Biomimetic apatite doped with Eu ³⁺ , Tb ³⁺	Continuous method of co-precipitation	>1mm	/	DNA		Colloidal stabilization
48	Stoichiometric hydroxyapatite	Co-precipitation	100nm	/	Drug (Acid Tranexamic)		Oncology
9	Bio-inspired apatite	Co-precipitation	100-400nm (depends on the length of the PEG)	Stabilizing agent (PEG)	Stabilizing agent (PEG) Drug (Acid folic)	Electrostatic interaction Mechanism B (R-PO ₃ ²⁻) and Electrostatic interaction (COO ⁻)	Dermatology

66	Biomimetic carbonated apatite	Co-precipitation	~30nm	/	Antibody (human IgGs)	/	Oncology
69	Nanocrystalline apatite	Co-precipitation	~74nm	/	Drug (Methotrexate and Acid folic)	Electrostatic interaction	Oncology
	Nanocrystalline apatite doped with Fe ²⁺		~120nm				
45	Ceramic hydroxyapatite	Commercial	/	/	Drug (3-piperazine-bis (benzoxaborole))		Antibacterial and antifungal
	Nanocrystalline hydroxyapatite	Co-precipitation					
46	Stoichiometric hydroxyapatite	Co-precipitation and thermal treatment	/	/	Aminopropylethoxysilane	« covalent » bond	/
	Nanocrystalline apatite	Co-precipitation					
69	Poorly crystalline hydroxyapatite	Co-precipitation	Heterogeneous size	/	Amino acid (L-Lysine and DL-Leucine)		/
86	Hydroxyapatite	Co-precipitation	10-20 x 40-100nm	/	Heparin		Hematology
50	Stoichiometric hydroxyapatite	Co-precipitation	/	/	Bisphosphonate (Risendronate and Tiludronate)	Electrostatic interaction Mechanism B (R-PO ₃ ²⁻)	Bone disorder (Osteoporosis)
	Nanocrystalline hydroxyapatite						
51	Nanocrystalline hydroxyapatite	Co-precipitation	/	/	Bisphosphonate (Tiludronate)	Electrostatic interaction Mechanism B (R-PO ₃ ²⁻)	Bone disorder (Osteoporosis)
54	Biomimetic nanocrystalline apatite	Co-precipitation	/	/	Cytidine monophosphate	Electrostatic interaction Mechanism B (R-PO ₃ ²⁻)	/
52	Biomimetic nanocrystalline apatite	Co-precipitation	100-200 μm	Sieved	Adenosine monophosphate	Electrostatic interaction Mechanism B (R-PO ₃ ²⁻)	/
	Carbonate apatite						
53	Biomimetic nanocrystalline apatite	Co-precipitation	/	/	Adenosine triphosphate	Electrostatic interaction Mechanism B (R-PO ₃ ²⁻)	/
	Carbonate apatite						
65	Carbonate apatite	Co-precipitation in DMEM	/	Calcium concentration	Drug (Cisplatin and Paclitaxel)		Oncology

64	Carbonate apatite	/	/	/	SiARN		Oncology
40,41	Hydroxyapatite	Wet precipitation	213 nm (Pdl = 0.26)	Citrate	Colistin	Electrostatic interaction between negative charge of the citrate and positive charge of the Colistin	Genetic disease

Table 7: Summary of apatite NPs-based strategies

Description of the PhD thesis objectives

Biomedical research is increasingly interested in the use of biofunctional materials and in particular vectors for the transport and delivery of active ingredients for local treatments, less invasive and more targeted than systemic treatments. Drug (nano)vectors are extensively studied in oncology but also more recently in hematology, dermatology or for genetic diseases. In addition to a possible protection of the bioactive molecule via its association with particles, NPs also allow the possibility of combining several biologically-active agents for synergy, or to exert a certain control on the release of the active ingredients under a given stimulus. It can be, for example, the hydrolysis of a covalent bond or through the selective dissolution of the vectors triggered by a low local pH value encountered locally in the case of inflammation or bacterial activity (wounds, post-surgery, chronic disease, cancer etc.). Many drug carriers either organic- or inorganic-based have been considered to this day, but research is still in progress for seeking higher efficacy, biocompatibility, biodegradability and (multi)functionality. Bone-inspired apatite NPs constitute a judicious choice thanks to its biomimetic character close to natural bone mineral composition and structure, and to its interesting adsorption properties. Indeed, apatite presents a greater biocompatibility and biodegradability as well as a lower cytotoxicity than polymer and silicon-based vectors, for example.^{67,87} In addition, apatite has a higher stability than liposome-based vectors allowing for a better control of drug release.⁶⁷ Moreover, thanks to their pH sensitivity, apatite NPs will progressively be degraded *in vivo* to give rise to natural metabolites such as calcium or phosphates ions.⁶⁷ Finally, the degradation of apatites leads to an increased concentration of calcium ions which may take part in healing processes (e.g. blood clotting) and can help causing the apoptosis of diseased cells.^{88,89}

As was seen previously, several synthesis routes have been tested to prepare nanometric apatite particles. Stabilizing agents appear as the most relevant way to control the size and limit the agglomeration of apatite particles to generate colloidal suspensions. These particles, which have been studied extensively at CIRIMAT for several years, are formed of a calcium phosphate mineral core close to the chemical composition of bone mineral – thus intrinsically biocompatible – coated with an organic corona whose primary purpose is to stabilize the particles by controlling their agglomeration state. But to this day, these stabilizing agents did not confer additional biological activity to the apatite NPs, and therapeutic agents had to be associated in a subsequent step by adsorption via a post-synthesis of the colloiddally-stabilized NPs.

The aim of this research project consisted in stabilizing apatite nanoparticles in colloidal suspension via innovative peptide-based stabilizing agents which will then play a dual role: 1) stabilizing the NPs in colloidal form and 2) conferring *simultaneously* a tailorable biological activity via the selection of peptide used. These NPs should be able to play the role of Nano

vectors of these bioactive peptides, in particular for the treatment and healing of complex wounds. The objectives of this PhD were therefore:

1. To develop the synthesis of two types of novel bioactive peptide-based stabilizing agents: P(Peptide) and P(PEG3K)-Peptide,
2. To ensure that the novel stabilizing agents did not prevent the formation of biomimetic apatite NPs,
3. To assess if stable, colloidal suspensions of these multifunctional peptide-apatite hybrid nanoparticles could be obtained,
4. To evaluate biologically *in vitro* the peptide-apatite hybrid phosphocalcic nanoparticles prepared in view of the treatment of complex wounds, in particular aiming wound healing and an antibacterial effect,
5. To start studying the formulation of apatite-based NPs suspensions for wound care, typically through dressings or spray approaches.

Chapter 2 - One-pot co-precipitation
synthesis and characterization of peptide-
decorated colloidal hybrid apatite
nanoparticles

In Chapter 1, we presented methodologies developed to control the size of apatite particles, by using stabilizing agents such as AEP and P(PEG) during their synthesis; and we also pointed out the possibility to confer additional biological properties via the post-synthesis adsorption of drugs or targeting agents.

The first goal of this PhD project was to demonstrate, as a proof of concept, the possibility of a one-pot synthesis of colloidal apatite NPs stabilized by peptides. Interestingly, these peptides would then play a dual role, providing also some additional biological properties to the particles. In this work, we selected three peptide sequences: Ac-LRGDNK-NH₂, H-GDPGYIGSR-NH₂ and H-AhXRR-NH₂. These peptides were chosen for their biological properties (cell adhesion peptides to promote wound healing and the fight against infections) but also to illustrate the possibility to use apatite NPs as a tailorable platform for different peptides. Moreover, these peptide sequences will further be functionalized with a phosphonate-contain moiety at different positions (i.e. respectively on the side chain of a C-terminal Lysine and on the N-terminus for the last two ones) to prove the flexibility and general character of our strategy, and with the goal to expose a phosphonate moiety for efficient grafting to apatite surfaces. From these sequences, two families of novel peptide-containing stabilizing agents, inspired by known and simple stabilizing agents, were synthesized.

The first type consisted of a peptide sequence functionalized at its N-terminus (for the peptides H-AhXRR-NH₂ and H-GDPGYIGSR-NH₂) or on the side chain of a C-terminal Lysine (Ac-LRGDNK-NH₂) by 3-(diethoxyphosphoryl)propionic acid. We hypothesized here that the molecular weight of the peptides and especially the charges present would stabilize the NPs by electrostatic repulsion as in the case of AEP. These new stabilizing agents will be named "P(Peptide)" in the rest of this manuscript.

The second type consisted of a peptide sequence functionalized by a PEG amino acid (3 000 - 5 000 g.mol⁻¹) to avoid the NPs agglomeration by steric hindrance. They will be named "P(PEG)-peptide".

The synthesis of these two types of peptide-based stabilizing agents as well as the synthesis and characterization of the resulting apatite NPs obtained with these molecules will be presented in this chapter.

I. Generalities about peptide synthesis and apatite co-precipitation synthesis

A. Proteogenic amino acids - Solid phase synthesis – Fmoc/tBu Strategy

1. Proteogenic amino acids

An amino acid (AA) is formally any organic molecule bearing a carboxylic acid and an amine function. Proteogenic amino acids, which composed peptides (less than 50 AA) and proteins (more than 50 AA), are all alpha amino acids. They share an identical skeleton composed of a carboxylic acid and an amine (primary amine in all cases except for Proline) separated by an alpha carbon which carries different side chains (R) (Figure 22). This alpha carbon is chiral except for Glycine in which R = H.⁹⁰

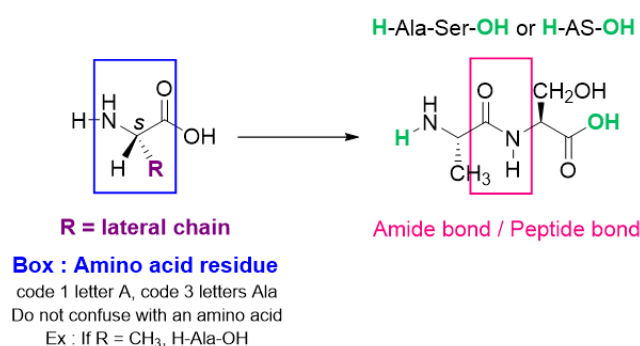


Figure 22 : General structure of an Amino Acid (AA) and N-ter and side-chain protected Amino acid. The stereochemistry is noted L when using Fisher's representation or (S), except for Cys which is (R)

Even if a large number of AAs can be found in Nature or chemically synthesized, only 22 AAs are encoded by DNA and used in ribosomal protein synthesis.⁹¹ Two of them are pretty rare (selenocysteine and pyrrolysine) and the remaining 20 compose the vast majority of protein sequences. These AAs are named either by a one-letter code or by a three-letter code (see section I.A.5 - Table 8). Although peptides are naturally synthesized from N-ter to C-ter, chemists synthesize the peptide from C-ter to N-ter on solid support to avoid epimerization problems.

2. Principe of SPPS synthesis

The synthesis of the peptides carried out in this work, was performed using solid phase peptide synthesis (SPPS).^{92–95} Reported for the first time by Nobel price Brice Merrifield in 1963⁹⁶, SPPS is the most frequently used method to chemically synthesize peptides due to its efficiency, simplicity and speed. This method relies on a solid support: a resin bead composed of a polymer matrix and a linker, on which the C-terminal amino acid of the target sequence is anchored. After loading of the first amino acid, AA1, the peptide sequence is assembled linearly from the C-terminus to the N-terminus by repetitive cycles of N-terminal deprotection

and amino acid coupling (Figure 23). Indeed, the carboxylic acid of AA2 is coupled to the previous amino acid by chemically forming an amide bond (-CONH, or “peptidic” bond) with the free amine of AA1, previously deprotected, and so on until the last AA. This peptide coupling requires a prior activation of the carboxylic acid into an electrophilic function carrying a good leaving group (X). The anchoring of the growing peptide chain on the solid support through the linker allows for simple and fast removal of the unreacted species, deprotection and coupling reagents, as well as solvents. Once the synthesis is terminated, the peptide is cleaved from the linker by a specific treatment (e.g. trifluoroacetic acid). The type of the linker will determine the nature of the C-terminal end of the peptide released from the support.⁹⁷

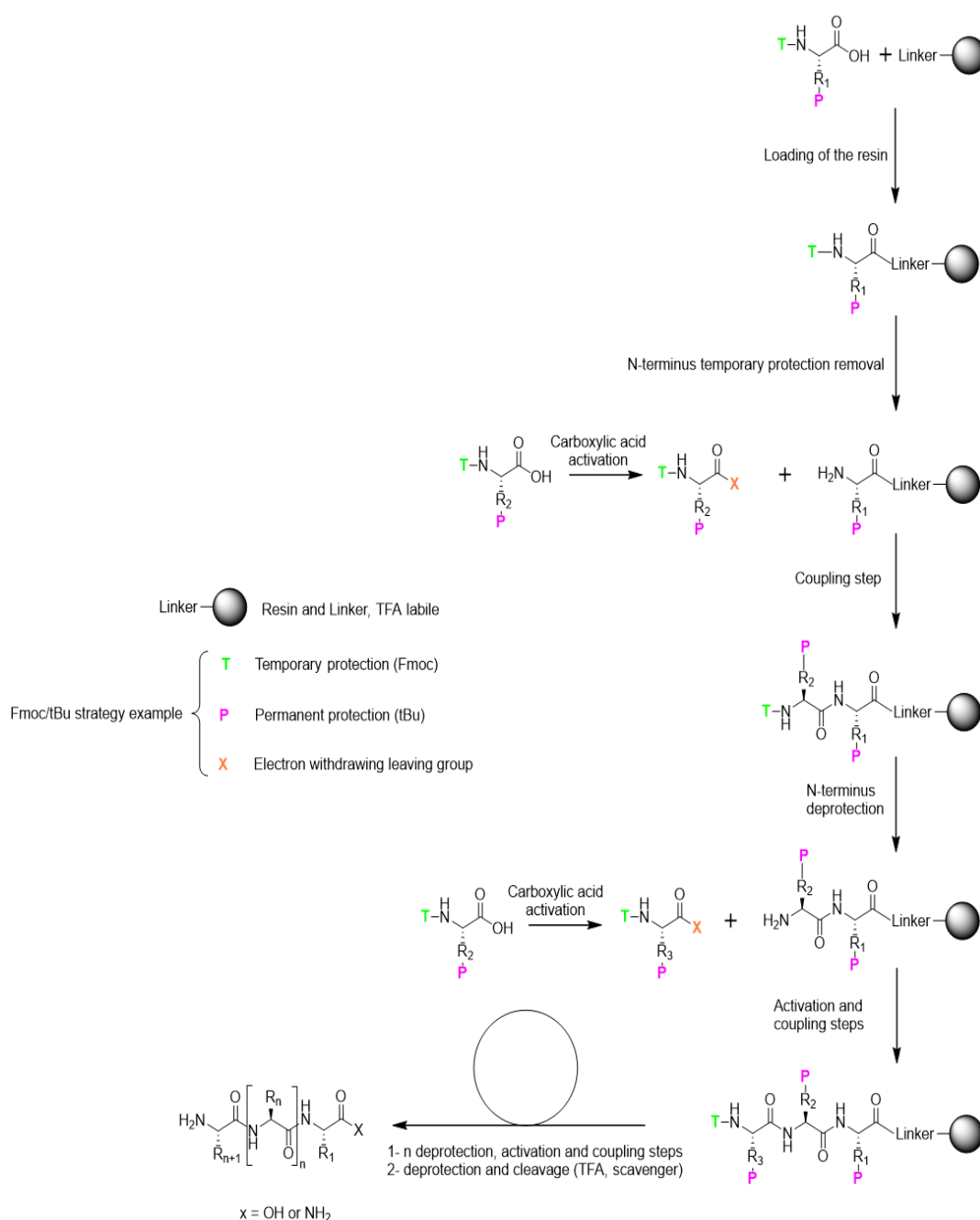


Figure 23 : Solid support synthesis of peptide (SPPS)

3. Choice of Fmoc/tBu strategy

The two main strategies for SPPS synthesis are called Fmoc (fluorenylmethoxycarbonyl)/tBu or Boc (tert-butoxycarbonyl)/Bzl.

This T/P notation refers to the nature of the protective grouping of AAs. "T" is called temporary protection because it is removed at the end of each cycle of peptide synthesis and "P" is called permanent protection because it is removed at the end of the synthesis at the same time as the peptide is released from the linker placed on the C-terminal side.

The choice of linker will depend on the C-ter function of the desired peptide and the removal of side chain groups after cleavage. It is indeed important that the T-protection is selectively removed without affecting the P-protection and without cleaving the peptide. However, at the end of the synthesis it is necessary to both cleave the peptide and remove the P-protective groups.

In the Boc/Bzl strategy, a trifluoroacetic acid (TFA) treatment is required after each coupling step to remove the temporary protecting group of the Boc amine function. On the contrary, the side chain protections (Bzl) as well as the linker of the solid support are resistant to TFA but can be cleaved by treatment with a strong acid such as anhydrous hydrofluoric acid.

The best known strategy, and the one used in this PhD project, is the Fmoc/tBu method (Figure 24).⁹⁴ It is based on an orthogonal protecting group strategy. This approach uses the base-labile N-Fmoc urethane group for protection of the amino function and an acid-labile group (tBu) to protect the side chains. Usually, the use of a secondary amine (piperidine (pip) in N, N-dimethylformamide (DMF)) is used to remove the Fmoc protecting group at each step while the P-protectors as well as the peptide cleavage is done in acidic condition (TFA). The latter strategy has the advantage that the temporary and permanent orthogonal protections are removed by different mechanisms, allowing milder acidic conditions to be used for final deprotection and peptide cleavage.

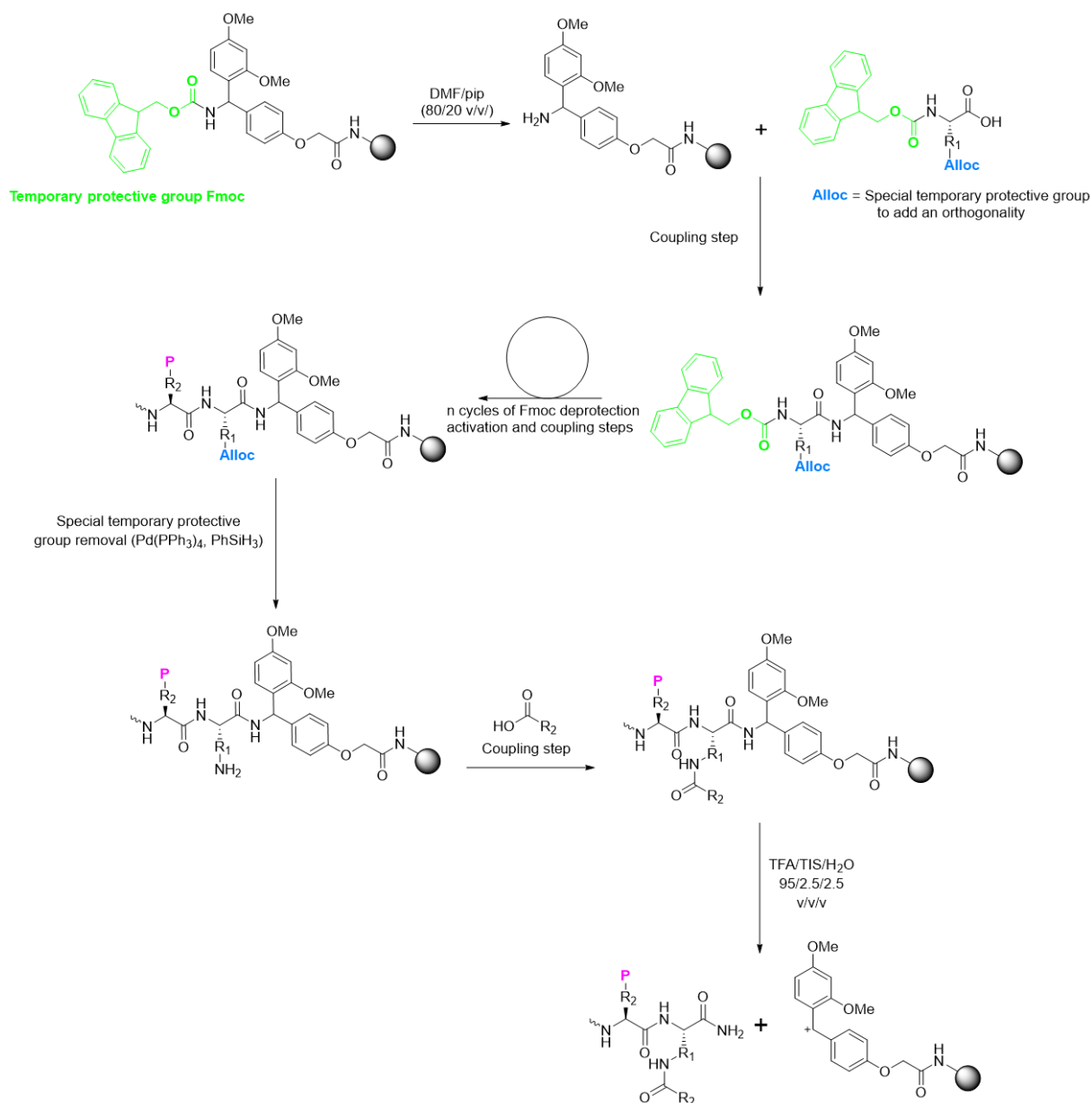


Figure 24: General principle of SPPS by Fmoc/tBu strategy for the preparation of C-terminal amidated peptide on a resin carrying a Rink Amide linker. P represents permanent, acid-labile protections

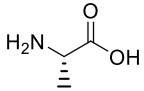
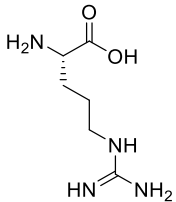
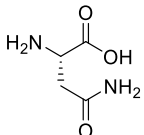
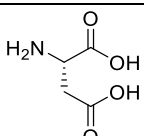
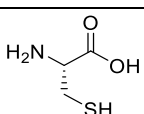
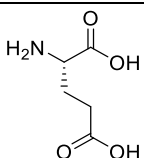
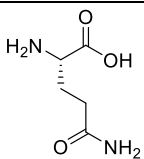
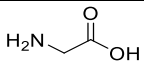
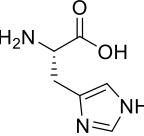
4. Notion of orthogonality

Sometimes, an in-process derivatization on the side chain of an AA is necessary to create a 3rd orthogonality (Figure 24). In the frame of this project, this orthogonality is created on the Lysine side chain. For this purpose, an adequate temporary protection replaces the permanent protection. Generally, an Alloc protection is used because it is insensitive to TFA and piperidine. The smooth removal of Alloc group in neutral conditions with catalytic amounts of Pd(PPh₃)₄ in the presence of PhSiH₃ as a scavenger for the allyl system permits orthogonality with the most common protecting groups.⁹⁸ In other words, the Alloc protection can be

removed without cleaving the peptide or removing the Fmoc protection in order to graft a molecule onto the Lysine side chain.

5. List of commercial AAs for the Fmoc/tBu strategy

AAs can be purchased for the SPPS synthesis with a temporary protection (T) on the amine and a 'permanent' protection (P) on the side chain for the Fmoc/tBu or Boc/Bzl strategies. The table below (Table 8) summarizes the 20 AAs used in Fmoc/tBu SPPS and the rationale for keeping the side chain protected.

AAs full name	1-letter code	3-letters code	Chemical structure	AA derivative employed in Fmoc/tBu strategy	Necessity of lateral chain protection
Alanine	A	Ala		Fmoc-Ala-OH	/
Arginine	R	Arg		Fmoc-Arg(Pbf)-OH	The amine functions are not very reactive but it is necessary to protect them in case of long or strong activation Pbf protection improves the solubility of arginine and to avoid the formation of β -lactam during coupling
Asparagine	N	Asn		Fmoc-Asn(Trt)-OH	Prevents dehydration into β -cyanoalanine & aspartimide and glutarimide formation
Aspartic acid	D	Asp		Fmoc-Asp(OtBu)-OH	Protection for selective activation of the carboxylic acid α during coupling step
Cysteine	C	Cys		Fmoc-Cys(Trt)-OH	Protection to avoid S-acylation and S-alkylation, and the formation of unwanted disulfide bridges
Glutamic acid	E	Glu		Fmoc-Glu(OtBu)-OH	Protection for selective activation of the carboxylic acid α during coupling step
Glutamine	Q	Gln		Fmoc-Gln(trt)-OH	The amine functions are not very reactive but it is necessary to protect them in case of long or strong activation
Glycine	G	Gly		Fmoc-Gly-OH	/
Histidine	H	His		Fmoc-His(Trt)-OH	To avoid auto-epimerization during activation

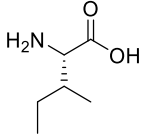
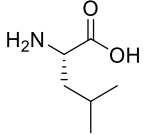
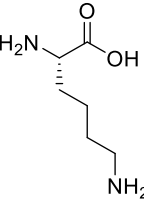
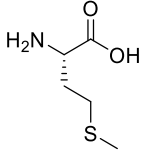
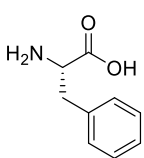
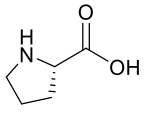
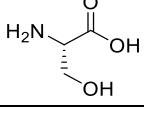
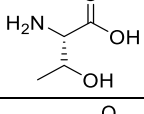
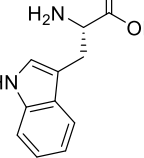
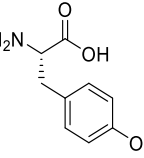
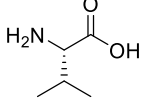
Isoleucine	I	Ile		Fmoc-Ile-OH	/
Leucine	L	Leu		Fmoc-Leu-OH	/
Lysine	K	Lys		Fmoc-Lys(Boc)-OH	The protection serves to promote Na chemoselectivity toward Na or Nδ during coupling
				Fmoc-Lys(Alloc)-OH	The temporary protection Alloc allows orthogonality
Methionine	M	Met		Fmoc-Met-OH	/
Phenylalanine	F	Phe		Fmoc-Phe-OH	/
Proline	P	Pro		Fmoc-Pro-OH	/
Serine	S	Ser		Fmoc-Ser(OtBu)-OH	Alcohol can be acylated by the activated amino acid, when an excess is used.
Threonine	T	Thr		Fmoc-Thr(tBu)-OH	Alcohol can be acylated by the activated amino acid, when an excess is used
Tryptophane	W	Trp		Fmoc-Trp(Boc)-OH	The indolic nitrogen is not very nucleophilic, so it is not necessarily necessary to protect it, but the position of the indole nitrogen is likely to make electrophilic SN or oxidations in acid medium
Tyrosine	Y	Tyr		Fmoc-Tyr-OH	Phenol can be acylated in the presence by the activated amino acid
Valine	V	Val		Fmoc-Val-OH	/

Table 8 : List of proteogenic AAs and their protections for the Fmoc/tBu strategy

6. Description of each step of the SPPS peptide synthesis with the Fmoc/tBu strategy

a. Loading of the first AA on the linker of the resin bead

Choice of the resin

As previously explained, the solid support strategy is based on the use of resin beads. The resin used for the SPPS peptides synthesis is in the form of a porous bead (10 μm - 0.5 mm) composed of a polymer matrix (PS, PEG, PA, PEG-PS...) and a linker on which the first amino acid is grafted. The resin beads are insoluble in all common solvents but swell well in organic solvents. This property is important because the linkers are generally located within the polymer matrix forming a resin bead (less than 1% is on the surface), which requires swelling of the polymer matrix to allow diffusion of solvents and reagents into the interior (Figure 25).

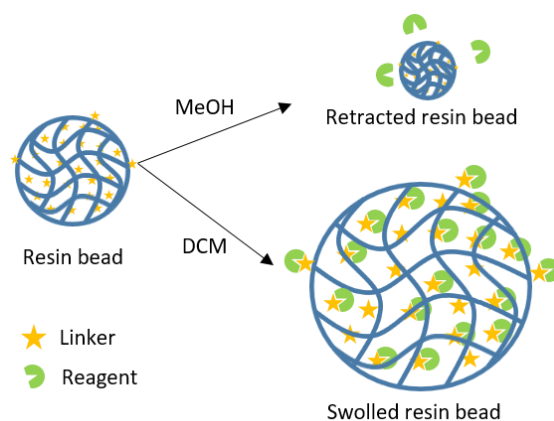


Figure 25: Principle of resin bead strategy for SPPS peptide synthesis

Cross-linked polystyrene (PS) is the most used polymer matrix for the synthesis of short peptides, thanks to its large range of loading available its mechanical and chemical stability and its good swelling in the usual synthesis solvents (DMF and DCM) allowing a good diffusion of the reagents within the network. Polyamide (PA), PEG based and PEG-PS composite resins are more hydrophilic matrix and are often kept for the synthesis of difficult sequences and long peptides.

In addition to the choice of the polymer matrix, another important parameter to consider is the loading of the resin. Loading is defined as the amount of linker material per gram of resin ($\text{mmol}\cdot\text{g}^{-1}$). The choice of the resin will be determined by the size of the peptide. Indeed, the higher the loading, the more steric hindrance could impair the synthesis of the peptide leading to uncompleted coupling steps.

At last, the choice of the linker is essential because it determines the nature of the C-terminus of the peptide after cleavage as well as the chemical conditions used to cleave the bond between the linker and the peptide. The principal categories of peptides are C-terminus

carboxylic acid or primary amide. During my PhD to types of Rink Amide resin, yielding to a C-terminus amide peptides were used to synthesize the peptide-based stabilizing agents (Table 9).

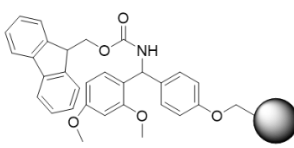
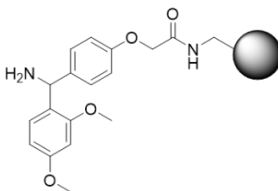
Resin name	Polymer matrix	Linker	Termination of the C-terminus	Loading (mmol.g ⁻¹)	Cleavage conditions
Fmoc-Rink Amide	Reticulated PS		Amide	0.94	TFA/H ₂ O/TIS 95/2.5/2.5 v/v/v
H-Rink Amide ChemMatrix	Reticulated PEG			0.50	

Table 9 : Resins used during the PhD project

Loading of the first AA on the linker

The first step of a SPPS peptide synthesis is to anchor the carboxylic acid of the first N-protected C-terminal amino acid (AA1) residue to a reactive function on the linker. In the Fmoc/tBu strategy, this anchorage may be an ester bond, formed from a hydroxyl group in the case of hydroxymethylphenoxy linker or a chloro group in the case of a 2-chloro chlorotriyl linker. The linkage can also be done through an amide bond in the case of the rink amide linker. After cleavage, either a C-ter carboxylic acid or a C-ter primary amide is obtained. Linkers behave as a C-terminal protection (Figure 23), named “permanent protection” as it is kept intact during the whole cycles of SPPS, being cleaved at the end of the stepwise peptide assembly.

b. Temporary protective group Fmoc removal

The protection of the primary amine of the AA must be temporary because it must be removed to allow the coupling of the next AA.⁹⁹ Generally, an N-urethane group (Fmoc, Boc, Cbz...) is used to protect the primary amine of the AA.¹⁰⁰ This protecting group, in addition to directing the elongation of the peptide, also allows decreasing or avoiding the formation of oxazolone which can in turn be epimerized by proton abstraction (Figure 26).^{95,101} Indeed, the presence of an oxygen gives an electron-donor effect which destabilizes the anionic form of oxazolone, thus preventing the abstraction of the alpha proton and finally limiting the epimerization. The protective role of urethanes against epimerization also explains the predominance of the C to

N strategy. Furthermore, the urethane protection is chosen because it can deprotect under moderate conditions so as not to deteriorate the integrity of the peptide and cleave the peptide.

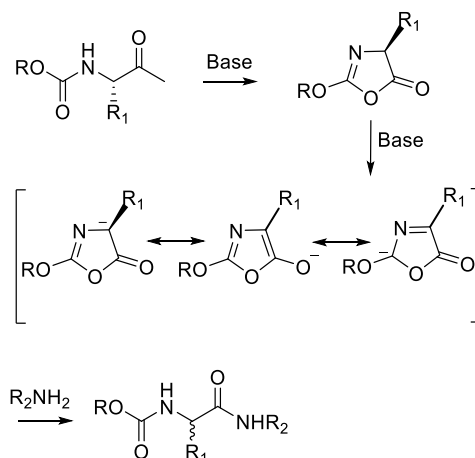


Figure 26: Formation of oxazolone, a side reaction of AAs coupling

In the case of the Fmoc/tBu strategy, the urethane group used is the Fmoc. Fmoc is deprotected by the action of a secondary amine (piperidine) which can remove the proton of the fluorenyl ring, leading to the formation of dibenzofulvene (DBF) and a carbamic acid, represented in Figure 27 below. The latter decarboxylates spontaneously. The released DBF is removed by filtration from the resin and can even be measured by UV to control the amount of amino acid ready to react on the resin.

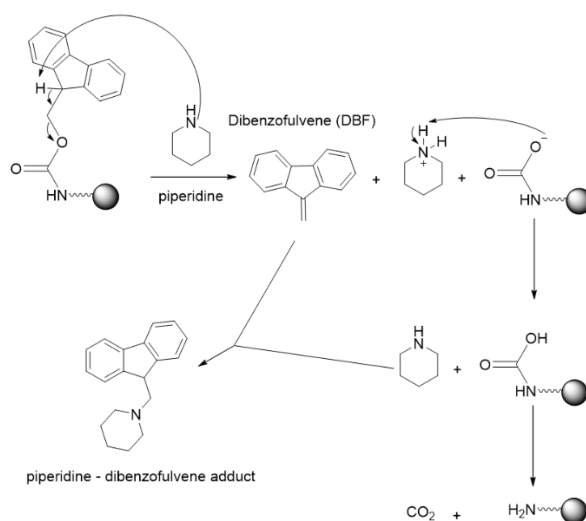


Figure 27 : Fmoc deprotection process

In this work, the Fmoc groups were deprotected by two successive DMF/piperidine treatments (80/20; v/v) for 10 minutes.

c. Carboxylic acid activation with HATU – coupling step

An amide bond between 2 AAs cannot be formed without activating the carboxylic acid function. Many activating reagents have been developed for this purpose in SPPS. However, they all proceed in the same way. The principle of the activation is to convert the unreactive carboxylic acid (R-COOH) into an active ester (R-CO-X), where X is an electron withdrawing and good leaving group (Figure 28 - Figure 23). The doublet of the N-terminus amine of the peptidyl resin can now attack the carbonyl through a nucleophilic substitution reaction, removing XH as a leaving group and yielding an amide bond. Importantly, the formation of an active ester proceeds first through the formation of a carboxylate which attacks the coupling reagent. Consequently, basic conditions are necessary during coupling.

As already stated, many coupling reagents have been developed. The three main categories used in SPPS are (i) phosphonium (e.g. PyAOP, BOP, PyBOP), (ii) uroniums (e.g. HATU, HBTU)^{101,102} which both proceed through the same mechanism and necessitate the use of a tertiary amine to form the carboxylate; and (iii) carbodiimides (e.g. EDC, DCC, DIC) used in the presence of an auxiliary nucleophile agent (e.g. HOBt, HOAt, Oxyma, N-hydroxysuccinimide (NHS)) to avoid O-N acyl shift side reaction.

In this PhD project, we mainly used HATU ((dimethylamino)-N,N-dimethyl(3H-[1,2,3]triazolo[4,5-b]pyridin-3-yloxy)methaniminium hexafluorophosphate)¹⁰² as activation reagent in the presence of diisopropylethylamine (DIEA) as a tertiary amine organic base. The activation mechanism is presented in Figure 28.

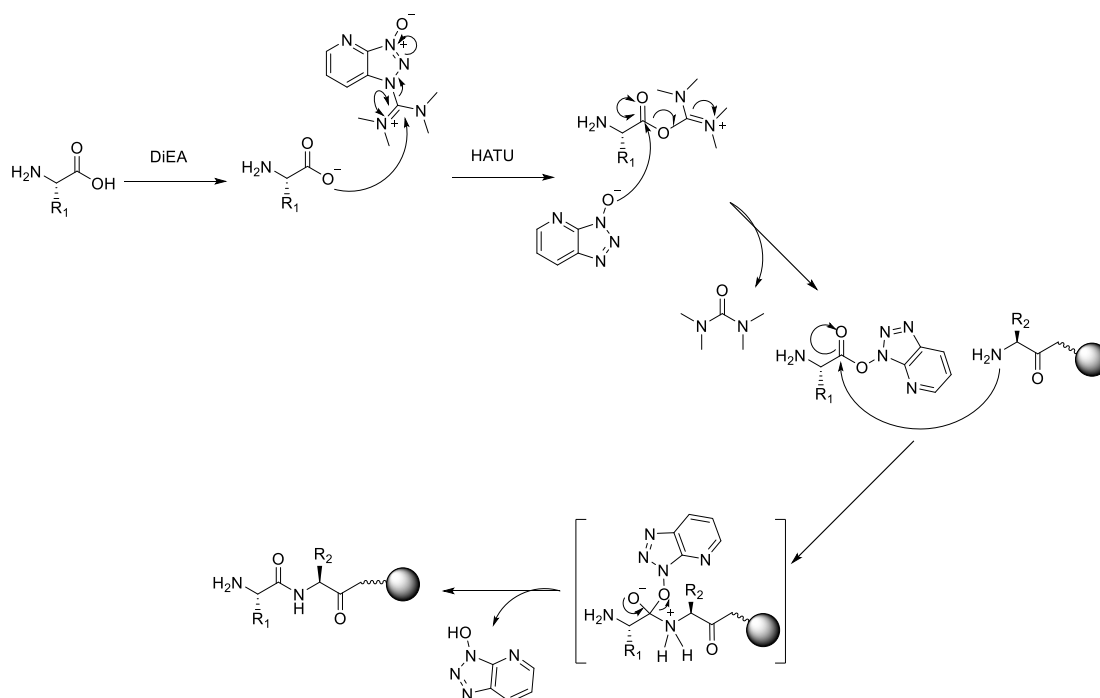


Figure 28 : Mechanism of HATU activation of carboxylic acid

Control of the coupling steps without cleaving is essential for successful peptide synthesis and a number of qualitative tests have been developed. One of them commonly used is the Kaiser test based on the reaction of ninhydrin with amines. Ninhydrin (2,2-dihydroxyindan-1,3-dione) is an organic molecule used as a developer of amino acids by the following reaction (Figure 29).⁹⁴

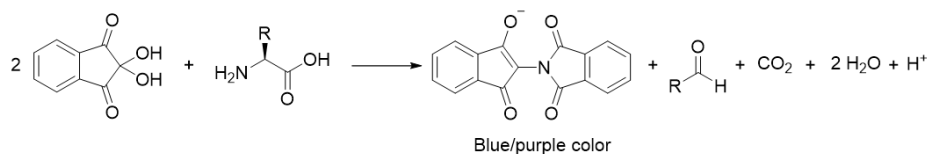


Figure 29 : Reaction of Ninhydrin with amines: Kaiser test

For this, a solution of ninhydrin, phenol and acetic acid is prepared (protocol described in chapter 4). The phenol and KCN accelerate the reaction. A few resin beads carrying the forming peptide are dipped into this solution. If the beads turn blue, then the test is positive and free amines are still available. In other words, the coupling has not taken place quantitatively. If the color is difficult to come, the solution can be heated slightly.

d. Linker cleavage and side chain protection removal

Once the peptide is completed, the last 'T' Fmoc protection in N-ter is removed. After this step, the N-ter can be left in amine form or acetylated to either block this position or to retain the activity of the peptide.

The cleavage step detaches the peptide from the linker. The protective groups of the side chains are also removed at this step. Peptide cleavage is performed during 1 hour with a mixture of TFA/TIS/H₂O (95/2.5/2.5, v/v/v). Triisopropylsilane (TIS) and water are used as carbocation scavengers to avoid side reactions during peptide deprotection by reacting with carbocations created during deprotection of the alkylatable side chains (especially on the electron-rich aromatic rings of Tyr and Trp and on the sulfur atom of Met and Cys).

The cleaved resin is removed by filtration and the desired deprotected peptide is obtained in solution in TFA. After concentration of the TFA under vacuum, the peptide is precipitated in diethyl ether (Et₂O) and washed twice with the same solvent.¹⁰³

During the synthesis of a long, difficult peptide or with unusual intermediate deprotections, a microcleavage can be performed. A few resin beads are removed and the peptides are cleaved from the linker as for a final cleavage. The obtained peptide is analyzed by Liquid Chromatography - Mass Spectrometry (LC-MS). This step allows checking precisely the structure of the peptide before proceeding to the next step.

B. Synthesis of colloidal nanoparticles of apatite stabilized by an organic corona

CIRIMAT has developed a method for the synthesis by co-precipitation of colloidal apatite NPs stabilized by stabilizing agents (i.e. AEP^{34,38,75} and P(PEG)⁴⁴). This general procedure, described below, has been used as a reference procedure in this PhD project.

The general procedure pursued to obtain 25 mL of colloidal suspension of hybrid NPs in the presence of stabilizing agents is described below. In this work, the colloidal suspension was obtained by first mixing a calcium nitrate tetrahydrate $\text{Ca}(\text{NO}_3)_2 \cdot 4\text{H}_2\text{O}$ solution (x mmol, 6.5 mL) with the stabilizing agent ($\text{R-PO}_3\text{H}_2$) solution (y mmol, 12.5 mL). The molar ratio of each component depends on the desired $\text{R-PO}_3\text{H}_2/\text{Ca}$ molar ratio (y/x). The pH was then adjusted around 9-10 with ammonia solution to obtain the deprotonated form R-PO_3^{2-} of the organic phosphonate and facilitate its chelation with calcium ions from the medium. An ammonium hydrogenphosphate $(\text{NH}_4)_2\text{HPO}_4$ solution ($x/3$, 6.5 mL) was then added to the mixture and the pH was re-adjusted to 9-10 with ammonia solution. At this step, amorphous calcium phosphate forms as observed previously.¹⁰⁴ A maturation time was required by heating the compound at 100°C for 16 hours to provide thermal energy and favor the reorganization of ions into an apatite structure (Figure 30). When this synthesis is carried out in the presence of a stabilizing agent as is the case here, there is a competition between the inorganic orthophosphate ions and the organic moiety for the calcium ions; and the maturation step allows reaching an equilibrated state with a controlled state of agglomeration. The NPs are purified by dialysis to remove the unreacted ions and organic molecules, using a previously set up methodology.³⁵ Purification by dialysis consists in introducing the colloid suspension (~25 mL) into a tubular dialysis membrane and then placing the filled membrane in a beaker containing around 800 mL of distilled water.

The cutoff threshold of the dialysis membrane has to be adapted to the molecular weight of the unreacted moieties, and especially of the stabilizing agent used. For example, a cutoff of about 6-8 kDa has been used in previous studies to purify AEP-functionalized NPs while a cutoff of 12-14 kDa has been chosen to purify P(PEG)-functionalized NPs.^{35,44} The unreacted molecules and the ions left in solution are then transferred from the dialysis tube into the water beaker by means of a concentration gradient (Figure 31). This procedure, developed by Ahmed Al-Kattan *et al.*³⁵ showed that a plateau was reached approximately every 4 hours and that it was necessary to renew the water after this time. Furthermore, it was shown that 3 cycles of 4 hours and one cycle of 16 hours (at night) were necessary for optimal purification.

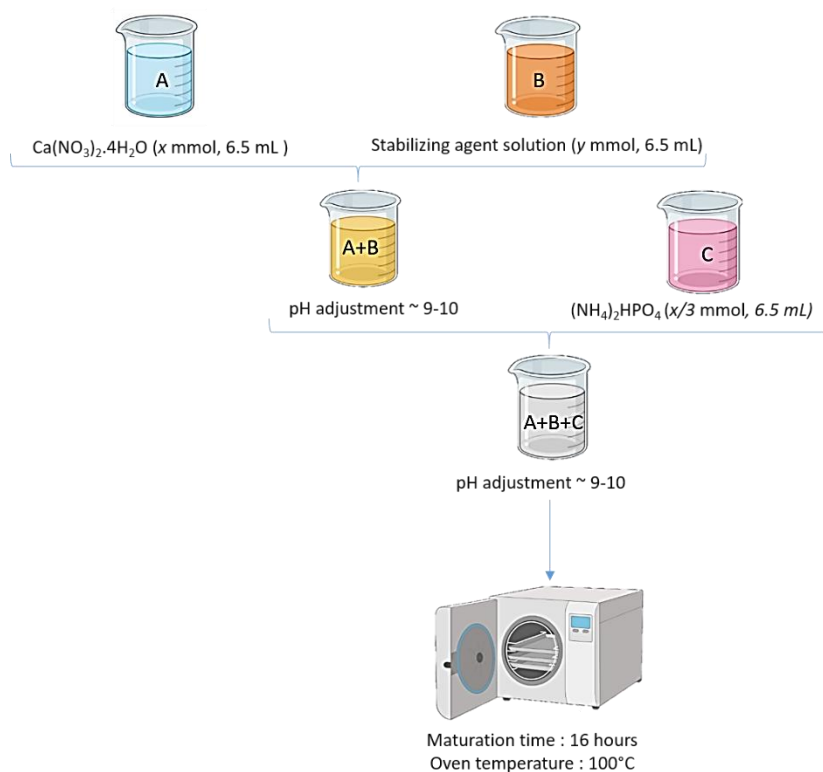


Figure 30: Reference synthesis protocol to obtain colloidal NPs in the presence of stabilizing agents

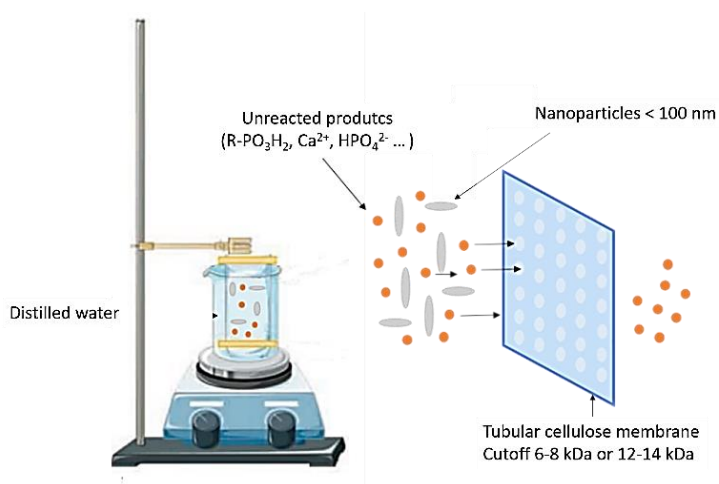


Figure 31: Principle of dialysis purification

II. Synthesis and characterization of hybrid peptide-apatite nanoparticles obtained from 2-aminoethylphosphonate-analog, P(Peptide)

In this PhD project, two families of new stabilizing agents were synthesized to obtain peptide-based colloidal hybrid NPs. In this section, the synthesis of the first family of peptide-based

stabilizing agents, named P(Peptide) will be detailed (II.A) as well as the synthesis (II.B) and characterization of the obtained particles (II.C).

A. Synthesis of new peptide-based stabilizing agent from 2-aminoethylphosphonate-analog, P(Peptide) 6 and 7

The goal of this project was to stabilize colloidal apatite NPs with peptides using a one-pot synthesis. Thus, the peptide-based stabilizing agents, P(Peptide), surrounding the NPs should play both a stabilization/size-controlling role *and* simultaneously provide additional biological properties depending on the chosen peptide sequence. For that, the isoelectric point (pHi) of P(Peptide) should be lower than 9-10 (see reference protocol section II.B) in order to be positively charged during the apatite synthesis (Table 10).

Phosphonate end-groups were shown, as mentioned above, to exhibit a high affinity for the surface of apatite. Thus, the first strategy was to functionalize the N-terminus of the H-GDPGYIGSR-NH₂ peptide **2'** or the Lysine side chain of the Ac-LRGDNK-NH₂ peptide **1'** with a phosphonate group using an analog of 2-aminoethylphosphonate (AEP) to give the generate the bioactive stabilizing agents described in Table 10. The peptide H-AhXRR-NH₂ was not studied at this stage.

Name	Sequence	pHi
P(RGD)	Ac-LRGDNK(PO ₃ H ₂ CH ₂ CH ₂ CO)-NH ₂	8.2
P(YIGSR)	PO ₃ H ₂ CH ₂ CH ₂ CO-GDPGYIGSR-NH ₂	7.0

Table 10 : Sequences and pHi of peptide-based P(Peptide) stabilizing agents

Functionalization at the N-terminus or on the side chain allowed for the versatility of functionalization but, more importantly, it allowed retaining the activity of the peptides. Indeed, these peptides exert their biological activity through binding to membrane receptors of cells. It was therefore important that the fibronectin RGD and laminin YIGSR motifs were left unmodified and were well oriented and exposed at the external periphery of the NPs to facilitate their interaction with their surroundings. Furthermore, it was shown that tyrosine deletion or arginine substitution in YIGSR peptide sequence resulted in a significant loss of activity if not protected by other AAs, stressing that the sequence was important to keep the activity.¹⁰⁵ Moreover, in fibronectin and laminin glycoproteins, the C-terminal and N-terminal end of the YIGSR and RGD sequences are not free as they are engaged in linkages with other neighboring AAs. In order to mimic the natural environment, the C-terminal end of the peptide was converted to an amide after resin cleavage and the N-terminal end was acetylated on solid support at the end of the synthesis.

As reported in chapter 1, several organic groups can interact with the ions located on the surface of apatite crystals. Here, an organic phosphonate group was chosen because the

interaction between apatite calcium and phosphonate groups of the organic moiety was found to be stronger than with a carboxylate, sulfonate or borate group (see chapter 1). Moreover, a phosphonate group instead of a phosphate group was used to avoid hydrolysis of the phosphorylated part.

The two target peptides P(RGD) **6** and P(YIGSR) **7** are presented below. We planned their synthesis fully on solid support, coupling a phosphate containing moiety (3-phosphonopropanoic acid **3**) after selective deprotection of the suitable primary amine, on solid support.

1. Peptidyl resin **1** and **2** synthesis on solid support with Fmoc-tBu strategy

These new peptide-based stabilizing agents P(RGD) **6** and P(YIGSR) **7** were synthesized on solid support using the Fmoc/tBu strategy and a Rink Amide PS resin (0.47 mmol.g^{-1}) to obtain a C-ter amide terminus after the cleavage step. As previously explained, the precursor of **6**, the peptidyl resin **1** was acetylated at the N-terminus and a temporary Alloc protection was used on the Lysine side chain to deprotect it in an orthogonal manner before introducing the analogue of AEP (Figure 32).

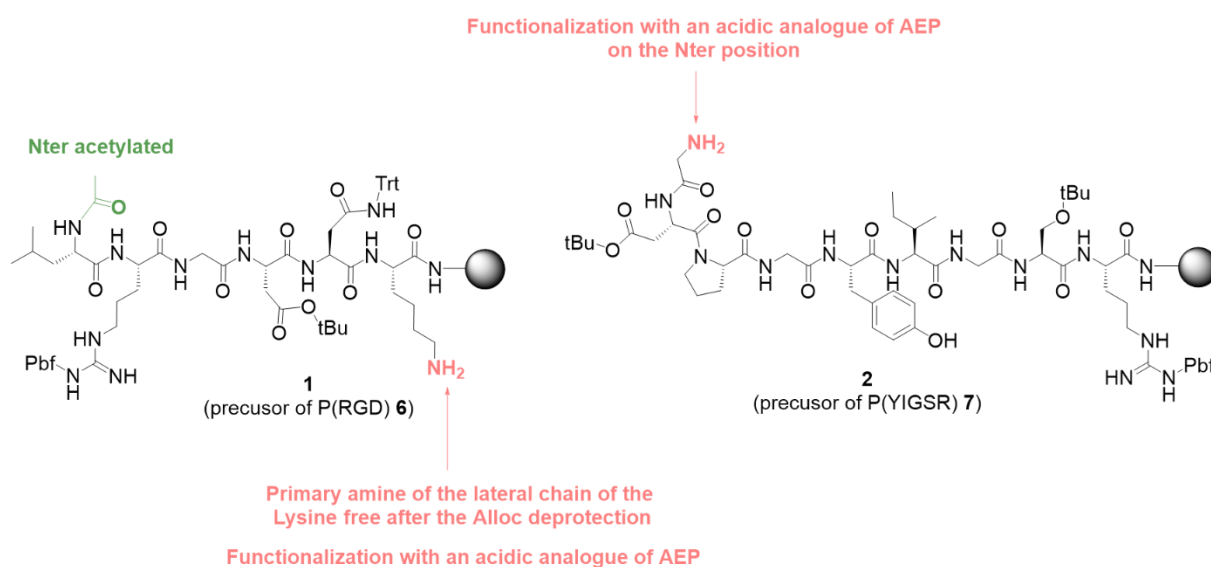


Figure 32 : Strategy to functionalize the peptidyl resin **1** and **2** with an acidic analogue of AEP in view of obtaining the new peptide-based stabilizing agents P(RGD) **6** and P(YIGSR) **7**

Once peptidyl resin **1** and **2** were synthesized, microcleavages were performed to obtain the corresponding unprotected peptides **1'** and **2'**. LC-MS analyses were performed to verify the structure of the peptides **1'** and **2'** including Alloc deprotection and acetylation in the case of the peptide **1'** (Table 11).

Name	Resin	Loading (mmol.g ⁻¹)	Resin mass engaged (mg)	MW (g.mol ⁻¹)	Retention time (min)	Purity %
1	Rink	0.47	860	743	0.71	86
2	Amide PS		694	921	0.80	87

Table 11 : Microcleavage LC-MS analysis of peptidyl resin **1** and **2**

Based on LC-MS analyses, the peptides **1'** and **2'** were obtained with a purity higher than 80% showing that the acetalization and Alloc deprotection took place successfully.

2. Functionalization of the peptidyl resin **1** and **2** with 3-phosphonopropanoic acid **3** on solid support

To functionalize the peptidyl resins **1** and **2**, the 3-phosphonopropanoic acid **3** was used. The carboxylic acid of compound **3** was activated by the coupling agent HATU in the presence of DIEA to be coupled to the free primary amines of **1** and **2** (i.e in N-terminal of **2** and Lysine side chain of **1** - Figure 33).

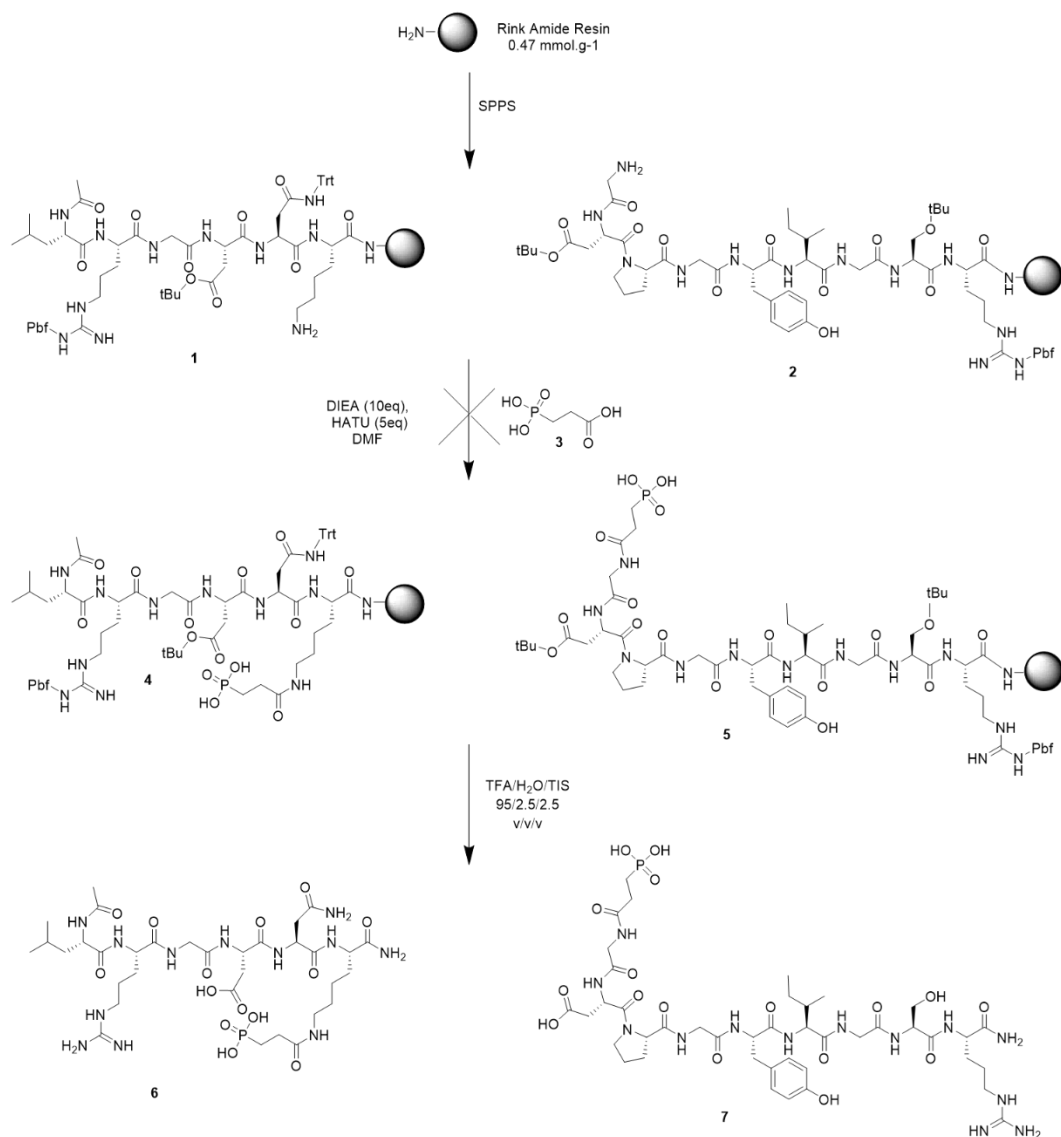


Figure 33 : Functionalization of the peptidyl resins 1 and 2 with the 3-phosphonopropanoic 3 acid

It is worth noting, that amide formation is conceivable in the presence of an unprotected phosphonic acid if the amount of base is controlled. Indeed, using about 2eq of base it is normally possible to activate only the carboxylic acid (pKa 4 - 5). An -OH group of the phosphonic acid (pKa 1.5 - 2) is also deprotonated under these conditions but the carboxylate formed remains more basic and more nucleophilic and is therefore the preferred site for peptide coupling (Figure 34). However, in case of excess of base, the phosphonic acid (pKa 1.5 - 2 and 8) is totally deprotected leading to its activation. The phosphonate will then be more reactive and more nucleophilic than the carboxylic acid.¹⁰⁶

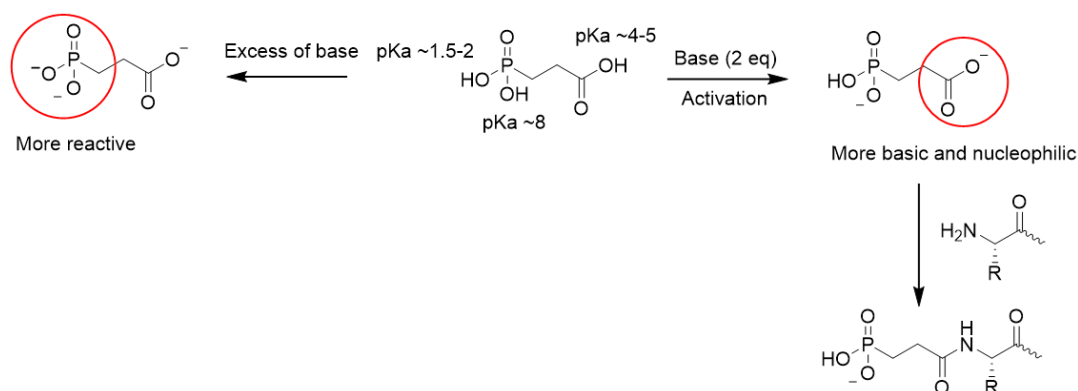


Figure 34 : Amide formation in the presence of a phosphonic acid

For these reasons, 5eq of 3-phosphonopropanoic acid **3** was deprotonated with 10eq of DIEA and pre-activated with 5eq of HATU before being coupled to the free primary amine present on peptidyl resin **1** and **2** (Figure 32). The coupling was performed twice during 15 minutes. According to the positive Kaiser test performed between each coupling, free amines were still present (blue resin beads visible), proving that the coupling did not take place quantitatively. Since the Kaiser test was not quantitative, the peptide was cleaved from the support and analyzed by LC-MS showing that the coupling reaction had not occurred at all. The initial peptides **1'** and **2'** were recovered. These results seemed to show that carboxylic acid 3-phosphonopropanoic **3** was not activated to allow coupling with the primary amines of peptidyl resins **1** and **2**.

3. Functionalization of the peptidyl resin **1** and **2** with the (diethoxyphosphoryl)propionic acid **9** on solid support

In an attempt to circumvent this problem, we used a protected version of compound **3**, the 3-(diethoxyphosphoryl)propionic acid **9**. The diethylphosphonate allows activation of the carboxylic acid without the risk of activating the phosphonate moiety when using a higher DIEA equivalent number and a longer coupling time.

Compound **9** was obtained by acid hydrolysis of the ethyl 3-(diethoxyphosphoryl)propionate ester **8** by using HCl, H₂O in acetone at 60°C for 30 minutes under stirring (Table 12 - Figure 36). Compound **9** (5eq) was pre-activated by adding a DIEA until pH 8-9 and HATU (5eq). After 5-10 minutes of pre-activation, the solution was added dropwise to the peptidyl resins **1** and **2**. After 15 minutes, in contrast to the reaction with the 3-phosphonopropanoic acid **3**, the coupling was completed as confirmed by a negative Kaiser test and a micro cleavage followed by a LC-MS analysis which shows that the peptides were deprotected on the side chains and had the phosphodiester group (Figure 36). Peptidyl resins **10** and **11** were obtained whatever the peptide (Table 12).

Name	n _{engaged} (mmol)	MW (g.mol ⁻¹)	Retention time (mins)	Purity %	Yield %	m _{obtained} (g)
9	10	210	/	/	95	2.1
10	/	935	1.00	84	/	/
11	/	1112	1.01	84	/	/
6	/	879	/	/	56	0.20
7	/	1056	/	/	41	0.14

Table 12 : Microcleavage and cleavage LC-MS analyses of the intermediate **10** and **11** and of the final P(RGD) **6** and P(YIGSR) **7**

4. Dealkylation of compound **10** and **11** to obtain the new peptide-based stabilizing agents **6** and **7**

Finally, the diethylphosphonate moiety was deprotected through the McKenna reaction, using 10eq of trimethylbromosilane (TMSBr) in a polar aprotic solvent (ACN) to convert the dialkylphosphonate to a bis(trimethylsilyl) ester (Figure 35).^{107–111} As far as we know, this reaction has never been carried out on a support and had therefore been tested here to solid support synthesis with similar solvent and equivalent number that in the solution.

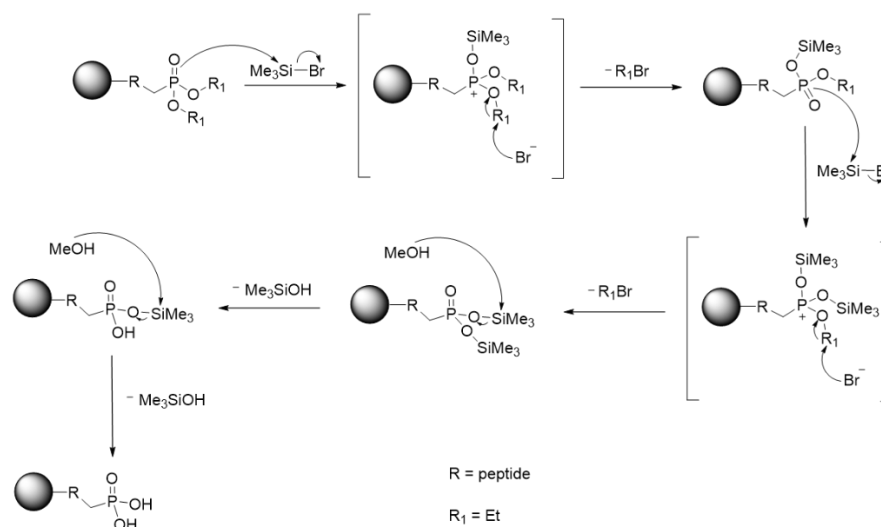


Figure 35 : Mechanism of the McKenna reaction to deprotect the diethylphosphonate on solid support

The reaction was performed in ACN under stirring and argon overnight. The resin was then washed with ACN and MeOH in order to remove the bis(trimethylsilyl)esters and to obtain the target acid **4** and **5**. After cleavage from the resin, the final compounds P(RGD) **6** and P(YIGSR) **7** were obtained (Table 12). The final products **6** and **7** were only analyzed by liquid-state NMR (see chapter 4)

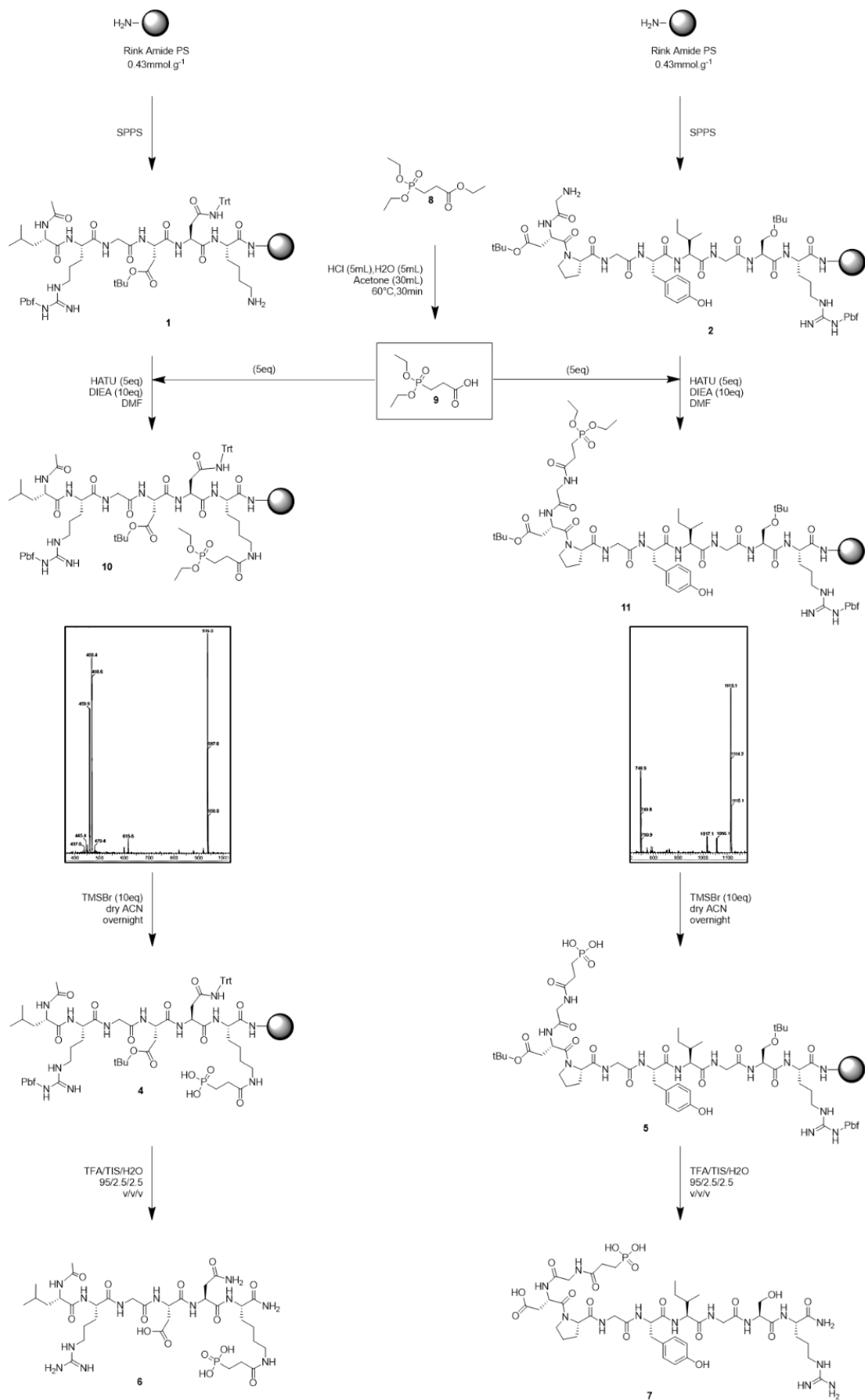


Figure 36 : General synthesis of peptide-based stabilizing agents P(RGD) **6** and P(YIGSR) **7** on solid support

B. Synthesis of apatite particles surrounded with a mixture of P(Peptide) and AEP

As discussed in Chapter 1, many synthetic ways exist to obtain a sub-stoichiometric biomimetic apatite close to bone mineral. Here, we used a co-precipitation synthesis methodology at 100°C for 16 hours (overnight) starting from a mixture of aqueous solutions of calcium nitrate and di-ammonium hydrogenphosphate at pH ~ 9.5 as described in Chapter 1 section I.B.^{52,54,86,112} Based on previous results using AEP as stabilizing agent³⁸, a R-PO₃H₂/Ca ratio equal to 0.5 was chosen for the synthesis of NPs in this section. Indeed in the case of AEP, this ratio allowed obtaining a colloidal suspension of a weakly crystallized apatite phase close to bone mineral.³⁷ In order to obtain here a colloidal suspension with the peptide-based stabilizing agent P(Peptide) and to observe its influence on the apatite structure, state of crystallinity and particles size, a co-adsorption study was performed with various starting proportions of these two stabilizing agents (AEP and P(Peptide)). The same overall molar quantity of stabilizing agent was divided in the following ratios 100/0, 90/10, 75/25, 50/50, 25/75 and 0/100 between AEP and P(Peptide) (Figure 37). For comparative assessments, a non-colloidal apatite sample was also prepared in this study, by following exactly the same procedure as above, but in the absence of stabilizing agent.

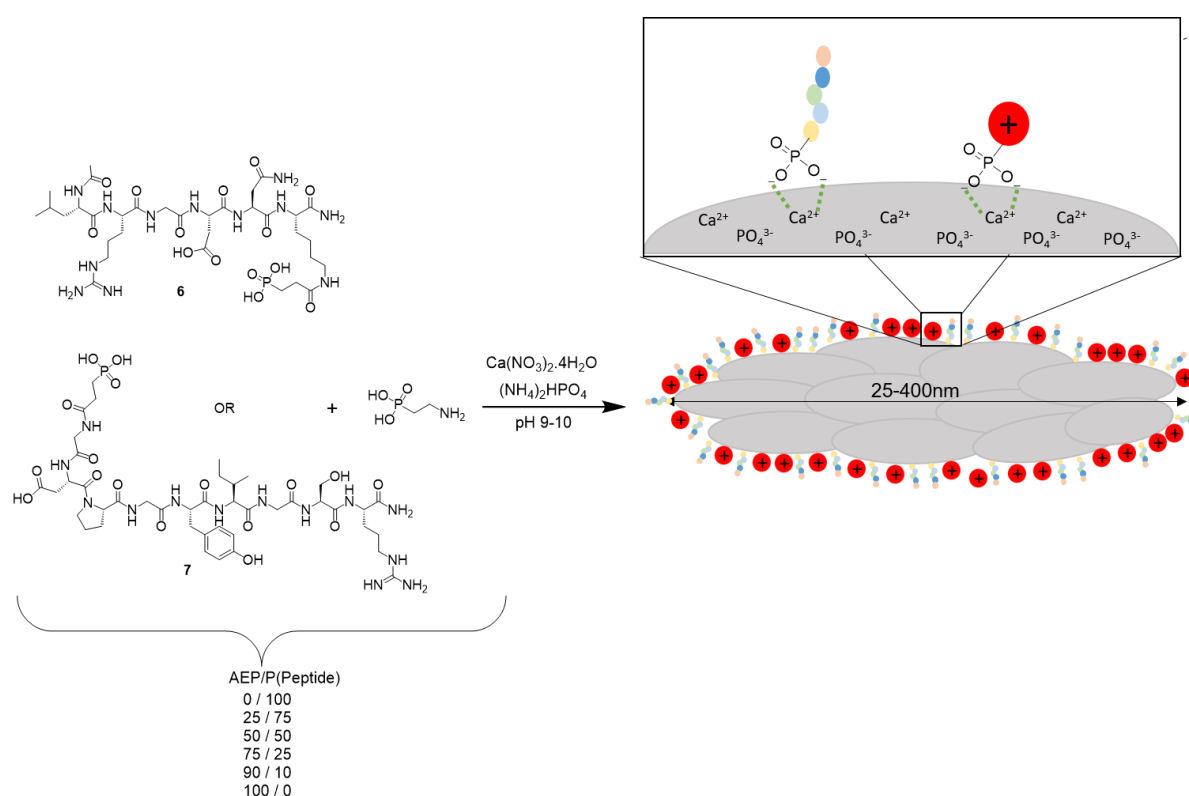


Figure 37 : NPs synthesis with different ratios between AEP and P(RGD) **6** or P(YIGSR) **7**

Moreover, it was important to verify if P(RGD) **6** and P(YIGSR) **7** were stable during the particles synthesis in such conditions. A solution of P(RGD) **6** and P(YIGSR) **7** in water (0.197 mmol) at basic pH (~ 9-10) was so placed in an oven at 100°C during 16 hours. According to

the LC-MS analyses, the peptide-based stabilizing agents **6** and **7** did not show any modification or alteration due to these experimental conditions.

C. Results and characterizations of apatite particles surrounded with a mixture of P(Peptide) and AEP

As described in chapter 1, when AEP (higher pK_a value of 10.5) was used as stabilizing agent (in sufficient amount), it was possible to limit the agglomeration of apatite NPs thanks to efficient electrostatic repulsion effects induced by the primary protonated amine of AEP which creates a positive charge screen around the particle at $pH \sim 9$. However, in the case of the P(RGD) **6** and P(YIGSR) **7** compounds tested in this work, the initial charge of pure AEP was no more available due to the peptide functionalization. However, we assumed that the molecular weight of the peptide (< 1 kDa) could generate a small steric hindrance effect high enough to prevent the agglomeration of the NPs, and that the positive charges of the P(Peptide) itself at pH 9-10 could induce additional stabilization, typically by the presence of the protonated guanidine of arginine (pH_i of P(RGD) = 8.2 and pH_i of P(YIGSR) = 7.0). Unfortunately, as explained below, our results indicated that these initial hypotheses were not valid.

1. Observations of the suspensions obtained after maturation

As expected, after one night (16 h) of maturation at $100^\circ C$ the observation of the two controls showed that in the presence of the AEP (NPs 1) a homogeneous, nearly transparent suspension characteristic of a stable colloidal suspension was obtained whereas without stabilizing agent a white precipitate was clearly visible at the bottom of the pillbox (Figure 38). We considered here that a suspension is colloidal and stable when the particles are dispersed in the liquid phase and remain so over time, i.e. they do not aggregate into macroscopic particles or decant. A suspension will in contrast be considered as unstable when the particles that compose it aggregate and sediment after a few hours.

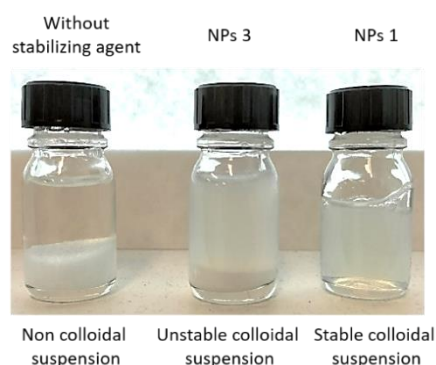


Figure 38 : Picture of stable colloidal (NPs 1), unstable (NPs 3) and non-colloidal (without stabilizing agent) suspensions

Unfortunately, in case of a mixture of AEP and P(Peptide), a stable colloidal suspension was obtained for only NPs 2 and 7 having a majority amount of AEP (i.e 90/10 – Table 13). In contrast, for the ratios 50/50 (NPs 4 and 9) and 75/25 (NPs 3 and 8), the suspended particles sedimented over time (~2 hours) resulting in an unstable suspension (Table 13 - Figure 38). The results also seemed to be independent of the nature of the peptide used, as almost similar results were obtained. When the quantity of AEP was further reduced (ratio 25/75 and 0/100), a white precipitate at the bottom of the flask was directly obtained (NPs 5 and 10), similar to the control without any stabilizing agent (Figure 38).

These first observations showed that the only presence of P(Peptide) **6** or **7** around the particles was not sufficient to act as stabilizing agents, neither by steric hindrance nor by electrostatic repulsion, contrarily to our initial expectations.

Id	AEP	P(RGD) 6	P(YIGSR) 7	Observations
NPs1	100	0	/	Colloidal
NPs2	90	10	/	Colloidal
NPs3	75	25	/	Unstable suspension
NPs4	50	50	/	Unstable suspension
NPs5	25	75	/	Non colloidal
NPs6	0	100	/	Non colloidal
NPs7	90	/	10	Colloidal
NPs8	75	/	25	Unstable suspension
NPs9	50	/	50	Unstable suspension
NPs10	25	/	75	Non colloidal
NPs11	0	/	100	Non colloidal

Table 13 : Observations of suspension after maturation time for NPs 1 to 11

An approximate length of the P(Peptide) was estimated by considering only the peptide part because the phosphonate moiety was similar for each stabilizing agents. The common backbone of AAs is composed of one C-C bond (1.54 Å) and one C-N bond (1.47 Å) inducing an AA length of about 3.01 Å. The peptides Ac-LRGDNK-NH₂ **1'** and H-GDPGYIGSR-NH₂ **2'** possessing respectively 6 and 9 AAs have thus an estimated length (~18.06 Å for peptide **1'** and ~27.09 Å for peptide **2'**) well below that of the PEGs (~206.47 Å) used in previous studies to stabilize the particles by steric hindrance.

Although the P(Peptide) exposes positively charged endgroups, stabilization by electrostatic repulsion was not effective either. One explanation was that the P(Peptide) compounds certainly interacted between them and with apatite surfaces and may ultimately promote the agglomeration of the particles upon uncontrolled electrostatic interactions. Indeed, the protonated guanidine of the Arginine present on the both P(RGD) **6** and P(YIGSR) **7** may interact electrostatically with the apatite surface. If this is the case, these charged endgroups were no longer available to electrostatically repel the particles. For electrostatic repulsion to occur with the peptides, a linker between the phosphonate and the peptide might have been

required to keep the peptide away from the apatite surface, avoid unwanted electrostatic interactions between adjacent particles and to essentially promote particle stabilization by steric hindrance.

2. Physicochemical characterizations of the particles surrounded by a mixture of P(Peptide) and AEP

Although a colloidal suspension was not systematically obtained, the hybrid particles contained in the precipitating medium were probably associated with at least some extent of P(Peptide) moiety. They could thus still be useful for some future biomedical applications that would not require a nanometric or controlled (nano)particle size. To try to understand our observations and also to assess the size and shape of the obtained particles, analyses by Dynamic Light Scattering (DLS) and Transmission Electron Microscopy (TEM) were carried out. Moreover, it was also interesting at this stage to determine the chemical nature of the particles obtained. Indeed, an apatitic structure was systematically obtained during the formation of colloids in the previous studies using pure AEP^{37,38}, but in our case unstable suspensions/precipitates were observed in the co-presence of P(Peptide) suggesting that the structure of the material precipitated could be different. X-Ray Diffraction (XRD) and Fourier Transform Infrared Spectroscopy (FTIR) analyses were performed to answer this question. Additionally, it was essential to know if hybrid organic/inorganic particles were indeed obtained in these conditions and to determine the corresponding grafting density, i.e. the number of grafted molecules per nm² of particle surface. To do so, liquid-state NMR analyses and in particular ³¹P ERETIC and quantitative proton NMR were carried out.

a. XRD analysis

The XRD patterns of the particles surrounded with AEP/P(RGD) **6** mixtures as stabilizing agent are shown in Figure 39, for different starting proportions from 25/75 to 90/10 (NPs 2 to 5). For the sake of comparison, the typical XRD diagram of stoichiometric hydroxyapatite (HA) was also added along with the corresponding (*hkl*) labeling of the main diffraction lines relative to the PDF file #00-009-0432.

As may be seen, very similar XRD patterns were obtained in all cases. The presence of an apatitic phase in these compounds can be hypothesized from the large diffraction band observed with a maximum around $2\theta = 32^\circ$, but the poor resolution of the XRD diagrams points to a rather low overall crystallinity. This conclusion could however somewhat be altered by the underlying background of the support (plastic) of the diffractometer in link with the limited amount of powder available for the analyses in dried form. In order to better visualize the apatite phase itself, a subtraction of the background signal was thus carried out for the typical example of NPs 5 (i.e AEP/P(RGD) = 25/75), as shown in Figure 40. The refined pattern then better points out the characteristic features of a moderately crystallized apatite, as

already noticed in a previous work (PhD thesis of Ahmed Al-Kattan, CIRIMAT, Toulouse) in the presence of pure AEP.³⁵

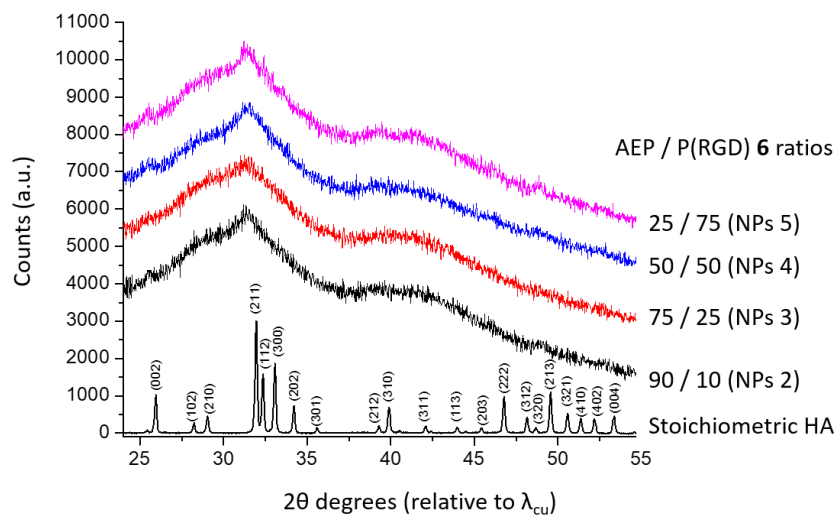


Figure 39 : XRD patterns of particles surrounded by a mixture of AEP / P(RGD) 6

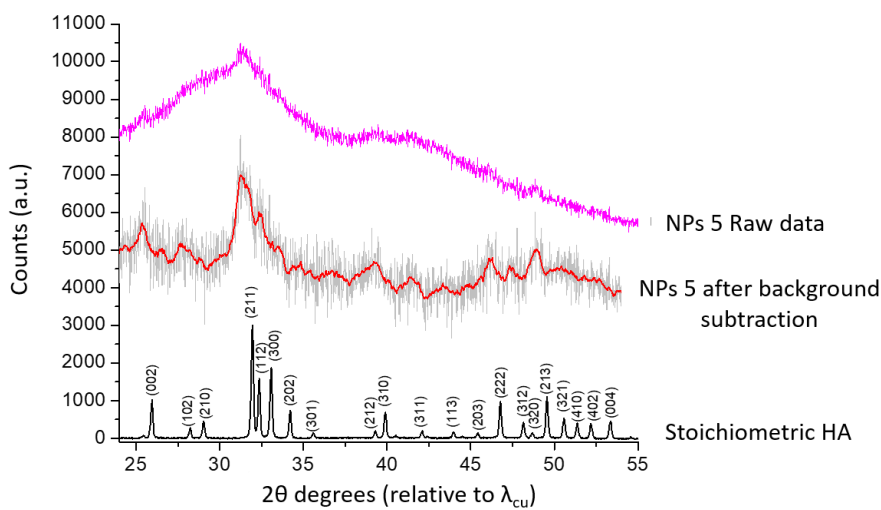


Figure 40 : XRD patterns of NPs 5 (ratio AEP / P(RGD) 6 = 25/75) after background subtraction

Similarly, in the absence of P(Peptide), the reference colloidal apatite NPs clearly exhibit rather close crystallographic features, which are also close to those of natural bone mineral as shown on Figure 41 and already discussed by A. Al-Kattan.

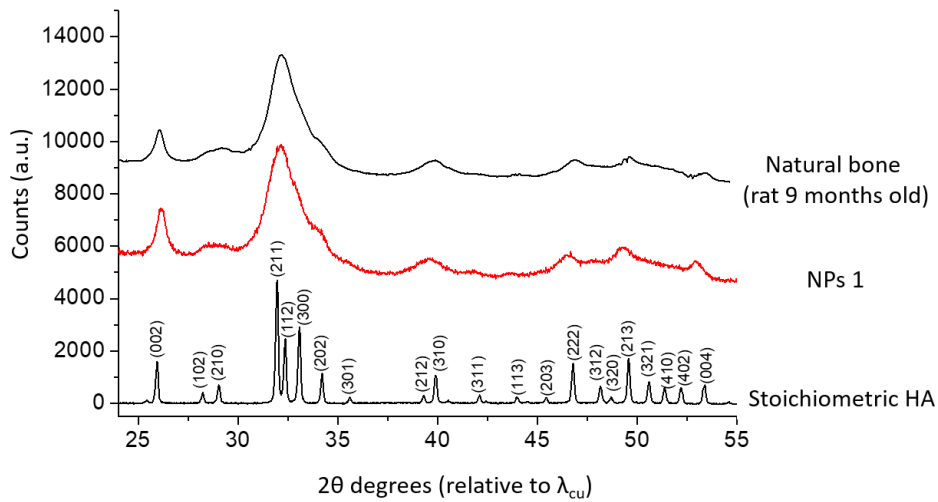


Figure 41 : XRD patterns of natural bone, NPs 1 (100% AEP) and stoichiometric HA

In this PhD work, the presence of the P(RGD) **6** around the particles, independently of the AEP / P(RGD) **6** ratio, did not seem to have a significant effect on the XRD pattern and thus on the apatite characteristics; and it may be noted that similar conclusions can also be drawn with the P(YIGSR) **7** (Figure 42), with very close XRD patterns as for P(RGD) **6** (Figure 39).

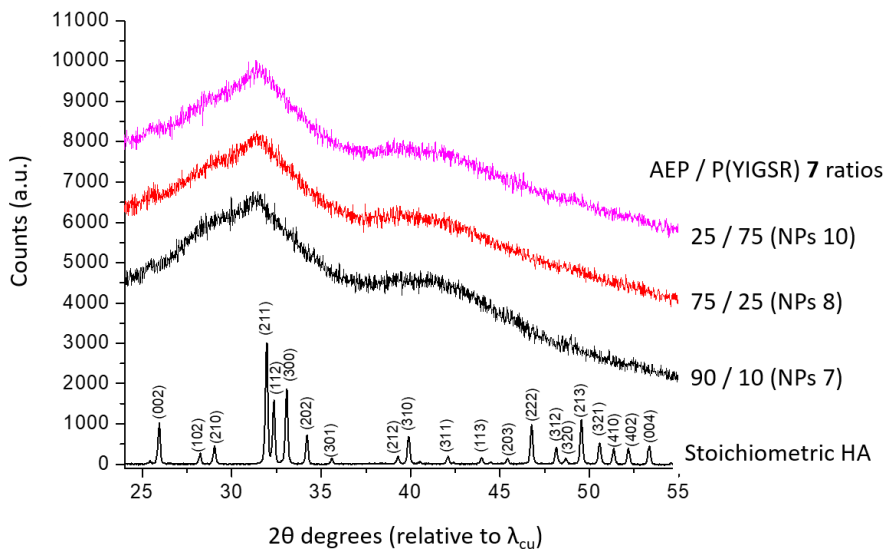


Figure 42 : XRD patterns of particles surrounded by a mixture of AEP / P(YIGSR) **7**

b. FTIR analysis

Due to the limited crystallinity suspected for the apatite phase, we also carried out FTIR analyses to further explore its characteristics. Figure 43 reports the typical case of NPs 5 (i.e

AEP/ P(RGD) **6** = 25/75). The comparison with a reference biomimetic apatite samples (internal collection of CIRIMAT, sample prepared at RT with 7 days of maturation) showed a very high similarity of spectral features in the mid-IR domain. To inspect in deeper details of the apatitic phase, a zoom has been made around the $\nu_4(\text{PO}_4)$ domain (Figure 43a). As may be seen, the characteristic features of a non-stoichiometric, biomimetic apatite can be observed for this compound, with especially the occurrence of HPO_4^{2-} ions presumably in both apatitic and non-apatitic chemical environments (as previously described for example by Vandecandelare *et al.*¹¹³) and these results were reinforced by the Fourier self-deconvolution (apodization) processing of the FTIR spectra as shown on Figure 43b. These conclusions agree well with the above-mentioned XRD results by pointing out the presence of a moderately-well crystallized, biomimetic apatite phase.

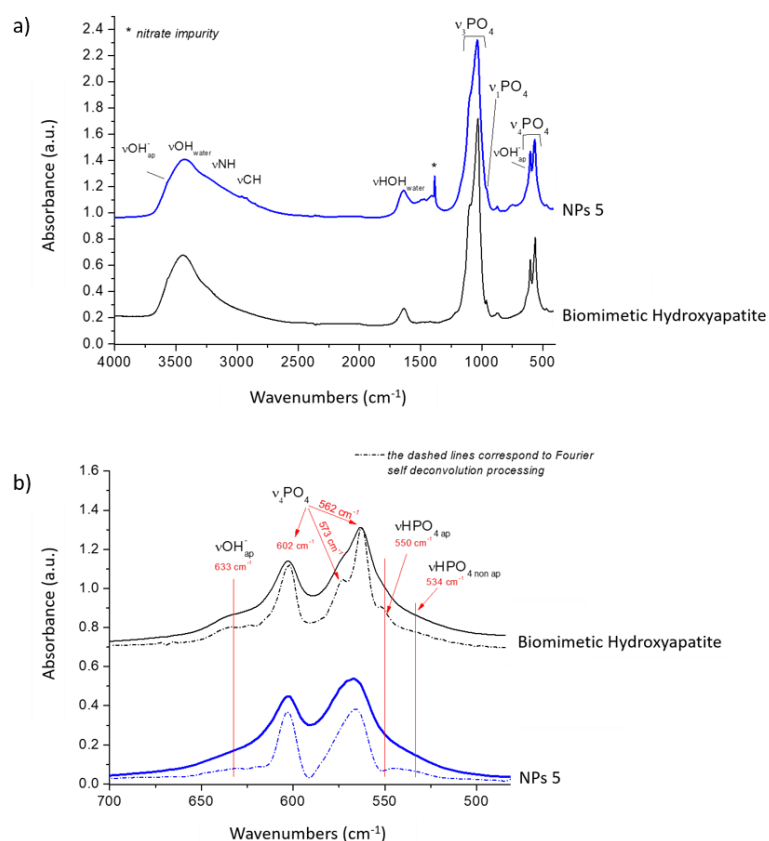


Figure 43 : FTIR Spectra of particles surrounded by AEP / P(RGD) **6** 25/75 (NPs 5)

c. RAMAN analysis

For complementary analyses, RAMAN spectra were recorded on NPs 3-5 and 8-10. The main results are reported respectively in Figure 44 a and b. In all cases, the characteristic bands of the apatite phase appeared essentially unchanged independently of the P(Peptide) **6** or **7** used and its proportion relatively to pure AEP. The $\nu_1(\text{PO}_4)$ band corresponding to the P-O

symmetrical stretching vibration showed in particular no significant change neither in width nor in position, unveiling the absence of major changes for the apatite phase in presence. On the other hand, the ν C-H band around 2 800-3 000 cm^{-1} was a characteristic feature of the organic components attached to the particles. It may then be remarked that, after intensity normalization of spectra relatively to the $\nu_1(\text{PO}_4)$ band, analysis of the ν C-H band intensity indicated that the amount of total associated organic components increased for the samples with AEP/P(RGD) **6** as follows: 25/75 (NPs 5) < 75/25 (NPs 3) < 50/50 (NPs 4) and for the samples with AEP/P(YIGSR) **7** as follows: 75/25 (NPs 8) < 25/75 (NPs 10).

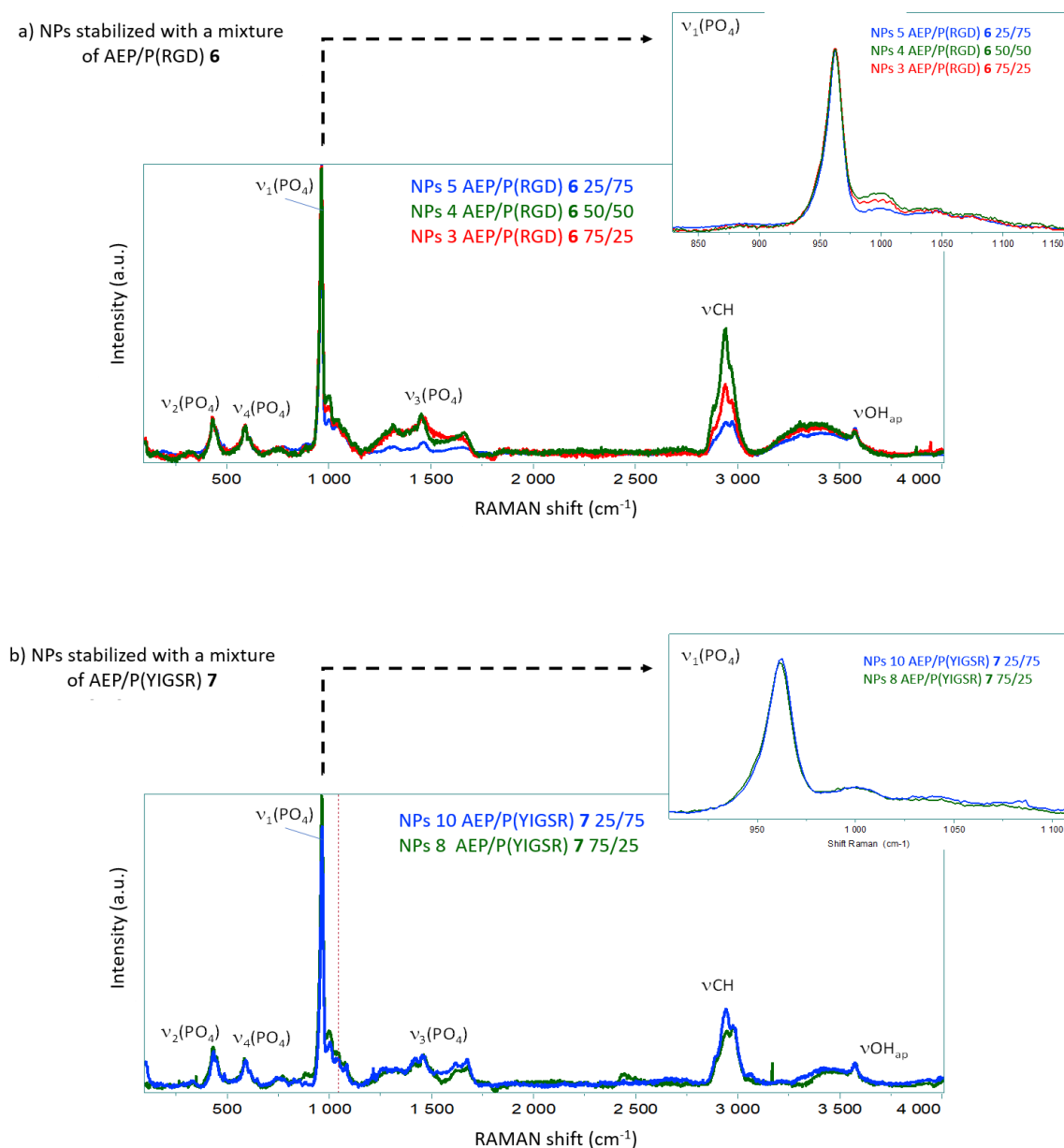


Figure 44 : RAMAN spectra of NPs stabilized with a mixture of a) AEP/P(RGD) **6** and b) AEP/P(YIGSR) **7**

Since the peptide moieties have more C-H bands in their structure than AEP, the order found for the P(RGD) **6** peptide did not follow the initial expectations considering the starting

reactants used. These findings compare well with the data from ERETIC ^{31}P liquid-state NMR (Table 12) showing that the syntheses carried out with this AEP/P(Peptide) approach did not lead to controlled systematic changes in the amount of organic components finally attached onto the apatite particle surface.

d. Determination of particles size thanks to DLS analysis and TEM imaging

DLS analysis and TEM imaging are two characterization techniques that provide information on particle size. However, the size of the particles observed by TEM corresponds to the length (L_{NPs}) and width (I_{NPs}) of the inorganic part of the organic molecule only, whereas DLS gives information on the hydrodynamic diameter of the particle (D_h) which corresponds to the size of the inorganic part plus the size of the corona and its hydration shell (Figure 45).

In addition, previous studies on AEP-stabilized particles showed that the particles were composed with several crystallites (Chapter 1 section II.B.2.a)³⁷ Therefore, it is also important here not to confuse these two parameters with the size of the individual crystallites that aggregate to form the nanoparticles.³⁷ The crystallite size can be obtained with XRD ($d_{\text{crystallite}}$) analysis by using the Scherrer's equation as explained in chapter 1.

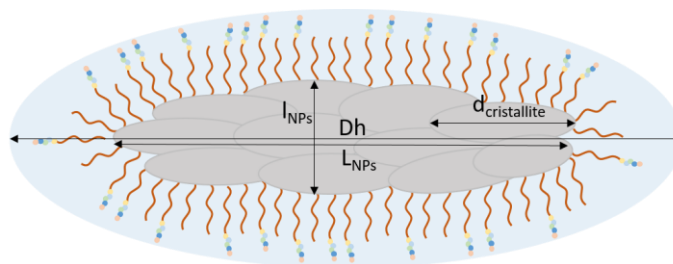


Figure 45 : Difference and complementarity between size parameters obtained by DLS, DRX and TEM

TEM imaging

TEM imaging analysis allowed us to obtain information about the size and shape of the inorganic part of the particles in a more precise way. To this aim, a drop of colloidal suspension was placed on a TEM grid. Once the drop was dried, the particles were observed. Unfortunately, in spite of dilution tests, most of the TEM images were difficult to analyze because of a very important agglomeration of the particles certainly caused by the evaporation of the drop during the sample preparation. Analyses carried out on the colloidal suspensions NPs 2 and 7 showed particles with a different shape in comparison with NPs stabilized with AEP alone (Figure 46).

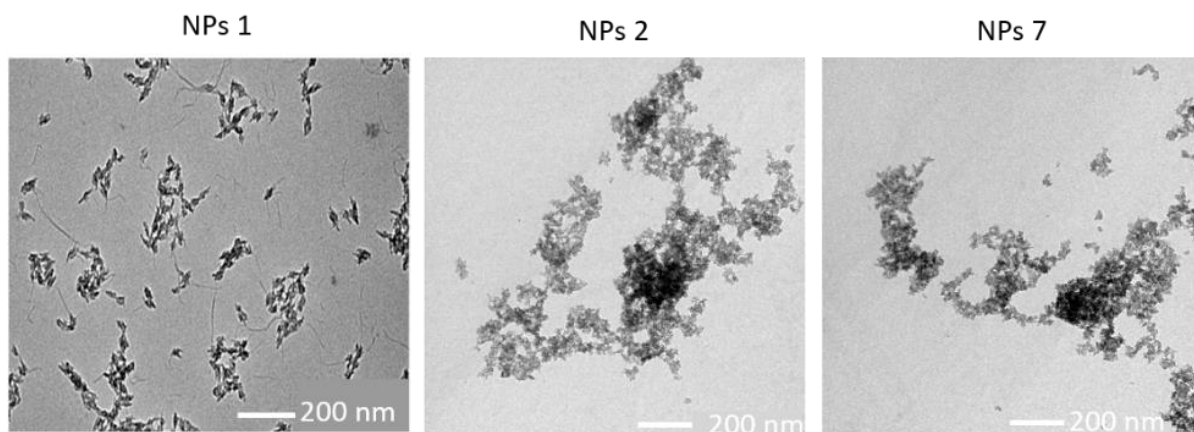


Figure 46 : TEM imaging of NPs stabilized with 100% of AEP (NPs 1), with a mixture of AEP/P(RGD) 6 90/10 (NPs 2) and with a mixture of AEP/P(YIGSR) 7 90/10 (NPs 7)

According to the TEM images, an agglomeration of small particles or crystallites into larger particulate entities, partially disrupted by the analysis, seems visible. Although this phenomenon is most likely accentuated during TEM analysis due to the preparation of the samples on the grid, we hypothesized that this agglomeration was due to the presence of the P(Peptide). Indeed, although the phosphonate group has a greater affinity with the apatite surface than the guanidinium ions of the Arginine, the close distance between the peptide in P(Peptide) and the particle surface could facilitate the interactions between them but also with the other (adjacent) particles present around them, thus facilitating the agglomeration. These interpretations were found in agreement with the DLS analyses giving particle sizes above 300 nm.

DLS analysis

The principle of DLS is based on the emission of a beam (laser) at a known intensity (I_{incident}) which is sent on the particles in suspension and the follow-up of changes in direction. The laser beam gets re-oriented by the particles, in a way that is dependent on the size of the particles encountered thanks to the Stokes-Einstein relation. The smaller the particle size, the less the wavelength is absorbed by the particle and the higher the reflected/diffused intensity (Figure 47).

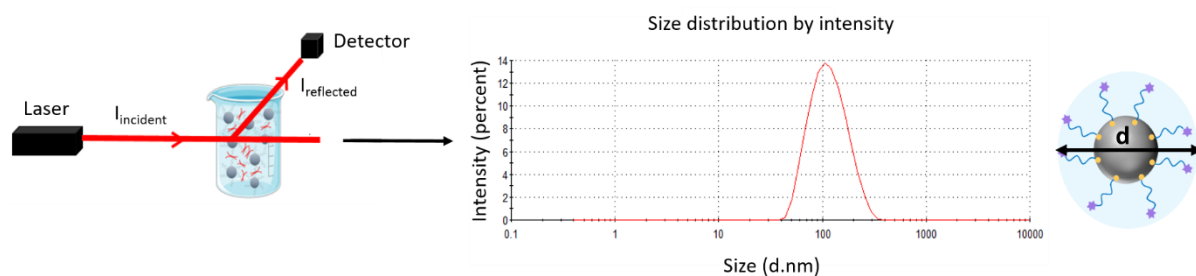


Figure 47 : Principe of Dynamic Light Scattering (DLS)

DLS analyses were performed only on the colloidal suspensions (NPs 2 and 7 - Figure 48). The results showed that the particles obtained had a significantly larger size (> 300 nm) than the NPs prepared with a pure AEP corona (NPs 1 - 25 nm¹⁰⁴) (Table 14).

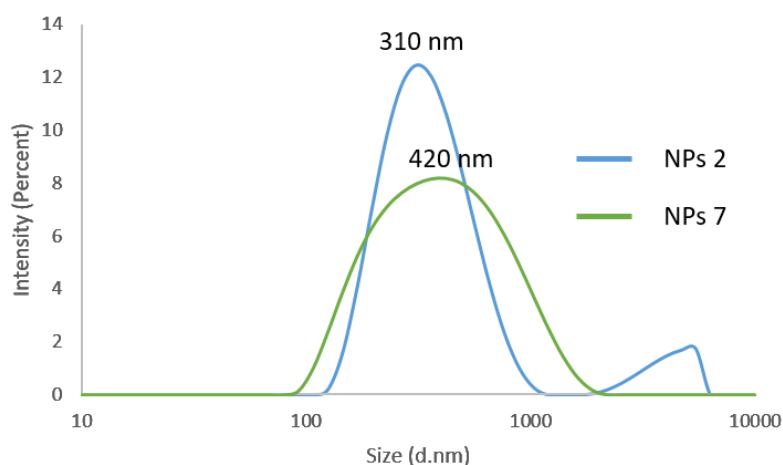


Figure 48 : DLS analysis of NPs surrounded with a mixture of AEP/P(RGD) 6 90/10 (NPs 2) and with a mixture of AEP/P(YIGSR) 7 90/10 (NPs 7) (Table 14)

These data confirmed that the P(Peptide) molecules present on the surface of the particles were not sufficient to prevent efficiently the agglomeration of the particles by electrostatic repulsion even if the zeta potential measurements confirmed a positive charge around the NPs (Table 14). The size larger than 300 nm observed here was coherent with the optical observations of unstable sedimenting suspensions.

Id	AEP	P(RGD) 6	P(YIGSR) 7	Size (nm)	Pdl	Zeta Potential pH 7,2 (mV)
NPs1	100	0	/	25	0.07	4.8
NPs2	90	10	/	388	0.23	4.0
NPs7	90	/	10	358	0.54	5.25

Table 14 : DLS analyses of NPs 1, 2 and 7

As explained earlier, DLS results may overestimate the actual particle size due to the hydrodynamic diameter considerations. In addition, DLS is ideal for spherical particles due to its operating principle, but is not well suited to analyze particles with a high aspect ratio. In the latter case, DLS only gives a rough estimate of the particle size, and especially more about the largest dimension of the particles (e.g. the large diameter of an ellipsoid) which contributes more to the obscuration of the laser during the analysis than the smaller dimensions.

e. Liquid-state NMR

Liquid-state NMR was performed to determine the grafting density, *i.e.* the number of organic molecules grafted to the surface of an apatite NPs. Our strategy was to determine the exact concentration of the organic molecules grafted around the apatite NPs (NPs 1 to 11) using the common organic phosphonate moiety of all the stabilizing agents (AEP and P(Peptide)) and the ERETIC ^{31}P NMR. In the case of co-grafting between AEP and P(Peptide) (NPs 2-5 and 7-10), quantitative ^1H NMR would allow us to assess the actual ratio between each adsorbed stabilizing agents. By combining these two methods, it would be possible to determine the exact concentration of peptide around the apatite NPs. Moreover, by using the grafting density and Flory's equation we hoped to determine the conformation of the AEP/P(Peptide) stabilizers around the apatite surface.

To do so, 1 mL of the colloidal suspension was centrifuged to ensure the removal of any molecules that might have been released or remained even after purification by dialysis. The supernatant was removed and the still wet powder was freeze-dried, and the amount of dry powder obtained was weighed thoroughly. For non-colloidal samples, a precise mass of powder has been weighed. To release the grafted organic molecules in view of NMR titration, the NPs were dissolved with 100 μL of 1 M hydrochloric acid (HCl). Finally, 500 μL of deuterated water (D_2O) was added and the whole solution was incorporated in an NMR tube.

^{31}P NMR ERETIC

ERETIC NMR allows determining the absolute quantification of the stabilizing agents grafted around the NPs. In our case, the ERETIC NMR analyses were run on the Phosphorus 31 (^{31}P) nucleus because it was possible to dissociate the apatitic inorganic phosphates (~ 0 ppm) from the organic phosphonates belonging to the stabilizing agents P(Peptide) and AEP (~ 25 - 26 ppm). In order to obtain an accurate concentration of grafted AEP/P(Peptide) stabilizers, a calibration curve had to be performed. A standard range between 0.1 mM and 100 mM was realized to this aim. This calibration curve allowed us to link the area under the peak and the phosphorus concentration (see Chapter 4). Once this calibration curve was established, the sample including the dissolved NPs of unknown concentration was run in phosphorus NMR under the same conditions. The results showed that the P(Peptide) were present around the particles in sufficient quantity to consider their biological applications and in particular for the treatment of wounds. Indeed, studies have shown that a concentration of RGD and YIGSR around 1-3mM showed positive effects on the proliferation and migration of fibroblasts¹¹⁴⁻¹¹⁶ (Table 15).

Id	AEP	P(RGD) 6	P(YIGSR) 7	[R-PO ₃ H ₂] (mM)	Yield %
NPs1	100	0	/	2.19	11
NPs2	90	10	/	2.27	11
NPs3	75	25	/	1.91	9
NPs4	50	50	/	4.92	25
NPs5	25	75	/	1.05	5
NPs6	0	100	/	ND	ND
NPs7	90	/	10	ND	ND
NPs8	75	/	25	2.39	12
NPs9	50	/	50	6.86	35
NPs10	25	/	75	12.87	65
NPs11	0	/	100	N	ND

Table 15 : Concentration of stabilizing agents AEP/P(Peptide) present in 1mL of colloidal suspension (NPs 1 to 11) estimated by ³¹P ERETIC NMR (ND: Not Determine)

This information was used to calculate the grafting yield of the stabilizing agents grafted on the particle surface as the ratio of the total amount of stabilizer involved in the synthesis and the amount of grafted material.

¹H quantitative liquid-state NMR

However, ERETIC ³¹P NMR did not allow differentiating between AEP and P(Peptide) co-grafted in some cases on the surface of the particles. In order to have an idea of the percentage of each of these two molecules on the surface, quantitative ¹H liquid-state NMR was performed. Unfortunately, due to a too low concentration, the detection limit of the proton quantification was reached. Furthermore, the proton signals obtained were of very poor quality and overlapped, preventing the correct integration of protons characteristic of each molecule and obtaining a relative quantification of the grafted stabilizers. Therefore, calculations to determine the grafting density and the conformation of the molecules around the particles using Flory's equations could not be performed here.

D. Conclusion

The objective of this part of the work was to synthesize a first family of peptide-based stabilizing agents, P(Peptide) to (i) stabilize apatite particles through electrostatic repulsion and obtain nanometer size particles and (ii) to confer additional biological properties to the particles through the use of P(Peptide). The synthesis of the peptidyl resin **1** and **2** as well as their functionalization by the 3-(diethoxyphosphoryl)propionic acid **9** on the side chain of Lysine or on the N-terminal, respectively was done on resin. The stabilizing agents P(RGD)

6 and P(YIGSR) **7** were obtained in sufficient quantity (93% and 94% respectively) and with good purity (56% and 41%, respectively). Once the new bioactive stabilizing agents P(Peptide) were obtained, they were added (sometimes with a mixture of AEP as discussed in the text) in the synthesis medium in view of one-pot precipitation of apatite-peptide hybrid particles following the reference protocol. A colloidal suspension could be obtained only when the amount of AEP was in majority (AEP/P(Peptide)= 90/10 - NPs 2 and 7) and unstable colloidal suspensions could be obtained with the ratios 75/25 (NPs 3 and 8) and 50/50 (NPs 4 and 9). The results showed that the P(Peptide) present around the particles did not allow limiting efficiently the agglomeration by neither electrostatic despite the positively charged around the particles, as confirmed by DLS. No nanometric particles with controlled size could be obtained with this approach. However, the presence of P(Peptide) did not seem to interfere with the structure of the apatite formed, since a moderately crystallized apatite phase was obtained in all cases, with or without the presence of P(Peptide). Finally, the amount of stabilizing agents grafted around the particles was sometimes determined by liquid ERETIC ^{31}P NMR when the sensitivity of the apparatus allowed it. Unfortunately, the grafting density and thus the conformation of the stabilizing agents AEP/P(Peptide) could not be determined here because of some missing data such as the precise particle size. Moreover, the quantitative ^1H NMR was not possible here because of the very low concentration and the bad quality of the NMR spectra. For these reasons, the P(Peptide) concentration was also not determined here. These conclusions suggest that there is a need to position peptide moieties farther away from the apatite surface and to control the colloidal stability by a stronger effect. In the next part of the study, a PEG linker was thus used to this aim.

III. Synthesis and characterization of hybrid peptide-apatite nanoparticles surrounded by new peptide-based stabilizing agents P(PEG3K)-Peptide

We have seen previously that the stabilizing agents P(Peptide) was not sufficient by itself to stabilize the particles in a stable colloidal suspension despite the exposed charges. Therefore, we devised a second family of peptide-based stabilizing agents by conjugating a bioactive peptide sequences at the end of a PEG chain (3 000 to 5 000 $\text{g}\cdot\text{mol}^{-1}$) bearing a phosphonate moiety. This new family will be named in this manuscript, P(PEG3K)-Peptide. In this way, the colloidal suspension and nanometric size particles should be obtained by steric hindrance. We hypothesized that adding a small molecule to the end of a long PEG chain would not disrupt the stabilizing agent effect already reported^{9,43} and will additionally move away from the surface, thus abolishing or limiting the peptide-apatite interactions. We hoped by this way to control the agglomeration state of the particles and obtain a homogenous nanometric and controlled size. Moreover, we hoped to well expose the bioactive peptide around the surface of the particles and retain their biological activity.

Herein, we used the two peptide sequences already described in part I, H-GDPGYIGSR-NH₂ and Ac-LRGDNK-NH₂ which will be conjugated to the carboxylic acid function of a PEG through

their N-terminal or the side chain of the C-terminal Lysine, respectively. A third peptide sequence (H-AhxRR-NH₂) analog of an amphipathic antibacterial peptide, was also selected to be modified at its N-terminus. In the following of this project, these stabilizing agents P(PEG3K)-Peptide synthesized from these three peptides will be named as reported in Table 16.

Name	Sequence
P(PEG3K)-RGD	Ac-LRGDNK(PO ₃ H ₂ CH ₂ CH ₂ CO-PEG3K)-NH ₂
P(PEG3K)-YIGSR	PO ₃ H ₂ CH ₂ CH ₂ CO-PEG3K-GDPGYIGSR-NH ₂
P(PEG3K)-AhXRR	PO ₃ H ₂ CH ₂ CH ₂ CO-PEG3K-AhxRR-NH ₂
P(PEG3K)-NEt ₂	PO ₃ H ₂ CH ₂ CH ₂ CO-PEG3K-NEt ₂

Table 16 : Sequences of the new family of peptide-based stabilizing agents P(PEG3K)-Peptide

For the same reasons as for the AEP trials, the anchor used for attachment to the apatite surface was again a phosphonate group, attached to the other side of the PEG moiety in this case. In this section, the synthesis of the second family of peptide-based stabilizing agents P(PEG3K)-Peptide will be detailed (III.A) as well as the synthesis (III.B) and characterization of the obtained particles (III.C).

A. Synthesis of new peptide-based stabilizing agents, P(PEG3K)-Peptide and synthesis of the simple stabilizing agent P(PEG3K)-NEt₂

The first step was to synthesize the three new peptide-based stabilizing agents P(PEG3K)-Peptide and the simple stabilizing agent P(PEG3K)-NEt₂ to perform in the following co-adsorption as previously with AEP and P(Peptide) (Table 16). We have explained in chapter 1 that the length of the PEGylated chain had an influence on the size of the NPs obtained ranging from 350 nm (MW_{PEG} 530 g.mol⁻¹) to 130 nm (MW_{PEG} of 5 000 g.mol⁻¹).⁴⁴ To obtain nanometric size particles, we decided here to use PEGs with a molecular weight around 3 000 to 5 000 g.mol⁻¹. Moreover, PEGs containing a carboxylic acid moiety were necessary in order to allow the coupling with the primary amine of the peptides (i.e on the N-terminal of the peptide H-GDPGYIGSR-NH₂ and H-AhxRR-NH₂ or on the side chain of the Lysine for the peptide Ac-LRGDNK-NH₂) or with the diethylamine (NEt₂).

We first planned the synthesis of P(PEG3K)-Peptide fully on solid support, coupling the commercial and already phosphonated PO₃H₂CH₂CH₂CO-PEG5K-COOH (named P(PEG5K)-COOH) after selective deprotection of the suitable primary amine, on solid support. Initially, the P(PEG5K)-COOH had been used in a study at CIRIMAT, as stabilizing agent in previous study.⁴³

1. Functionalization of peptidyl resin **2** with the P(PEG5K)-COOH **12** on solid support with Fmoc-tBu strategy

a. Peptidyl-resin **2** synthesis

The first synthetic attempt was done on the peptidyl resin **2** (i.e corresponding to the peptide H-GDPGYIGSR **2'** after cleavage - Figure 49). This peptidyl resin **2** was synthesized by a Fmoc/tBu SPPs strategy on a Rink Amide PS resin (0.94 mmol.g^{-1}) as described in section I. After a selective removal of the N-terminal Fmoc protection, a microcleavage was performed to check the structure of the associated peptide **2'** before the N-terminal functionalization with P(PEG5K)-COOH **12**. The peptide H-GDPGYIGSR-NH₂ **2'** was well obtained with 93% of purity.

b. Functionalization of the N-terminal of the peptidyl resin **2'** with a P(PEG5K)-COOH **12**

The functionalization of the N-terminal of the peptidyl resin **2** on solid support with the commercial P(PEG5K)-COOH **12** was performed in the same way we introduced the 3-(diethoxyphosphoryl)propionic acid **9** during the synthesis of P(Peptide) stabilizing agents (Figure 49). The P(PEG5K)-COOH **12** (5eq) was dissolved in DMF and its carboxylic acid was pre-activated with HATU (5eq) in presence of DIEA (10eq). After 5-10 minutes of pre-activation, the solution was poured on the resin. As previously explained, carboxylic acid activation and peptide coupling can occur in the presence of a phosphonic acid if the amount of base is controlled (2eq maximum). To follow the reaction, resin samples were taken at several time points from the syringe and microcleavages were performed followed by LC-MS analyses. The presence of PEG could never be observed at any time points.

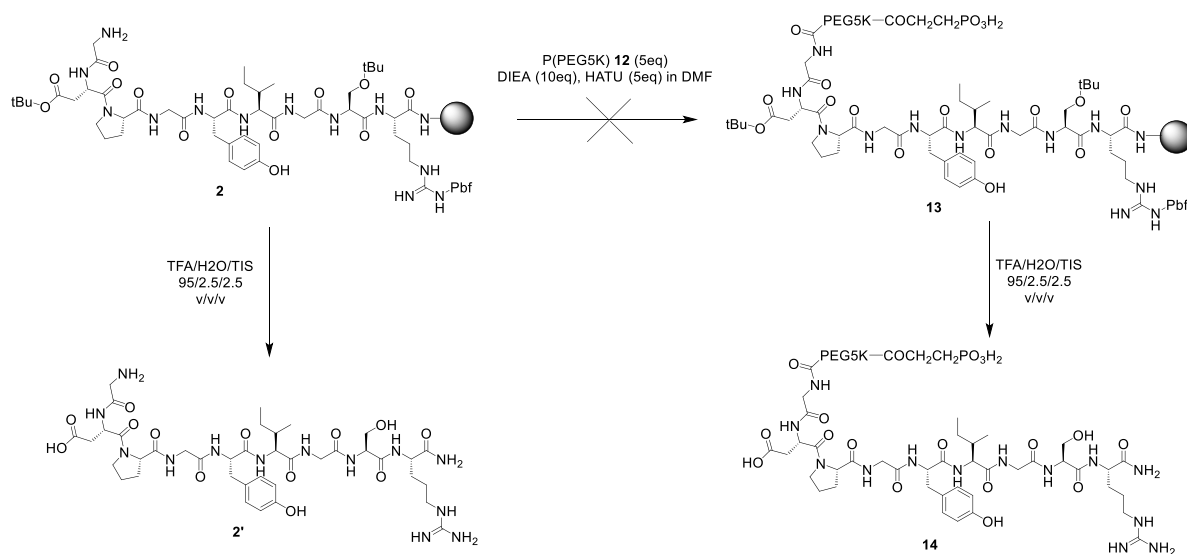


Figure 49 : Functionalization of the peptidyl resin **2** with the commercial P(PEG5K)-COOH **12** by using a SPPS synthesis

We hypothesized that 2eq of DIEA wasn't sufficient to deprotonate the carboxylic acid of P(PEG5K)-COOH **12** and so activate it with the coupling agent HATU. To increase equivalent number of DIEA a dialkylphosphonate was necessary and used as for the P(Peptide) synthesis. We hypothesized also that the loading (0.94 mmol.g^{-1}) was probably too high to allow the coupling between a long PEGylated chain and a solid supported peptide. As explained in Section I.A.6, the resin beads are microporous cross-linked materials (PS in our case), with 99% of the linker present inside the bead and only 1% on the surface. The high loading means that a quite high density of peptide is expected inside the matrix making it more difficult for large molecules such as P(PEG5K)-COOH **12** to penetrate inside the resin bead and couple to the free amine of the supported peptide. We cannot also exclude that the PEG chain in the PS resin was folded in a way which prevented the carboxylic acid from coupling to the free primary amine of the peptide.

However, the PEGylation of a peptidyl resin using a carboxymethylated PEG was already reported in the literature on a MBHA-Rink amide resin (0.27 mmol.g^{-1}).¹¹⁷ In this paper, the carboxymethylated PEG was activated by benzotriazol-1-yloxytris(diethylamino)phosphonium hexafluorophosphate/*N,N*-Diisopropylethylamine (BOP/DIEA) method. Solid phase PEGylation was found to be efficient for PEGs with molecular weight between 750 and 2 000 g.mol^{-1} . A very high coupling efficiency of about 95% was obtained after 8 hours of reaction. In the case of PEGs with a molecular weight of 5 000 and 10 000 g.mol^{-1} the reaction was found to be much slower than their lower molecular weight counterparts and were only completed in about 50% yield, even after 72 h (Table 17).

Time (h)	Concentration of NH ₂ -resin (uncoupled) ($\mu\text{mol/g}$)			
	PEG ₇₅₀	PEG _{2 000}	PEG _{5 000}	PEG _{10 000}
0	143.8	143.8	143.8	143.8
4	10.9	26.5	88.1	98.4
24	0	8.2	80.2	77.8
28	0	7.2	73.9	73.6
48	0	7.2	72.7	72.8
72	0	7.2	72.5	72.9

Table 17 : Pegylation of peptidyl resin: the influence of PEG length (adapted from ¹¹⁷)

According to the authors, solid phase PEGylation is therefore possible using a loading around $\sim 0.27 \text{ mmol.g}^{-1}$ and a PEG with a molecular weight shorter than $5\,000 \text{ g.mol}^{-1}$. Therefore, we decided to use a phosphonated PEG containing (i) a carboxylic acid on one side, (ii) a protected dialkylphosphonate on the other side and (iii) having a lower molecular weight around $2\,000 - 3\,000 \text{ g.mol}^{-1}$. Since this kind of molecule was not found commercially, a FmocNH-PEG3K-COOH **15** was purchased ($\text{MW} = 3\,000 \text{ g.mol}^{-1}$). We hoped to pre-activate the carboxylic acid of **15** under the same conditions as before (HATU, DIEA) and then couple it with the primary N-terminal amine of peptidyl resin **2** (Figure 50). If PEGylation of peptidyl resin **2** did occur, we considered coupling the 3-(diethoxyphosphoryl)propionic acid **9** to the end of the PEG chain

after Fmoc deprotection (Figure 50). Moreover, in order to observe the influence of the loading on the PEGylation of the peptide on solid support, three Rink Amide PS resins were used with three different loadings (0.94, 0.47 and 0.3 mmol.g⁻¹).

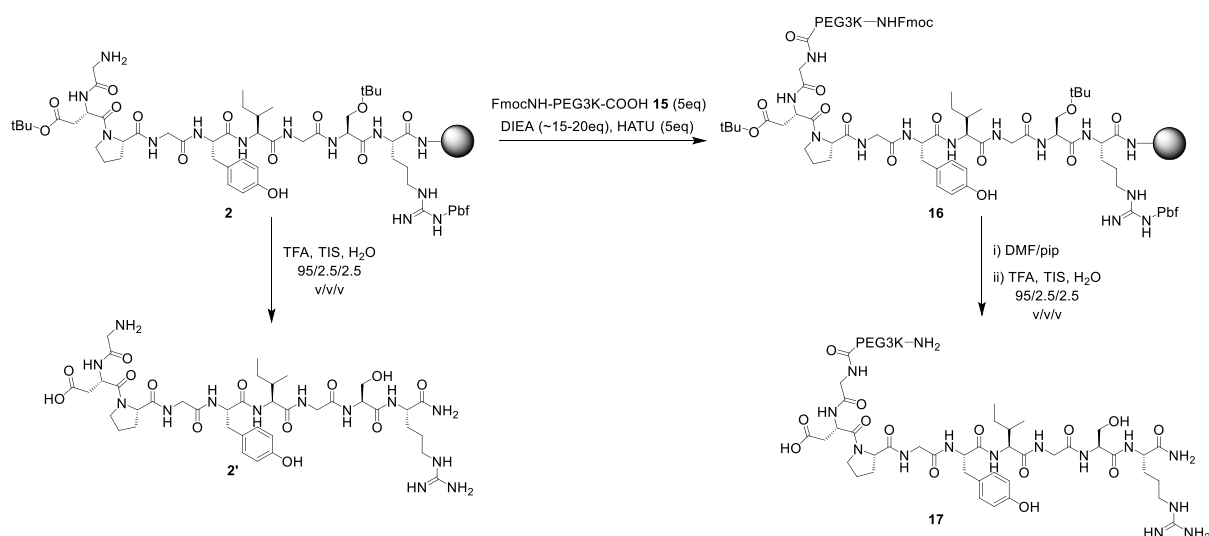


Figure 50 : PEGylation of peptidyl resin **2** with FmocNH-PEG3K-COOH **15** and different initial loadings of 0.94, 0.47 and 0.3 mmol.g⁻¹

2. Functionalization of the N-terminal amine of the peptidyl resin **2** with a FmocNH-PEG3K-COOH **15** on solid support

The functionalization of the N-terminal amine of the peptidyl resin **2** was performed in the same conditions as before but with a higher equivalent number of DIEA (~15-20 until pH 8-9) to ensure the deprotonation of the carboxylic acid of the FmocNH-PEG3K-COOH **15**. In order to verify if the coupling had taken place, we performed a UV titration of the Fmoc protecting group by taking resin samples at different time points (Table 18).⁹⁴

Time (h)	Coupling rate % loading 0.94mmol.g ⁻¹	Coupling rate % loading 0.47mmol.g ⁻¹	Coupling rate % loading 0.3mmol.g ⁻¹
0	0	0	0
4	0	5	4
8	0	6	6
24	3	10	11

Table 18 : Results of a Fmoc dosage after the terN functionalization of the peptidyl resin **2** with a FmocNH-PEG3K-COOH **15** on solid support

According to the UV titration the functionalization of the peptidyl resin **2** with the FmocNH-PEG3K-COOH **15** on a 0.94 mmol.g⁻¹ Rink Amide PS resin was not efficient even after 24 hours (3% of coupling rate). It was confirmed by LC-MS analysis performed after cleavage, which showed the presence of (almost) only peptide **2'**. The low amount of crude product obtained (11.2 mg) did not enable us to purify it and retrieve the desired product **16**. In contrast, the

functionalization performed on a less loaded resins (i.e. of Rink Amide PS with an initial loading around 0.47 mmol.g^{-1} and 0.3 mmol.g^{-1}) went forward over time according to UV titration analyses. The LC-MS analyses indicated that the peptide **2'** was still the major product in both cases (10 and 11% of coupling rate after 24 hours of reaction). The low amount of crude product obtained (32.6mg and 44.2mg) did not enable us to purify it and retrieve the desired product **16**.

According to the results, we assumed here that the steric hindrance induced by a long PEGylated chain was the main parameter that prevented the synthesis of P(PEG3K)-Peptide on solid support. Moreover, as a quite large amount of each final molecule ($\sim 1\text{-}2\text{g}$) was required to perform the multiple syntheses of the hybrid NPs, the SPPS synthesis method was not selected for the rest of the work.

*3. Synthesis of P(PEG3K)-Peptide **27**, **28**, **29** and P(PEG3K)-NEt₂ **30** with a multi-steps synthesis in solution*

We demonstrated that the main problem of PEG coupling on solid support was the steric hindrance. Thus, we decided to perform the reaction in solution. The main challenge of the P(PEG3K)-Peptide **27**, **28**, **29** and P(PEG3K)-NEt₂ **30** synthesis was to avoid the separation of different PEGylated compounds which share similar physicochemical properties and cannot be easily separated by precipitation, extraction or even preparative HPLC. To avoid the tricky purifications which would lead to product loss, a strategy was developed to obtain the desired and final compound **27**, **28**, **29** and **30** in a significant yield without any purification.

*a. Synthesis of the PO₃Et₂(PEG3K) **21***

Our strategy was first to synthesize the compound PO₃Et₂CH₂CH₂CO-PEG3K-COOH **21** (named PO₃Et₂(PEG3K)-COOH) through a multi-step synthesis (Figure 51). For that a dialkylphosphonate was preferred over unprotected phosphonates to activate the carboxylic acid of **21** in presence of phosphonate group as explained before. For this reason, the ethyl 3-(diethoxyphosphoryl)propionic acid **9** was used. As the coupling will be done in solution, we used a Boc-protected amino acid PEG (BocNH-PEG3K-COOH **19**). Indeed, Fmoc deprotection in solution requires a more complicated treatment to remove the dibenzofulvene adducts (see part I.B.6). In contrast, Boc deprotection by treatment with TFA (95%) and TIS/H₂O as scavengers (2.5% of each), only generates isobutene, tertbutanol or silylated species that can be removed during workup and TFA evaporation.

The first step was an acid hydrolysis of the compound **8** to obtain a carboxylic acid **9** which was then activated with DIEA until pH 8-9 and HATU (5eq) during 5-10 min (Figure 51). Then, the NH₂-PEG3K-COOH **20**, previously obtained from **19** by Boc removal in acidic conditions, was added dropwise for one hour. This pre-activation step avoided possible side reactions of **20**, as an intramolecular cyclization of the PEG or the coupling of two PEG chains together.

Moreover, in order to avoid a mixture between $\text{PO}_3\text{Et}_2(\text{PEG3K})$ **21** and $\text{NH}_2\text{-PEG3K-COOH}$ **20**, compound **9** was added in excess. Unfortunately, precipitation in Et_2O yielded of a mixture between these two compounds (**21** and **9**) even after extensive washings to remove the excess of **9**. This result could be explained by the instability of the activated intermediate of **9** by HATU. Although very reactive, this activated intermediate can be hydrolyzed, in particular by the presence of water in the solvents, and give back the carboxylic acid form. For this reason, this activated intermediate of **9** has not been isolated.

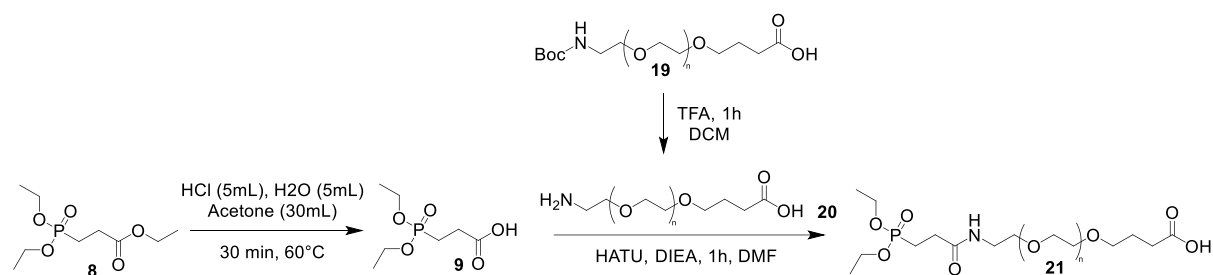


Figure 51 : First attempt for the synthesis of $\text{PO}_3\text{Et}_2(\text{PEG3K})$ **21**

To remedy to this solubility problem, the carboxylic acid **9** was activated with a benzotriazole group, less reactive but more stable, in the presence of pyridine and the anhydride propylphosphonique (T3P) (Figure 52).¹¹⁸ This N-acyl benzotriazole **18** was isolated after several extraction with ethyl acetate (EtOAc) and recovered after an evaporation of the solvent under vacuum. The product was analyzed by LC-MS (Chapter 4) and ^1H NMR (Figure 53) and was obtained with 83% of purity and 50% of yield (445mg).

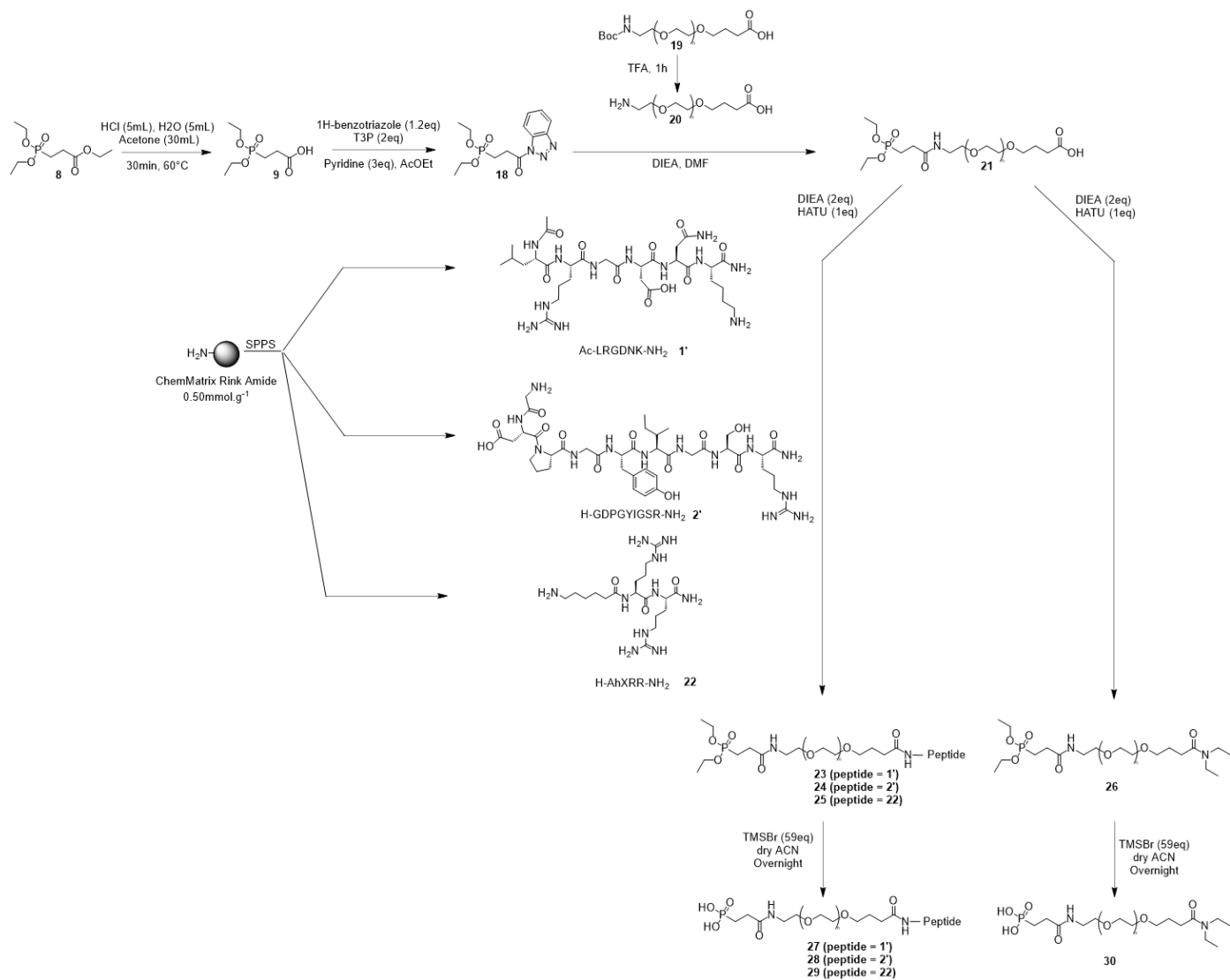


Figure 52 : Multi-step synthesis of the P(PEG3K)-Peptide **27**, **28**, **29** and P(PEG3K)-NEt₂ **30**

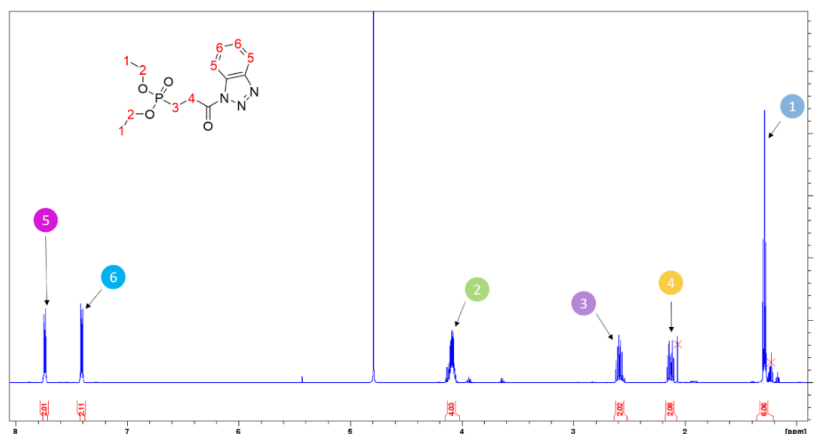


Figure 53 : ^1H NMR of the *N*-acyl benzotriazole **18**

The reaction between *N*-acyl benzotriazole compound **18** and $\text{NH}_2\text{-PEG3K-COOH}$ **20**, was finally performed in the presence of DIEA during 1 hour. For the same reason as before, **18** was added in excess. The desired product, $\text{PO}_3\text{Et}_2(\text{PEG3K})$ **21** was precipitated in Et_2O and the powder obtained was washed with EtOAc three times to remove the excess of reactant **18**. LC-MS analysis was performed to check if the reaction was successful but it was difficult to identify the products. Only one broad peak was visible corresponding in mass to the molecular weight of a +44 monomer (see chapter 4).

For this reason, the powder was analyzed by liquid-state NMR (^1H , ^{13}C , ^{31}P NMR and 2D NMR such as ^1H - ^1H COSY, ^{13}C - ^1H HSQC and ^{13}C - ^1H HMBC) in D_2O (see Chapter 4). The interpretation of the ^1H NMR analysis alone was not sufficient to determine if the coupling had taken place or if the two molecules (**18** and **21**) were present individually in the product.

Thanks to the heteronuclear ^{13}C - ^1H HMBC NMR analysis, it was possible to observe the amide carbonyl (174.1ppm), formed during the reaction, correlated with specific H-7 (3.44 ppm) of the PEG on one side and with H-4 (2.56 ppm) and H-3 (2.23 ppm) of the phosphonate group on the other side (Figure 54). In this way, we successfully proved that the coupling occurred.

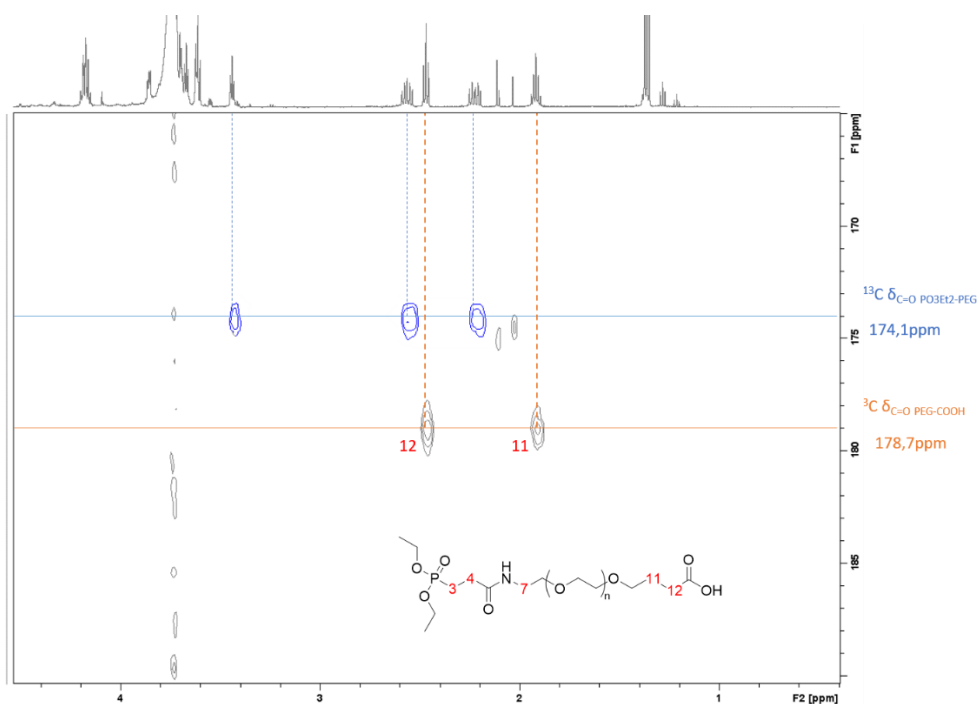


Figure 54 : ^{13}C - ^1H HMBC NMR of $\text{PO}_3\text{Et}_2(\text{PEG}3\text{K})$ **21** ; calibrated with the PEG signal (e.g. PEG : 3.74 ppm - ^1H / 69.6 ppm - ^{13}C)

However, this analysis did not give any information on the presence or absence of the two reagents **18** and **20**. The disappearance of aromatic H-5 (7.74 ppm) and H-6 (7.40 ppm) of the benzotriazole group in the ^1H NMR spectra showed that N-acyl benzotriazole **18** was totally removed after the washings (Figure 55).

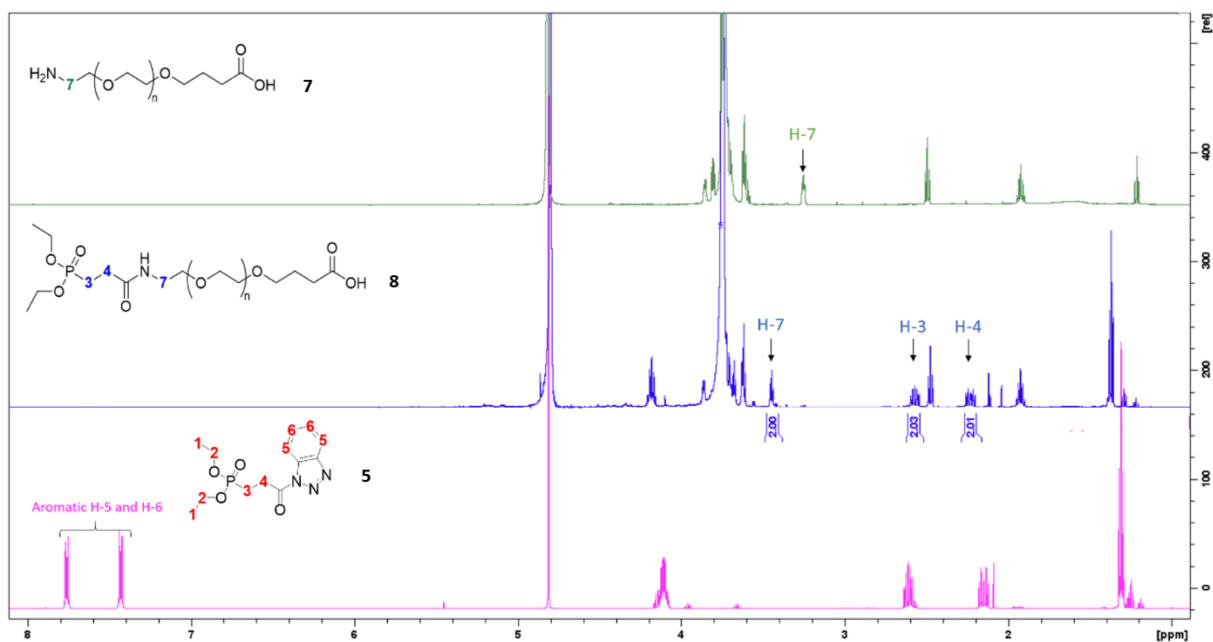


Figure 55 : Superposition of the ^1H NMR spectra of the desired product **8** and the two reagents **5** and **7**

Moreover, the peak corresponding to the H-7 of the PEG at 3.25 ppm was shifted after coupling to 3.44 ppm (Figure 55). The absence of the peak at 3.25 ppm in the ^1H NMR of the desired product **21** showed also that all of reagent **20** reacted totally.

By integrating the characteristic protons H-3 and H-4 belonging to the phosphonated part of **21** and H-7 of PEG part, the phosphorylation rate could be determined. Indeed, if 100% phosphorylation of the $\text{NH}_2\text{-PEG3K-COOH}$ **20** has been obtained (i.e. there is no more $\text{NH}_2\text{-PEG3K-COOH}$ **20** in the product obtained), it means that the integration of H-3 and H-4 (corresponding to two protons) should be the same as the integration of H-7 (also corresponding to two protons) of PEG. Here, we obtained 100% of PEG phosphorylation (Figure 55) and 100% of yield.

b. SPPS peptides synthesis **1'**, **2'** and **22**

The second step of our strategy was to synthesize the peptides **1'**, **2'** and **22** on solid support SPPS with a Fmoc/tBu strategy and a Rink Amide ChemMatrix (0.47 mmol.g^{-1}) to obtain C-terminal amidated terminus after cleavage step. As previously explained peptide **1'** was acetylated at the N-terminus. In addition, a Lysine with a temporary Boc protection instead of Alloc on the side chain was used here. In this way, this permanent Boc protection would be removed during the cleavage step. The products were obtained with a good purity according to the LC-MS analyses (Table 19).

Peptide name	Sequences	Mass resin engaged (g)	Molecular Weight (g.mol^{-1})	Retention time (min)	Purity after purification %	Yield %	Obtained (mg)
1'	Ac-LRGDNK-NH ₂	1.21	743	0.73	98	32	135
2'	H-GDPGYIGSR-NH ₂	0.94	921	0.81	95	41	167
22	H-AhXRR-NH ₂	2.4	442	0.18	89	48	60

Table 19: Sequences of the peptides **1'**, **2'** and **22**

These peptides were also analyzed by NMR (^1H , ^{13}C , ^{31}P and 2D NMR such $^1\text{H-}^1\text{H}$ COSY, $^{13}\text{C-}^1\text{H}$ HSQC and $^{13}\text{C-}^1\text{H}$ HMBC) to identify especially the $\epsilon\text{-CH}_2$ of the Lysine in peptide **1'** (4.27 ppm), the CH_2 of the Glycine in peptide **2'** (3.86-3.82 ppm) and the CH_2 of the 6-aminohexanoic in peptide **22** (3.0 ppm) for the later PEGylation rate.

c. Functionalization of the primary amine of peptides **1'**, **2'** and **22** with the $\text{PO}_3\text{Et}_2(\text{PEG3K})$ **21** and synthesis of $\text{PO}_3\text{Et}_2(\text{PEG3K})\text{-NET}_2$ **26**

Once the peptides and the $\text{PO}_3\text{Et}_2(\text{PEG3K})$ **21** synthesized, the synthesis of not only the $\text{PO}_3\text{Et}_2\text{CH}_2\text{CH}_2\text{CO-PEG3K-Peptide}$ **23**, **24** and **25** but also the synthesis of $\text{PO}_3\text{Et}_2\text{CH}_2\text{CH}_2\text{CO-PEG3K-NEt}_2$ **26** can be performed as follows (Figure 52). For ease of reference, the resulting products will be named as indicated in Table 20.

Number	Name	Sequence
23	PO ₃ Et ₂ (PEG3K)-RGD	Ac-LRGDNK(PO ₃ Et ₂ CH ₂ CH ₂ CO-PEG3K)-NH ₂
24	PO ₃ Et ₂ (PEG3K)-YIGSR	PO ₃ Et ₂ CH ₂ CH ₂ CO-PEG3K-GDPGYIGSR-NH ₂
25	PO ₃ Et ₂ (PEG3K)-AhXRR	PO ₃ Et ₂ CH ₂ CH ₂ CO-PEG3K-AhXRR-NH ₂
26	PO ₃ Et ₂ (PEG3K)-NEt ₂	PO ₃ Et ₂ CH ₂ CH ₂ CO-PEG3K-NEt ₂
27	PO ₃ H ₂ (PEG3K)-RGD	Ac-LRGDNK(PO ₃ H ₂ CH ₂ CH ₂ CO-PEG3K)-NH ₂
28	PO ₃ H ₂ (PEG3K)-YIGSR	PO ₃ H ₂ CH ₂ CH ₂ CO-PEG3K-GDPGYIGSR-NH ₂
29	PO ₃ H ₂ (PEG3K)-AhXRR	PO ₃ H ₂ CH ₂ CH ₂ CO-PEG3K-AhXRR-NH ₂
30	PO ₃ H ₂ (PEG3K)-NEt ₂	PO ₃ H ₂ CH ₂ CH ₂ CO-PEG3K-NEt ₂

Table 20 : Reference number, name and sequence of compounds obtained during the multi-steps synthesis (Figure 52)

After the carboxylic acid activation of PO₃Et₂(PEG3K) **21** (1eq) with the presence of the DIEA until pH 8-9 and HATU (1eq) the previously synthesized peptides Ac-LRGDNK-NH₂ **1'**, H-GDPGYIGSR-NH₂ **2'** and H-AhXRR-NH₂ **22** or the diethylamine (NEt₂) were added in excess (2eq) dropwise.

The products PO₃Et₂(PEG3K)-RGD **23** and PO₃Et₂(PEG3K)-YIGSR **24** were obtained by precipitation in Et₂O and several washings with acetone to remove the excess of peptides **1'** and **2'** respectively. The visible precipitate was the excess of peptides. The supernatant was so recovered and the solvent was evaporated under vacuum. The product was then obtained by precipitation in Et₂O with 100% of yield (Table 22). The compound PO₃Et₂(PEG3K)-NEt₂ **26** was also obtained by precipitation in Et₂O and the excess of NEt₂ was removed this time with several Et₂O washings. The precipitate was recovered quantitatively (Table 22) and dried in the desiccator.

However, the excess of H-AhXRR-NH₂ peptide **22** was unfortunately not possible to separate from the desired product PO₃Et₂(PEG3K)-AhXRR **25** by simple washing. For this reason, the crude product obtained was purified by preparative HPLC but a very low yield (12%) was obtained. Indeed, the product came out in the injection peak and a lot of amount of the product was lost. We therefore decided to run the reaction with 1.1eq of peptide to minimize the peptide contaminant compared to the desired compound PO₃Et₂(PEG3K)-AhXRR **25**. We assumed here, that the unreacted peptide will always be present in the synthesis of the particles. However, we hypothesized that the small amount of residual H-AhXRR-NH₂ peptide **22** would not interfere with particle synthesis and the stabilizing agent role of the PEG.

The synthesis of these products was followed by many questions. Indeed, at the end of the syntheses it was necessary to make sure that the reagents, namely the peptides or the NEt₂ put in excess, were no longer present or in negligible quantity. It was also important to check if the PO₃Et₂(PEG3K) **21** reagent was still present in the crude product or not. However, the

LC-MS analyses of these new stabilizing agents were complicated by the presence of PEG as said before. NMR analyses were therefore performed but the presence of peptides further complicated the analyses.

In the same way as previously, a heteronuclear ^{13}C - ^1H HMBC analysis was used to observe the correlations between the carbonyl amide formed ($^{13}\text{C}=\text{o}$ PEG3K-peptide in Table 21) and the neighboring protons. The observation of the ^{13}C - ^1H HMBC spectra of the products **23**, **24**, **25** and **26**, showed that the amide carbonyl formed during the coupling reaction correlated with H-11' and H-12' of the PEG on one side and H-13 and H-14 of the NEt_2 or the $\epsilon\text{-CH}_2/\text{CH}_2$ of the peptides on the other side (Figure 56 - Table 21).

Compounds	$^{13}\text{C}=\text{o}$ PEG3K-peptide (ppm)	H-12' protons of PEG (ppm)	H-11' protons of PEG (ppm)	CH_2 protons of peptide or H-13 and H-14 of NEt_2 (ppm)
23	175.9	2.32	1.88	3.20
24	176.7	2.39	1.89	3.93
25	174.1	2.36	1.92	3.22
26	174.6	2.52	1.91	3.39-3.46

Table 21 : ^{13}C - ^1H HMBC NMR Correlation between the $\text{PO}_3\text{Et}_2(\text{PEG3K})$ **21** and the peptides or NEt_2

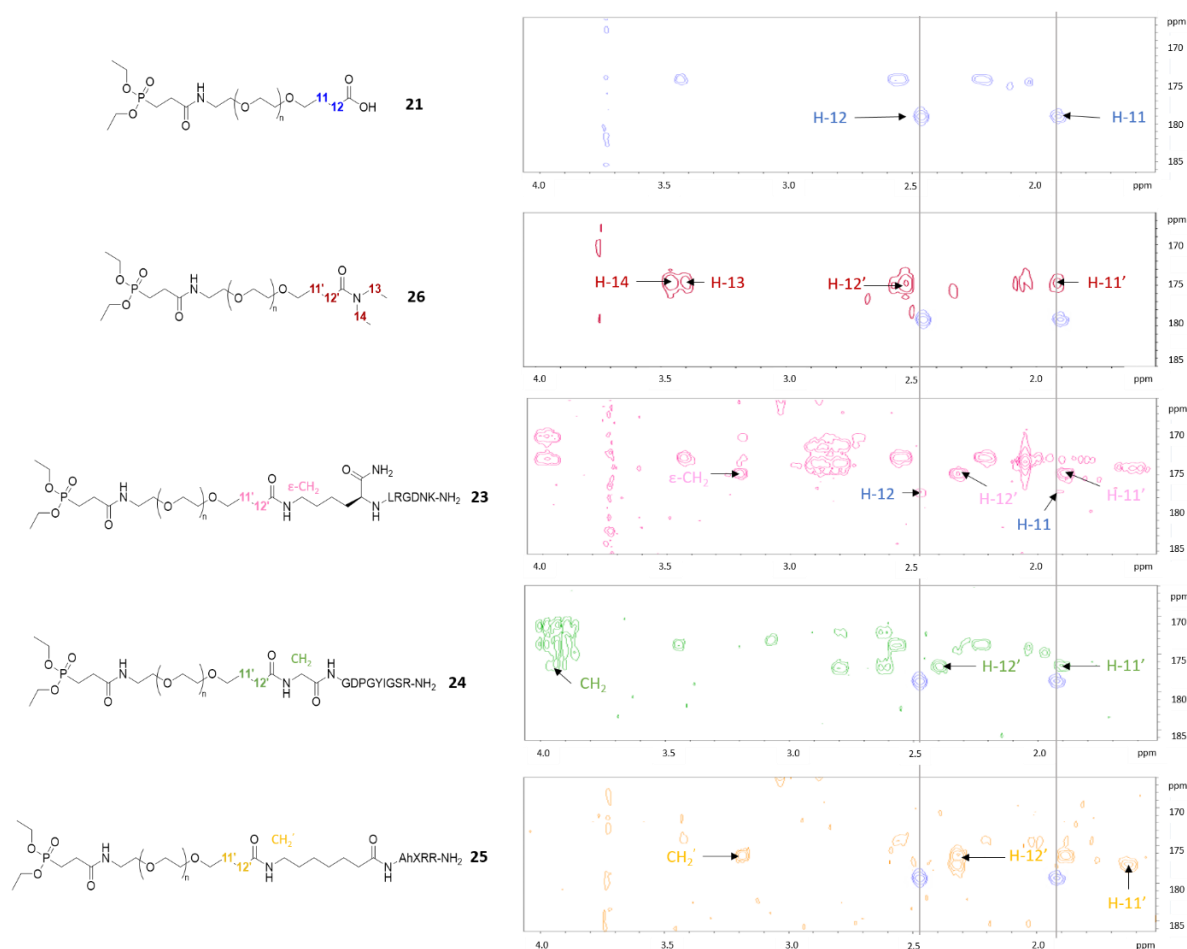


Figure 56 : Observation the amide carbonyl formed during the coupling between peptides or NEt_2 with the carboxylic acid of the $\text{PO}_3\text{Et}_2(\text{PEG3K})$ **21**

Moreover, the ^{13}C - ^1H HMBC allowed us to observe if unreacted $\text{PO}_3\text{Et}_2(\text{PEG3K})$ **21** was still present or not thanks to the visible acid carbonyle (178.7 ppm) which correlates with H-12 (2.47 ppm) and H-11 (1.92 ppm) of the PEG (Figure 56). Only in the case of $\text{PO}_3\text{Et}_2(\text{PEG3K})$ -RGD **23**, the heteronuclear NMR analysis above showed the presence of unreacted $\text{PO}_3\text{Et}_2(\text{PEG3K})$ **21**.

However, the analyses of ^{13}C - ^1H HMBC NMR did not allow us to conclude if a free peptide or NEt_2 form also co-exist in the product especially for the peptide H-AhXRR- NH_2 **22** because it was added in slight excess and impossible to remove with washings. To reach this information, H-11' and H-12' of the PEG (Table 21) were integrated as a reference for each compound. Then, characteristic protons of the peptides (0.88-0.93 ppm – CH_3 of the leucine for peptide **1'**, 7.13 ppm – aromatic proton of the tyrosine for **2'**, 1.14 ppm – CH_3 of the NEt_2) were integrated on the ^1H NMR. The ratio of the integration between the reference and the characteristic protons of the peptides gave the PEGylation rate (Table 22). Unfortunately, it was not possible to identify a well isolated peak from peptide H-AhXRR- NH_2 **19** and so not possible to calculate this ratio.

Compounds	n_{engaged} (mmol)	MW (g.mol $^{-1}$)	PEGylation rate %	m_{obtained} (mg)	Yield %
23	0.063	3888	96	245	100
24	0.12	4065	100	488	100
25	0.06	3570	82	214	100
26	0.06	3570	82	492	100

Table 22 : PEGylation rate, yield and masse obtained of compounds **23**, **24**, **25** and **26**

d. Dealkylation of the $\text{PO}_3\text{Et}_2(\text{PEG3K})$ -Peptide **23**, **24**, **25** and $\text{PO}_3\text{Et}_2(\text{PEG3K})$ - NEt_2 **26**

Finally, the diethylphosphonate was totally deprotected by using the McKenna reaction under argon. Compounds **23**, **24**, **25** and **26** (0.05 mmol) were solubilized in dry DCM before adding the TMSBr (8eq). The reaction was followed by liquid-state ^{31}P NMR which allowed us to distinguish the diethylphosphonate (31.26 ppm) from the phosphonic acid (29.47 ppm - Figure 57) after methanolysis. Indeed, after precipitation of ~1mL of the reaction solution in diethylether (Et_2O), a bis(trimethylsilyl) ester form of the crude product was obtained which requires a methanol treatment before NMR analysis. After 4 hours of reaction, ^{31}P NMR analyses showed no change (Figure 57). For this reason, 20eq of TMSBr was added to the solution. Two hours after this addition, fully deprotected (29.47 ppm) and mono ethyl phosphonate species (30.88 ppm) were observed. 30eq were therefore added again to push the reaction to the desired form. After one night of reaction, the dealkylation was complete.

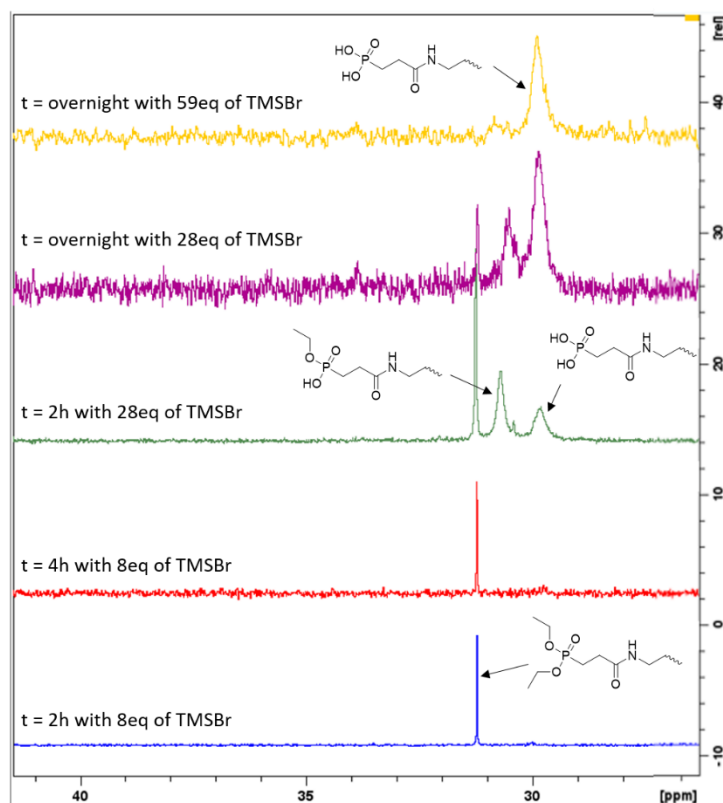


Figure 57 : Evolution of the dialkylphosphonate with McKenna reaction

Thanks to this study, we decided to run the subsequent deprotections using directly 59 eq of TMSBr overnight. At the end, the solution was concentrated and the trimethyl silyl form of the crude compounds were recovered after Et₂O precipitation. The bis(trimethylsilyl) ester formed was removed thanks to several MeOH washings. The final compounds were precipitated with the Et₂O and the oil were obtained quantitatively.

4. Conclusion

In conclusion, the synthesis of P(PEG3K)-Peptide **27**, **28** and **29** on solid support was unsuccessful. Therefore, a multi-step synthesis was developed and the desired products **27**, **28** and **29** supposed to act as new peptide-based stabilizing agents for the one-pot synthesis of peptide decorated hybrid apatite NPs were obtained in sufficient quantity. Furthermore, the reference stabilizing agent P(PEG3K)-NEt₂ **30** was also obtained. The synthesis of hybrid NPs decorated with these new stabilizing agents is described in the following.

B. Synthesis of apatite particles surrounded with a mixture of P(PEG3K)-Peptide **27**, **28**, **29** and P(PEG3K)-NEt₂ **30**

In order to synthesize colloidal apatite NPs surrounded by an organic corona of P(PEG3K)-Peptide **27**, **28** and **29**, a co-precipitation synthesis described in part I.B was carried out. The

underlying idea was thus to directly precipitate the apatite phase *in the presence of* the P(PEG3K)-Peptide in view of *in situ* stabilization. We hypothesized that adding a small moiety to the end of PEGylated chain would not disturb the role of the PEG described in previous studies.^{43,119} In order to obtain here a colloidal suspension with the P(PEG3K)-Peptide as stabilizing agent and to observe its influence on the apatite structure, state of crystallinity and particles size, a co-adsorption study was performed with various starting proportions of the two stabilizing agents P(PEG3K)-NEt₂ and P(PEG3K)-Peptide. The same overall molar quantity of stabilizing agent was divided in the following ratios 100/0, 75/25, 50/50, 25/75 and 0/100 between P(PEG3K)-NEt₂ and P(PEG3K)-Peptide.

At the stage of the protocol development (proof of concept) intended in this PhD work, and in order to valorize as much as possible the prepared organic moieties, the final volume of colloidal suspension and the molar quantity were reduced and divided by 4 to obtain finally 6.375 mL of NPs suspension. For comparative assessments, a non-colloidal apatite sample was also prepared in this study, by following exactly the same procedure as above but in the absence of stabilizing agent. This series of materials will help us to (i) assess the influence of the P(PEG3K)-peptide on the composition, shape, size, crystallinity, (ii) to study the possibility to combine different types of phosphonated organic molecules in a single step around the apatite surface and in the perspective of biological assays, (iii) to vary the number of bioactive peptides in a sample while keeping the same number of particles, and vice versa.

1. Optimization of R-PO₃H₂/Ca ratio

a. Co-precipitation synthesis of the NPs with different R-PO₃H₂/Ca ratios

Before starting the synthesis of NPs with the stabilizing agents P(PEG3K)-Peptide **27**, **28** and **29**, it was important to check the role of the initial R-PO₃H₂/Ca ratio in the medium, and to determine the most appropriate value for the next experiments. As a reminder, the ratio R-PO₃H₂/Ca allows determining the quantity of stabilizing agent used during the synthesis (see part I.B). An insufficient amount of stabilizing agent may prevent the obtainment of a colloidal suspension while too much would be useless if the particles have reached their maximum adsorbed amount. Moreover, this ratio can have an impact of the apatite particles (size, structure, crystallinity state, grafting density...). As a large amount of product was needed to perform these experiments, the stabilizing agent P(PEG3K)-NEt₂ **30** was used as a model. Nanoparticles with different R-PO₃H₂/Ca ratios (0.005, 0.008, 0.01, 0.016, 0.032, 0.128) were synthesized (NPs 12 to 17) and purified by dialysis following the protocols described previously (part I.B).

b. Results and characterizations of apatite particles synthesized with several R-PO₃H₂/Ca ratios

Observations of the suspensions obtained after maturation

As expected according to the previous study performed in the CIRIMAT, a colloidal suspension was obtained for the R-PO₃H₂/Ca ratio equal to 0.016.⁴⁴ The first observations after the maturation time showed homogeneous, translucent suspensions with no sedimentation, characteristic of stable colloidal suspensions whatever the R-PO₃H₂/Ca ratio tested (Figure 58).



Figure 58 : Picture of colloidal suspensions obtained for different R-PO₃H₂/Ca starting ratios: (0.005, 0.008, 0.01, 0.016, 0.032, 0.128) giving rise to NPs 12 to 17

To choose a value of the ratio well suited for the next experiments with P(PEG3K)-Peptide, it was important to perform some characterizations to understand the impact of the ratio R-PO₃H₂/Ca on the obtained particles. As the stabilizing agent P(PEG3K)-OCH₃ was shown in a previous study to exhibit a slight role of crystallization inhibitor for apatite⁴⁴, it is very likely that a high ratio of R-PO₃H₂/Ca could give weakly crystallized apatite particles. In contrast, the agglomeration of the NPs was probably less hindered by a low ratio, thus probably inducing higher particle sizes potentially beyond the nanometric scale. Moreover, a low R-PO₃H₂/Ca ratio would probably lead to a lower grafting rate, which could be a limitation for future biological tests.

We recall here that the proof of concept that we wanted to demonstrate in this PhD project was to obtain (by one-pot synthesis) colloidal suspensions composed of biomimetic apatite particles close to bone mineral and of nanometric size thanks to the use of peptide-based stabilizing agents. Several physicochemical characterizations were thus carried out to validate our hypotheses and are reported in the following. In particular, XRD was carried out to get information on the structure and state of crystallinity of the particles. TEM and DLS were run to assess the size and shape of the particles. Finally, ³¹P ERETIC liquid-state NMR was performed to determine the concentration of stabilizing agents P(PEG3K)-NEt₂ **30** in the colloidal suspensions and consequently the corresponding grafting rate and the conformation of the stabilizing agent around the apatite surface using the Flory's equations.

XRD analyses of NPs 12 to 17

XRD analyses of the prepared hybrid NPs 12 to 17 clearly showed the identifiable crystallographic signature of an apatitic phase by comparison with the biomimetic apatite reference described in chapter I (Figure 59). However, a decrease in crystallinity could be observed (less resolved peaks) as the R-PO₃H₂/Ca ratio increased. For high values of R-PO₃H₂/Ca, illustrated here by the point at R-PO₃H₂/Ca = 0.128, the apatitic crystallographic signature became barely visible, suggesting a compound close to amorphous. For lower values of R-PO₃H₂/Ca, typical apatite features can on the contrary be distinctly identified, showing the crystal growth inhibiting role of the stabilizing agent. Furthermore, the presence of additional peak(s) at least at $2\theta \approx 23^\circ$ was also visible and with an increasing intensity as the the R-PO₃H₂/Ca ratio increased, which can be attributed to the organic component according to M.Choimet *et al.*⁴⁴ Indeed, as PEG chains are lengthy, some degree of organization can occur among the adjacent lateral chains, thus leading to some 3D ordering in the dry state and to contributions to the XRD pattern.

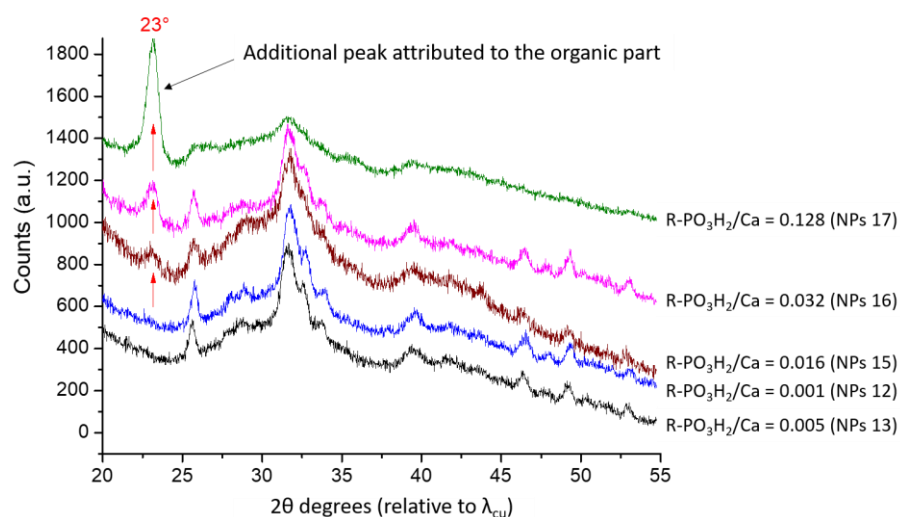


Figure 59 : XRD patterns of NPs 12-17 (the NPs 14 sample was not analyzed due to too little product remaining)

These XRD analyses showed that the amount of P(PEG3K)-NEt₂ **30** involved in the synthesis of the particles had an influence on the crystallinity state of the apatite. To obtain apatite particles close to the bone mineral, thus weakly crystallized, the R-PO₃H₂/Ca ratios between 0.005 and 0.032 have been retained. The highest ratio of 0.128 was too high and led to a CaP compound of too low crystallinity to be further used here.

DLS analyses of NPs 12 to 17

DLS results showed that the particle size was strongly impacted by the starting R-PO₃H₂/Ca ratio, ranging from 391 ± 7 nm for a ratio equal to 0.005 down to 126 ± 4 nm for the highest

ratio tested at 0.128. The lower the amount of stabilizing agent used in the synthesis, the larger the particle size (Table 23), which may be expected from a lower degree of stabilization by steric hindrance of the PEG moiety. Moreover, within colloidal suspensions, the particles size could be considered as rather homogeneous, with polydispersity indices ranged between 0.23 and 0.32, allowing us to consider the obtainment of a monomodal distribution.

Theoretical		DLS			TEM	
Id	R-PO ₃ H ₂ /Ca	Size (nm)	Pdl	Zeta Potential pH 7,2 (mV)	I _{NP} (nm)	L _{NP} (nm)
NPs12	0.001	346±7	0.27	7.2	35	153
NPs13	0.005	391±4	0.28	4.8	52	151
NPs14	0.008	388±6	0.23	4.0	24	176
NPs15	0.016	167±5	0.24	1.7	25	117
NPs16	0.032	147±2	0.25	1.9	27	108
NPs17	0.128	126±4	0.32	1.6	59	70

Table 23 DLS and TEM characterizations of hybrid P(PEG3K)-NEt₂ **30**/apatite NPs 12-17 with different R-PO₃H₂/Ca

These results proved that the amount of P(PEG3K)-NEt₂ **30** involved in the medium during apatite precipitation noticeably influences the particle size. The stabilizing agent P(PEG3K)-NEt₂ **30** was thus shown to prevent/control, as expected, the degree of agglomeration of the NPs (most likely by steric hindrance taking in consideration the length of the PEG chain). We hypothesized that the lower the quantity of P(PEG3K)-NEt₂ **30** involved in the synthesis, the lower the number of stabilizing agents around the particle, thus inducing an increase in the size of the nanoparticles because the steric hindrance was minimized. These first DLS analyses thus allowed us to highlight the influence of P(PEG3K)-NEt₂ **30**, acting as stabilizing agent, on the particles size, although DLS likely overestimated the particle dimensions (i.e. measurement of the hydrodynamic diameter, and hypothesis on the spherical shape of the particles as explained in part II.C.2.d). In order to obtain more accurate information on the actual shape and size of the particles, TEM imaging was performed.

TEM imaging of NPs 12 to 17

In view of TEM observations, a drop of colloidal suspension was placed on a TEM grid. Once the drop was dried, the particles were observed. Unfortunately, without any dilution of the colloidal suspension before placing drop on the TEM grid, it was impossible to observe individual particles because of the large number of particles and the potentially additional agglomeration of the particles due to the sample preparation/drying (Figure 60). With a 100-fold dilution, the individual particles could be observed, showing a homogeneous size and rod-shape on all samples.

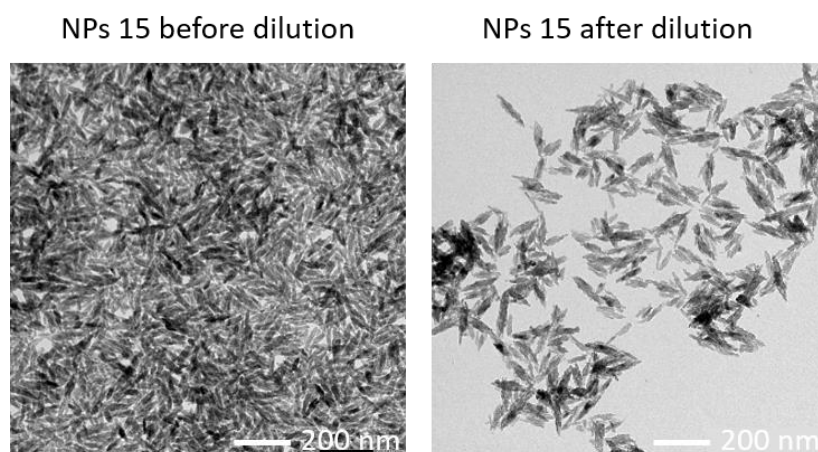


Figure 60: TEM imaging of NPs 15 before and after the dilution

Moreover, the order of magnitude of the particle size confirmed the DLS measurements. From TEM images, the particle size was observed to vary from 153 nm in length / 35 nm in width for a ratio of 0.001, to 70 nm in length / 59 nm in width for a ratio equal to 0.128 (Table 23). These analyses confirmed that nanometric size particles were obtained and that their size could be controlled by the amount of stabilizing agent used in the synthesis. This may prove particularly helpful for the future design of biomedical applications depending on the clinical needs. A deeper analysis of the TEM images indicated that the NPs were polycrystalline aggregates composed of several nanometric size crystallites, as may be seen in Figure 61. Unfortunately, the quality of the TEM images did not allow us to directly measure the crystallites size.

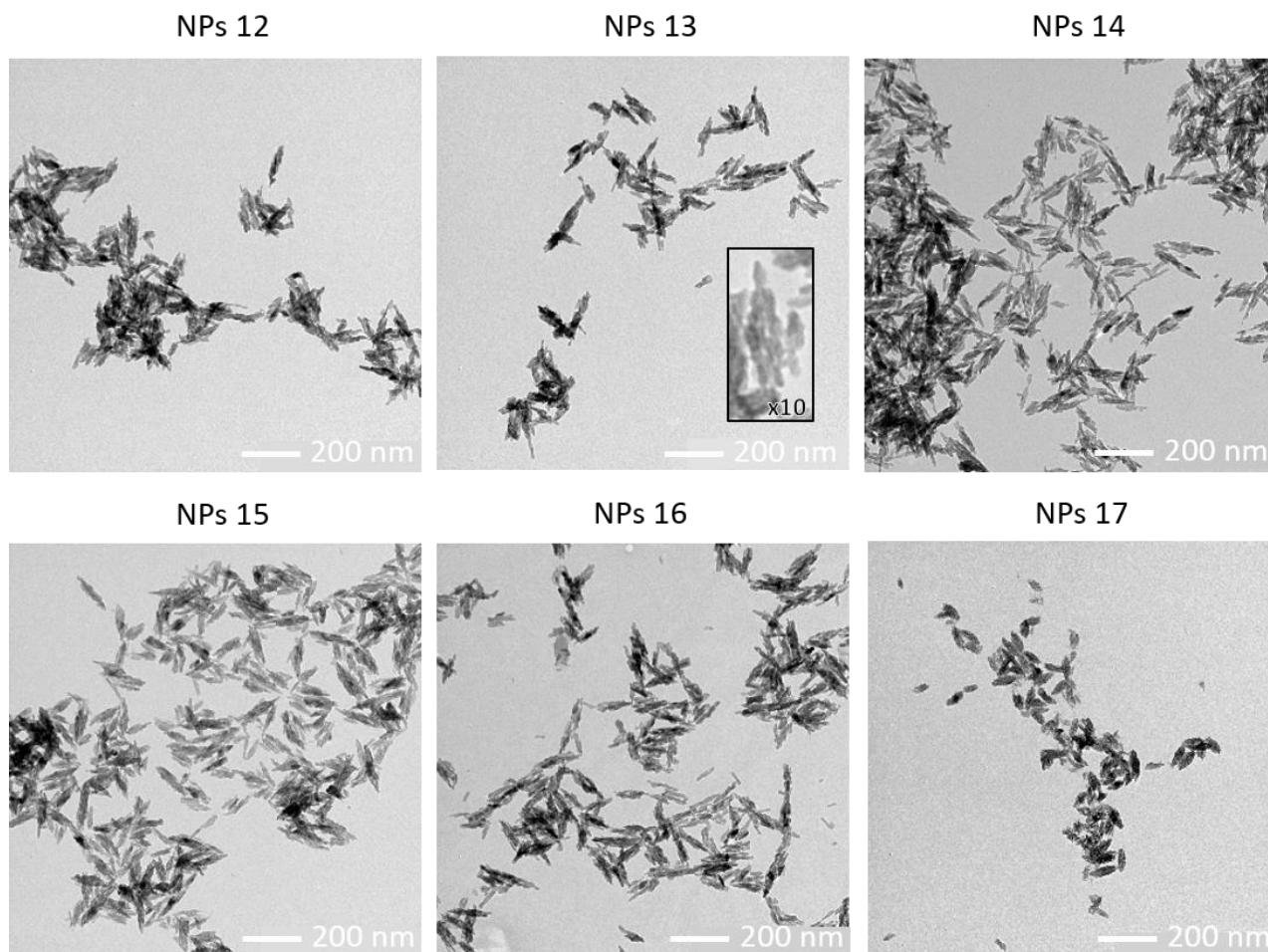


Figure 61 : TEM imaging of the P(PEG3K)-NEt₂ **30**/apatite NPs 12-17 prepared with different R-PO₃H₂/Ca ratios

Determination of the concentrations of the P(PEG3K)-NEt₂ **30** grafted around the NPs 12-17 during the synthesis

To know the exact concentration of P(PEG3K)-NEt₂ **30** grafted around the NPs 12-17, liquid-state NMR analyses were performed. The ERETIC NMR method was again used here. As previously, ³¹P ERETIC NMR allowed us to dissociate the apatitic (inorganic) phosphates (~0 ppm) from the organic phosphonates belonging to the stabilizing agents P(PEG3K)-NEt₂ **30** (~25-26 ppm). In order to obtain an accurate concentration of grafted P(PEG3K)-NEt₂ **30** stabilizing agent, a calibration curve with phosphoric acid was performed as previously, in the range 0.1 - 100 mM to correlate the area under the peak and the phosphorus concentration. Once the calibration curve was established, the sample including the dissolved NPs of unknown concentration was run in ³¹P NMR under the same conditions to get the exact concentrations of the P(PEG3K)-NEt₂ **30** grafted around the NPs during the synthesis.

To prepare a NMR tube, 1 mL of colloidal suspension was centrifuged to ensure removal of any molecules that might have been released or remained even after purification by dialysis.

The supernatant was removed and the still wet powder was washed with water several times and freeze-dried. The amount of dry powder obtained was weighed thoroughly ($\sim 70 \pm 10$ mg). To release the grafted organic molecules, the NPs were dissolved with 100 μ L of 1M hydrochloric acid (HCl). Finally, 500 μ L of deuterated water (D_2O) was added and the whole solution was introduced in the NMR tube.

As expected, the concentration (mM) of P(PEG3K)-NEt₂ **30** grafted around the NPs 12-17 increased when the R-PO₃H₂/Ca ratio increased as well (Table 24).

Id	R-PO ₃ H ₂ /Ca	n ₃₀ (mM)	Grafting density (30/nm ²)	Rf/D	Conformational regime
NPs12	0.001	0.98	0.02	0.55	Intermediate
NPs13	0.005	2.19	0.07	1.07	Brush
NPs14	0.008	2.27	0.13	1.43	Brush
NPs15	0.016	2.76	0.23	1.90	Brush
NPs16	0.032	5.11	4.97	8.91	Brush
NPs17	0.128	6.68	7.64	9.45	Brush

Table 24 : ³¹P ERETIC NMR characterizations of P(PEG3K)-NEt₂ **30**/apatite hybrid NPs obtained with different R-PO₃H₂/Ca ratios

Calculation of grafting density from liquid-state NMR analyses of NPs 12-17

To determine the grafting density, *i.e.* the number of P(PEG3K)-NEt₂ **30** grafted to the surface of an apatite NP, it was necessary to first calculate the surface of one NP. The calculation to determine the grafting density was described in the following thanks to the example of the NPs 15, corresponding to the R-PO₃H₂/Ca ratio equal to 0.016.

Knowing the size, and thus the volume of a particle, its density ($d = 3.1 \text{ g.mL}^{-1}$), and the mass of NPs recovered in 1mL of colloidal suspension after freeze-drying ($m(\text{NPs}) = 60 \text{ mg}$), the number of particles can be determined. We considered here that the rod shape of the particle seen in TEM was comparable to a cylinder whose height would correspond to the length (L_{NP}) and the diameter to the width (l_{NP}) of the NPs.

$$V(\text{NP}) = \pi \times L \times l = 200\,000 \text{ nm}^3 = 2.2 \times 10^{-16} \text{ cm}^3$$

Equation 1 : Determination of the volume of NPs cylinder NPs 15 with a R-PO₃H₂/Ca equal to 0.016 (Table 23)

$$\text{Nb}(\text{NP}) = \frac{m(\text{NP})}{V(\text{NP}) \times d} = 8.45 \times 10^{13} \text{ particles}$$

Equation 2 : Determination of the number of NPs obtained in 1mL of colloidal suspension NPs 15

In addition, the number of stabilizing agent molecules P(PEG3K)-NEt₂ **30** present in 1 mL of a colloidal suspension was determined from the ³¹P ERETIC NMR analyses (Table 24).

$$\text{Nb}(\mathbf{30}) = n(\mathbf{30}) \times N_A = 2.76 \cdot 10^{-7} \times 6,02 \cdot 10^{23} = 1.66 \times 10^{24} \text{ of } \mathbf{30}$$

*Equation 3 : Determination of the number of stabilizing agents P(PEG3K)-NEt₂ **30** in 1mL of colloidal suspension (Table 23)*

Knowing the number of NPs present in 1 mL of colloidal suspension and considering a cylindrical shape of the NPs, we can determine the surface corresponding:

$$S(\text{NP}) = \text{Nb}(\text{NP}) \times \left(\pi \times \frac{l^2}{2} + \pi \times L \times l \right) = 7.38 \times 10^{18} \text{ nm}^2$$

Equation 4 : Determination of the surface of a cylindrical NPs 15 with r the radius of the particle obtained by TEM (Table 23)

Finally, the grafting density could be obtained (Table 23):

$$\text{Nb} \left(\frac{\mathbf{30}}{\text{nm}^2} \right) = \frac{\text{Nb}(\mathbf{30})}{S(\text{NP})} = 0.23 \text{ of compound } \mathbf{30}/\text{nm}^2$$

*Equation 5 : Determination of the number of P(PEG3K)-NEt₂ **30** per nm² on NPs 15*

In the case of NPs 15, we can conclude that 0.23 stabilizing agent P(PEG3K)-NEt₂ **30** was grafted per nm². The same calculations were performed the NPs 12 to 17 (Table 23) and the evolution of the grafting density as a function of the R-PO₃H₂/Ca ratio was drawn in Figure 62.

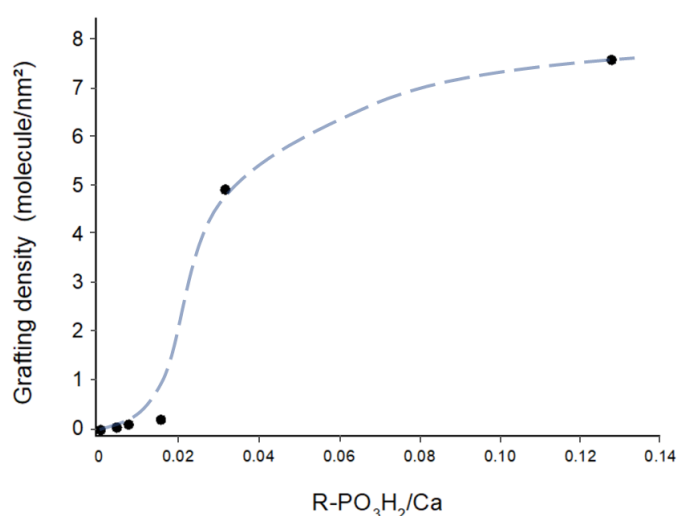


Figure 62 : Curve representing the grafting density as a function of the R-PO₃H₂/Ca ratio

The results obtained show that the grafting density of the P(PEG3K)-NEt₂ **30** around the apatite surface increased as the R-PO₃H₂/Ca ratio increased. Although there is a clear tendency to ultimately reach a stabilized value, no actual plateau was obtained in the range studied, showing that the adsorption maximum was not fully reached. We assumed that during the synthesis, the hybrid NPs were formed in order to graft a maximum of P(PEG3K)-NEt₂ **30** around it. So, the surface area of the material increased as the R-PO₃H₂/Ca ratio increased, leading to a diminution of the size of the particles as evidenced by DLS and TEM (Table 23).

Combined with Flory's equation¹²⁰, the conformation of the organic molecules P(PEG3K)-NEt₂ **30** around the NPs could be determined. Depending on the grafting density and the length the grafted molecules, P(PEG3K)-NEt₂ **30** may either "align" close to each other in "brush" or comb-like conformation or instead crumble at the surface, forming mushroom-like structures inducing lower grafting densities (Figure 63). According to Adumeau *et al.*¹²⁰, PEG conformation on the surface of NPs can be deduced from the Rf/D ratio, where D is the average distance between two anchoring points and Rf is Flory's radius that roughly corresponds to the space that the PEG chain may occupy. D and Rf can be calculated from the equations below:

$$D = 2(\pi\sigma)^{-\frac{1}{2}}$$

Where σ is the surface grafting density (molecules/nm²) determined here by ERETIC ³¹P NMR analysis (Table 23)

$$Rf = \alpha N^{\frac{3}{5}}$$

Where α is the effective monomer length = 0.358 nm for PEG and N is the degree of polymerization (~68), which is deduced from the PEG length.

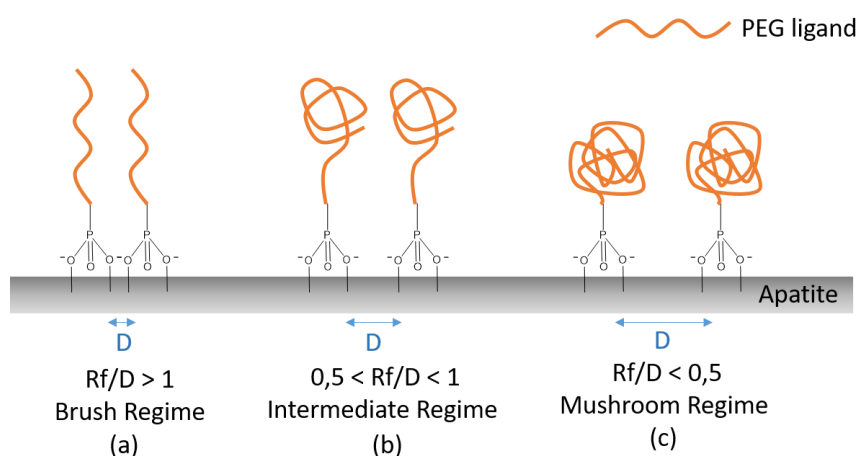


Figure 63 : Conformation of organic molecule around a particle thanks to Flory's equation

Results obtained by applying Flory's equation (Table 24) indicate that the R_f/D ratio was systematically greater than 1 (except for the lower $R\text{-PO}_3\text{H}_2/\text{Ca}$ ratio NPs 12), thus indicating that the grafted organic molecules had a brush conformation. The brush regime means that PEG chains are lengthy and that some degree of organization can occur among the adjacent lateral chains, thus leading to some 3D ordering in the dry state which confirms our hypothesis about the presence of the peak at 23° on XRD diffractogram (Figure 59). Moreover, these results are very promising for the upcoming experiments and biomedical uses. Indeed, considering that the peptides at the end of the PEG chain would not disrupt its role as a stabilizing agent, we can expect that the new P(PEG3K)-peptide **27**, **28** and **29** stabilizing agents would also be in brush conformation. The peptides would be well exposed to facilitate the interaction with the external environment.

c. Conclusion

In conclusion, the ratio $R\text{-PO}_3\text{H}_2/\text{Ca}$ equal to 0.016 seemed to be a good compromise to obtain nanosized particles, a biomimetic apatite close to the bone mineral and a grafting density sufficiently important in view of further analyses and biological experiments. Moreover, the brush regime obtained was a good sign, because we could expect similar results with the novel bioactive stabilizing agent P(PEG3K)-Peptide, so as to provide well-exposed peptidic moieties for facilitated interactions with cells/tissues/outer environments. Therefore, this ratio was chosen for the rest of the experiments.

2. Synthesis of apatite nanoparticles surrounded with P(PEG3K)- NEt_2 **30** and P(PEG3K)-Peptide **27**, **28** and **29**

As explained before, the stabilizing agent P(PEG3K)- NEt_2 **30** exerted a stabilizing effect by steric hindrance to limit the agglomeration of apatite NPs and stabilize them in colloidal suspension. As explained before, we therefore considered that adding a peptide whose molecular weight did not exceed 1 kDa (<30 nm of length) at the end of a long ~63 mer PEGylated chain (~206 nm) would not disturb the stabilizing agent effect of P(PEG3K)- NEt_2 **30**. Moreover, various ratio of P(PEG3K)-Peptide **27**, **28** and **29** and P(PEG3K)- NEt_2 **30** were tested (100/0, 25/75, 50/50 and 75/25) in order to observe the influence of the P(PEG3K)-Peptide and to test the co-administration of the two molecules. Finally, the same co-precipitation synthesis described before was used with a $R\text{-PO}_3\text{H}_2/\text{Ca}$ fixed to 0.016 (Figure 64).

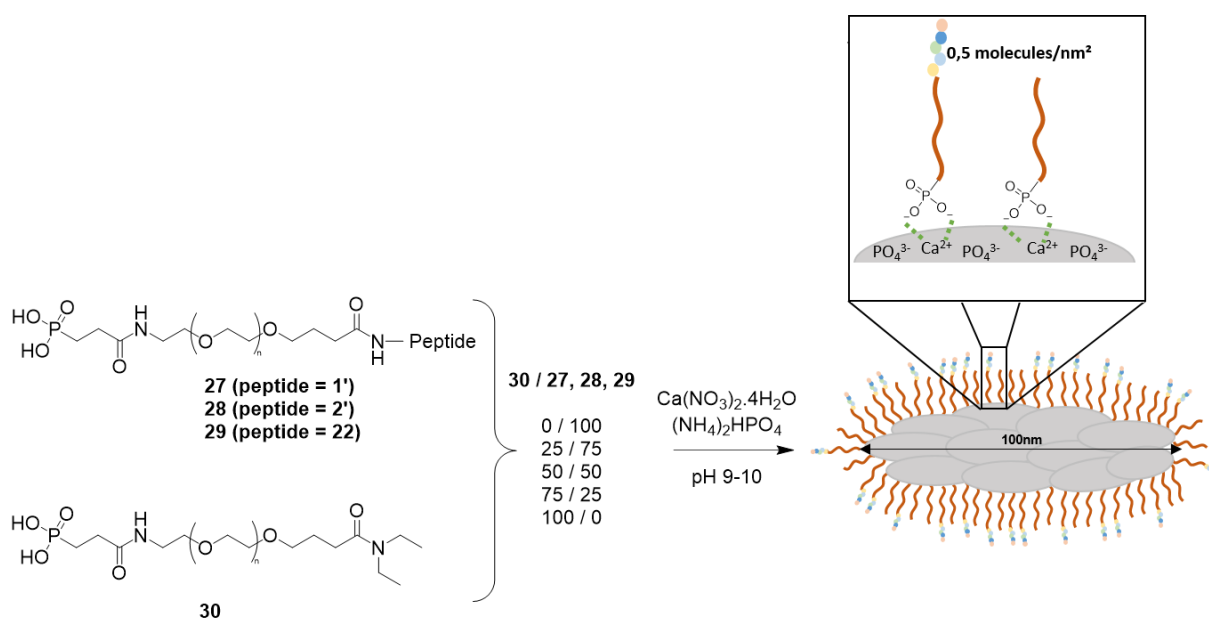


Figure 64 : Synthesis of colloidal NPs of apatite stabilized with P(PEG3K)-Peptide **27**, **28**, **29** and P(PEG3K)-NEt₂ **30**

3. Results and characterization of apatite particles surrounded with a mixture of P(PEG3K)-NEt₂ **30** and P(PEG3K)-Peptide **27**, **28**, **29**

a. Observations of the apatite particles obtained after the maturation time

Whatever the peptides studied and the ratio between P(PEG3K)-Peptide **27**, **28**, **29** and P(PEG3K)-NEt₂ **30**, a homogeneous, close-to-transparent suspension characteristic of a stable colloidal suspension was obtained, whereas without stabilizing agent a white precipitate was clearly sedimented at the bottom of the flask. Upon first observations and comparing with NPs 15 stabilized with P(PEG3K)-NEt₂ only and the same R-PO₃H₂/Ca ratio (i.e 0.016), we were able to confirm that the peptide added at the end of PEGylated chain had no deleterious influence on the stabilizing properties offered by the PEG3K chain due to the steric hindrance. Thanks to these first observations, the proof of concept of stabilizing apatite NPs with peptide-based stabilizing agents was validated.

We have previously seen that apatite NPs 15 surrounded with P(PEG3K)-NEt₂ **30** with a ratio R-PO₃H₂/Ca equal to 0.016 gave biomimetic apatite NPs with a low degree of crystallinity. For this reason, XRD and FTIR analyses were performed to observe the influence of P(PEG3K)-Peptide on the structure of the NPs and its crystallinity state.

Moreover, our proof of concept also consisted in obtaining particles of controlled nanometric sizes in the presence of a peptide-based stabilizing agent. DLS and TEM analyses were thus also performed to determine the size, size distribution and shape of the colloidal NPs obtained, and also to observe the influence of the P(PEG3K)-Peptide **27**, **28** and **29** on the latter. In addition, TEM analyses performed on the previous NPs stabilized with only P(PEG3K)-

NEt₂ showed the polycrystalline character of the obtained apatite NPs (Figure 61). TEM images and XRD analyses will thus also be carried out to investigate the polycrystalline character of the NPs as well as the size of the crystallites composing them.

In view of biological tests on these new bioactive hybrid apatite NPs, it was finally important to determine the grafting density of the NPs. For this purpose, as previously, liquid-state NMR analyses were carried out and in particular ³¹P ERETIC NMR. The concentration of P(PEG3K)-Peptide grafted to the colloidal NPs in suspension was indeed an important information for the realization and interpretation of the biological tests. This concentration was determined by combining ³¹P ERETIC NMR spectra with quantitative ¹H NMR. From the grafting density, the conformation of the stabilizing agents around the NPs was determined using Flory's equations. Finally, solid-state NMR analyses were carried out for further examine the type of grafting and demonstrate the role of the phosphonate end-group.

b. XRD analyses

First, the apatite NPs surrounded with a mixture of P(PEG3K)-NEt₂ **30** and P(PEG3K)-RGD **27** (NPs 18 to 21) were analyzed by XRD in order to determine the structure and crystallinity state of the obtained NPs, and to follow the effect of an increase of the relative proportions between the two molecules (Figure 65). These results were compared with the NPs 15 obtained previously with P(PEG3K)-NEt₂ **30** as stabilizing agent and a R-PO₃H₂/Ca ratio equal to 0.016 (Figure 59).

According to the XRD patterns (Figure 65), P(PEG3K)-Peptide did not seem to strongly modify the crystallographic characteristics of the apatite phase, as only a minor decrease in crystallinity could be detected.

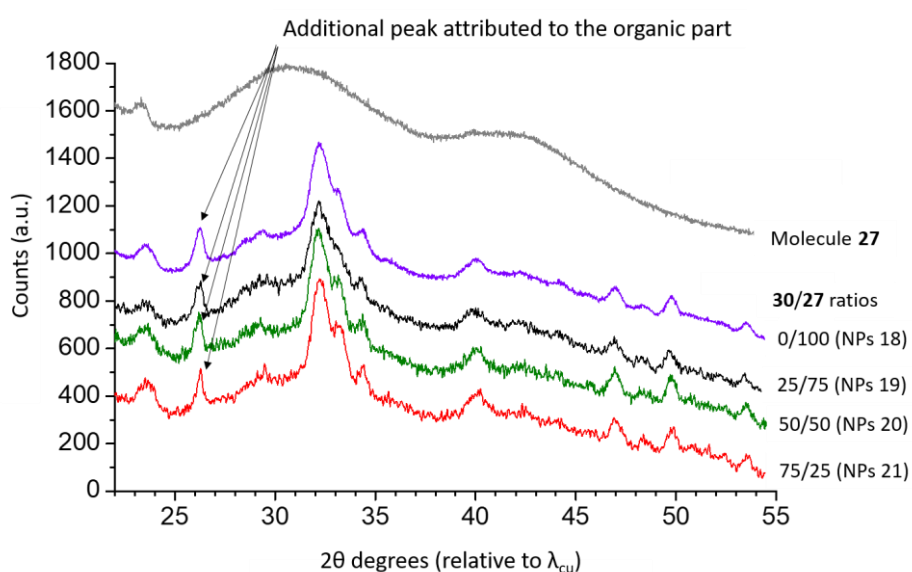


Figure 65 : X-Ray Diffraction pattern of NPs functionalized with different ratios of P(PEG3K)-NEt₂ **30**/P(PEG3K)-RGD **27**

However, as previously, the organic component of the NPs – most likely the long PEG chains – created contributed to the XRD pattern typically around $2\theta \approx 23^\circ$. Also, the support of the diffractometer generated an amorphous background (in link with the limited amount of sample to be analyzed), thus preventing a good observation of the structural features of the apatitic core of the NPs (grey curve, Figure 65). Therefore, the background of the organic/support was eliminated on the two samples with the highest amount of P(PEG3K)-Peptide (NPs 18 and 19) so as to better highlight the underlying apatite phase. The apatitic phases obtained for these two samples were then clearly visible, and led to very similar overall diagrams. They were characteristic of a rather well crystallized apatite phase (Figure 66 a and b).

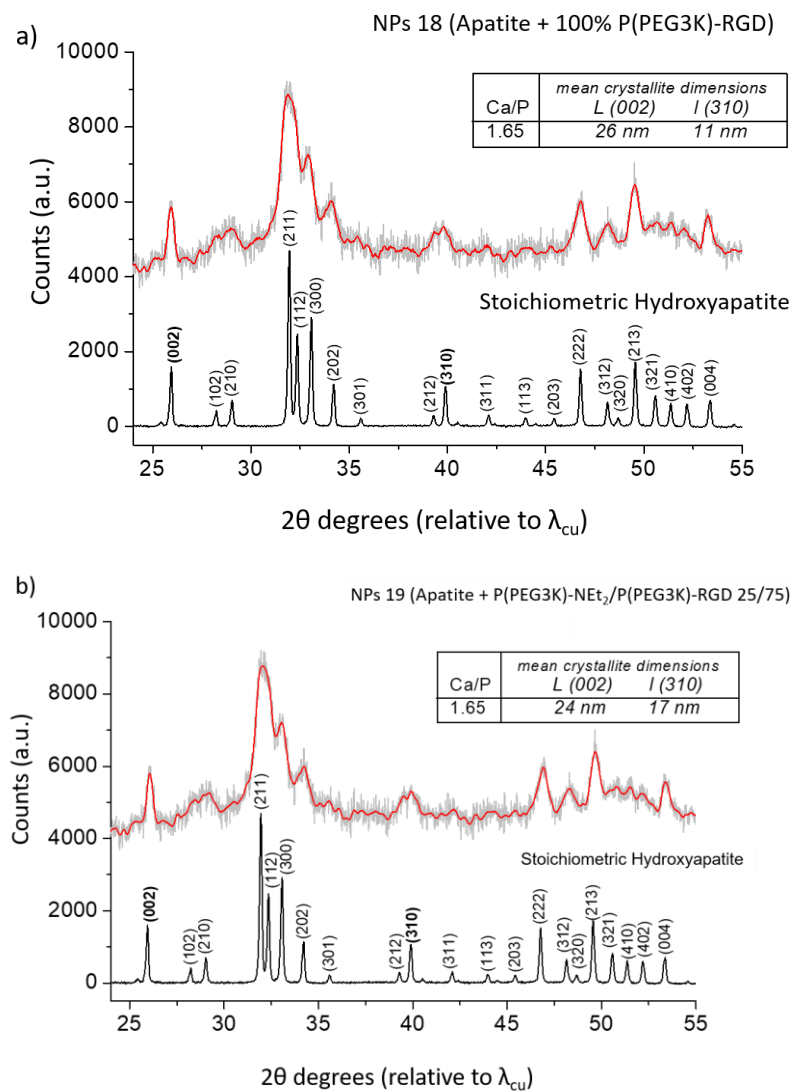


Figure 66 : XRD patterns of NPs surrounded with a mixture of P(PEG3K)-NEt₂ **30**/P(PEG3K)-RGD **27** – a) 0/100 - NPs 18 and b) 25/75 – NPs 19). The tabulated data report the mean crystallite dimensions as drawn from Scherrer's equation as well as the Ca/P ratio estimated from heating the samples at 1000°C for 15 h

Application of Scherrer's equation (described in chapter 1) to the lines (002) and (310) allowed us to estimate the average length (along the c-axis of the crystal structure) and the

width/depth of the crystallites (in perpendicular directions) composing the apatitic phases contained in both samples. The calculated values (Figure 66), $L(002) \approx 24\text{-}26\text{ nm}$ and $l(310) \approx 11\text{-}17\text{ nm}$ confirmed the nanometric dimensions of these compounds. Moreover, a second analysis after calcination in air at $1\ 000^\circ\text{C}$ for 15 hours, according to ISO 13779-3 standard, allowed to estimate the Ca/P molar ratio by confronting the HA/TCP (tricalcium phosphate) proportions obtained to a calibration curve obtained with known HA/TCP mechanical mixtures. The Ca/P value reached was close to 1.65, thus slightly lower than 1.67 characteristic of a stoichiometric HA, thus highlighting a slight under-stoichiometry of the apatite phase composing our NPs.

The same analyses were performed on the NPs functionalized with the two others P(PEG3K)-YIGSR-NH₂ **28** and P(PEG3K)-AhXRR **29** (Figure 67 and Figure 68). The same conclusions could be drawn from these analyses showing that the nature of the peptide did not have a significant influence on the structure of the NPs.

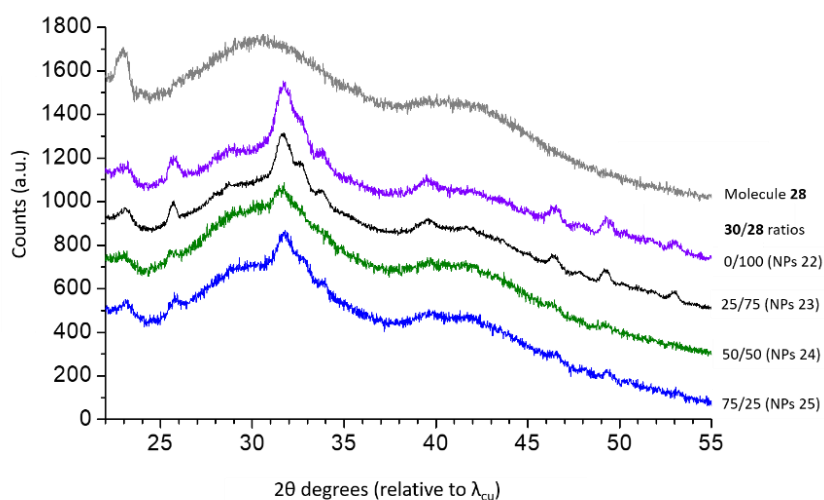


Figure 67: XRD patterns of apatite NPs surrounded with a mixture of P(PEG3K)-YIGSR **28** and P(PEG3K)-NEt₂ **30** (NPs 22-25)

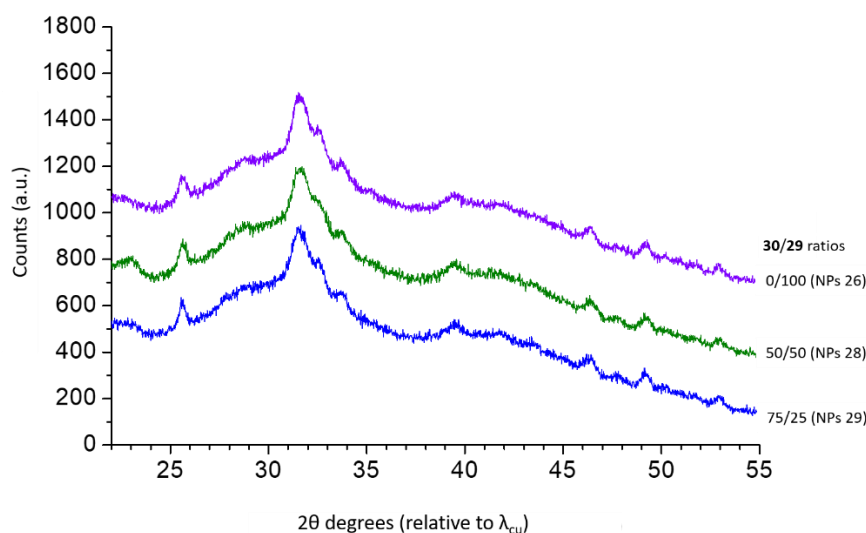


Figure 68: XRD patterns of apatite NPs surrounded with a mixture of P(PEG3K)-AhXRR **29** and P(PEG3K)-NEt₂ **30** (NPs 26, 28 and 29)

These results suggested that the peptide moiety was probably far enough from the apatite crystal surfaces so as not to modify significantly the apatite crystallization during synthesis.

c. FTIR analyses

To further explore the characteristics of the apatite phase, FTIR analyses were performed. The NPs 18 (surrounded with 100% of P(PEG3K)-RGD **27**) as well as NPs 15 (surrounded with P(PEG3K)-NEt₂ **30**) and a biomimetic apatite reference sample (synthesized at room temperature and cured for 7 days) were also analyzed for comparison (Figure 69). Results demonstrated that the colloidal NPs shared the same general characteristics of the typical biomimetic apatite sample, and that the presence of the peptide at the end of PEG chain did not seem to drastically alter the characteristics of the apatite. In that, these findings were in good agreement with XRD datas. On the FTIR spectrum of the colloidal NPs 18, additional bands were also detectable, which can be attributed to the organic fraction of PEG and peptides, such as the C-H and N-H vibrational modes as indicated in the Figure 69. These bands were also easily identifiable in the spectrum related to the pure P(PEG3K)-RGD molecule **27**, as expected.

Further information about the apatite phase could also be found around the $\nu_4(\text{PO}_4)$ domain in the 450-700 cm^{-1} range, and Figure 70 reports the corresponding zoomed-in view of the spectra of NPs 18 and the reference biomimetic apatite sample. Here, the spectrum of the colloidal NPs was analyzed after subtraction of the contribution of P(PEG3K)-RGD **27** (organic part) to better highlight the apatitic features.

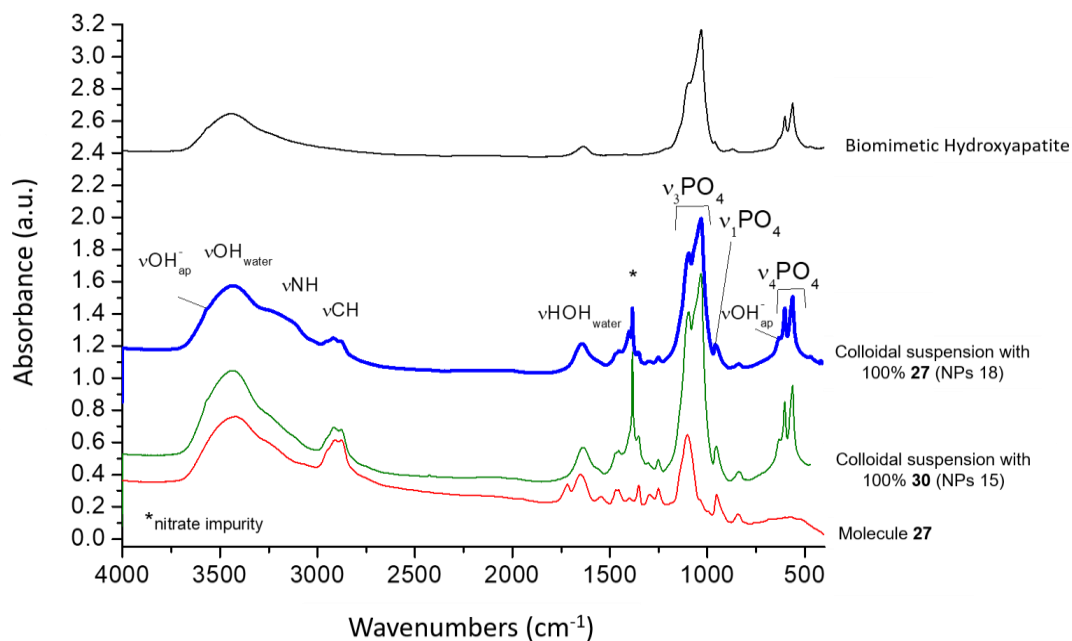


Figure 69 : FTIR analyses of NPs surrounded with 100% P(PEG3K)-RGD **27** (NPs 18) as well as with 100% P(PEG3K)-NEt₂ **30** (NPs 15). For comparison purposes, the FTIR spectra of the molecule P(PEG3K)-RGD **27** alone and a typical biomimetic apatite (matured 7 days at RT) have been added

Figure 70 shows that the intensity of the band at 632 cm⁻¹ assignable to apatitic OH⁻ ions is more pronounced for NPs 18 than for the biomimetic apatite reference, while the HPO₄ signature appears less visible. These conclusions were confirmed by the spectral enhancement treatment via Fourier auto-deconvolution (dashed lines in Figure 70). These results indicate that the apatite phase present in NPs 18 is closer to stoichiometry than the biomimetic apatite reference sample matured 7 days at RT. These findings are also in good agreement with the XRD results indicating a rather well crystallized apatite phase that was close to or only slightly non-stoichiometric (Ca/P ≈ 1.65).

FTIR analyses on NPs surrounded by P(PEG3K)-YIGSR **28** and P(PEG3K)-AhXRR **29** were not analyzed but we assumed that similar results would be obtained since the XRD analyses were very similar.

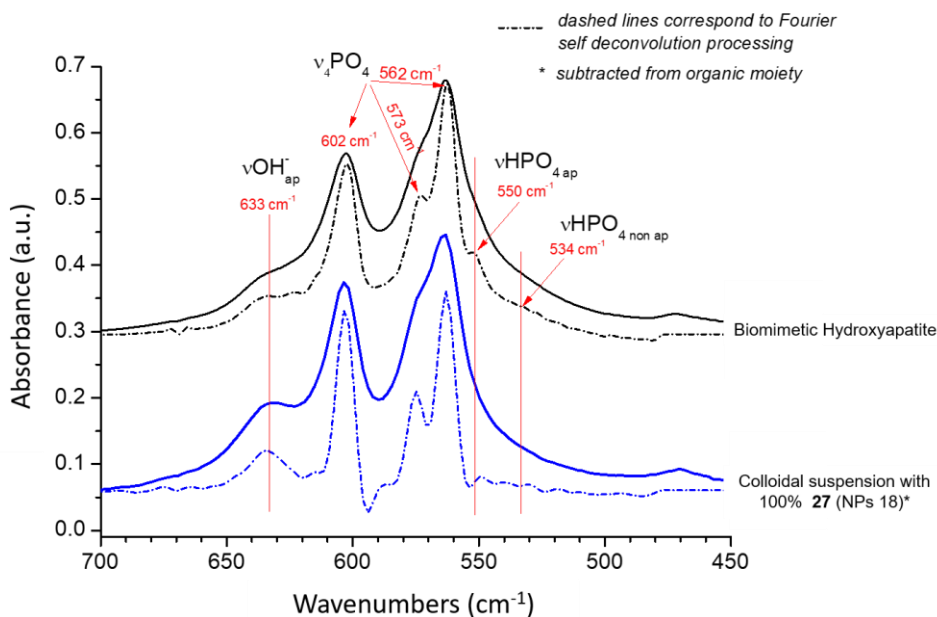


Figure 70 : Zoomed-in view around the $\nu_4(\text{PO}_4)$ domain of the FTIR spectra of NPs 18 and the reference biomimetic apatite sample

d. RAMAN Spectroscopy

As done previously for the AEP-based approach, complementary analyses were performed by RAMAN spectroscopy. (Figure 71) showed the illustrative example of the colloidal apatite NPs NPs 18 (surrounded with 100% of P(PEG3K)-RGD **27**). For comparative purposes, the RAMAN spectrum of the NPs 15 (surrounded with 100% P(PEG3K)-NET₂ **30**) was also added as well as the spectrum corresponding to the pure P(PEG3K)-RGD molecule **27**.

Both NPs 15 and 18 showed extremely comparable spectral features. These results indicated in particular that the apatite phase was not noticeably modified by the presence of the peptide moiety at the end of the PEG chain (as seen by similar positions and shapes of bands related to ν_1 to $\nu_4(\text{PO}_4)$ bands), thus stressing again the similarity of the apatite phases in presence in all these samples. The additional bands can be assigned to the organic part of the particles, as seen by comparison with the RAMAN spectrum of the pure P(PEG3K)-RGD molecule **27**; the slight variations in RAMAN features of the organic moiety being most likely attributable to slight changes in the PEG end-group with or without peptide functionalization.

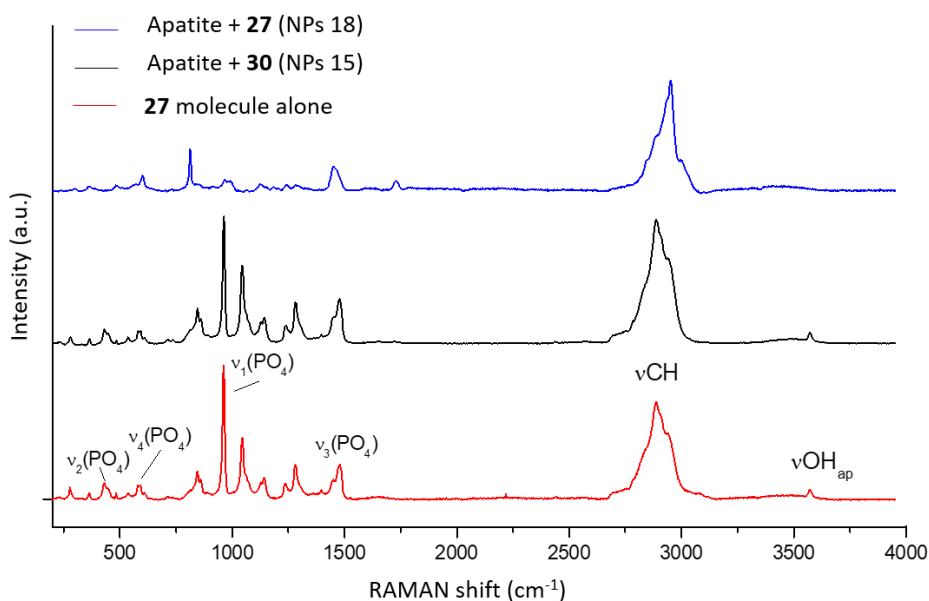


Figure 71 : RAMAN spectra for apatite NPs surrounded with 100% P(PEG3K)-RGD **27** (NPs 18) or with 100% P(PEG3K)-NEt₂ **30** (NPs 15) and for the pure P(PEG3K)-RGD molecule **27**.

e. Solid-state NMR analyses

In order to probe the interaction between the stabilizing agents and the surface of the apatite particles, and better assess the mode of grafting involved, solid-state NMR ¹H and ³¹P analyses were carried out in collaboration with the LCMCP laboratory at Sorbonne University (Th. Azaïs, G. Laurent).

Characteristic features obtained in the example of the colloidal apatite NPs 18 (surrounded with 100% P(PEG3K)-RGD **27**) are summarized in Figure 72. By ¹H NMR in simple magic angle spinning mode (MAS), the characteristic resonance of apatitic protons from OH⁻ ions at $\delta(^1\text{H}) = 0$ ppm¹²¹ as well as that of CH₂ groups in the P(PEG3K)-RGD **27** organic moiety leading to a rather thin peak at $\delta(^1\text{H}) = 3.6$ ppm were clearly detected (along with other minor contributions from the organic part), as shown on Figure 72a, confirming the presence of both the inorganic and organic components in the sample, as expected.

By ³¹P cross polarization (CP) analysis ($t_{\text{CP}} = 1$ ms), the typical signature of apatitic PO₄³⁻ ions can be seen at $\delta(^{31}\text{P}) = 2.7$ ppm, with a slight asymmetry at its basis (discussed below). The CP mode allowed transferring polarization from abundant spins to less abundant ones to increase the sensibility, which was necessary here as the phosphonate (organic) groups were only located at some surface sites on apatite particles while the inorganic phosphate ions were very numerous in the whole apatite crystals.¹²¹ In such CP mode, two additional peaks can be noticed at 33 and 25 ppm (Figure 72b), that could correspond to two modes of

adsorption/surface coordination of the phosphonate group of the stabilizing agent P(PEG3K)-RGD **27**: either monodentate via one P-O bond or bidentate via two P-O bonds. Generally speaking, the more a phosphate group is condensed, the more its chemical shift δ decreases. Therefore, the first signal at 33 ppm could correspond to the monodentate interaction while the second peak could be related to the more expanded bidentate configuration.

At this stage, ^1H - ^{31}P hetero-correlation (HetCor) measurements were carried out to visualize protons close to the P of the apatite phase and close to the organic moiety, typically the P(PEG3K)-RGD **27**, leading to two-dimensional (2D) spectra (Figure 72c).

For apatite, we then can identify the proton signature from the OH^- ions at 0 ppm, but also some amount of protons characteristic of P-OH groups (typically in HPO_4^{2-} ions for non-stoichiometric apatites) and/or of H_2O . These additional proton signatures were responsible of the broadening of the bottom of the ^{31}P peak mentioned above. For the organic moiety, the protons from the CH_2 groups linked to P gave a peak centered at 4 ppm. They gave a clearly widened signal compared to the peak of PEG mentioned above and detected by direct acquisition of the ^1H signal (see above). This can be explained by their increased rigidity due to the grafting process to the particle surface.

Then, a 2D CP BACK NOESY ^1H - ^1H analysis was run (the acronym NOESY stands for “Nuclear Overhauser Effect Spectroscopy”, and relates to the same type of experience as EXSY for “EXchange Spectroscopy”). In the first dimension (horizontal axis), double CP ^1H - ^{31}P - ^1H allowed polarizing the protons located close to P. In the second dimension, ^1H spin diffusion allows probing the proximity of the protons correlating with the first dimension. This approach was described by Von Euw *et al.*¹²² Here, the parameters used are MAS = 12.5 kHz, $t_{\text{CP1}} = t_{\text{CP2}} = 1$ ms, $t_{\text{diff spin}} = 100$ ms. In these conditions, the presence of peaks out of the diagonal, indicated by red circles (●) in Figure 72d, allows stating that the OH^- from apatite and at least some CH_2 groups from PEG are located close to each other, which agrees well with the grafting of the P(PEG3K)-RGD **27** on the surface of apatite.

Finally, a 2D SQ-DQ ^{31}P - ^{31}P analysis was made (where SQ and DQ stand respectively for Single Quantum and Double Quantum). This mode allows probing the very short distances between ^{31}P (< 5-6 Å) by retro-introducing the ^{31}P - ^{31}P dipolar interaction, and Figure 72e reports the obtained data. Note that some degree of auto-condensation of the P(PEG3K)-RGD **27** cannot be totally ruled out as there was a mark on the diagonal. However, the peaks positioned out of the diagonal are informative on such ^{31}P - ^{31}P proximity. Thereby, we confirmed the success of the grafting procedure by the fact that the P from P(PEG3K)-RGD **27** were correlated with the P from apatite, and this can be stated for the two modes of grafting, namely mono- and bidentate. The presence of a high T1 noise (vertically along the apatite signal) prevented from seeing well the two out-of-diagonal peaks to the right, however the two on the left were clearly visible.

All of the above results from solid-state NMR therefore confirm that our approach using the phosphonate group of P(PEG3K)-RGD **27** as an anchoring end-group was successful, thus leading to colloidal stabilization of apatite NPs, as exemplified here with a P(PEG3K)-RGD **27** characteristic conjugate.

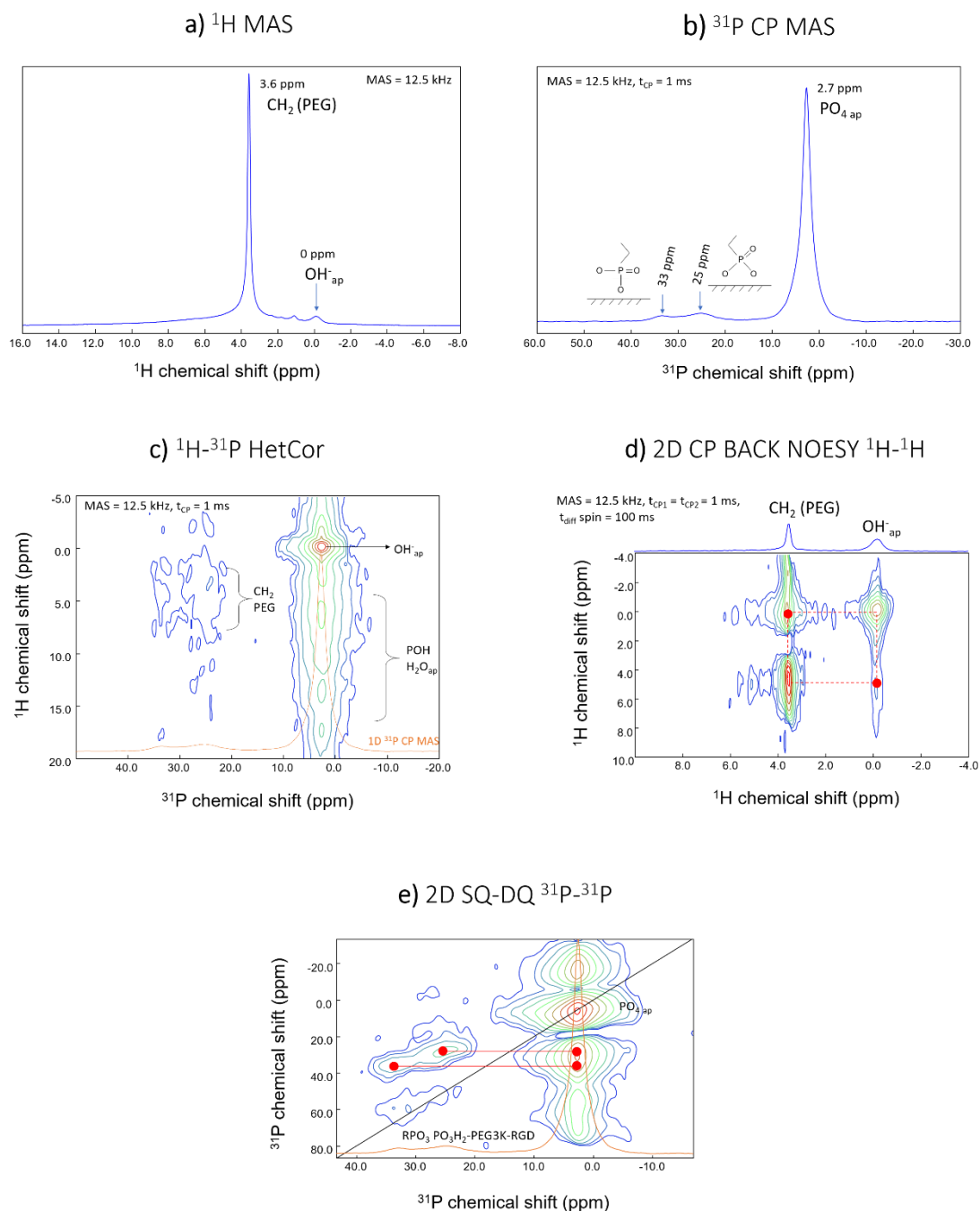


Figure 72 :Solid-state NMR analyses of apatite NPs surrounded with 100% P(PEG3K)-RGD **27** (NPs 18)

f. Determination of the NPs size thanks to DLS analysis and TEM imaging

DLS allowed us to determine a first approximation of the size and size distribution of the particles in colloidal suspension. As seen previously, the particle size depends on the length of the PEGylated chain⁴⁴ and on the R-PO₃H₂/Ca ratio used for the synthesis. For a length of 3 kDa and a ratio R-PO₃H₂/Ca equal to 0.016, nanometric size particles of about 167 nm were previously obtained (III.B.1.b). The DLS results obtained for the NPs 18 to 29 (surrounded with P(PEG3K)-Peptide) demonstrated that the presence of peptides at the end of PEG chain did not seem to influence noticeably the size of the particles (Table 25). The size of the particles surrounded with 100% P(PEG3K)-Peptide **27**, **28** and **29** (NPs 18, 22 and 26, respectively) were very slightly larger (< 200 nm) than those surrounded with the different ratios (NPs 19-21, 23-25 and 27-29).

Peptides*	Theoretical				DLS			TEM	
	Id	R-PO ₃ H ₂ /Ca	% P(PEG3K)-NEt ₂	% P(PEG3K)-Peptide*	Size (nm)	Pdl	Zeta Potential pH 7.2 (mV)	Size width (nm)	Size length (nm)
RGD	NPs18	0.016	0	100	154	0.25	-0.16	50	133
	NPs19	0.016	25	75	113	0.13	0.7	32	84
	NPs20	0.016	50	50	109	0.13	0	31	101
	NPs21	0.016	75	25	102	0.13	3.2	40	82
YIGSR	NPs22	0.016	0	100	204	0.26	-0.46	33	101
	NPs23	0.016	25	75	104	0.13	-0.9	31	84
	NPs24	0.016	50	50	112	0.11	0.4	36	91
	NPs25	0.016	75	25	107	0.11	3.7	27	103
AhXRR	NPs26	0.016	0	100	196	0.25	8.31	53	120
	NPs27	0.016	25	75	/	/	/	/	/
	NPs28	0.016	50	50	144	0.22	5.91	62	112
	NPs29	0.016	75	25	174	0.20	0.07	53	147

Table 25 : DLS and TEM characterizations of NPs 18 to 29

Moreover, as the proportion of P(PEG3K)-NEt₂ **30** increased, the size of the particles decreased from about 200 nm to 100 nm. In addition, the presence of peptides at the end of the PEG chain did not prevent the formation of a colloidal suspension with a monomodal dispersion of NPs, because the polydispersity index (Pdl) was comprised between 0.11 to 0.26. Although DLS was more suitable for spherical particles, the TEM results obtained were in the same range (Table 25). Homogenous rod-shape NPs were obtained even with the presence of the peptides at the end of PEG chain and whatever the ratio between stabilizing agents (Figure 73).

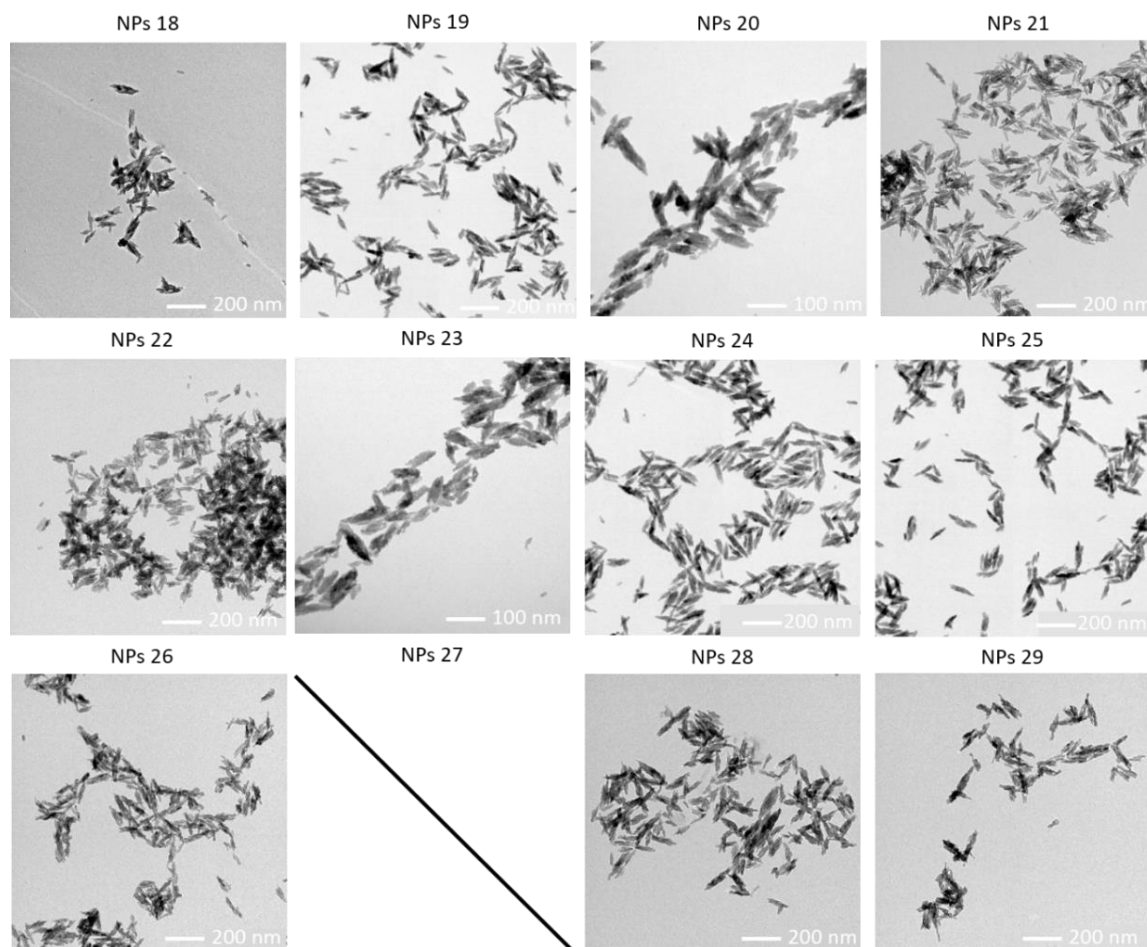


Figure 73 : TEM imaging of apatite NPs surrounded by different ratios of P(PEG3K)-Peptide **27**, **28**, **29**/ P(PEG3K)-NEt₂ **30** (NPs 18 to 29)

g. Liquid-state NMR analyses to determine (i) the grafting density (ii) the conformation of the stabilizing agents around the NPs and (iii) the peptide concentrations

As described previously (part III.B.1.b) liquid-state NMR analyses were used to determine the conformation of the stabilizing agents grafted to the surface using Flory's equations. To do this, it was first necessary to determine the stabilizing agent concentration in 1 mL of colloidal suspension and to deduce the grafting density by estimating the surface of one particle using TEM images (Figure 74). The peptide concentration was determined by combining the ³¹P ERETIC NMR and ¹H quantitative NMR.

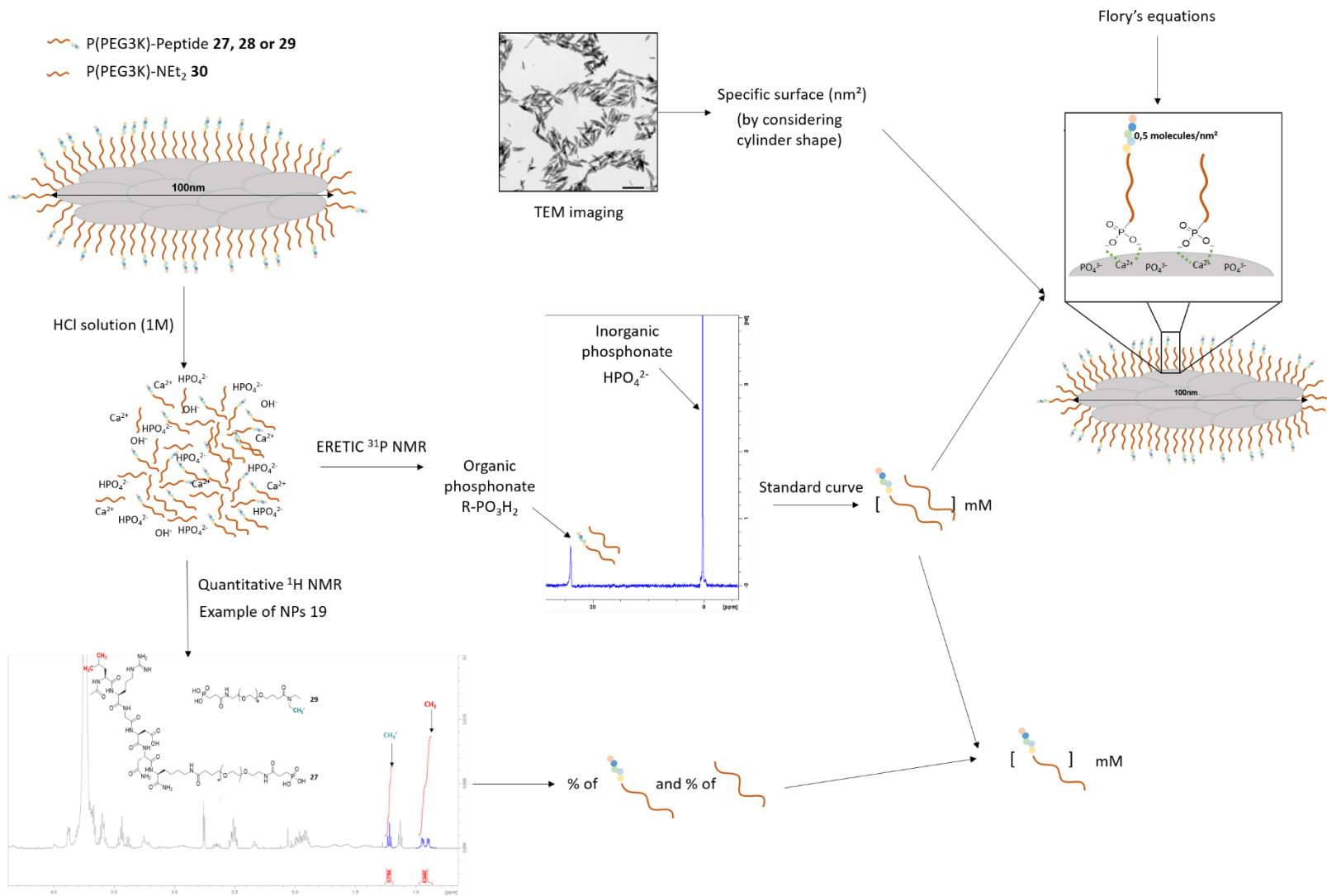


Figure 74 : General procedure to obtain (i) stabilizing concentration in 1 mL of colloidal suspension, (ii) grafting density, (iii) conformation of the stabilizing agents around the NPs and (iv) peptide concentration in 1 mL of colloidal suspension

Determination of the stabilizing agent concentration of the NPs 18-29

Firstly, ERETIC ^{31}P NMR analyses were performed to determine the exact concentration of stabilizing agents (mixture of P(PEG3K)- NEt_2 **30** and P(PEG3K)-Peptide) grafted during the synthesis around the apatite surface. The results showed that the average concentration of stabilizing agents in 1 mL of colloidal suspension for NPs 18 to 21 was 2.74 mM (Table 26). By comparison with the molar quantity of stabilizing agents used in the synthesis, we can deduce a grafting yield of about 42%. Whatever the ratio between stabilizing agents studied, similar results were obtained proving that the peptide added at the end of the PEG chain did not hinder the grafting of the stabilizing agent. Similar results were obtained for NPs 22 to 25 surrounded by different ratios of P(PEG3K)- NEt_2 **30** and P(PEG3K)-YIGSR **28** (Table 26). It may be noted however that the concentration of stabilizing agents grafted around the NPs 26 to 29 were surprisingly much lower, of the order of 0.6 mM for 100% P(PEG3K)-AhXRR **29** (NPs 26) and 13 mM for the ratio 75/25 (NPs 29) (Table 26). These results were not understandable, and we believe that an error has been made during the synthesis (these experiments will have to be repeated).

Determination of the grafting density of NPs 18-29

Secondly, we calculated the surface of one NP in the same way as before (see III.B.1.b). We considered a cylindrical particle shape, took into account the length and width parameters obtained via TEM images (Table 25) and used the concentration of stabilizing agents in 1 mL of colloidal suspension (Table 26). A grafting density around 0.5 molecules/ nm^2 was obtained for NPs 18-25 (i.e surrounded by a mix of P(PEG3K)- NEt_2 **30**/ P(PEG3K)-RGD **27** or P(PEG3K)-YIGSR **28**). Note that, as expected, the results with NPs 26-29 were completely different and not interpretable.

Determination of the stabilizing agent conformation around the NPs 18-29

In order to use these bio-inspired apatite NPs for various biomedical applications, it was important at this stage to ensure that the peptides present at the end of the PEGylated chains were properly presented/exposed around the NPs to allow interactions with external media, cells or even bacteria. For this purpose, Flory's equations were applied in the same way as for NPs 12-17 surrounded by P(PEG3K)- NEt_2 **30** with different R- $\text{PO}_3\text{H}_2/\text{Ca}$ ratio (see part III.B.1.b). As a reminder, the P(PEG3K)- NEt_2 **30** stabilizing agents were in Brush conformation around NPs 12-17 whatever the R- $\text{PO}_3\text{H}_2/\text{Ca}$ ratio tested.

The application of Flory's equations on NPs 18-29 again proved that the addition of peptides at the end of the PEGylated chain had no influence. Indeed, the R/D ratio higher than 1, obtained in each case, showed that the stabilizing agents P(PEG3K)-Peptide were again grafted with a brush regime on the NPs meaning that the peptides were correctly oriented to provide

biological activity, depending on the peptide nature (Table 26). The brush regime means that PEG chains are lengthy and that some degree of organization can occur among the adjacent lateral chains, thus leading to some 3D ordering in the dry state which confirm our hypothesis about the presence of the peak at 23° on XRD diffractogram (Figure 65). These results complemented the solid-state NMR or RAMAN results, proving that the P(PEG3K)-Peptide stabilizing agents were grafted to the surface of the NPs by the phosphonate group and any electrostatic interactions between the peptides and the apatite surface was involved.

Determination of the peptide concentration in 1 mL of colloidal suspension by using ^1H quantitative liquid state NMR

However, these previous analyses could not differentiate the stabilizing agents P(PEG3K)-NEt₂ **30** and the P(PEG3K)-Peptide **27**, **28** and **29** when used in mixtures (case of NPs 19-21, 23-25 and 27-29). The concentration obtained encompassed both molecules as the phosphonate group, common to both molecules, was considered during the ERETIC ^{31}P NMR. As the biological properties were provided by the peptide moieties, the concentration of peptides-based stabilizing agents only had to be determined to perform the upcoming biological experiments. For this purpose, a quantitative ^1H NMR method was used. In the following, the method was described with the example of NPs 19 surrounded with a mixture of P(PEG3K)-NEt₂ / P(PEG3K)-RGD equal to 25/75.

First, characteristic protons of each molecule were integrated and the integrations obtained were divided by the corresponding theoretical protons to obtain an approximation of the molecular quantity of each molecule. For example, the -CH₃' of the NEt₂ (1.23 ppm) was integrated for 3.78 and was divided by 3H to give the molecular quantity equal to 1.26. The same procedure was performed with two -CH₃ –corresponding to 6H) of the isopropyl of the Leucine present in P(PEG3K)-RGD (0.93-0.88 ppm) and the molecular quantity obtained was 0.89. To determine the percentage of the P(PEG3K)-RGD, the molecular ratio 0.89 was divided by the total molecular quantity, 2.15. In this case, the stabilizing agent quantity was shared with 40% of P(PEG3K)-RGD and 60% P(PEG3K)-NEt₂. This procedure was performed on each NPs and reported in the Table 26.

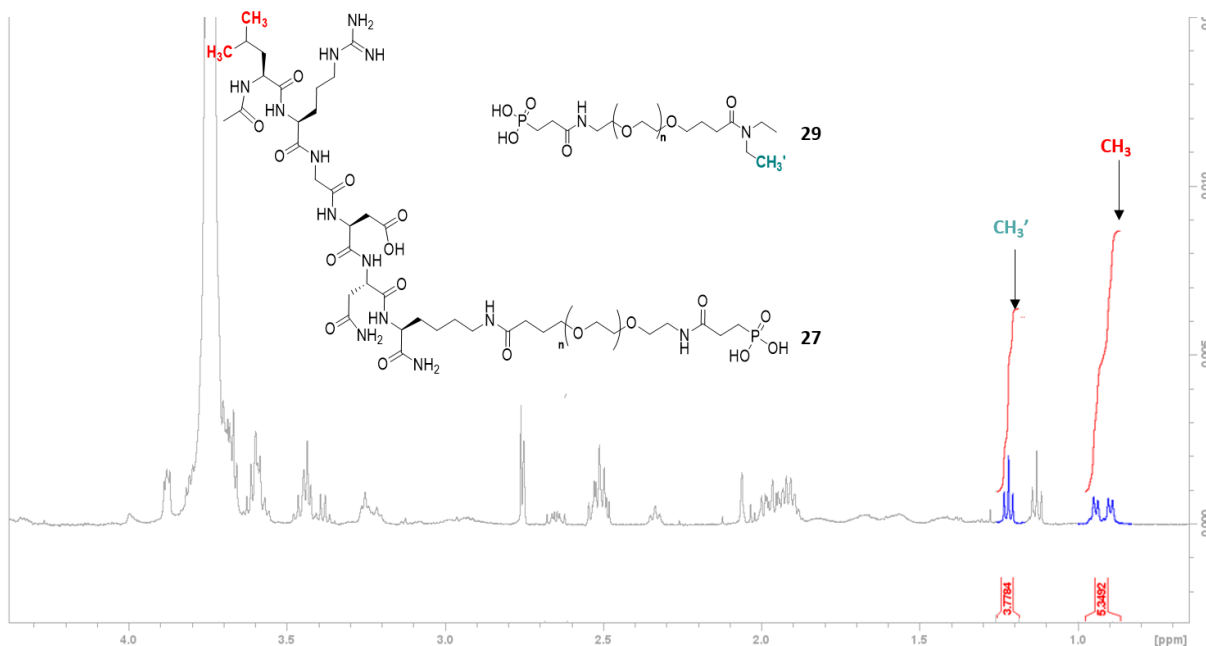


Figure 75 : ^1H quantitative NMR spectra of NPs 19 surrounded by P(PEG3K)- NEt_2 / P(PEG3K)-RGD 25/75

In the case of P(PEG3K)-YIGSR, the aromatic protons of the Tyrosine (6.84 ppm) were integrated. Unfortunately, it was not possible to find a clearly identifiable peak to integrate a proton belonging to the AhXRR peptide present in the stabilizing agent P(PEG3K)-AhXRR and therefore to determine its concentration. The exact concentration of P(PEG3K)-Peptide was possible by combining these results with the concentration of stabilizing agent obtained previously by ^{31}P ERETIC NMR. The concentration of P(PEG3K)-RGD was comprised between 2.25 to 0.21 mM and the concentration of P(PEG3K)-YIGSR was comprised between 1.91 to 0.71 mM. The concentrations obtained for P(PEG3K)-RGD and P(PEG3K)-YIGSR are promising for future biological tests, especially for cell healing, since the optimum concentration used in the literature was in the range of 1-3 mM.^{114,123,124}

Theoretical					Quantitative ¹ H NMR		ERETIC ³¹ P NMR					
Peptide	Id	R-PO ₃ H ₂ /Ca	P(PEG3K)-NEt ₂	P(PEG3K)-Peptide	% P(PEG3K)-NEt ₂	% P(PEG3K)-Peptide*	[R-PO ₃ H ₂] (mM)	[Peptide] (mM)	Synthesis yield %	Grafting density (molecules/nm ²)	Rf/D	Conformational regime
RGD	NPs18	0.016	0	100	0	100	2.25	2.25	35	1.05	4.09	Intermediate
	NPs19	0.016	25	75	60	40	2.27	0.67	35	0.43	4.44	Brush
	NPs20	0.016	50	50	80	20	2.95	.044	46	0.47	4.57	Brush
	NPs21	0.016	75	25	92	8	3.49	0.21	54	0.59	4.92	Brush
YIGSR	NPs22	0.016	0	100	0	100	1.91	1.91	30	0.55	2.96	Brush
	NPs23	0.016	25	75	33	66	2.91	1.79	45	0.47	4.42	Brush
	NPs24	0.016	50	50	67	33	3.48	1.06	54	0.48	4.59	Brush
	NPs25	0.016	75	25	80	20	3.86	0.71	60	0.62	5.24	Brush
AhXRR	NPs26	0.016	0	100	0	100	0.04	0.04	0.6	ND	ND	ND
	NPs27	0.016	25	75	/	/	/	/	/	/	/	/
	NPs28	0.016	50	50	ND	ND	0.48	ND	7.5	ND	ND	ND
	NPs29	0.016	75	25	ND	ND	0.85	ND	13	ND	ND	ND

Table 26 : Liquid-state NMR characterizations of NPs 18 to 2

Conclusion

Our results showed that the incorporation of stabilizing agents P(PEG3K)-Peptide alone or in a mixture with P(PEG3K)-NEt₂ in the synthesis of apatites allowed obtaining colloidal suspensions, whatever the peptide studied, composed of biomimetic apatite NPs, quite close to the bone mineral. Our hypothesis that the addition of a small molecule at the end of a long PEGylated chain would not disturb the role of stabilizing agent of PEG was thus validated. TEM and DLS analyses showed particles of rather homogeneous nanometric size with an ellipsoidal shape whatever the NPs synthesized. The presence of P(PEG3K)-Peptide around the apatite also has no influence on the grafting density (~0.5 molecules/nm²) and on the brush conformation of the latter around the NPs. Finally, the grafting strategy through the phosphonate end-group was validated, involving both mono- and bi-dentate surface complexes.

IV. Conclusion

The objective of this project was, in a first stage, to validate the proof of concept of obtaining colloidal suspensions of hybrid (organic/inorganic) apatite-based nanoparticles, with a homogeneous size, thanks to bioactive peptide-based stabilizing agent that could provide specific biological properties in addition to a stabilizing effect. To this aim, two novel types of peptide-based stabilizing agents have been conceptualized, prepared and evaluated in this work.

The first family of peptide-based stabilizer, P(Peptide), was prepared and tested but did not allow us to successfully reach the fixed objectives mentioned above. Indeed, despite the exposure of charges by the selected peptidic moieties, no stable colloidal suspension was obtained, and the particles were found to agglomerate in micron-sized objects in an uncontrolled way. In these compounds, the apatite phase in presence was found to exhibit a rather low crystallinity close to that of bone mineral. Even if our initial objective of obtaining stable suspensions has not been reached for this first type of stabilizing agent, the analyses showed that the P(Peptide) had effectively been grafted on the surface of apatite. Such particles might thus prove useful in some future works to act as carriers of bioactive peptides in some biomedical applications where monomodal and/or nanometric particle sizes are not necessary.

The second type of peptide-based stabilizing agent P(PEG3K)-Peptide was instead found to reach the objectives fixed at the start of this project. The presence of the peptide moieties at the other end of the phosphonated PEG chain did not perturb the stabilizing role of the PEG, and colloidal suspensions of hybrid peptide-decorated apatite NPs were successfully obtained. According to our analyses, the obtained hybrid particles indeed exhibited homogeneous nanometric dimensions and were rod-shaped. They are composed of an apatite core slightly

sub-stoichiometric covered by an organic corona grafted by way of a phosphonate group attached to one end of the PEG chain. The peptide moieties were covalently attached to the other end of the PEG molecules during the synthesis of the P(PEG3K)-Peptide conjugates. The latter was shown, via a set of complementary data and application of Flory's equation, to be organized in brush conformation, indicating that the peptide moieties will remain exposed at the external surface of the NPs where the biological action is required. These findings thus point out that such NPs stabilized by phosphonated PEG can be used as a platform for a wide range of peptide-related strategies, where the nature and characteristics of the peptide(s) can be selected on the basis of clinical needs. We also quantified the grafting density of the stabilizing agents on the apatite particles surfaces, and showed the possibility to co-adsorb P(PEG3K)-NEt₂ and P(PEG3K)-Peptide in variable amounts, which also widens the possibility to adjust the peptide contents on the NPs surface.

The above findings thus suggest that these new hybrid NPs, whose bio-inspired character comes both from the apatite component (close to bone mineral) and the peptide component (close to natural biomolecules), could be advantageously used for the delivery of bioactive peptides. This could be exploited in a large variety of applications, as in wound healing which is the illustrative application field selected in the rest of this study. The potential release of the peptide moieties from the NPs will have to be studied in a dedicated work. This release is expected to be especially facilitated in inflammatory and/or infectious contexts where a local acidification may occur, which is a favorable condition to activate apatite dissolution (and therefore the release of any adsorbed molecule). This can be seen as the potential asset of a "smart releasing device" for which the delivery of the peptides (and any bioactive ions incorporated in the apatitic core of the NPs) would all the more increase as the local environment is inflammatory or infected. A derivative of these new bioactive stabilizing agents could also be envisioned by adding a pH-sensitive or enzyme-sensitive linker to further control the peptide delivery even without direct apatite dissolution. Furthermore, the co-adsorption between two different peptide-based stabilizing agents is anticipated to be possible from our tests, and could widen the possibility offered by peptide-apatite hybrid NPs.

Chapter 3 - Toward the treatment of complex wounds

I. Wounds and healing process of complex wounds

A. Skin composition – Wound definition – Healing process

1. Skin structure

Skin is the largest and heaviest organ in our body. In adults, it represents an average of 2.3 m² and about 10 to 16% of the total body mass.¹²⁵ Skin plays the role of a barrier which protects the organs and tissues against external aggressions (microorganisms, UV...) and also allows for the perception of different sensations such as touch, temperature, pressure or pain thanks to its nerve endings.

Skin is composed of 3 main layers (Figure 76):

- Hypodermis
- Dermis
- Epidermis

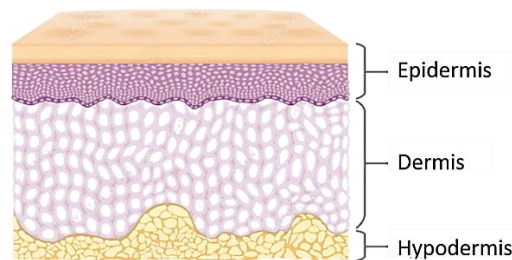


Figure 76 : Skin layers

a. Hypodermis

The hypodermis is a loose, highly vascularized connective fatty tissue located deep within the skin, beneath the dermis. It separates the skin from the fibrous membranes surrounding organs such as muscles and bones, forming a protective cushion. It is mainly composed of adipocytes grouped in lobules and separated from an extracellular matrix (ECM) composed of mast cells, fibroblasts, macrophages and collagen fibrils.¹²⁶

b. Dermis

The dermis supports, nourishes and connects the epidermis and hypodermis. The dermis is made up of cells, mainly fibroblasts and extracellular material. Of mesenchymal origin, fibroblasts have the role of synthesizing and maintaining the ECM. They ensure the synthesis of collagen, elastins and structural glycoproteins. These cells are very active during the healing

process. Immune system cells also reside in the dermis. Indeed, macrophages (that phagocytose cellular debris and pathogens), dermal dendritic cells (that trigger the immune system reaction by presenting antigens) and mast cells (that produce neuromediators responsible for the process of hypersensitivity, inflammation, bacterial or parasitic defense) are found in the dermis. It can be divided into two parts.¹²⁷ A superficial part, called "papillary dermis" containing fine, isolated collagen fibers and a deeper, denser part (80% of the total thickness) called "reticular dermis" composed of thicker collagen fibers in bundles, elastic fibers, small arterioles, venules, small nerves, pilosebaceous follicles, and sweat gland extractor ducts.

c. Epidermis

The epidermis is a squamous multi-layered epithelium that is in permanent contact with the outside world because it covers the dermis. The epidermal cells are mainly keratinocytes (90-95%) responsible for the synthesis of keratin, a protein involved in skin impermeability. Several cell layers exist due to the differentiation of these cells, a phenomenon called keratinization.

2. Definition of acute wounds and healing process

a. Acute wound definition

A wound is a rupture of the skin layer which consequently exposes the organism to a danger. Acute wounds occur after surgery or trauma (falls, first-degree burns, cuts, bites, chilblains, abscesses) and follow all phases of healing. The healing process of an acute wound takes place over a period of about 14 days and can be followed by a period of about two years for the complete remodeling of the damaged tissue.¹²⁸

b. Healing process

The healing process of acute wounds follows four consecutive and interdependent steps. The usual healing phases are: rapid hemostasis, adapted inflammation, proliferation and regeneration of the epidermis (Figure 77).^{126,129}

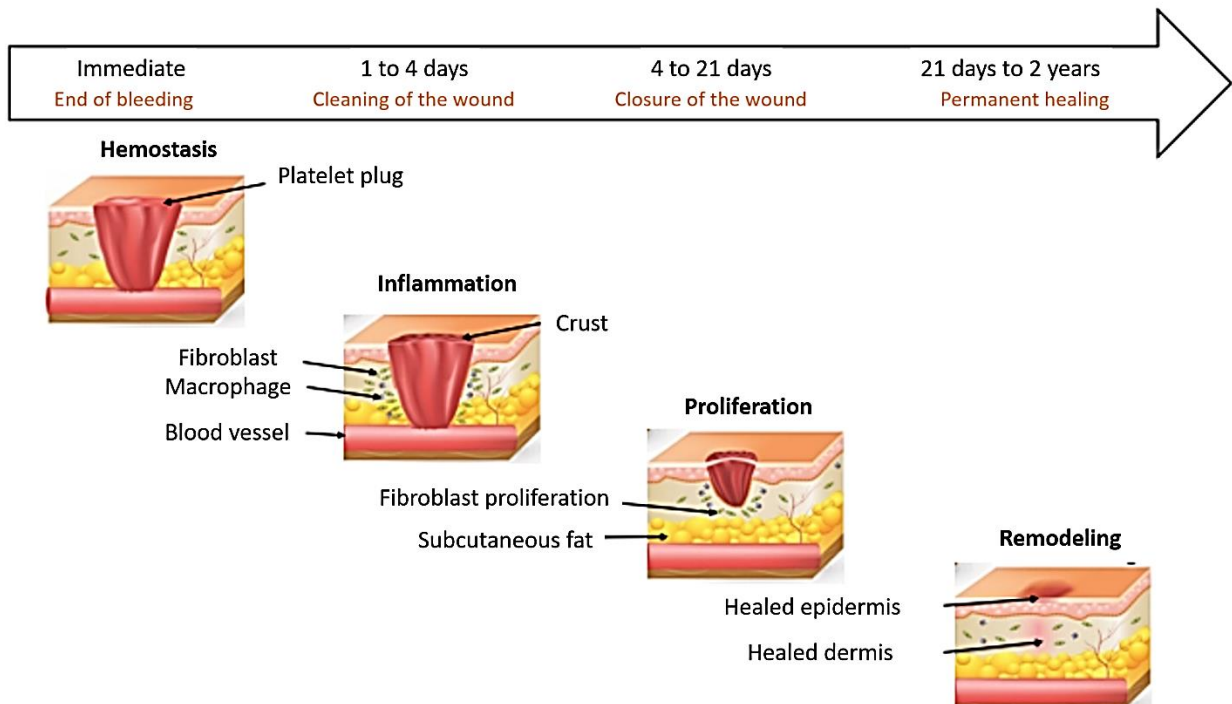


Figure 77 : Healing process of an acute wound

Hemostasis

When a cutaneous wound affects the dermis, the blood vessels are altered and the bleeding generated must be stopped as quickly as possible; this is the role of hemostasis.^{127,130} It is itself composed of 3 steps.¹³¹ The first step, called primary hemostasis, is vascular spasm, which reduces blood flow, minimizes blood loss and promotes the accumulation of blood platelets and coagulation factors through vasoconstriction. This accumulation allows for the formation of a thin membrane called a platelet plug, which covers the vascular breakage. Then, during the second phase called coagulation, red and white blood cells and platelets are captured by the fibrin filaments to consolidate the platelet clot. Finally, during the last stage of fibrinolysis, the blood clot is resorbed by the fibrinolytic system, resulting in normal blood flow.¹³²

Inflammation

Inflammation usually ends within 48-72 hours but can last up to 7 days.¹³³ This phase allows for the removal of organisms and infectious debris from the wound. Once the bleeding is controlled, the inflammatory cells migrate to the breach to begin the adapted inflammation stage.¹³⁴ Macrophages, mast cells and dendritic cells are cells of the white blood cell family that can detect a pathogen through their receptors. This subsequently leads to the secretion of chemical mediators of inflammation such as histamine, serotonin, pro-inflammatory cytokines and eicosanoids.¹³⁵ The presence of these mediators will enable the dilation of the blood capillaries and thus increase the blood flow at the inflammatory site. The cells in the capillaries will then open up to facilitate the passage of leukocytes and lymph. This

phenomenon is the cause of the heat, redness and swelling. The pain is due to the stimulation of the nerve endings. Next, leukocytes move from the blood into the tissues because they are attracted by the chemical mediators of inflammation. The monocytes, differentiated into macrophages on arrival in the tissues and granulocytes will perform phagocytosis. Phagocytosis consists in the uptake and degradation of foreign elements by the phagocytic cells.

Proliferation

It occurs 2 to 10 days after the cutaneous interruption. In this stage, the skin breach is sealed with the platelet plug, the wound is closed with a crust formed during the vascularization phase, and the wound is cleansed with inflammation. The next step allows for wick closure and tissue repair. Angiogenesis allows for the formation of new blood vessels from the ones that already exist. In the embryo, this is the initial stage because it implies a supply of gas and nutrients and it also gives instructions for the morphogenesis of the organs. In adults, angiogenesis occurs mainly in the case of wounds, hypoxia, cancer or in the case of the cyclic ovary during pregnancy. This stage is regulated by the distribution of stimulators and inhibitors.

Remodeling

Remodeling occurs 2 to 3 weeks after the injury and may last for several months.¹³⁶ The duration of this phase is affected by the size of the wound and whether it was initially closed or left open. Remodeling consists of the development of the epithelium and the maturation of the skin by fibroblasts.¹³⁷ Fibroblasts stimulate the production of collagen responsible for the elasticity and extensibility of the skin.

3. From acute wound to chronic wound

A wound is considered chronic if it has not undergone the classic steps of healing within 3 months after an injury.¹³⁸ It remains in a prolonged inflammatory step with an inability of the skin cells to close the wound, putting the damaged tissue at risk for serious infection.^{139,140} In fact, colonization of a wound by microorganisms is a common phenomenon that does not lead to infection if it remains reasonable.¹⁴¹

Several factors such as the presence of foreign bodies, necrotic tissue or infection slow down the healing process. These patient-dependent factors depend on age, nutrition or general health conditions. For example, advanced age leads to a decrease in the immune system while malnutrition will lead to calorie and protein deficiencies that will disrupt the healing process. Vitamin A deficiency can lead to an inadequate immune response, while vitamin C deficiency will lead to a decrease in collagen production by fibroblasts, which is useful for remodeling.

Finally, patients with diseases such as diabetes are prone to chronic wounds. Diabetic foot ulcers are one of the most devastating and common complications of diabetes. Diabetic foot ulcers are always accompanied by hypoxia.¹⁴² It may be the result of inadequate perfusion and angiogenesis both of which impair wound healing. Hypoxia can intensify the early inflammatory response of normal wound healing and, as a result, increase levels of oxygen radicals which prolong tissue damage.¹⁴³ Hyperglycemia can also worsen oxidative stress when the production of reactive oxygen species exceeds the antioxidant capacity.¹⁴⁴ *In vitro*, atypical sugars can be toxic to fibroblasts and neutrophils; therefore, they may lead to an increased susceptibility to infection.¹⁴⁵ Moreover, patients who are immunocompromised or undergoing heavy treatment such as chemotherapy are also more likely to develop this type of wound.

4. Current treatment of chronic wounds

Complex wounds represent a major public health problem as they affect 37 million people worldwide and generate very high healthcare costs.

Many external factors are involved in the healing process such as pressure, temperature, humidity and pH. For example, humidity is an important factor that must be controlled because fibroblasts require a water content of 70%, otherwise their metabolic activities are decreased and do not allow for optimal healing.¹⁴⁶ Conversely, excess humidity can promote bacterial infection through biofilm formation. pH is also an important element in wound healing. In an acute wound that heals normally, the pH is about 5.5-6.6, while in an infected wound, the pH is very slightly acidic at about 6.5.¹⁴⁷

The control of these simple parameters is essential to achieve an optimal environment for scar tissue formation. Treatments for complex wounds must therefore respect this environment but are not always sufficient to heal and fight against bacterial infection. In order to maintain an optimal healing environment and to protect the wound from infection, dressings (bandages) are usually used.

The first role of a dressing is to raise an artificial barrier between the outside and the body, mainly to prevent infections. A wide range of commercially available dressings is available including “modern” dressing forms based on sprays, hydrogels, hydrocolloids, etc. These forms of dressings may also add another role to the dressing in delivering bioactive agents (e.g. antibacterial ions, pro/anti-inflammatory) in a controlled manner to the wound.¹³⁶

Antibiotics are commonly used (generally by systemic oral administration) to treat chronic wounds when they are infected. Unfortunately, they are becoming less and less effective over time due to increasing bacterial resistance. According to the World Health Organization, antibiotic resistance is one of the greatest threats to global health and can affect all patients, regardless of age or health status. These bacteria can infect humans and animals, and the

infections they cause are more difficult to treat than those caused by non-resistant bacteria. In 2019, approximately 1.2 million patients died from microbial infections related to this bacterial resistance in the world. For all these reasons, alternative treatments must be found quickly, including via local treatments. Different alternatives are being studied involving for example antibacterial ions (Cu^{2+} , Zn^{2+} ...) ^{148,149}, bacteriophages ¹⁵⁰ or antibacterial peptides ^{151,152} for example.

II. Our objective: apatite nanoparticles surrounded by P(PEG3K)-Peptide for the treatment of complex wounds

The use of apatite in biomedicine seems judicious taking into account its « intrinsic » biocompatibility, biodegradability (leading to natural metabolites). We believed that they can be exploited for wound healing applications not only for the above cited advantageous but also because they are solid compounds that may provide added stability to the healing tissues. Additionally, apatite compounds can release Ca^{2+} ions which could help the formation of the platelet plug during the first step of the healing process, namely hemostasis. ^{88,89} Indeed, Ca^{2+} ions enhance platelet aggregation in platelet-rich plasma, and the bonding of Ca^{2+} ions converts fibrinogen to insoluble fibrin which compose the platelet plug. This phenomenon occurs in particular for weakly crystallized, biomimetic/non-stoichiometric apatites which are very resorbable like the NPs synthesized in this work. Moreover, the degradation of apatite particles is accelerated at acidic pH ¹⁵³, and is faster with small particles. The deposition of biomimetic apatite NPs on the wound with a slightly acidic pH would thus likely result in the release of Ca^{2+} ions, but also of other ions present within the apatite phase prepared (e.g. antibacterial doping ions such as Cu^{2+} or Zn^{2+} ^{154,155}) and in our case, the release of the new stabilizing agents containing active peptides which form the organic corona.

For these reasons, we planned to examine the potential of our hybrid apatite-peptide particles (NPs 18, 22 and 26 – Table 26) surrounded by P(PEG3K)-Peptide **27**, **28** and **29** in dermatology, and more specifically for wound healing and/or antibacterial action. We hypothesized here that a synergistic effect between apatite and peptides could take place to promote wound healing.

A. Apatite NPs surrounded by pro-adhesion peptides-based stabilizing agents 27 and 28 to promote wound healing

In order to assess the biological effect of the pro-adhesive peptides-based stabilizing agents **27** and **28**, containing RGD or YIGSR sequences and grafted on the NPs surface, two types of *in vitro* tests have been performed on fibroblast cells: biocompatibility evaluations and preliminary scratch assays. These experiments were performed in the laboratory of Prof. Liisa Kuhn at UConn Health University in Connecticut (USA) during my 2-months PhD internship.

1. Pro-adhesion peptides

Cell adhesion peptides originate from the extracellular matrix. RGD and YIGSR are adhesion peptides that originate from the fibronectin and laminin proteins, respectively, that make up the ECM.^{105,115,116,156} These peptides promote cell adhesion, spreading and migration.

RGD is known to interact with many integrin cell surface receptors which link the extracellular matrix to the cytoskeleton. The link between the RGD peptide and the cell surface receptor induces activation of members of the RhoGTPase family rearranging the cytoskeleton and subsequently allowing for cell attachment and propagation. In addition, fibronectins play a crucial role in dermal and epidermal cell migration.^{156–159}

The laminin YIGSR peptide comes from the 929-933 sequence of the β 1 chain and is known to enhance the collagen synthesis of human dermal fibroblasts. YIGSR pentapeptide demonstrated to be a useful agent for reconstruction of equivalent skin model because it stimulates the epidermal proliferation and the formation of basement membrane.^{160,161}

Previous studies have shown that tyrosine deletion or arginine substitution in YIGSR peptides resulted in a significant loss of activity.¹⁰⁵ For these reasons, and to realize the P(PEG3K)-Peptide **27** and **28** in this work, other amino acids were added to finally obtain the following peptides: Ac-LRGDNK-NH₂ **1'** and H-GDPGYIGSR-NH₂ **2'**. These peptides were selected due to their extracellular mechanism because the release of the therapeutic agent is not considered here.^{161,162}

2. General considerations for biocompatibility and proliferation experiments on NIH/3T3 fibroblast cells

a. Choice of cells studied

Under normal conditions, the spontaneous process of wound healing is divided in four overlapping steps: hemostasis, inflammation, proliferation and remodeling. This process involves interactions between epidermal and dermal cells as well as the extracellular matrix. Several types of cells, by contributing in wound repair, were identified like platelets, neutrophils, macrophages and fibroblasts.¹⁶³ Here, murine fibroblasts were studied: NIH/3T3 mouse fibroblasts (ATCC CRL-1658). Fibroblasts are the most abundant cell type in connective tissues and are central players in organ homeostasis. Their main function is to maintain the structural integrity of connective tissues by secreting components of extracellular matrix like collagen, fibronectin, proteoglycans, hyaluronic acid and other miscellaneous molecular species. The recruitment of fibroblasts are necessary for tissue rebuilding in response to injury.^{164–166}

The NIH/3T3 cells were grown up to 70-80 % of confluency in T-75 flask with 89% DMEM, 10% Calf Bovine Serum (BCS) and 1% Penicilin streptomycin (Gibco, 10,000 U/mL) as culture medium.

b. Experiments design

The following experiments were performed with NPs 18 surrounded with 100% of P(PEG3K)-RGD and NPs surrounded with 100% of P(PEG3K)-YIGSR.

Determination of the initial concentrations

The first parameter to be taken into account in the elaboration of the experiments was the peptide concentration tested. Previous studies demonstrated the efficiency of RGD-peptide and YIGSR-peptide sequences for fibroblasts migration and proliferation with a concentration ranging from 1mM to 3mM.^{115,162,167} According the previous liquid-state NMR quantification (see part III.B.3.g), the concentration of RGD peptide and YIGSR peptide in 1 mL of colloidal suspension was respectively 2.25 mM and 1.91 mM which correspond to the range of reference concentrations found. For these reasons the colloidal suspension NPs 18 and 22 were used without any dilution with the initial concentrations.

Sample preparation

In addition, other parameters such as the amount of serum in the medium, the pH and solvent were taken into consideration in the design of these experiments.

As said before, the NIH/3T3 cells were grown up with 10% of BCS which helps the proliferation of the cells. For this reason, we decided to reduce the percentage of serum to 2% during the cells viability, proliferation and scratch experiments to only observe the effect of our NPs on the proliferation and migration. The pH of the colloidal suspensions was naturally around 7, therefore no modification was performed at this level. Furthermore, the NPs were suspended in water, potentially problematic because of the osmotic shock that causes the burst cells (cytolysis). For this reason, the colloidal suspensions were freeze-dried to remove all traces of water and re-suspended with a suitable volume of DMEM culture medium with 2% of BCS and 1% penicillin/streptomycin to obtain the desired peptide concentration. After a few minutes in an ultrasonic bath, a colloidal suspension was obtained again. Finally, prior to bringing the NPs suspended in the culture medium into contact with the cells, a UV light was undergone for 15 min for sterilization purposes.

Compounds and controls tested for biocompatibility experiments

For the biological experiments, peptides Ac-LRGDNK-NH₂ **1'** and H-GDPGYIGSR-NH₂ **2'** were slightly modified. Indeed, the primary amines at N-terminal of the peptide **2'** and the primary amine of the Lysine side chain of the peptide **1'** were acetylated to mimic the presence of PEG as in the final molecule. For this reason, the peptides Ac-LRGDNK(Ac)-NH₂ **1''** and Ac-GDPGYIGSR-NH₂ **2''** were synthesized on solid support with a Fmoc/tBu strategy and obtained with a purity of 95% and 98% respectively (see chapter 4).

In order to interpret correctly the biocompatibility results, it was important to evaluate the biocompatibility of each component of the NPs (peptides **1''** and **2''**, P(PEG3K)-Peptide **27** and **28** and NPs 15 surrounded with the stabilizing agent P(PEG3K)-NEt₂) as well as to the complete nano-system NPs 18 and NPs 22. In this way, it was possible to observe the contribution of each part of the NPs to the biocompatibility.

Furthermore, in order to understand the influence of the apatite in the results, we considered keeping the amount of apatite (mg/mL) fixed and varying the concentration of P(PEG3K)-p-Peptide and vice versa. For this purpose, NPs surrounded with different ratios of P(PEG3K)-NEt₂/P(PEG3K)-Peptide were synthesized (i.e. NPs 19 to 21 and NPs 23 – 25 see part III.B.2). Unfortunately, the amount of NPs synthesized was insufficient to perform these experiments. Therefore, NPs surrounded with 100% of P(PEG3K)-RGD (NPs 18) and of 100% of P(PEG3K)-YIGSR (NPs 22) were only tested here.

Evaluation methods

One of the techniques used routinely to evaluate cell viability and proliferation in Prof. Liisa Kuhn's laboratory is the CellTiter Blue test.^{168,169} This method is based on a small organic molecule called Resazurin. The conversion of Resazurin to Resorufin by metabolically-active cells results in the generation of a fluorescent product, as a result of the action of several different redox enzymes (Figure 78).

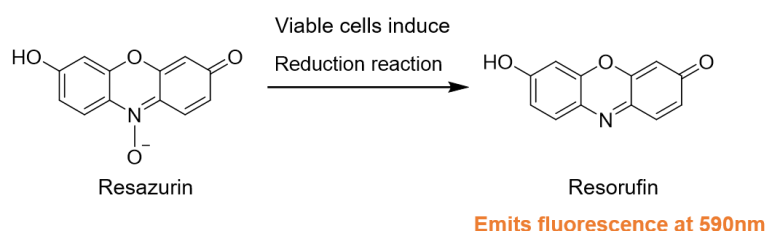


Figure 78 : Resazurin reduction induced by live cells leads to the fluorescent product Resorufin

Actually, fluorescence or absorbance can be used to record the cell viability because the absorbance maximum of Resazurin is 605 nm and that of Resorufin is 573 nm. However, the

fluorescent method is preferred because it is more sensitive. The intensity of fluorescence produced is proportional to the number of live cells. The protocol of the CellTiter Blue test is described in the experimental section (chapter 4). Hopefully, the apatite did not emit fluorescence at 590 nm and we could apply the CellTiterblue method to determine the cells viability and proliferation in the presence of apatite.

3. Biocompatibility and proliferation results

As explained before, each component of the NPs was tested for the biocompatibility evaluation. In this way, it was possible to observe the contribution of each part of the NPs composition to the measured biocompatibility. The components were added four hours after cell seeding to allow attachment and plates were incubated for 72 hours before assessing cell viability with the CellTiter Blue kit.

For NPs 18 (surrounded with P(PEG3K)-RGD) the concentration range of RGD peptide tested was from 2.25 mM down to 0.07 mM with 1:2 dilutions between wells. For NPs 22 (surrounded with P(PEG3K)-YIGSR), the concentration ranges of YIGSR peptide tested was from 1.91 mM down to 0.06 mM. NPs 15 surrounded with only the stabilizing agent P(PEG3K)-NEt₂ **30** (with a R-PO₃H₂/Ca ratio equal to 0.016) were also tested in these ranges of concentration. Control wells which allow to determine the number of cells corresponding to 100% of cells viability, received no products. The fluorescence of the wells was measured 2 hrs after adding 20 µL of the CellTiter reagent following the manufacturer's specifications.

As seen from the relative metabolic activity of the treatment groups vs. controls in Figure 79, the NPs 18 and 22 were biocompatible and had no negative effect on cells viability (assessed by the metabolic assay). Both NPs induced a proliferative effect over the 72 hours tested as evidenced by an increase in cell number relative to the controls without any compounds. A synergistic effect of each part of the multi-component NPs was observed and together they considerably increased the proliferation of the cells compared to the control.

From the above results, we can conclude that the apatite NPs surrounded by P(PEG3K)-Peptide (NPs 18 and 22) were biocompatible and the proliferation of NIH/3T3 fibroblasts was significantly boosted.

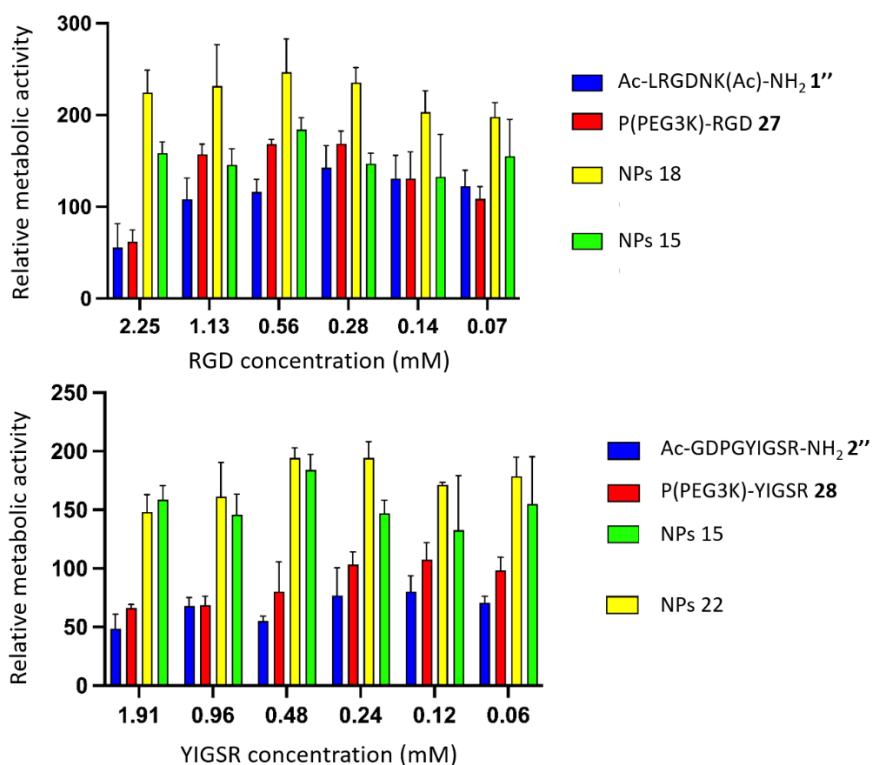


Figure 79 : Relative metabolic activity of i) NPs 15, 18, peptide 1'' and P(PEG3K)-RGD with a range of RGD peptide concentration from 0.07 to 2.25 mM and ii) NPs 15, 22, peptide 2'' and P(PEG3K)-YIGSR with a range of YIGSR peptide concentration from 0.06 to 1.91 mM

4. Preliminary scratch assays

After confirming biocompatibility and observing a proliferative effect on the NIH/3T3 fibroblast cells, the NPs 18 and 22 were then tested for their capacity to improve NIH/3T3 cell migration using a simplified *in vitro* wound healing assay known as a « scratch assay ».

For this purpose, cells in a culture medium containing 10% BCS were seeded in 96-well plates with a cell density equal to 40 000 cells/cm². Under these conditions, a monolayer of fibroblasts was obtained after an incubation time of only 24 hours. The percentage of BCS was for this step increased to 10% in order to reach cell confluence faster. This NIH/3T3 monolayer may be considered as a first rough approximation to mimic the skin. A straight scratch was produced (blue grid on Figure 80) in the middle of each well using a 300 microliter pipette tip and then the cell layer was washed with PBS to remove loose cells prior to addition of the test or control samples. Once the default in the cell layer was made, 100 µL of NPs 18 and 22 in culture medium containing 2% BCS was introduced in each well. The peptide concentrations studied were 1.13 mM for NPs 18 and 0.96 mM NPs 22. A negative control was performed by filling some wells with culture medium only. The closure of the cell monolayer wounds was examined periodically at specific time intervals (0, 16, 24, 36, and 48 hours) using a phase contrast light microscope with a 40x objective.

Cells that migrated into the *in vitro* wounded area were determined, for each replicate at each time point, by overlaying a grid on the original scratch areas and manually counting the cells. An automated image analysis program could not be used because of the NPs 18 and 22 settled over time and partially obscured the scratch area. The NPs 18 surrounded by P(PEG3K)-RGD completely obscured the scratch area preventing an accurate analysis, but cells in the wells treated with NPs 22 surrounded by P(PEG3K)-YIGSR could be distinguished. A small positive effect ($p = 0.01$, t-test) on *in vitro* wound closure at 24 hrs was observed due to the addition of NPs 22. Cell counts were 130 ± 9 for control and 165 ± 10 for NPs 22. At 48 hrs, the difference in cell counts (202 ± 13 for control vs. 258 ± 30) were also significant ($p = 0.04$, t-test). Significant differences were not observed at the other time points. At the beginning of the experiments, we can observe that the edges of the notches were less dense due to the migration of the cells. Then, at 24 hours, the division of the cells present in the center had time to take place. This explains the sudden jump in the number of cells at the scratch for NPs 22. The scratch test we performed showed that migration was increased by NPs 22 as well as proliferation. The positive effects of the NPs 22 on closure of the *in vitro* wound of the scratch assay indicated that the density sufficiently mimicked the nanoclustering present in the ECM. Let us note that since the cells in the scratch assay were not treated with an anti-proliferative drug, it is possible that the positive effect on closure of the *in vitro* wound was in part due to cell proliferation (that is enhanced by the NPs as we demonstrated before). Also, the possible intracellular uptake of some NPs by the NIH/3T3 cells was not studied here, but would further help to understand the biological effects of the NPs.

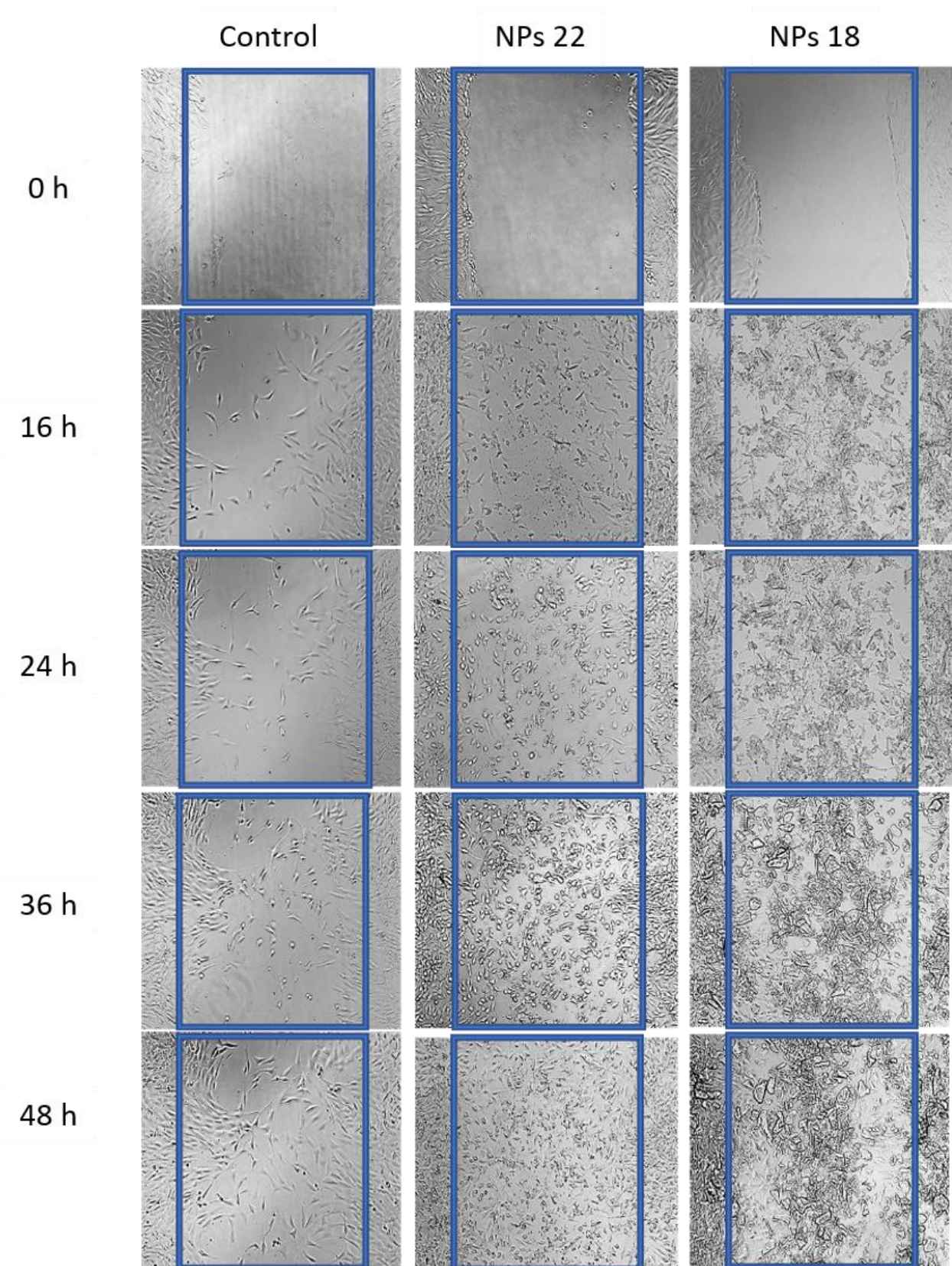


Figure 80 : Evolution of notch closure on the NIH/3T3 fibroblast monolayer over time in the presence of NPs 18 (1.13 mM) and NPs 22 (0.96 mM)

III. Other preliminary experiments

A. Antibacterial experiments

Antibacterial tests would also be necessary appropriate for applications in dermatology, and more particularly for the treatment of (chronic/complex) wounds. Indeed, bacterial infection is one of the major issues characteristic of complex wounds. First inconclusive tests were performed using an analog of the antibacterial peptide PalmRR-NH₂. PalmRR-NH₂ is a cationic amphipathic antibacterial peptide with activity against Gram-negative bacteria such as *P. aeruginosa* and *E. coli* but also against Gram-positive bacteria like *S. aureus*.¹⁷⁰ However, the long carbon chain of palmitic acid prevents the PEGylation of the peptide and thus the synthesis of a new antibacterial stabilizing agent of the P(PEG3K)-Peptide form. Therefore, aminohexanoic acid (AhX) was used instead of palmitic acid allowing us to keep the hydrophobic part of the peptide thanks to its carbon chain but also to add a free primary amine at the N-terminal of the tripeptide H-AhXRR-NH₂ allowing us to PEGylate the peptide (Figure 81). The synthesis of the new bioactive stabilizing agent P(PEG3K)-AhXRR was detailed in Chapter 2.

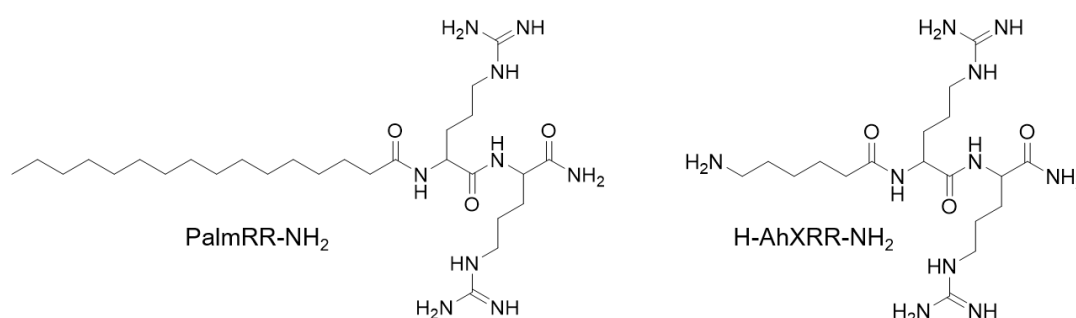


Figure 81 : Antibacterial peptide PalmRR-NH₂ and its analog H-AhXRR-NH₂

First experiments to determine the Minimal Inhibitory Concentration (MIC) of the stabilizing agent P(PEG3K)-AhXRR alone on the two bacterial strains *P. aeruginosa* and *S. aureus* were performed without success. Indeed, in solution the compound P(PEG3K)-AhXRR appeared to be a different molecule from the original palmitoylated antimicrobial peptide. While the latter is an amphiphilic cationic molecule, the compound P(PEG3K)-AhXRR displays a -PO₃H₂ functional group at the end of the hydrophobic chain. This moiety, required for the grafting, completely change the innermost nature of the peptide, turning it into a much more hydrophilic entity which may not be able to interact with bacteria membranes. Once attached to the surface, we assumed that the amphipathic nature of compound P(PEG3K)-AhXRR would be restored. For this reason, new antibacterial tests to determine the MIC of NPs 26 surrounded by the antibacterial stabilizing agent P(PEG3K)-AhXRR must be performed. The concentration range studied must be around the MIC of palmitic acid (i.e. 3.8 μM for the

bacterial strain *P. aeruginosa* and 1.9 μM for *S. aureus*). In the case where the nanoparticles show an antibacterial effect, *in vivo* tests on an infected wound model should be carried out.

B. Fibroblast membrane mobility experiments

In order to further investigate cell-NPs interactions, *in vitro* experiments have been initiated in collaboration with the ICBMS laboratory in Lyon (Ofélia Maniti, Thierry Granjon), using model apatite-peptide NPs stabilized with P(RGD) et P(YIGSR), and contacting them with primary human fibroblasts from patient's biopsies (Labskin Creations). The experiments were carried out by adding in the culture medium a patented agent (homemade Laurdan-derivative sensitive to the membrane polarity, named Dioll¹⁷¹) capable of spontaneously inserting in (phospho)lipid bilayers and whose fluorescence emission is related to the viscosity of its environment. Using this Dioll agent can thus be a way to inspect the degree of mobility of cell membranes, and thus by extension to potentially evidence a direct interaction between external particles or molecules and cell membranes.

This work aimed at checking whether or not the peptides YIGSR or RGD exposed by the NPs (in the P(PE strategy in this case) were modifying human fibroblast membrane mobility, which could be a sign of direct biological interaction between the exposed peptides and cell membranes. After addition of the Dioll and the NPs to the medium, and 1 night of incubation, the cells were retrieved and the fluorescence intensity was measured via a spectrofluorimeter at two characteristic wavelengths: at 440 nm (leading to the intensity I440, characteristic of the Dioll in gel phase – “rigid” state) and at 490 nm (I490, characteristic of the liquid crystal phase of the Dioll – “flexible” state) under excitation at 390 nm¹⁷². From these measurements, the GP parameter has then been calculated from the equation:

$$\text{GP} = \frac{(I440 - I490)}{(I440 + I490)}$$

The full experiments were made in triplicate, and the GP results considered correspond to the mean values. While a high GP value is indicative of a rigidified membrane, a low GP accounts for a fluid membrane.

Figure 82 reports the results obtained. Contacting the fibroblasts with the reference AEP-stabilized apatite NPs showed a clear rigidification effect compared to the control, with a significantly increased GP value (0.235 vs. 0.216), showing direct interaction between the AEP-covered surface of the particles and the cell membrane. A similar rigidification effect was seen with the apatite-P(YIGSR) particles. Instead, the apatite-P(RGD) particles did not generate a detectable change in the GP parameter and thus on membrane rigidity. Although these results were preliminary, they showed that i) the peptide moiety at least in the P(Peptide) approach was capable of interacting directly with the membrane of fibroblasts and ii) the nature of the

peptide can have an influence on the rigidity of the cell membrane. These experiments suggested that the YIGSR peptide seems to more strongly interact with fibroblast membranes compared to the RGD peptide.

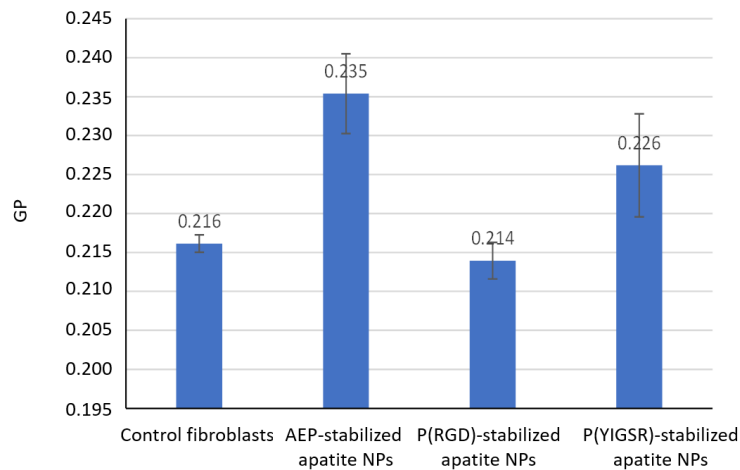


Figure 82 : Experiments of membrane rigidity on primary human fibroblasts with or without apatite NPs and P(RDG) or P(YIGSR) peptide functionalization

Similar experiments will have to be carried out with P(PEG3K)-Peptide which could not be done here due to time limitations; however, these data show that peptides exposed without a long linker such as PEG can already interact with cell membranes. It may thus be expected that the NPs exposing the peptides in an even more available conformation at the end of PEG chains will also allow successful direct peptide-cell membrane interactions. Cell internalization tests will also have to be carried out to further explore cell-NPs interactions and better apprehend the potential biological impact of such hybrid NPs.

C. Preliminary formulation assays

In this PhD project, preliminary studies on the formulation of medical devices involving such hybrid colloidal NPs were carried out. The NPs used for these first tests were NPs surrounded by the stabilizing agent AEP (with the goal to realize a first screening with these easier systems) and ionically doped with europium (1.5 mole % of Ca^{2+} ions were substituted by luminescent Eu^{3+} ions) in order to facilitate the observation of the distribution of the NPs. The objective was here to demonstrate that it was possible to incorporate colloidal apatite nanoparticles in various formulations. Three approaches were preliminarily investigated in this work: the impregnation of commercial dressings with the colloid, the *in situ* realization of dressings by freeze casting in the presence of the colloidal NPs, and the spraying of a suspension containing the NPs.

1. Impregnation on commercial dressings

Impregnation tests were carried out on four types of commercial dressings involving three different chemical compositions as follows:

- Aquacel Extra® (ConvaTec), carboxymethylcellulose
- Mepilex EM® (Mölnlycke Health Care), polyurethane
- Algo steril® (Brothier), alginate
- regular dressing kit of non-woven bandage (Raffin), cellulose

Each type of dressing was cut into 6 replicates of 2 cm x 2 cm pieces. Five of them were analyzed after immersion and the last one was used as reference. The dressings were then positioned on a custom-based 45°-tilted base (Figure 83). A colloidal suspension of apatite NPs – stabilized with AEP (NPs 1) for this proof of concept – was poured drop by drop on the dressing with the help of a syringe. This step was performed as many times as necessary by well humecting all of the dressing surface until a drop appeared at the bottom of the dressing and dripped out of the dressing, thus indicating that saturation was reached. The volumes were carefully recorded and are listed in Table 27, as well as the mean absorption rates by weight. Except for the Mepilex type, which absorbed a noticeably lower amount of colloid (close to 5 wt.%), the other three types led to absorption rates in the range 11-16.5 wt.%.

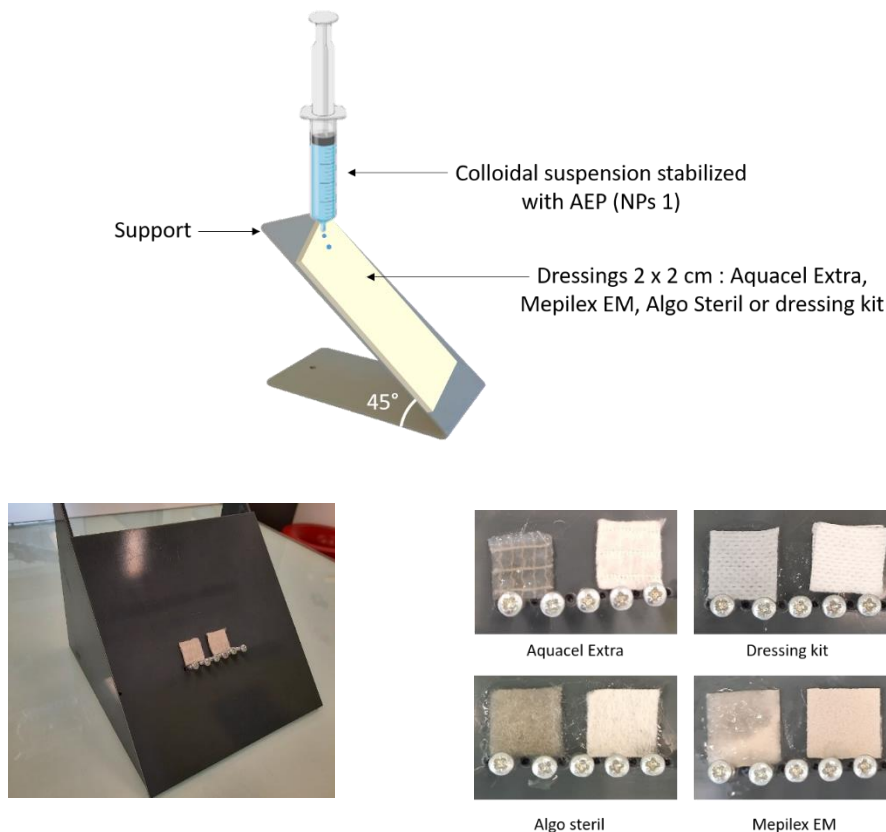


Figure 83: Custom-built set-up for the determination of the absorption at saturation of a colloidal suspension of apatite NPs (stabilized here with AEP) on different commercial dressings

Type of dressing	Saturation volume (mL)					Mean ratio $m_{\text{colloid}}/m_{\text{dressing}}$ (%)	Standard deviation
	1	2	3	4	5		
<i>N° of replicate</i>							
Aquacel Extra	0.8	0.9	0.9	0.9	0.9	15.3	0.7
Mepilex EM	0.6	0.9	1	0.8	0.8	4.6	1.1
Algo Steril	0.7	0.7	0.8	0.8	0.8	11.0	0.9
Dressing kit	1.1	1.1	1	1.1	1.0	16.5	0.9

Table 27: Maximum volume of colloidal apatite NPs at saturation (in mL) by dressing samples ($m \cong 0.06$ g) and mean absorption rate in wt. %

The dressings were observed by SEM before and after impregnation. The images (Figure 84) showed that the NPs were covering the fibers of the Algo steril and Aquacel Extra dressings uniformly. In the following, the alginate-based Algo steril was selected for further characterization.

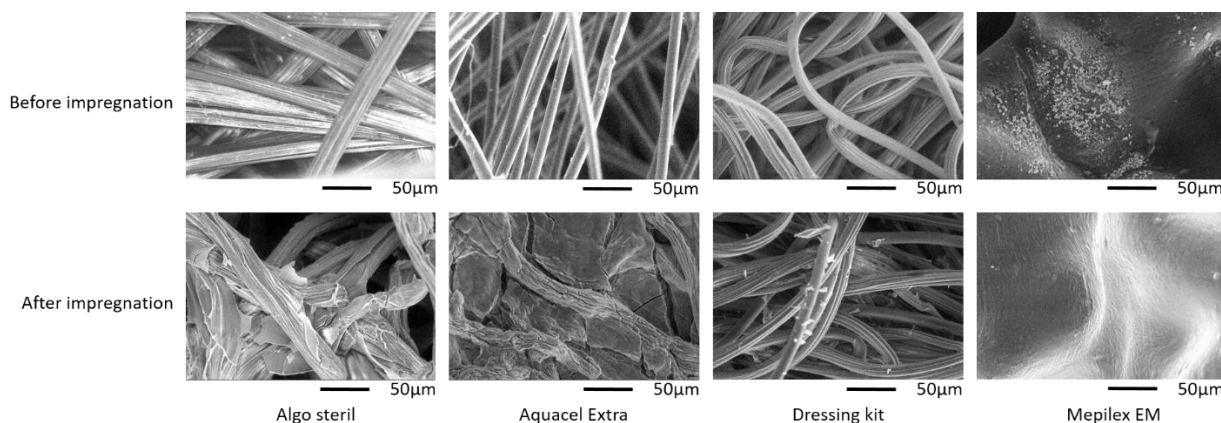


Figure 84 : SEM image before and after impregnation of dressings with colloidal suspension

RAMAN microscopy analyses were carried out, in the form of punctual spectra and 3D mapping, to further observe the covered alginate fibers of the Algo steril dressing. Europium-doped apatite NPs were used to follow the photoluminescence signal of Eu^{3+} ions which therefore co-localizes with the apatite phase, and this distinguish it from the alginate. Figure 85 shows that the fibers were well covered by apatite particles as evidenced by the 3D mapping.

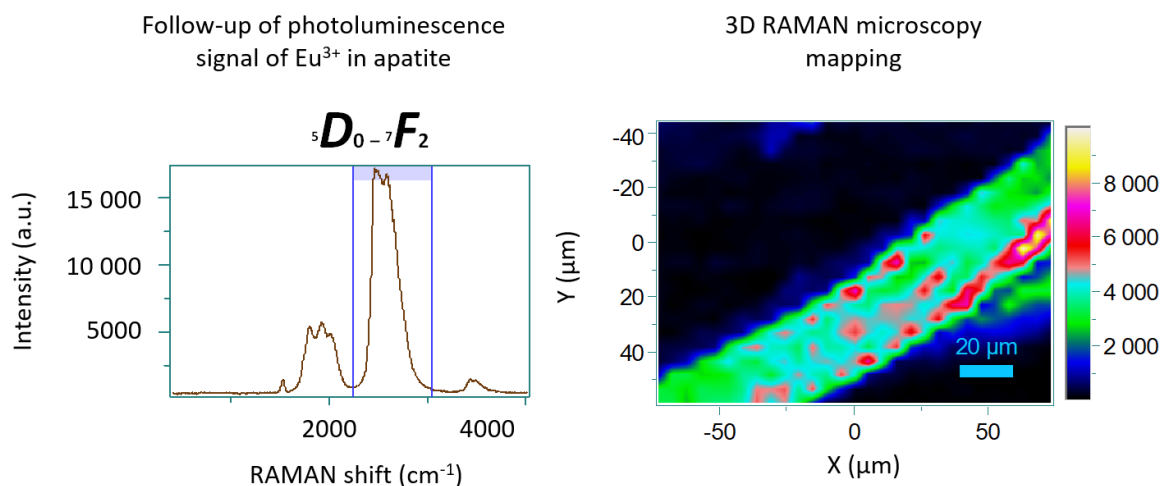


Figure 85 : RAMAN analyses: left: typical photoluminescence spectrum of Eu³⁺ ions (solution of europium nitrate) and right: 3D mapping on a fiber of alginate dressing (Algo steril) covered by dried colloidal apatite NPs

2. Direct fabrication of alginate dressings loaded with apatite NPs by freeze-casting

The previous methodology was based on the impregnation of commercial dressings in a subsequent step. This may allow clinicians to select, depending on the patients' conditions, the most appropriate apatite NPs formulation (e.g. associated with the most adequate peptide) and the right dose. It may however also be relevant to be able to propose already-loaded dressings, which was addressed here by direct fabrication of alginate 3D scaffolds/dried foams by freeze-casting in the presence of hybrid apatite NPs.

Freeze-casting is a methodology based on two essential steps: 1) the freezing of the solvent of a polymer (water in the case of alginate) with a controlled freezing front (evolution from bottom to top) so as to progressively generate columns of solvent crystals leading to the alignment of polymer chains and 2) the sublimation of the frozen solvent crystals to generate an open directional porous network. Typically this approach can lead to an open porous architecture¹⁷³ (Figure 86a) that may facilitate the passage of cells and fluids and, in the case of wounded zone, absorb some exudative liquid from the wound.

We have here fabricated our own 3D dressings based on alginate and in the presence of an increasing amount of colloidal apatite NPs in suspension (Figure 86 b and c). To this aim, the alginate powder was dissolved in water/apatite colloid, the suspension was homogeneously stirred typically using an Ultra Turrax® homogenizer, and the mixture was transferred into a mold with a copper base for improved heat transfer. The system was frozen down to -20 °C, leading to the crystallization of ice. After 5 hours, the freezing front had time to progress and stabilize, and the mold was transferred into a lyophilizer for sublimation of the ice crystals and obtainment of the final 3D scaffolds/custom-made dressing. The amount of colloid in the

initial mixture was varied at 0 (pure alginate as reference), 25, 50, 75 and 100%. As may be seen, cohesive porous scaffolds/dressings could indeed be successfully obtained in all cases. In order to verify the rather even distribution of the particles within the 3D porous network, europium-doped apatite NPs were used here to make them luminescent upon UV irradiation, especially due to the $^5D_0 \rightarrow ^7F_2$ transition of the Eu^{3+} ion (see Figure 85). By making the whole scaffold red/pink due to Eu^{3+} excitation under UV light (254 nm here), such Eu-doping indeed allowed us to check the successful presence and apparent homogeneous distribution of the hybrid NPs (under optical visualization) on the fabricated scaffolds, as illustrated in Figure 86b.

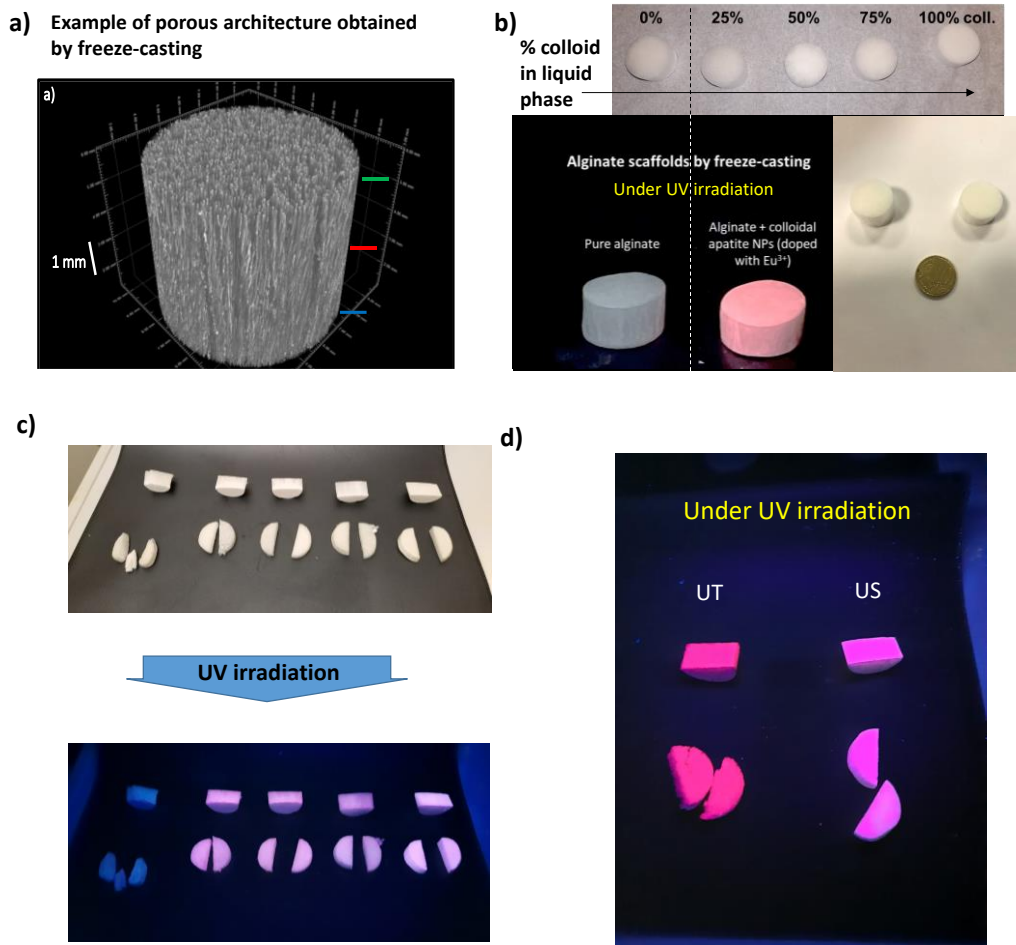


Figure 86 : Illustration of the freeze-casting approach to directly fabricate 3D dressings (here in alginate) loaded with hybrid apatite NPs. a) type of porous network obtained; b), c) and d) alginate dressings fabricated here by freeze-casting in the presence of Eu-doped apatite NPs, under UV light (254nm). In image d) two different types of homogenizing methods have been tested, namely the Ultra Turrax homogenizer (UT) and regular ultrasound (US)

Further characterization of the scaffolds is in progress, e.g. via X-Ray microtomography (μCT) to verify the internal porosity of the fabricated dressings and try to visualize the particles inside the porous network, and also by FEG-SEM for complementary assessments. Observation of a rather homogeneous pink color in the inside of the fabricated freeze-cast scaffolds by UV light (Figure 86c) however strongly suggested that the particles were indeed

well distributed in the whole porosity of the network. In this figure, due to the high number of samples to illuminate by UV at once, the UV light had to be placed a little farther, hence the slightly clearer nuance of pink; however, it can be seen that all samples containing the NPs had a pink taint compare to the first sample which is the NP-free sample. In Figure 86d we also compared two methods of homogenization of the liquid suspension prior to freeze-casting, namely the Ultra Turrax® (UT) homogenizer (used for all other samples) and regular ultrasound (US). Here, we show that, upon similar illumination conditions, the suspension homogenized with UT led to a redder color; this suggests a different aggregation/distribution of the particles in the scaffolds and will deserve more attention in future works.

From these preliminary results, it may thus be anticipated that it is possible to prepare dressing already loaded with our hybrid NPs, and in the dry state, which may facilitate storage sterilization and final use by nurses/clinicians. In this proof of concept, we deliberately decided to prepare alginate dressing of about 1 cm height if large wounded cavities were to be treated as in the diabetic foot complication, but the dimensions can be adapted depending on clinical needs and significantly thinner dressings can be made similarly by simply modifying the initial amount of liquid mixture used.

3. Spray

In the case of a wound, we also imagined spraying the colloidal NPs directly on the wound. This formulation would avoid smearing wounds with creams, especially for burns victims, which is very painful for the patient. The objective of this first test was to see if the colloidal suspensions could be sprayed and if the NPs were distributed uniformly. The colloidal suspension of apatite (stabilized here with AEP) and doped with europium diluted with different volumes of water (0, 20, 40, 60 and 80%) was introduced into a sprayer, and a distance of 10 cm was set between the spraying nozzle and the target. In these tests, the latter was selected to be filter paper to mimic the skin in a rough first approximation by such an organic and porous surface, as illustrated in Figure 87.

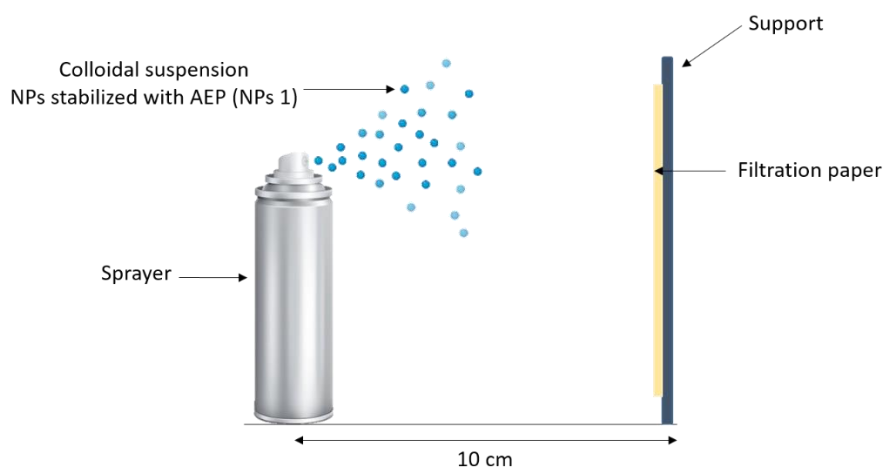


Figure 87 : Spraying test of colloidal NPs (stabilized by AEP and doped with Eu^{3+} ions)

These first tests showed that the sprayability was dependent on the concentration of colloid in the suspension. Indeed, the suspension with 80% of colloid and 20% of water was found to be more difficult to spray, which can likely be explained by an excessive amount of particles per unit volume leading to clogging. The lower concentrations tested in colloid in contrast appeared to be sprayable.

These observations indicate that, during the action of the sprayer, the particles at least reached the nozzle. To determine whether the particles had indeed been expelled from the nozzle and reached the target surface, observation of the target filter paper was made under UV light (254 nm in this case) to reveal the presence of europium ions (Figure 88). Although the spraying should be repeated, this figure points out the presence of red luminescent dots on the target paper where colloidal NPs had been sputtered, while this was not found for the spray using only water. Although very preliminary, these tests suggest that the development of sprayable formulations containing such NPs could be another appealing approach for the setup of tailorable medical devices using these hybrid compounds.

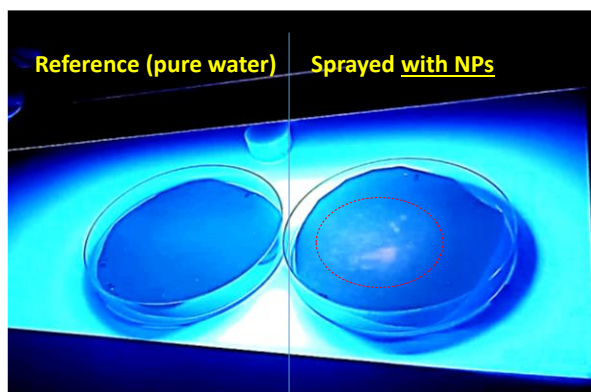


Figure 88 : Preliminary spray test using a suspension of 60% colloidal NPs in water, sprayed on filter paper, and reference (sprayed with pure water)

IV. Conclusion

Apatite nanoparticles surrounded by P(PEG3K)-RGD (nanoparticles 18) or P(PEG3K)-YIGSR (nanoparticles 19) have been tested for the treatment of complex wounds. Biocompatibility tests on NIH/3T3 fibroblasts not only confirmed the biocompatible character of these hybrid NPs but also showed a proliferative effect on them. Preliminary scratch tests were also performed by creating a notch in a fibroblast layer to mimic a wound. The results showed that the presence of the NPs accelerated the closure of the cut. However, the presence of agglomerated NPs hindered the interpretation of these results. Therefore, new experiments with more sophisticated methods and in the presence of cell markers should be performed. Moreover, extensive experiments must be performed in order to better understand the mechanisms of action that come into play to explain these preliminary results such as the internalization of NPs in NIH/3T3 fibroblasts.

The first antibacterial tests of the P(PEG3K)-AhXRR molecule on the two bacterial strains *P. aeruginosa* and *S. aureus* were not conclusive probably because of the $-PO_3H_2$ group present which adds a hydrophilic element to the molecule. Therefore, further tests should be performed using directly NPs surrounded by P(PEG3K)-AhXRR. We assume that chelation of the $-PO_3H_2$ group with apatite calcium will recover the amphiphatic nature of the peptide with only one hydrophilic group and one hydrophobic group and not one hydrophobic group surrounded by two hydrophilic groups.

Preliminary experiments were carried out on primary human fibroblasts and pointed out that the peptides presented at the periphery of colloidal apatite NPs could directly interact with fibroblast membranes, and in some cases even modify their rigidity.

In order to start investigating the potential of these new hybrid NPs for the treatment of wounds, first preliminary formulation tests were carried out, in the form of i) the post-impregnation of commercial wound dressings with “model” colloidal apatite NPs or ii) for the *in situ* preparation of alginate dressings/3D scaffolds via freeze-casting technology (allowing for the manipulation of thermally-metastable compounds). A third approach, namely through spraying tests of apatite colloid, was also initiated. Indeed, depending on the degree of healing and complexity of a wound, several types of formulations can be appropriate and clinically useful. The results showed that particles ionically doped with luminescent Eu^{3+} ions and stabilized by AEP could be incorporated in various formulations and quite homogeneously.

General conclusions

The main objective of this PhD project was to establish the proof-of-concept of the one-pot synthesis of nanosized colloidal apatite particles (NPs) stabilized by bioactive peptide(s), with illustrative applications for the treatment of complex wounds. Indeed, both apatite (contained naturally in bone and teeth biominerals) and peptides are particularly relevant for biomedical applications due to their “intrinsic” biocompatibility and inherent bioactivity. We hypothesized that peptide-decorated apatite NPs could provide a solid support for cell colonization/tissue repair and could simultaneously confer wound healing features via the progressive release of calcium ions (that may promote hemostasis/blood clotting) from the apatite phase and via the biological activity of the peptides exposed on the particles surface. Also, the apatite phase could ultimately be doped with bioactive ions such as anti-inflammatory/antibacterial Cu^{2+} or Zn^{2+} . In addition, the use of particles as peptide-carriers to keep peptide moieties at the vicinity of the wound site (as opposed to labile peptides simply solubilized in the medium) was considered as a strategic advantage. Also, phospho-calcic apatites are known to solubilize progressively in acidic conditions, which is likely encountered in inflammatory/infected conditions as in wounds or surgical sites. Thus, such peptide-decorated NPs may be seen as potentially “smart” nanosystems that should self-adjust their dissolution rate (and thus the release of their associated peptides/bioactive ions) all the more rapidly that the wound is inflamed/infected.

It can also be remarked that calcification processes in vertebrates, to form bones, dentin and enamel, are events that may only occur upon very particular conditions that are controlled locally by specific bone/tooth cells activity, and are not expected to happen outside of these conditions (except for certain very specific diseases leading to ectopic calcifications). In fact, body fluids are naturally supersaturated with respect to hydroxyapatite, which indicates that apatite crystals should theoretically be overwhelmingly present in the blood stream; but apatite precipitation does not uncontrollably occur due to the presence of several growth inhibitors naturally present in blood such as albumin (main protein in blood), pyrophosphate and carbonate ions, that prevent apatite crystallization/calcification phenomena. Thus, applications of apatite-based particles for other applications than for bone/tooth repair can largely be considered (as was reported on many occasions as for hematology, oncology and dermatology applications). Compared to other less bio-inspired mineral nanocarriers, apatite compounds are naturally present in the body and their dissolution leads to calcium and phosphate ions that can be reused by the body or eliminated.

In order to aim the treatment of wounds, disposing of well-defined particles appears allows a better control of the peptide loading, and consequently, a better control on the desired activity. However, apatite crystals have a natural tendency to agglomerate, leading to particles

with uncontrolled sized and shapes, unless a “stabilizing” or “dispersing” agent is used at the time of synthesis. According to a literature review, stabilizing agents exposing end-groups such as phosph(on)ates are able to control the extent of apatite crystals agglomeration – and sometimes limit crystal growth – either by electrostatic repulsion (i.e. with AEP) or by steric hindrance (i.e. P(PEG)), thus controlling the final apatite particle size. We thus selected phosphonate as an end-group to expose on the peptide conjugates to prepare, in view of efficient grafting to the apatite surface Ca^{2+} ions.

A first family of peptide-based stabilizing agents, P(Peptide) was synthesized on solid support by coupling 3-diethylphosphonopropionic acid on peptidyl resin **1** and **2**. The aim was to control the particle size by electrostatic repulsion and/or steric hindrance afforded by the peptides sequences. Apatite particles synthesized by co-precipitation ($\text{R-PO}_3\text{H}_2/\text{Ca} = 0.5$) with different proportions of AEP and P(Peptide) (i.e. 100/0, 90/10, 75/25, 50/50, 25/75, 0/100) did not give the expected result. A colloidal suspension could only be obtained when the amount of AEP was in vast majority (i.e. $\text{AEP/P(Peptide)} = 90/10$), while metastable suspensions were obtained with the ratios 75/25 and 50/50. These results thus showed that the peptides present around the particles were not effective to prevent agglomeration, by neither electrostatic nor hindrance repulsion. No nanometric particles of controlled size could be obtained by this approach, probably due to the proximity between charged groups from the peptide molecule and the surface of apatite, leading to uncontrolled interactions. The presence of P(Peptide) however did not seem to interfere with the structural features of the apatite phase formed, as shown from XRD and FTIR, since a moderately crystallized biomimetic apatite phase was obtained with or without P(Peptide). We concluded that there was a need to move peptide moieties farther from the apatite surface and to provide colloidal stability through a stronger sterical effect.

Therefore, a second family of peptide-based stabilizing agents, P(PEG3K)-Peptide was synthesized through a dedicated synthesis route. Apatite nanoparticles obtained by co-precipitation (typically with a ratio $\text{R-PO}_3\text{H}_2/\text{Ca} = 0.016$) with this stabilizer, possibly in co-presence of an increasing amount of P(PEG3K)- NEt_2 (i.e. $\text{P(PEG3K)-Peptide/P(PEG3K)-NEt}_2$ ratios of 100/0, 75/25, 50/50 and 25/75) allowed us to validate our initial proof of concept. Indeed, i) colloidal NPs were obtained in all cases with this new type of stabilizing agent, ii) TEM and DLS analyses showed that the particles were polycrystalline and exhibited homogeneous nanometric dimensions (with an ellipsoidal shape), iii) the mineral core of the particles was found by XRD, FTIR and RAMAN analyses to be composed of bio-inspired non-stoichiometric apatite whatever the peptide used, and iv) the presence of P(PEG3K)-Peptide around the apatite did not have a significant influence on the grafting density (~ 0.5 molecules/ nm^2) nor on the brush conformation of the latter around the NPs. This brush conformation evidenced from application of Flory’s equation (based on TEM and quantitative liquid-state NMR) is particularly appealing in our biomedical perspectives, since the peptides moieties were thus exposed toward the external periphery of the NPs and may be prone to

interact with the surrounding medium. On the other hand, solid-state NMR analyses proved the grating strategy through the phosphonate end-group, and evidenced both a monodentate and a bidentate mode of interaction.

In summary, novel hybrid apatite-peptide nanoscale particles with controlled features as well as an overall bio-inspired character were successfully obtained with the use of these new P(PEG3K)-Peptide stabilizing agents. Such NPs stabilized by P(PEG3K)-Peptide could be envisioned as a genuine platform for a wide range of peptide-related strategies, where the nature, characteristics and dose of the peptide(s) can be selected on the basis of clinical needs. In our case, these nanoparticles were tested with the view of applications in dermatology for the treatment of complex wounds that are associated with difficult healing and/or high infectious risks. These nanoparticles showed no cytotoxicity towards NIH/3T3 fibroblasts and, on the contrary, they were shown to quantitatively favor their proliferation, which is relevant for skin-related applications. In fact, our results even indicated a synergistic effect between the apatite phase and the peptides in this fibroblastic proliferation behavior. Preliminary “healing” tests were then carried out via scratch assays, starting from 2D films of confluent fibroblast cells. Our observations clearly indicated that the presence of our hybrid apatite-peptide NPs facilitated fibroblast proliferation/migration as visualized by the faster closure of the scratch, suggesting facilitated healing compared to the control without the NPs. It may be assumed that the solid support provided by apatite combined to the bioactive features of the peptide thus acted, as we had initially presupposed, like positive factors on this type of “healing” processes.

In order to start investigating the potential of these new hybrid NPs for the treatment of wounds, first preliminary formulation tests were carried out, in the form of i) the post-impregnation of commercial wound dressings with “model” colloidal apatite NPs or ii) for the *in situ* preparation of alginate dressings/3D scaffolds via freeze-casting technology (allowing for the manipulation of thermally-metastable compounds). A third approach, namely through spraying tests of apatite colloid, was also initiated. Indeed, depending on the degree of healing and complexity of a wound, several types of formulations can be appropriate and clinically useful.

Perspectives

The above results therefore suggest that these new hybrid NPs, whose bio-inspired character comes from both the apatite component (close to bone mineral) and the peptide component (close to natural biomolecules), could be advantageously used to carry/deliver bioactive peptides. This could be exploited in a wide variety of applications, such as in wound healing, which is the application domain chosen as illustrative example in this study.

The potential release of peptide moieties from the NPs will have to be studied in a dedicated work. This release should be particularly facilitated in inflammatory and/or infectious contexts where local acidification can occur, which is a favorable condition to activate the dissolution of the apatite (and thus the release of any adsorbed molecule or doping ion). This can be seen as a potential asset of a "smart delivery device" for which the delivery of peptides (and any bioactive ion incorporated into the apatite core of the NPs) would be all the more important that the local environment is more inflammatory or infected.

In this view, a derivative of these new bioactive stabilizing agents could also be considered by adding a pH-sensitive or enzyme-sensitive linker to further control peptide release even without the need for direct dissolution of the apatite. In addition, co-adsorption between two different peptide-based stabilizing agents is predicted to be possible from our tests, and could expand the possibilities offered by peptide-apatite hybrid NPs. Nonetheless, the selection of peptides that may have a direct "contact effect" (as the two adhesion peptides YIGSR and RGD used in this study) can also be widened to other such peptides as they bioactivity may only necessitate to be exposed on the outer surface of the NPs as we proved in our current strategy from the obtained brush conformation.

In addition, extensive biological testing will have to be performed to better understand the mechanisms involved in the wound healing tests realized so far. Both *in vitro* and *in vivo* will be needed to further demonstrate the pro-healing character of these hybrid NPs. It will also be interesting to check the potential effect of Ca^{2+} ion release (upon the progressive degradation of apatite) on blood clotting/hemostasis, and to investigate the advantages of apatite doping with anti-inflammatory/antibacterial ions to provide added/synergistic biofunctionalities to the NPs.

In order to further visualize notch closure in wound healing assays, cells would also benefit from being labeled in specific *in vitro* tests. In addition, NPs surrounded by a fluorescent peptide or ionically doped with luminescent ions (such as Eu^{3+} used in our preliminary formulation tests) could be used in order to explore the possible internalization of the NPs in NIH/3T3 fibroblasts or other relevant cell types. In the case of infected wounds, an

antibacterial effect of these NPs is essential. Preliminary experiments to determine the Minimal Inhibitory Concentration (MIC) of the stabilizing agent P(PEG3K)-AhXRR-NH₂ **29** on the two bacterial strains *P. aeruginosa* and *S. aureus* were performed, unfortunately the data obtained showed that this conjugate did not exhibit the expected antibacterial properties. Indeed, in solution, compound **29** appeared to be a very different molecule from the original palmitoylated antimicrobial peptide. While the latter is an amphiphilic cationic molecule, our conjugate **29** displays a -PO₃H₂ functional group at the end of the hydrophobic chain. The PO₃H₂ moiety, required for the grafting, completely changes the innermost nature of the peptide, turning it into a much more hydrophilic entity which may not be able to interact with bacterial membranes with the expected mechanism. Once attached to the surface, we assume that the amphipathic nature of compound **29** could be restored. For this reason, new antibacterial tests to determine the MIC of NPs surrounded by the antibacterial stabilizing agent P(PEG3K)-AhXRR-NH₂ **29** will have to be performed, which could not be done in the current PhD work due to time limitations.

Although several additional works will be needed to explore all of these perspectives – and potentially others – we believed that the current project allowed preparing a novel type of engineered peptide-decorated apatite nanoparticles with great potential in biomedicine, whether for the treatment of complex wounds or beyond.

Chapter 4 – Experimental section for Chapters 2 and 3

I. Experimental section for chapter 2

A. Commercial products and solvents

All solvents and reagents were used as supplied. Propylphosphonic anhydride solution in 50% of DMF was purchased in ABCR. Ammonium phosphate dibasic (>98%) was purchased in Acros Organics. 1H-benzotriazole was purchased in Alfa Aesar. N,N-dimethylformamide, methanol, ethyl acetate, dry dichloromethane, acetonitrile were purchased in Analytic lab (Castelnau-le-Lez, France). Acid trifluoroacetic, pyridine, piperidine, phosphoric acid were purchased in Carbo Erba. (Val de Reuil, France). Oxide deuterium was purchased in Eurisotop (Tewksbury, USA). Chlorydric acid, triethylsilane and calcium nitrate tetrahydrated were purchased in Fischer Chemical. N,N-dimethylmethaniminium hexafluorophosphate was purchased in Fluorochem (Dublin, Irland). Rink Amide PS resin (0.47 mmol.g^{-1}) and all Fmoc-AA-OH were purchased in Iris Biotech (Marktredwitz, Germany). ChemMatrix Rink Amide (0.49 mmol.g^{-1}) was purchased in PCAS BioMatrix (St-Jean-sur-Richelieu, Canada). BocNH-PEG3K-COOH was purchased in Rapp Polymer. Dichloromethane, Et₂O, diethylamine, bromotrimethylsilane, ammonia, ethyl 3-(diethoxyphosphoryl)propionate ester, N,N-diisopropylethyamine, palladium tetrakis triphenylphosphine, phenylsilane, 2-aminoethylphosphate, chloroform deuterium and sodium sulfate were purchased in Sigma-Aldrich (Steinheim, Germany). Acetone was purchased in VWR. The milliQ water was filtered on a purification system purchased from Millipore (Burlington, USA).

B. Equipment

1. High performance Liquid Chromatography coupled with Mass Spectrometry (LC-MS)

Samples for LC-MS analyses were prepared in a water/ACN mixture (50/50 v/v), containing 0.1% TFA. The LC-MS and UPLC-MS were controlled with MassLynx 4.0 software. The chromatographs were processed, visualized and analyzed with MassLynx 4.0 software. The LC-MS system used consists of a Waters Alliance 2695 HPLC, coupled to a Waters ZQ spectrometer (Manchester, UK) (positive electrospray ionization mode). Identification was performed using a Merck Chromolith Speed rod C18, 25 × 4.6 mm reverse phase column. A flow rate of 3 mL/min and a gradient of (0-100) % B over 2.5 min were used. Eluent A: 0.1% HCO₂H water; eluent B: 0.1% HCO₂H acetonitrile. Retention times (t_R) are reported in minutes. ESI+ mass spectra were acquired at a solvent flow rate of 100 μL/min via a split. Nitrogen was used as both the nebulizing and drying gas. Data were obtained in a scan mode ranging from 200 to 1600 m/z in 1s intervals; 4 scans were summed to obtain the final spectrum.

2. Purification by HPLC-preparative

Purification by HPLC-preparative was performed on a Gilson HPLC 2250, equipped with a reverse phase C18 column (Waters Deltapak C18 15 μ m 400x100mm). Standard conditions were elution system A (0.1% TFA water) and B (0.1% TFA acetonitrile) with a flow rate of 50 mL/min and a gradient of (0-100) % B with adapted times, at a detection wavelength of 214 nm.

3. Liquid Nuclear Magnetic Resonance (NMR)

All NMR experiments were performed at the « Laboratoire de Mesures Physiques », a technology platform of the University of Montpellier. The acquisitions were performed in D₂O at 25°C. Chemical shifts (δ) were reported in parts per million (ppm) using the residual non-deuterated peaks of these solvents as internal references (D₂O, δ (H) = 4.79 ppm and CDCl₃, δ (H) = 7.26 ppm). Signal multiplicity was reported as s (singlet), d (doublet), t (triplet), q (quartet), dd (split doublet), m (multiplet). The coupling constants (J) were measured in Hertz. The spectra were processed, visualized and analyzed with the Topspin 4.1.1 software (Bruker Biospin).

a. Instrumentations

The ¹H NMR spectra were recorded on different spectrometers:

- BRUKER Avance III NMR spectrometer - 500MHz (11.7 Teslas magnet) equipped with a Helium BBO cryoprobe (broadband, optimized for the observation of nuclei in the frequency range between ³¹P and ¹⁵N nuclei)
- BRUKER Avance III NMR spectrometer - 600MHz (14.1 Tesla magnet) equipped with a Prodigy TCI nitrogen cryoprobe (triple nuclei ¹H, ¹³C, optimized for ¹H detection)

b. Carbon

Proton decoupled ¹³C NMR spectra were recorded on BRUKER Avance III - 500 MHz spectrometers at Larmor ¹³C frequencies of 100 MHz and 125 MHz respectively.

c. Phosphorus

³¹P NMR spectra were recorded at 298 K in deuterated water (D₂O) on a Bruker Avance III 500 MHz spectrometer equipped with Helium BBO Cryoprobe operating at 202.47MHz. Coupling constants were measured in Hertz. Chemical shifts (δ) were reported in parts per million (ppm)

using residual non-deuterated solvents as internal references. Coupling constants were measured in Hertz.

d. 2D NMR experiments

The homonuclear g-COSY (TD-F2: 2048; TD-F1: 512; NS: 2 to 8), g-TOCSY (TD-F2: 2048; TD-F1: 512; NS: 8), NOESY (TD-F2: 2048; TD-F1: 512; NS 32) and heteronuclear ^{13}C - ^1H -gHSQC (TD-F2: 2048; TD-F1: 256; NS: 2 to 32) edited ^{15}N - ^1H -gHSQC (TD-F2: 2048; TD-F1: 128; NS: 32) edited and ^{13}C - ^1H gHMBC (TD-F2: 2048; TD-F1: 256 to 512; NS: 48 to 64) were performed on the BRUKER Avance III - 600MHz NMR spectrometer.

e. Quantitative experiments

NMR tube preparation

1 mL of a colloidal suspension was centrifugated (10 000 rpm) and the powder retrieved was washed several times with water before being freeze dried. The powder obtained was weighted before being dissolved in 100 μL of 1 M HCl solution. Then, 500 μL of deuterated water was added and the final mixture was put in NMR tube.

NMR Spectra Calibration

All NMR spectra were calibrated with the deuterium solvent signals (D_2O , $\delta(\text{H}) = 4.79$ ppm and CDCl_3 , $\delta(\text{H}) = 7.26$ ppm) except for the PEGylated compounds (**19** to **21** and **23** to **30**). In these cases, the NMR spectra were calibrated with PEG signals (e.g. PEG : 3.74 ppm - ^1H / 69.6 ppm - ^{13}C). The Chemical shift data were given in δ ppm.

Quantitative ^1H NMR

Quantitative ^1H NMR were recorded on 500 MHz spectrometer was used with relaxation delay of 30 seconds and number of 64 scans on spectral width of 7 000 Hz.

ERETIC ^{31}P NMR

The ^{31}P NMR spectra were recorded at 298K on a Bruker Avance III HD NMR spectrometer equipped with a broadband BBOF probe. The ^{31}P zgig pulse sequence was used with a spectral width of 32 465 Hz and 64 scans with a relaxation time of 16s. Spectra were processed with Topspin 3.6.2.

4. Solid-state Nuclear Magnetic Resonance

^1H and ^{31}P solid state NMR experiments were performed on a Bruker Avance III 300 WB spectrometer equipped with a dual channel 4BL probe. The Larmor frequencies of ^1H and ^{31}P were respectively 300 and 121 MHz. The sample was placed in a 4 mm diameter rotor and rotated at the magic angle (MAS = 12.5 kHz). The ^1H pulse recycle delay was 2 s. The t_{90° (^1H) pulse was 5 μs ($\nu_{\text{RF}}(^1\text{H}) = 50$ kHz).

The ^1H - ^{31}P Cross-Polarization (CP) MAS 1D and 2D (^1H - ^{31}P HetCor) spectra were recorded with a contact time of 1 ms. For the 2D spectrum, 128 slices were recorded for 720 scans per slice. The 2D ^1H - ^1H CP Back EXSY experiment consisted of a first block of ^1H - ^{31}P CP ($t_{\text{CP1}} = 1$ ms) and then a second block of $^{31}\text{P} \rightarrow ^1\text{H}$ CP ($t_{\text{CP2}} = 1$ ms) which maximizes the intensity of the ^1H resonances in the vicinity of the ^{31}P of the apatite phase and P(PEG3K)-RGD molecule. Then a ^1H spin diffusion block (EXSY type, $t_{\text{mix}} = 100$ ms) was added in order to allow for the diffusion of the ^1H magnetization. The off-diagonal ^1H peaks give information about a magnetization exchange between the resonances. For more information, see the article Von Euw et al. *Acta Biomater.* 2017.¹²²

CP enhanced ^{31}P - ^{31}P DQ-SQ spectrum was obtained using SC14 homonuclear recoupling.¹⁷⁴ ν_{MAS} was adjusted to 12.531 kHz in order to have a 180° ^{31}P pulse of 11.4 μs ($\nu_{\text{RF}}(^{31}\text{P}) = 43.860$ kHz). DQ excitation and reconversion times were $t_{\text{excit}} = t_{\text{reconv}} = 1.6$ ms, during which CW ^1H decoupling was applied at $\nu_{\text{RF}}(^1\text{H}) = 98$ kHz. Indirect and direct dimensions were decoupled using SPINAL-64 at $\nu_{\text{RF}}(^1\text{H}) = 72$ kHz. 32 slices with 3200 scans were acquired with a relaxation delay decreased to 1.3 s. For processing in the indirect dimension, forward linear prediction to 128 points was applied followed by 100 Hz line broadening apodization before Fourier transform. ^1H and ^{31}P chemical shifts (0 ppm) were set using TMS and H_3PO_4 85w% respectively.

5. Dynamic Light Scattering analysis (DLS)

The size and zeta potential of the NPs were carried out with Zetasizer Nano equipment (Nano-S) from Malvern Panalytical (France). The measurement parameters were as follows: a laser wavelength of 633 nm, a scattering angle of 173° , a measurement temperature of 25°C , a dispersant refractive index of 1.33 and material refractive index of 1.45. The pHs of the aqueous solutions were previously set with the addition of 2M HCl or 2M NaOH solutions.

6. Transmission Electron Microscopy (TEM) imaging

The colloidal suspensions were diluted by 100 before depositing a drop on the TEM grid. The sample was dried at room temperature on a TEM grid. TEM was carried out on a JEOL JEM-1400 flash transmission electron microscope, using an accelerating voltage of 120 kV. Formvar/carbon coated copper grids were employed for the sample deposition.

7. X-Ray Diffraction

The nature of the crystalline phases was studied using BRUKER D8 diffractometer in $\theta - 2\theta$ configuration, using a copper anticathode ($\lambda_{Cu} = 1.54056 \text{ \AA}$). For these analyses, the dialyzed colloid was previously lyophilized.

8. Fourier Transform Infrared (FTIR)

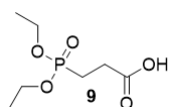
FTIR analyses were performed, for additional characterization, using a Nicolet 5700 spectrometer operating in the $400\text{--}4000 \text{ cm}^{-1}$ (resolution of 4 cm^{-1}) in transmission mode using the KBr pellet methodology.

9. RAMAN Spectroscopy

RAMAN microspectroscopy analyses were carried out on a Horiba Jobin Yvon LabRAM HR 800 apparatus using a continuous argon laser emitting at $\lambda = 532 \text{ nm}$ (13 mW). Analyses were made with x100 magnification at a numerical aperture of 0.9, leading to a spot diameter of $0.8 \text{ }\mu\text{m}$ for an axial resolution of $2.6 \text{ }\mu\text{m}$. A holographic network of 600 lines per mm gave a spectral resolution of 2 cm^{-1} . The spectra were recorded with an acquisition time of 30 seconds with 3 accumulations, in the $150\text{--}4000 \text{ cm}^{-1}$ spectral range. The spectra were processed with the LabSpec6[®] software, including the baseline correction.

C. Synthesis of hybrid peptide-apatite nanoparticles obtained from 2-aminoethylphosphonate-analog, P(Peptide)

1. Synthesis of 3-(diethoxyphosphoryl)propanoic acid **9**



Ethyl 3-(diethoxyphosphoryl)propanoate **8** (2.5 g, 10.5 mmol, 2.5 mL) was solubilized with 30 mL of acetone and poured in a 50 mL round bottom flask with two necks. 5 mL of HCl (37%) and 5 mL of water were quickly added to the solution. The mixture was placed under reflux and was stirred at 60°C during 30 minutes. The solvent was then evaporated using rotary evaporator and an uncolorless oil was obtained (2.1 mg, 95%). A NMR tube was finally prepared by adding one drop of the product and 500 μL of CDCl_3 . The product was analyzed by ^1H NMR and ^{31}P analyses.

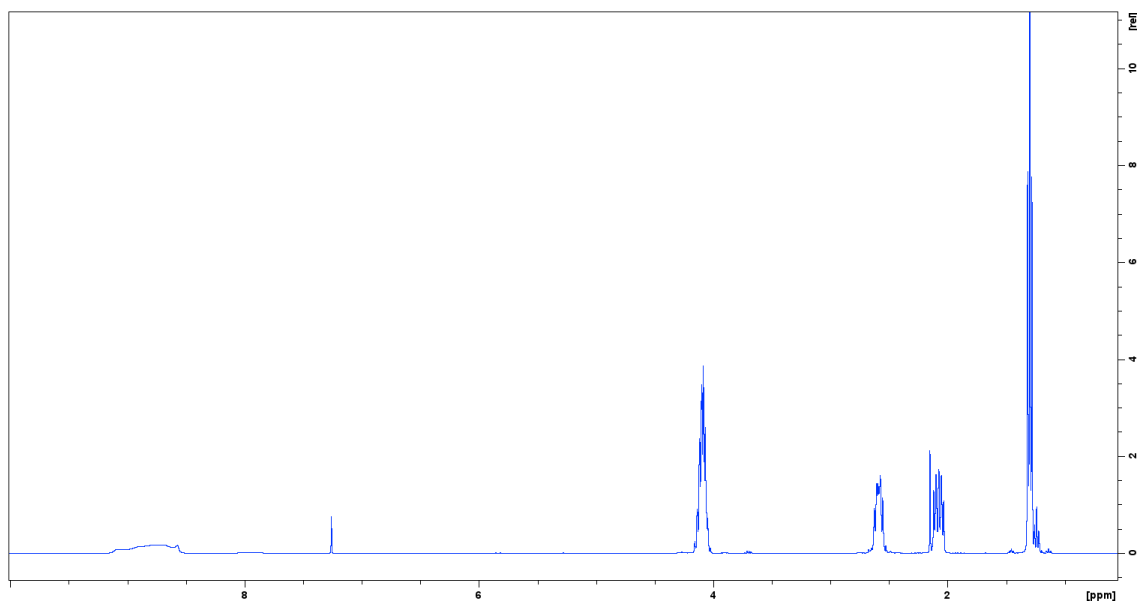


Figure 89 : ^1H NMR Spectrum of 3-(diethoxyphosphoryl)propanoic acid **9** (CDCl_3 , 600 MHz)

^1H NMR (600 MHz, CDCl_3 , 25°C) : δ (ppm) 1.30 (t, 6H, 1) ; 2.08 (q, 2H, 3) ; 2.59 (m, 2H, 4) ; 4.05 (m, 4H, 2)

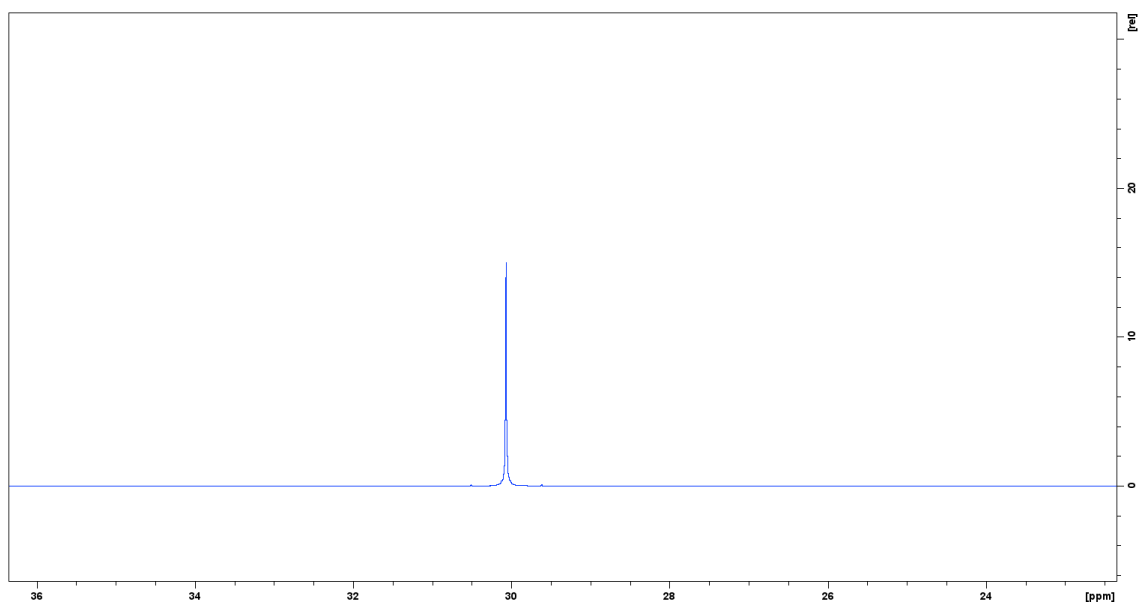
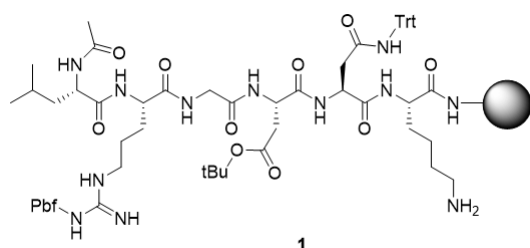


Figure 90: ^{31}P NMR Spectra of 3-(diethoxyphosphoryl)propanoic acid **9** (CDCl_3 , 600 MHz, 31.0ppm)

2. Peptidyl resin 1 and 2 synthesis

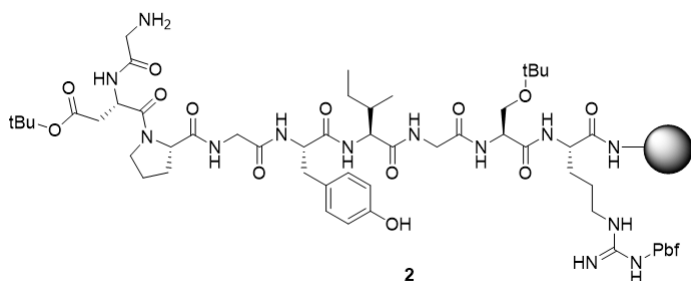
a. Peptidyl resin 1 (precursor of Ac-LRGDNK-NH₂ 1' peptide)



Synthesis by SPPS was made using the H-Rink Amide PS (0.47 mmol.g⁻¹, 0.86 g) resin in DMF. The first to the sixth coupling reactions were performed using Fmoc amino acid (6.3 mL, 5eq) / DIEA (1.09mL, 10eq) / HATU (6.3 mL, 5eq) mixture for 5 minutes twice with DMF washing steps in

between. The Fmoc removal steps were realized using piperidine/DMF (20/80 v/v) solution (15 mL) for 1 minute and performed twice. All washings were done successively with 15 mL of DMF, DCM and DMF after coupling steps and deprotection steps. N-Terminal acetylation was performed with 20% Ac₂O in DMF and DIEA (1%) for 15 minutes twice. The Alloc protection was removed in DCM with 0.25eq of palladium tetrakis triphenylphosphine followed by 25eq of phenylsilane. The reaction was agitated during 1 hour and performed twice. The solvent was removed and the resin was washed with DCM and DMF (x3). A microcleavage followed by LC-MS analysis (Figure 97) was realized to check the structure (86% of purity).

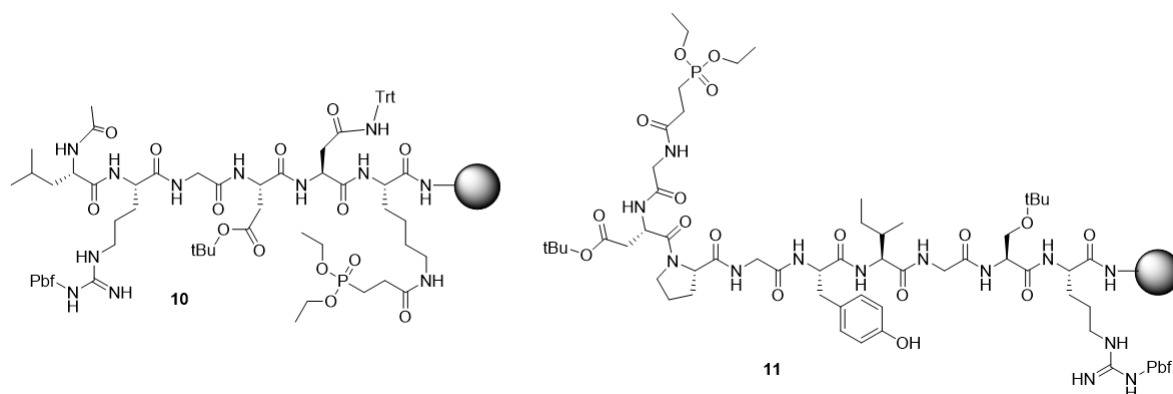
b. Peptidyl resin 2 (precursor of H-GDPGYIGSR-NH₂ 2' peptide)



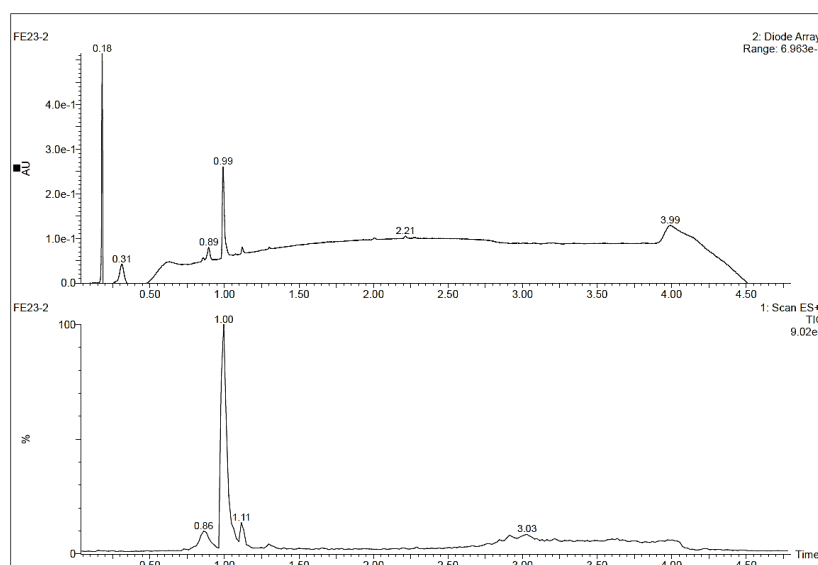
Synthesis by SPPS was made using the H-Rink Amide PS (0.47 mmol.g⁻¹, 0.69 g) resin in DMF. The first to the ninth coupling reactions were performed using Fmoc amino acid (3.82mL,5eq)/DIEA (664μL, 10eq)/HATU (3.82mL, 5eq) mixture

for 5 minutes twice with a DMF washing steps in between. The seventh coupling reaction was performed using the Fmoc-Pro-OH (3.82mL, 5eq)/DIEA (664μL, 10eq) / HATU (3.82mL, 5eq) mixture for 15 minutes twice in DMF. The Fmoc removal steps were realized using piperidine/DMF (20/80 v/v) solution (15 mL) for 1 minute and performed twice. All washings were done successively with 15 mL of DMF, DCM and DMF after coupling steps and deprotection steps. To check the peptide structure, a microcleavage followed by LC-MS analysis (Figure) was performed (87% of purity).

3. Functionalization of the peptidyl resin **1** and **2** with the (diethoxyphosphoryl)propionic acid **9** on solid support



The functionalization of the peptidyl resin **1** and **2** were performed using the 3-(diethoxyphosphoryl)propanoic acid **9** (5eq)/DIEA (30eq)/HATU (5eq) mixture for 10 minutes twice with a DMF washing steps in between. All washings were done successively with 15 mL of DMF, DCM and DMF after coupling steps and deprotection steps. To check structure of **10** and **11**, a microcleavage followed by LC-MS analyses were performed (84% and 84% of purity, respectively).



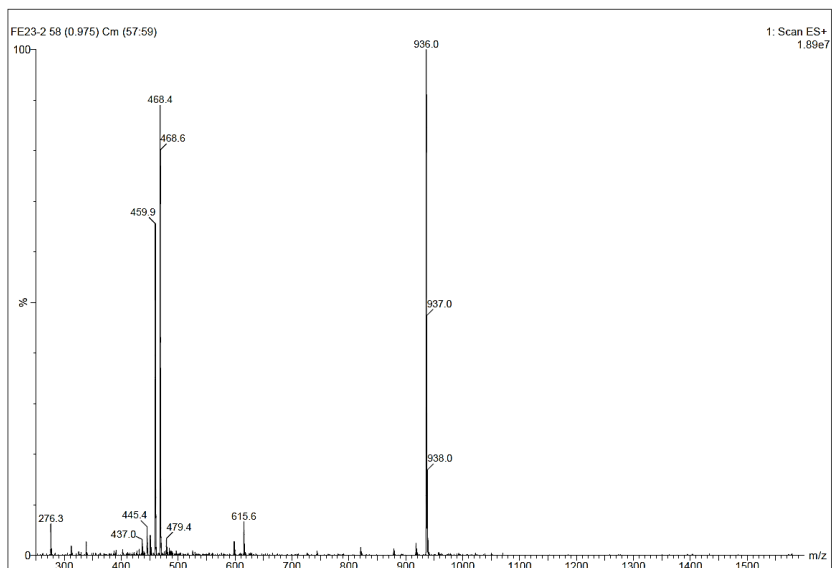
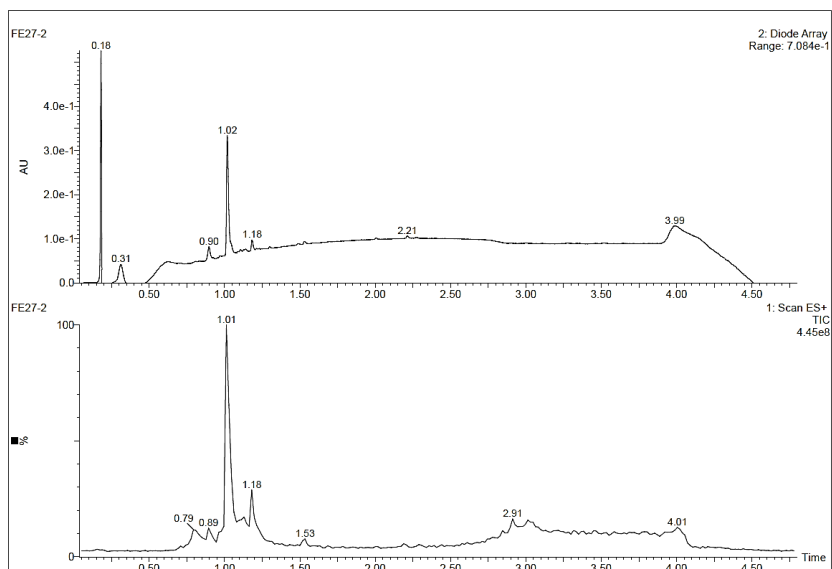


Figure 91 : LC-MS Spectra of compound 10

LC-MS (ESI+): tR = 1.0 min, m/z 936.0 [M+1H]⁺; m/z 468.4 [M+2H]²⁺



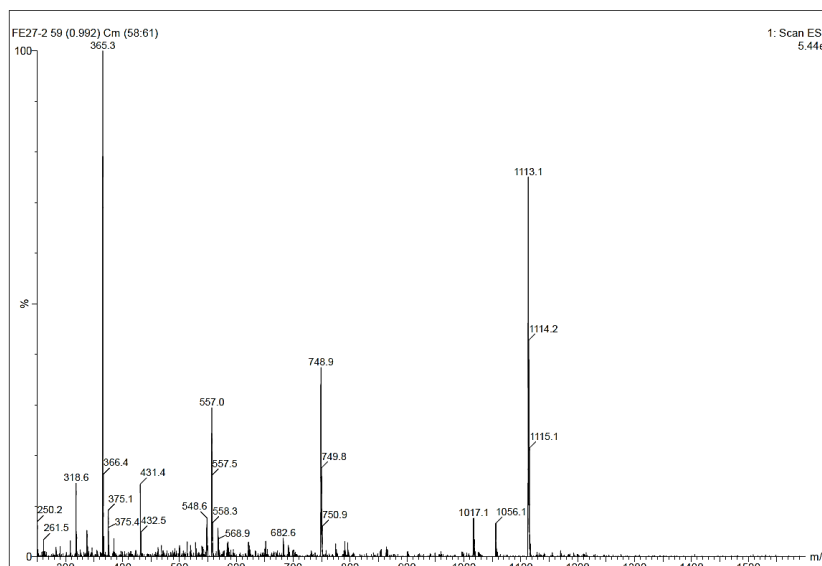
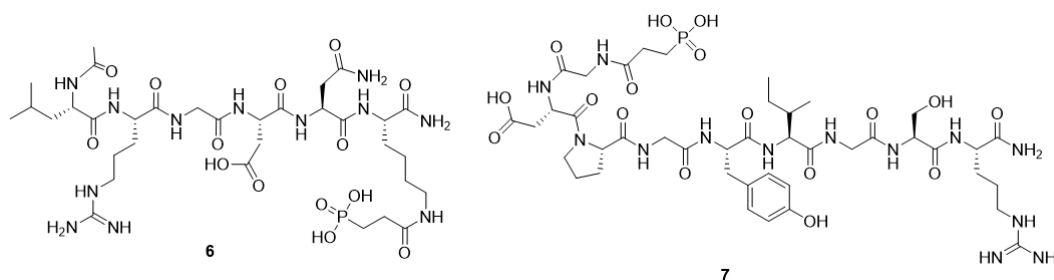


Figure 92 : LC-MS Spectra of compound **11**

LC-MS (ESI+): tR = 1.01 min, m/z 1113.1 [M+1H]⁺; m/z 557.0 [M+2H]²⁺

4. Dealkylation of compound **10** and **11** by using the McKenna reaction to obtain the new peptide-based stabilizing agents **6** and **7**



The peptidyl resin was washed with 15 mL of DMF and DCM twice for each. The resin was dried as much as possible under vacuum. The syringe containing the resin was placed under argon. 10 mL of anhydrous ACN was added to the syringe. The TMSBr (59eq) was added under argon and the solution was agitated overnight. The solvent was removed and resin was washed with 15 mL of ACN, MeOH and DCM twice for each. The peptide was cleaved from the resin with TFA/H₂O/TIS (95/2.5/2.5, v/v/v) mixture (2x1h30), concentrated with the rotary evaporator, recovered by precipitation in Et₂O. The powder was dried under vacuum. The products obtained **6** (197 mg, 56% of yield) and **7** (142 mg, 41% of yield) were analysed by NMR.

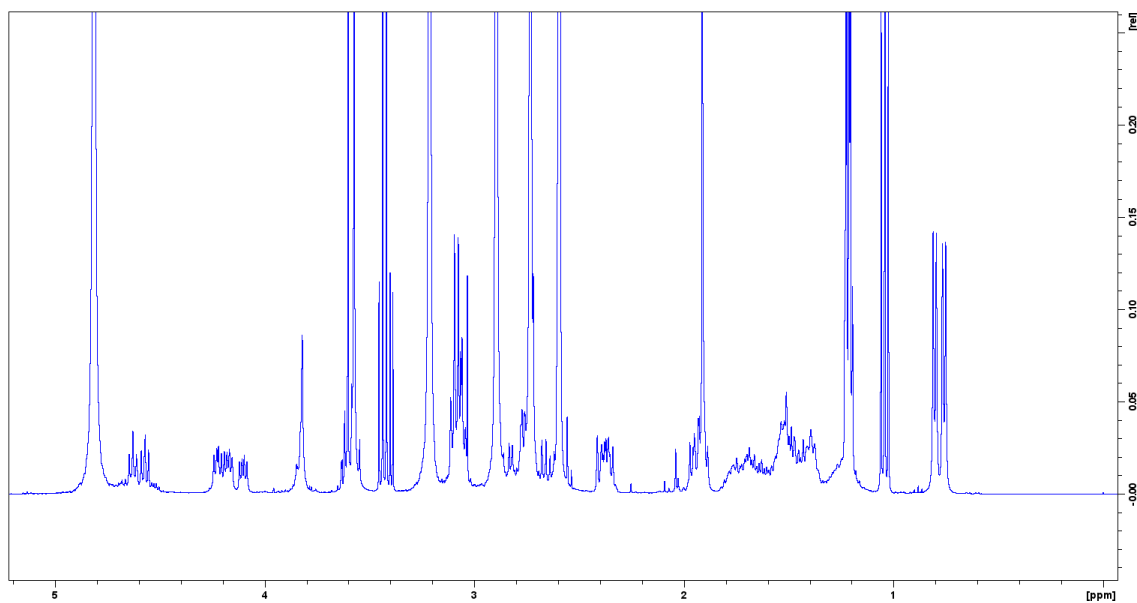


Figure 93 : ^1H NMR Spectrum of P(RGD) 6 (D_2O , 600 MHz)

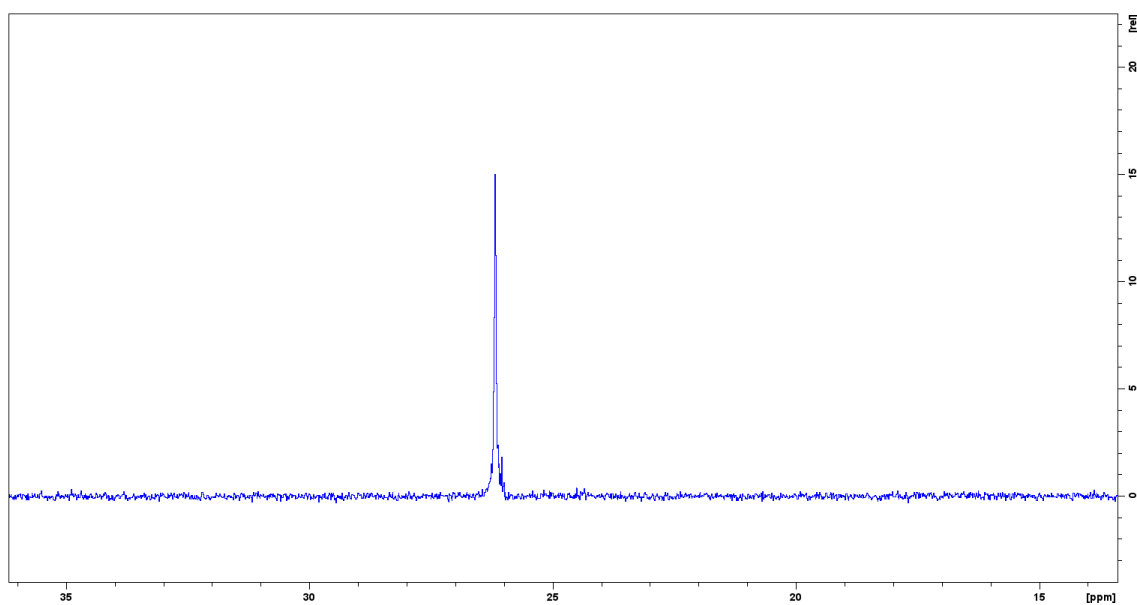


Figure 94 : ^{31}P NMR Spectrum of P(RGD) 6 (D_2O , 600 MHz, 36.32ppm)

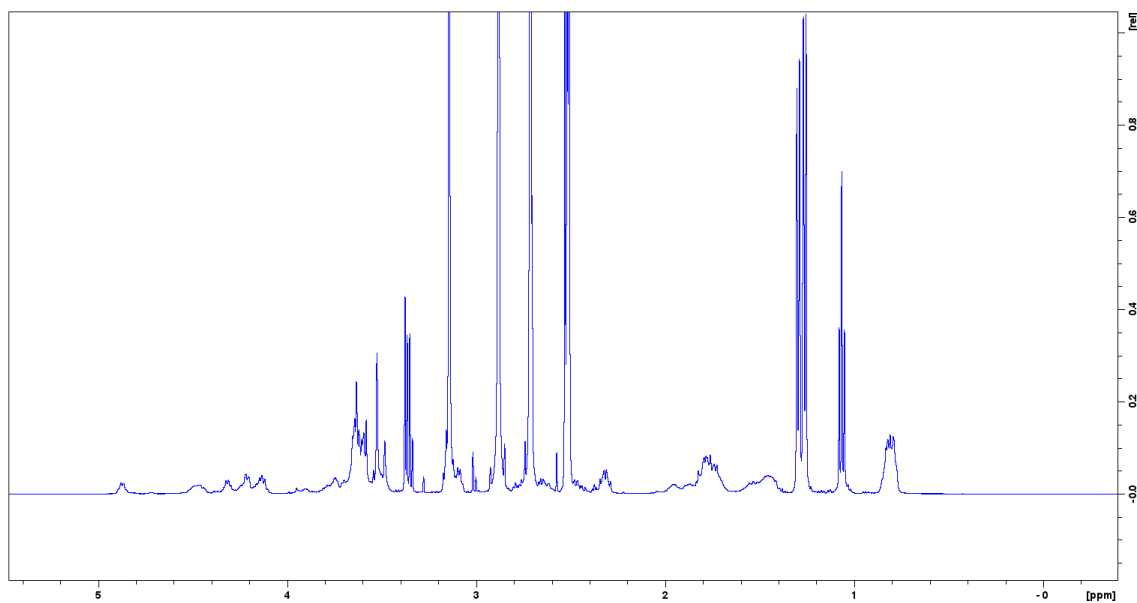


Figure 95 : ^1H NMR Spectrum of P(YIGSR) 7 (D_2O , 600 MHz)

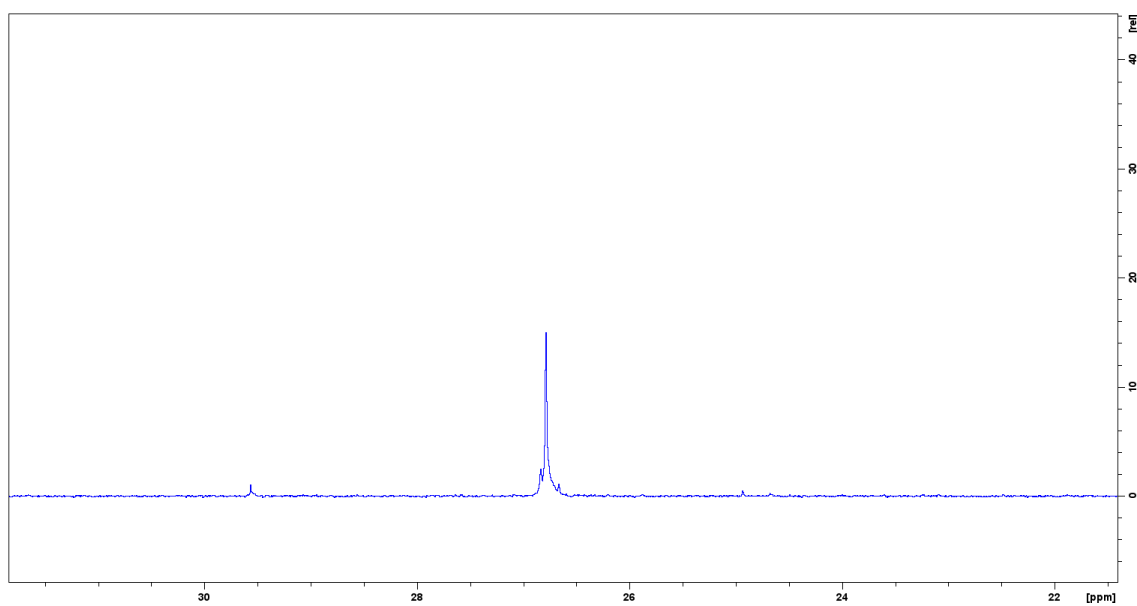
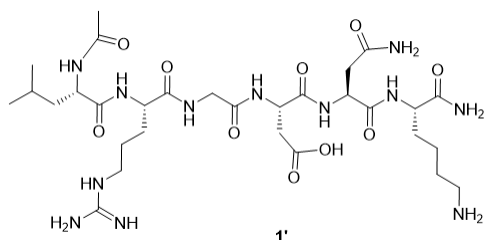


Figure 96 : ^{31}P NMR Spectrum of P(RGD) 6 (D_2O , 600 MHz, 26.76ppm)

D. Synthesis of novel bioactive peptide-based stabilizing agents P(PEG3K)-Peptide 27, 28, 29 and P(PEG3K)-NEt₂ 30

1. Synthesis of peptides 1', 2' and 22

a. Synthesis of Ac-LRGDNK-NH₂ 1'



Synthesis by SPPS was made using the H-Rink Amide ChemMatrix (0.47 mmol.g⁻¹, 1.2g) resin in DMF. The first to the sixth coupling reactions were performed using Fmoc amino acid (8.80mL, 5eq) / DIEA (1.52mL, 10eq) / HATU (8.80mL, 5eq) mixture for 5 minutes twice with a DMF washing step in between. The

Fmoc removal steps were realized using piperidine/DMF 20/80 v/v solution (15mL) for 1 minute and performed twice. All washings were done successively with 15mL of DMF, DCM and DMF after coupling steps and deprotection steps. N-Terminal acetylation was performed with 20% Ac₂O in DMF and DIEA (1%) for 15 minutes twice. The Alloc protection was removed in DCM with 0.25eq of palladium tetrakis triphenylphosphine followed by 25eq of phenylsilane. The reaction was agitated during 1 hour and performed twice. The solvent was removed and the resin was washed with DCM and DMF (x3). The peptide was cleaved from the resin with TFA/H₂O/TIS (95/2.5/2.5, v/v/v) mixture (2x1h30), concentrated under reduced pressure, recovered by precipitation in Et₂O. The powder was dried in the dessicator and obtained with 32% of yield (135mg, 98% of purity). The crude was analysed by LC-MS and NMR analyses.

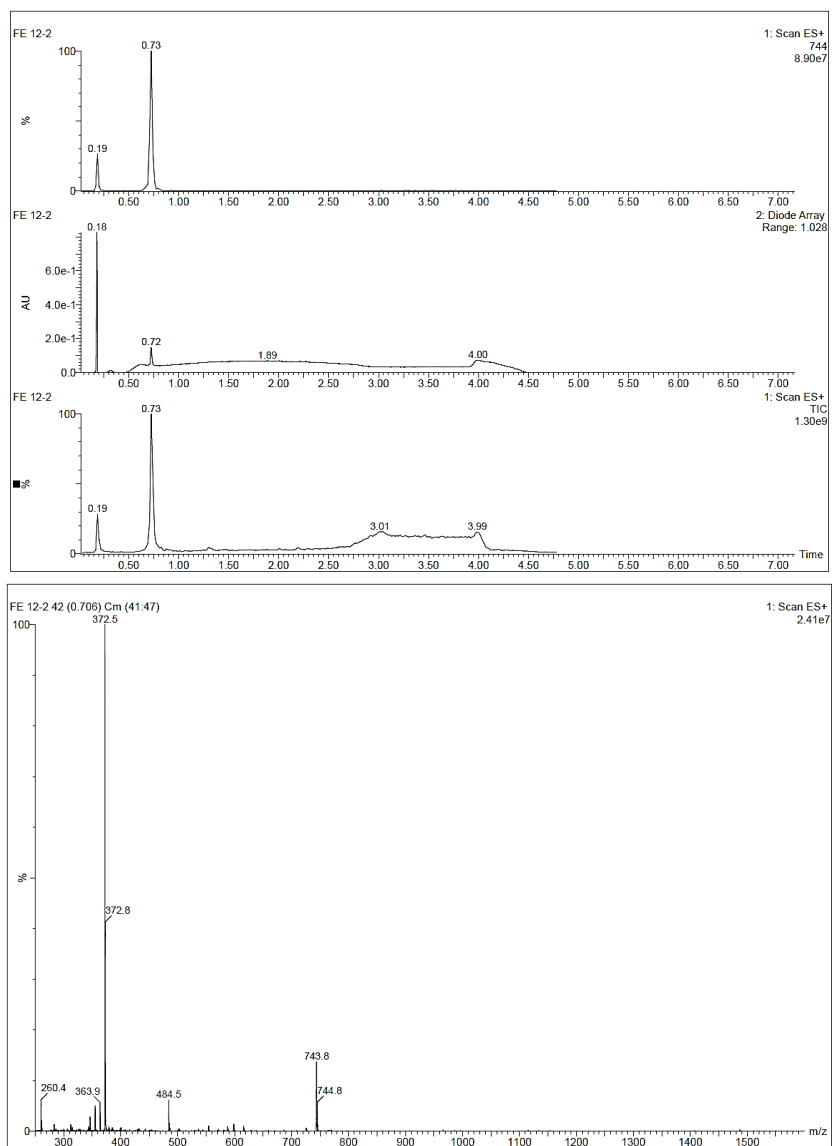


Figure 97: LC-MS Spectra of Ac-LRGDNK-NH₂ peptide 1'

LC-MS (ESI+): tR = 0.73 min, m/z 743.8 [M+1H]⁺; m/z 372.5 [M+2H]²⁺

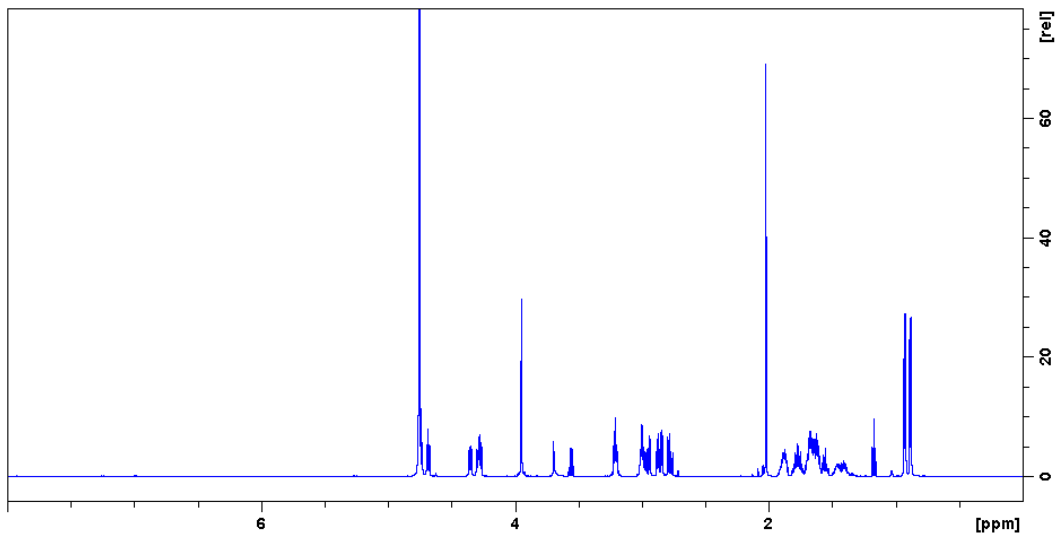


Figure 98: ^1H NMR Spectrum of Ac-LRGDNK-NH₂ peptide **1'** (D₂O, 600 MHz)

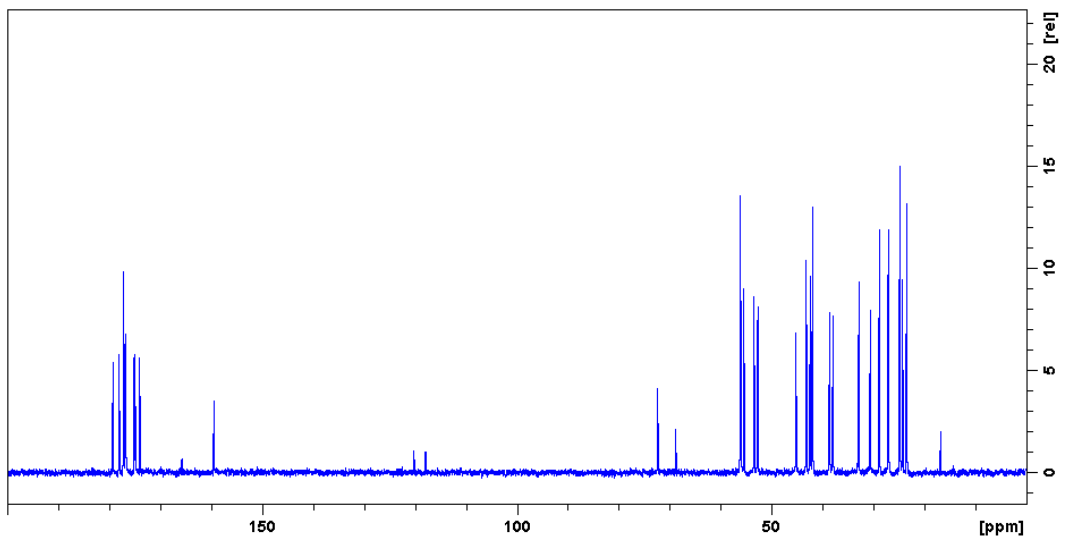


Figure 99: ^{13}C NMR Spectrum of Ac-LRGDNK-NH₂ peptide **1'** (D₂O, 600 MHz)

Ac-Leu-Arg-Gly-Asp-Asn-Lys-NH ₂							
		¹ H	¹³ C			¹ H	¹³ C
Ac	CH ₃	2,02	24,3	Gly	CH ₂	3,95	45,2
	C=O	x	177,2		C=O	x	174
Leu	CH _α	4,29	55,4	Asp	CH _α	4,74	52,7
	CH ₂ β	1,61 - 1,55	42,4		CH ₂ β	2,95-2,85	37,9
	CH (iso)	1,64	27	COOH	x	176,9	
	CH ₃ (iso)	0,93	24,9	C=O	x	175,1	
Arg		0,88	23,4	Asn	CH _α	4,68	53,4
	C=O	x	178,1		CH ₂ β	2,85-2,77	53,4
	CH _α	4,35	56,1	CONH ₂	x	177,2	
	CH ₂ β	1,88-1,78	30,6	C=O	x	174,9	
	CH ₂ γ	1,67-1,61	27,1	Lys	CH _α	4,27	56,1
	CH ₂ δ	3,21	43,2		CH ₂ β	1,87-1,76	32,9
	C=N	x	159,5		CH ₂ γ	1,46-1,40	24,8
	C=O	x	176,8	CH ₂ δ	1,67	28,9	

Table 28 : Protons and carbons chemical shift assignments of the peptide Ac-LRGDNK-NH₂ 1' (D₂O, 600 MHz)

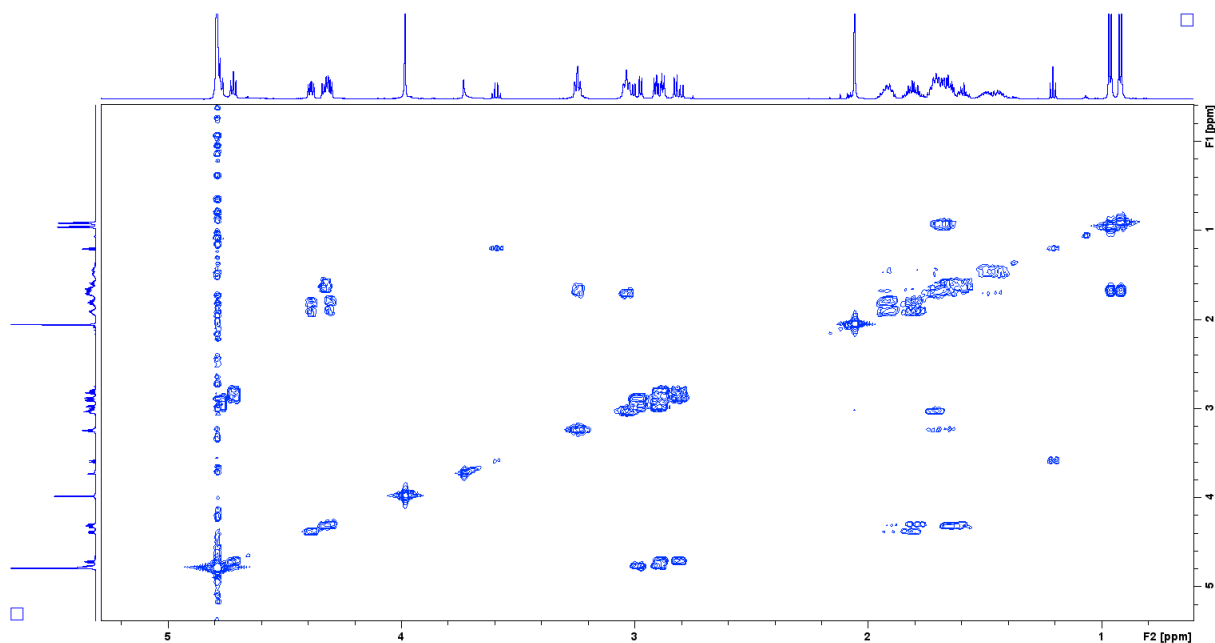


Figure 100 : ¹H-¹H COSY NMR Spectrum of Ac-LRGDNK-NH₂ peptide 1' (D₂O, 600 MHz)

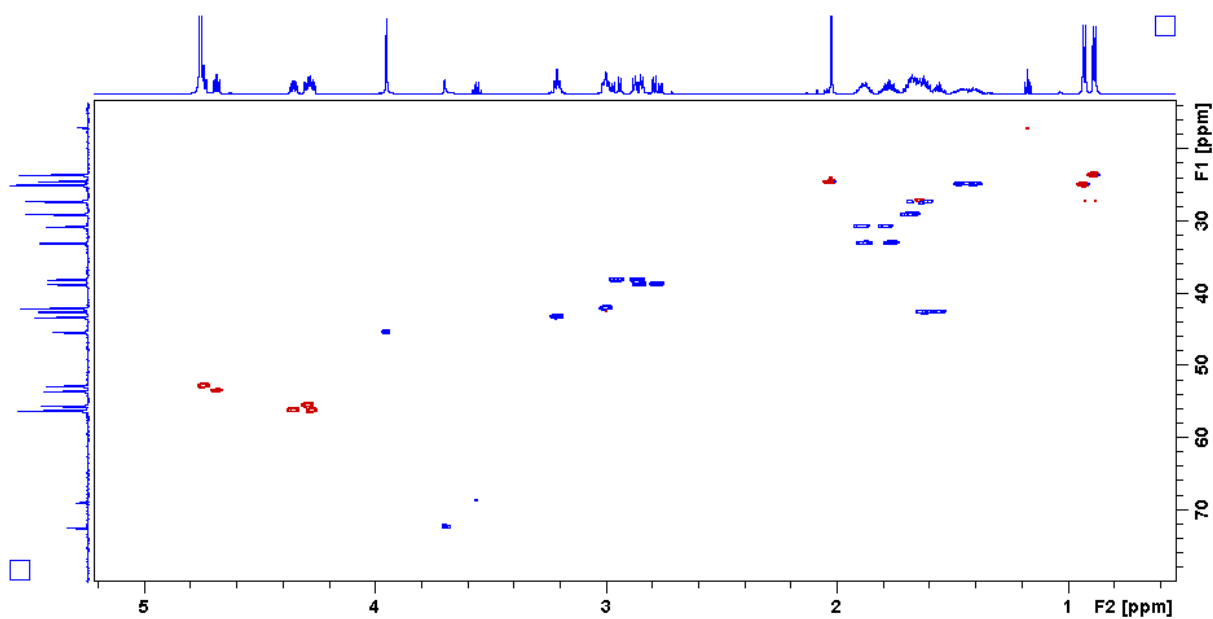


Figure 101: ^{13}C - ^1H HSQC NMR Spectrum of Ac-LRGDNK-NH₂ peptide 1' (D₂O, 600 MHz)

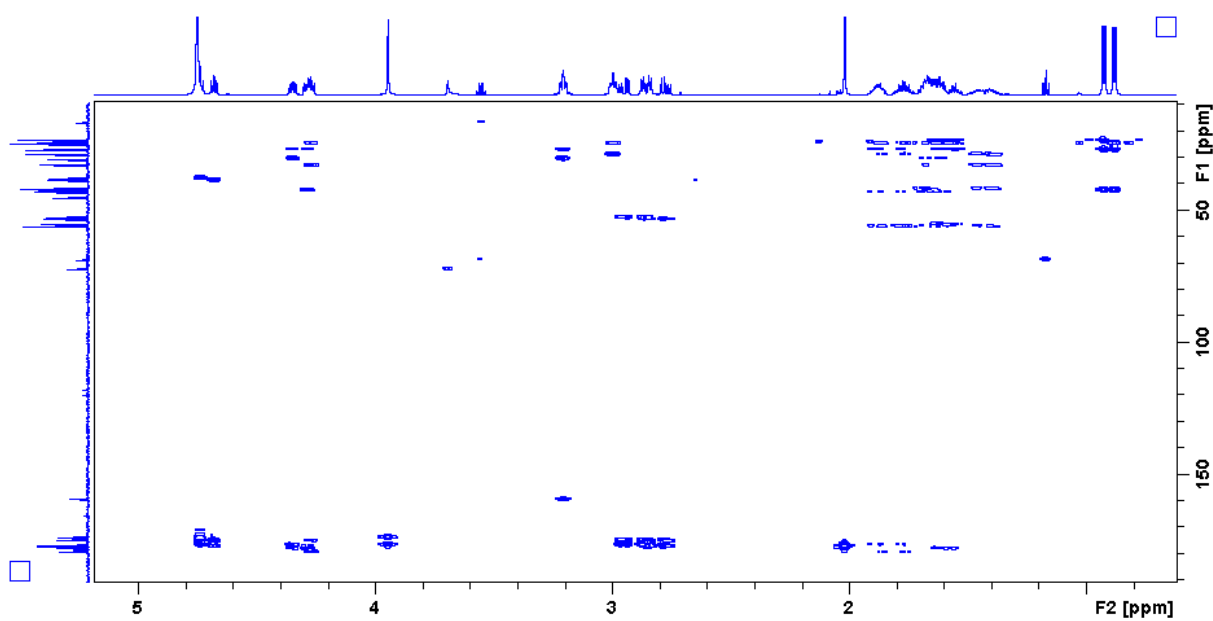
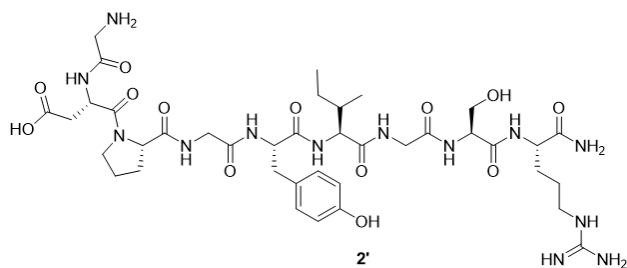


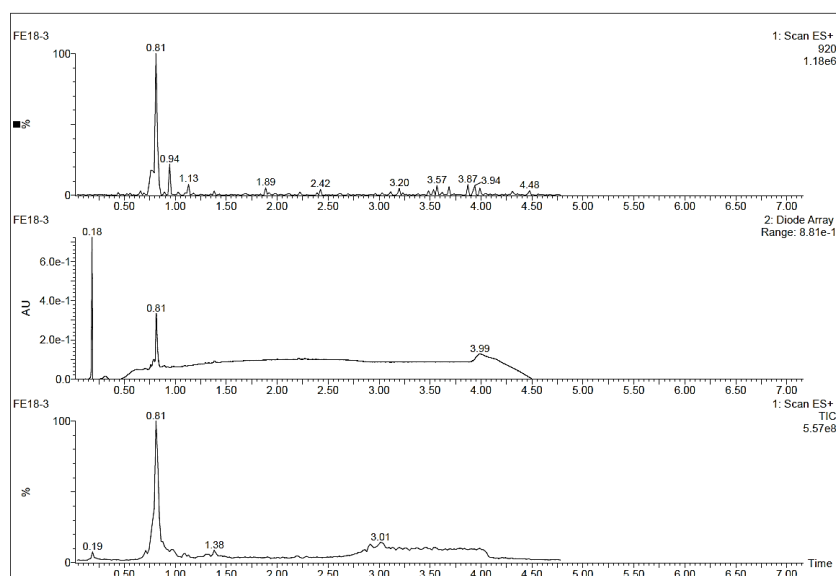
Figure 102: ^{13}C - ^1H HMBC NMR Spectrum of Ac-LRGDNK-NH₂ peptide 1 (D₂O, 600 MHz)

b. Synthesis of H-GDPGYIGSR-NH₂ 2'



Synthesis by SPPS was made using the H-Rink Amide ChemMatrix (0.47 mmol.g⁻¹, 0.94 g) resin in DMF. The first to the ninth coupling reactions were performed using Fmoc amino acid (5.17 mL, 5eq) / DIEA (889 μL, 10eq) / HATU (5.17 mL, 5eq) mixture for 5 minutes twice with a DMF washing

step in between. The seventh coupling reaction was performed using the Fmoc-Pro-OH (5.17 mL, 5eq) / DIEA (889 μL, 10eq) / HATU (5.17 mL, 5eq) mixture for 15 minutes twice in DMF. The Fmoc removal steps were realized using piperidine/DMF (20/80 v/v) solution (15 mL) for 1 minute and performed twice. All washings were done successively with 15 mL of DMF, DCM and DMF after coupling steps and deprotection steps. The peptide was cleaved from the resin with TFA/H₂O/TIS, 95/2.5/2.5, v/v/v mixture (2x1h30), concentrated under reduced pressure, recovered by precipitation in diethyl ether. The powder was dried in the dessicator and obtained with 41% of yield (167 mg, 95% of purity). The crude was analysed by LC-MS and NMR analyses.



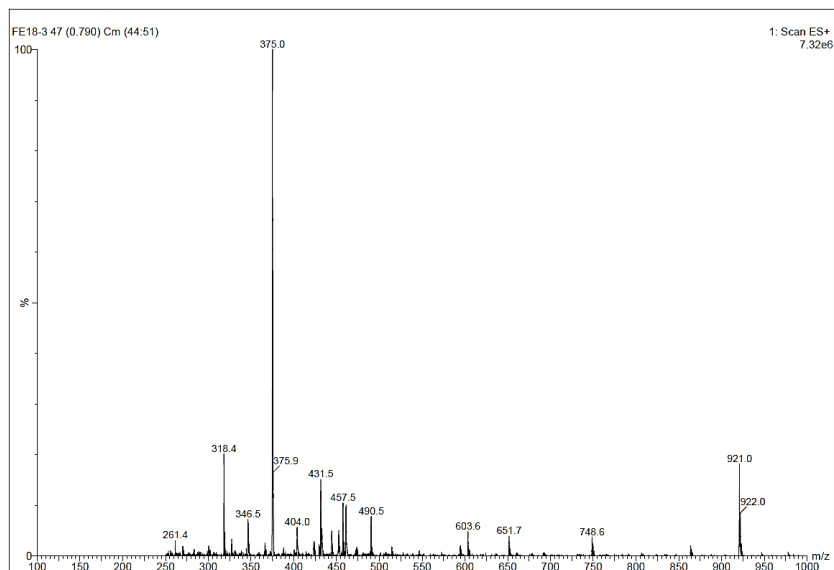


Figure 103 : LC-MS Spectra of H-GDPGYIGSR-NH₂ peptide 2'

LC-MS (ESI+): tR = 0.81 min, m/z 921.0 [M+1H]⁺; m/z 375.0 [M+2H]²⁺

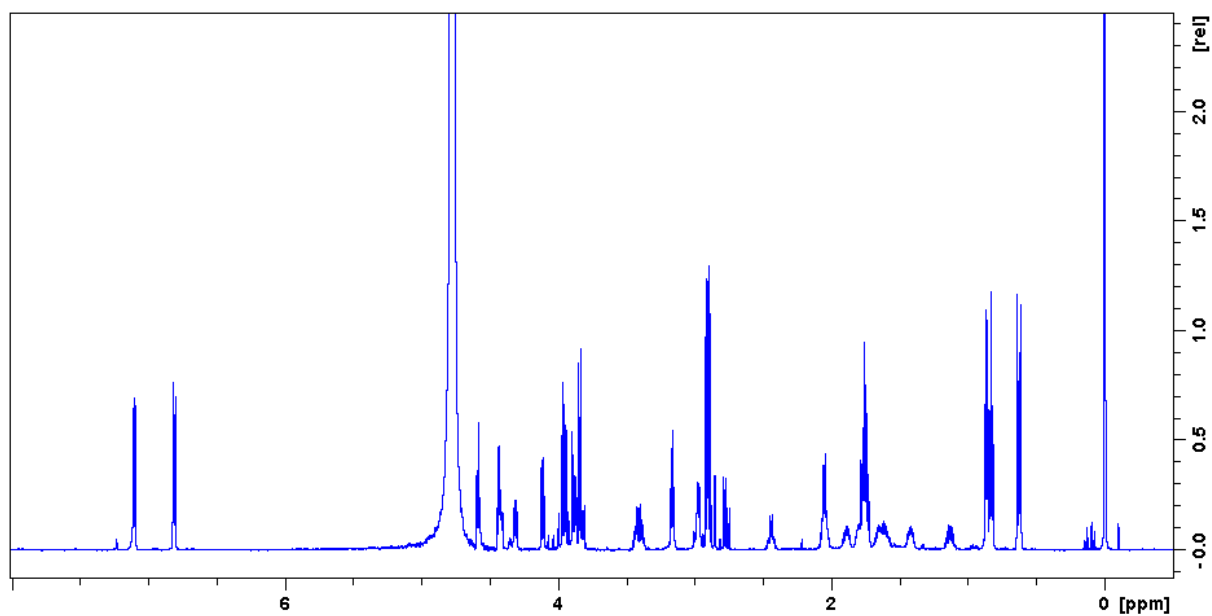


Figure 102: ^1H NMR Spectrum of H-GDPGYIGSR-NH₂ peptide **2'** (D₂O, 600 MHz)

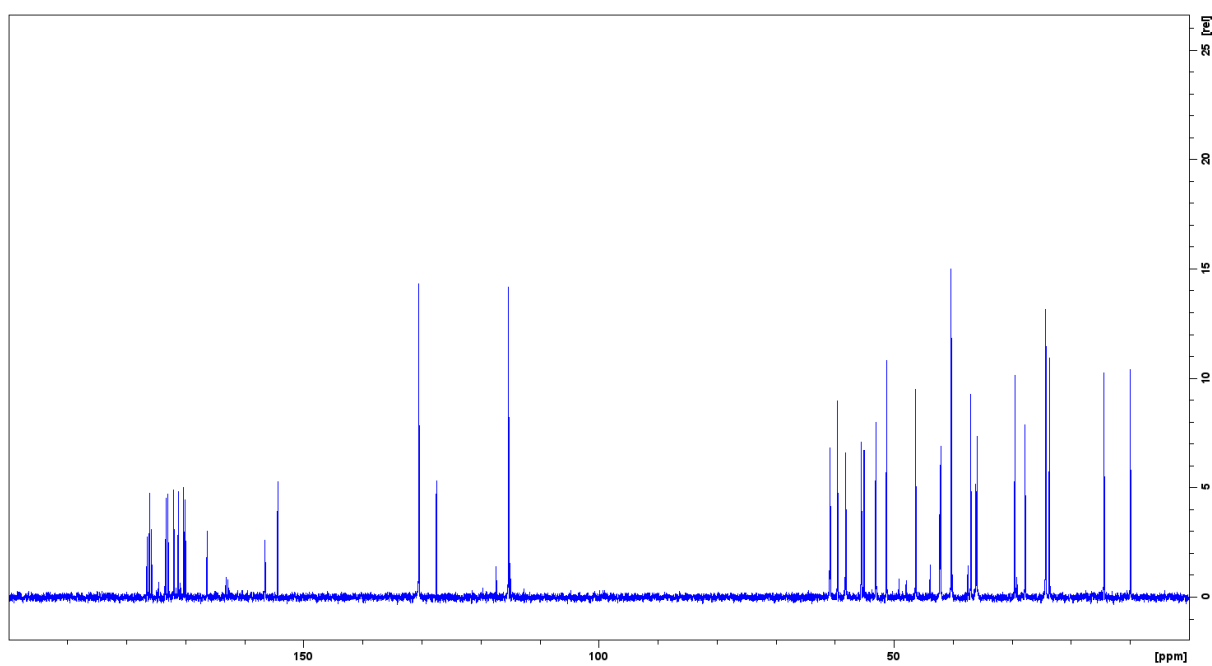


Figure 105: ^{13}C NMR Spectrum of H-GDPGYIGSR-NH₂ peptide **2'** (D₂O, 600 MHz)

H-Gly-Asp-Pro-Gly-Tyr-Ile-Gly-Ser-Arg-NH ₂							
		¹ H	¹³ C			¹ H	¹³ C
Gly	CH ₂	3,86-3,82	43,2	Ile	CH α	4,13	61
	C=O	x	169,2		CH β	1,83	38,8
Asp	CH α	4,58	54,1	CH ₃	0,89	17,3	
	CH ₂ β	2,87-2,77	39,9	CH ₂ γ	1,44-1,16	27,1	
	COOH	x	179,4	CH ₃	0,86	12,8	
	C=O	x	178,7	C=O	x	176,2	
Pro	CH α	4,42	62,4	Gly	CH ₂	3,94-3,88	44,9
	CH ₂ β	2,44-2,05	32,4		C=O	x	174,1
	CH ₂ γ	2,05	26,5	Ser	CH α	4,44	58,4
	CH ₂ δ	3,41	49,2		CH ₂ β - OH	3,88-3,83	63,7
	C=O	x	172,9		C=O	x	174,9
Gly	CH ₂	3,98-3,92	45,1	Arg	CH α	4,32	55,9
	C=O	x	173,2		CH ₂ β	1,89-1,75	30,7
Tyr	CH α	4,59	57,9	CH ₂ γ	1,65-1,61	27,1	
	CH ₂ β	2,98	39	CH ₂ δ	3,17	43,2	
	C η	x	130,4	C=N	x	159,4	
	CH	7,13	133,4	CONH ₂	x	179	
	CH		118,2				
	C η -OH	x	157,3				
	C=O	x	175,9				

Table 29 : Protons and carbons chemical shift assignments of the peptide H-GDPGYIGSR-NH₂ 2' (D₂O, 600 MHz)

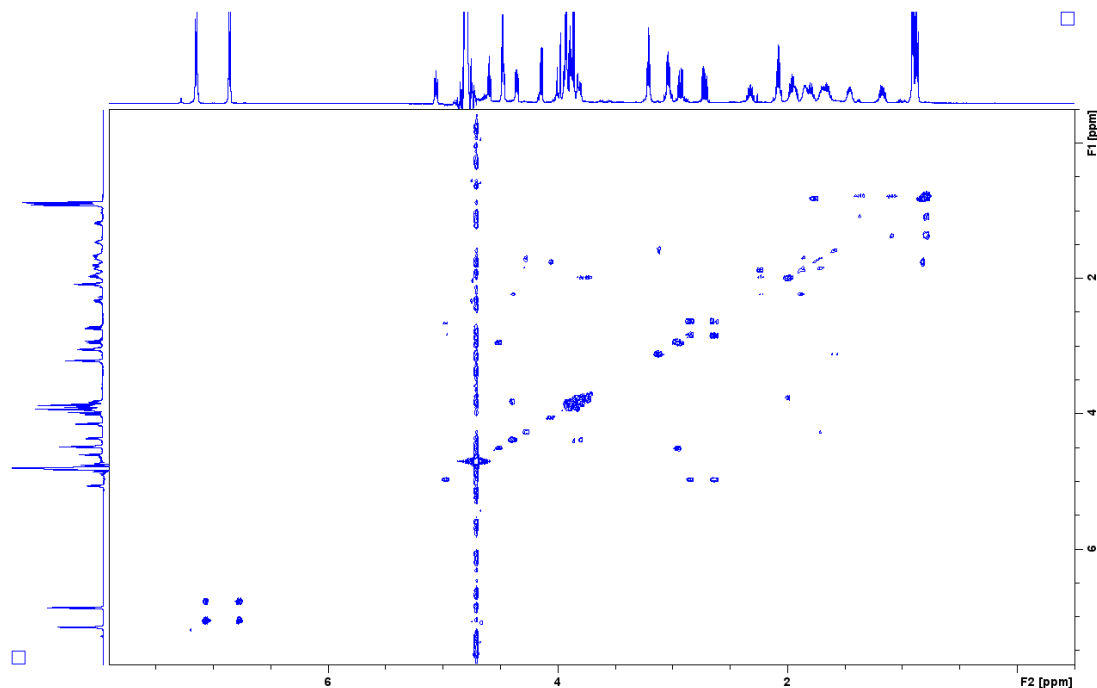


Figure 103 : ¹H-¹H COSY NMR Spectrum of H-GDPGYIGSR-NH₂ peptide 2' (D₂O, 600 MHz)

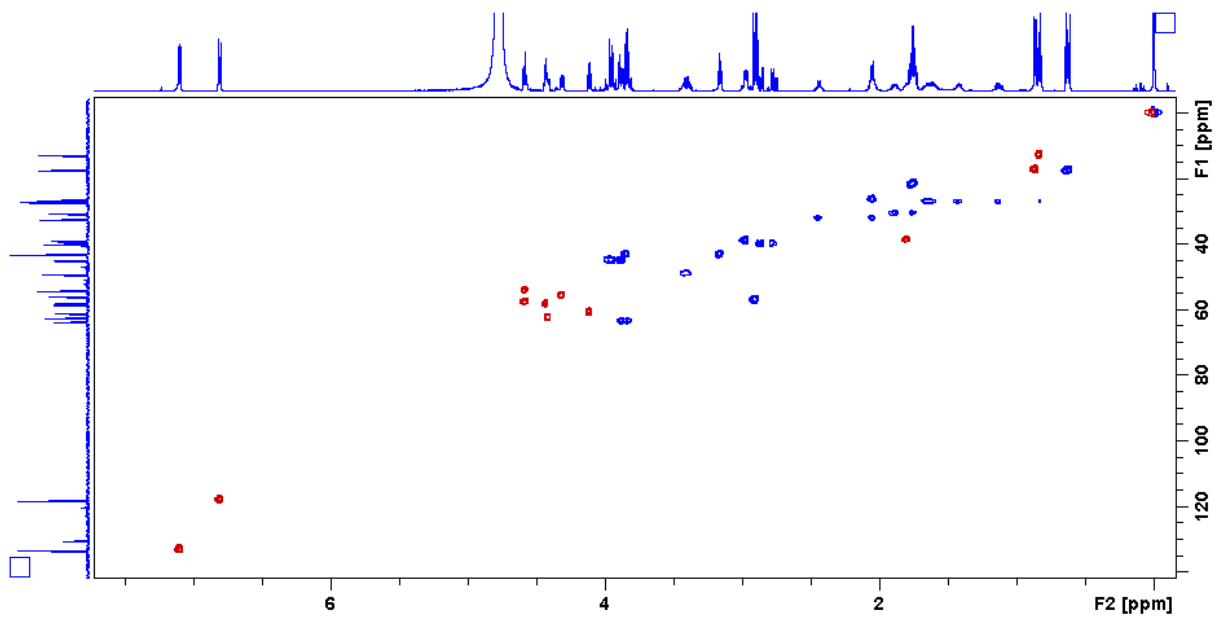


Figure 1047: ^{13}C - ^1H HSQC NMR Spectrum of H-GDPGYIGSR-NH₂ peptide 2' (D₂O, 600 MHz)

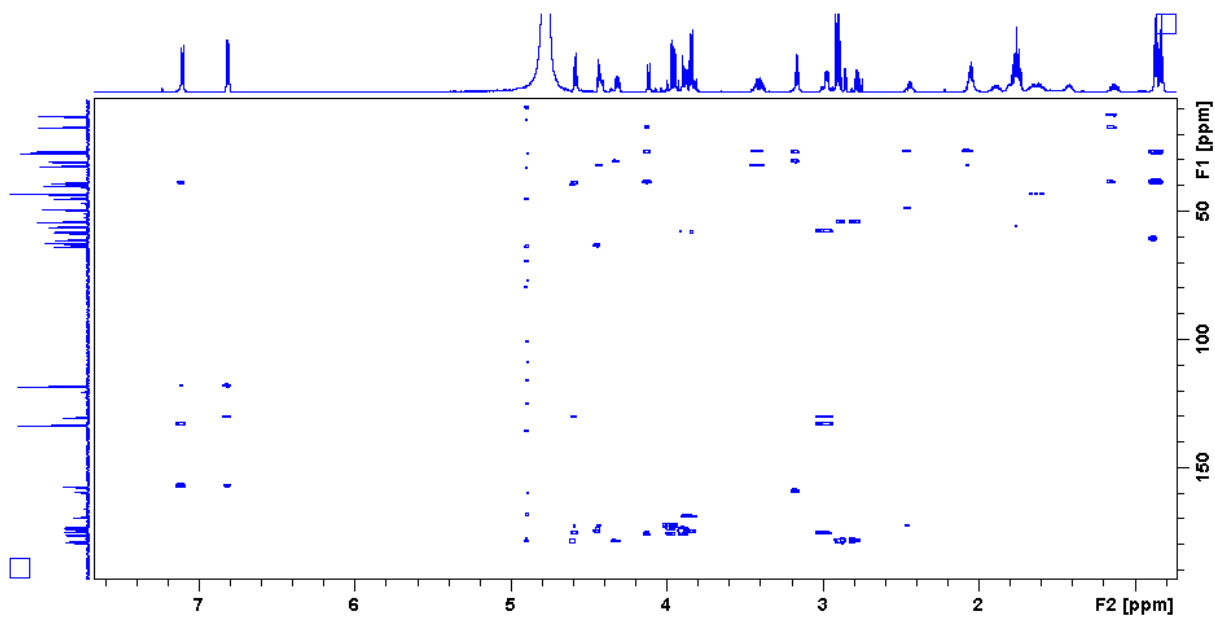
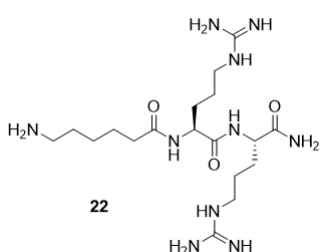
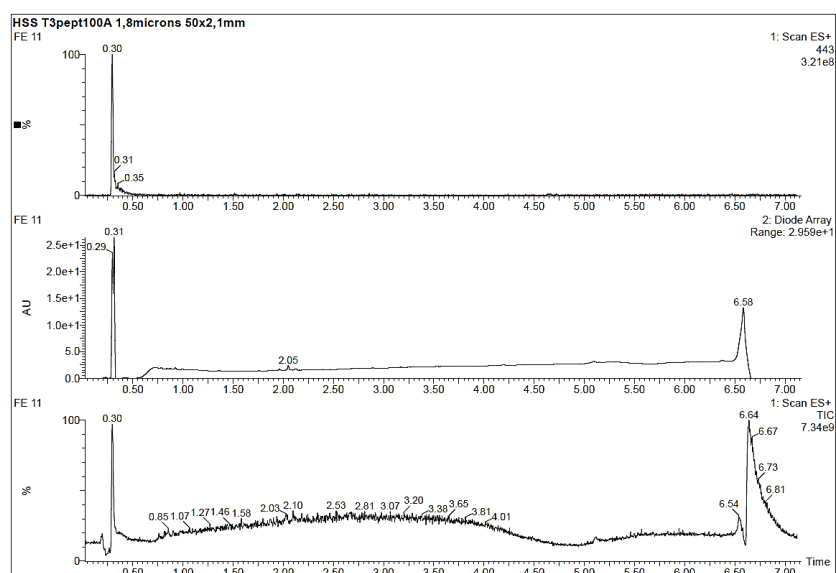


Figure 108: ^{13}C - ^1H HMBC NMR Spectrum of H-GDPGYIGSR-NH₂ peptide 2 (D₂O, 600 MHz)

c. Synthesis of H-AhXRR-NH₂ 22



Synthesis by SPPS was made using the H-Rink Amide ChemMatrix (0.47 mmol.g⁻¹, 0.6 g) resin in DMF. The first to the third coupling reactions were performed using Fmoc amino acid (1.75 mL, 5eq) / DIEA (311 μL, 10eq) / HATU (1.75 mL, 5eq) mixture for 10 minutes twice with a DMF washing step in between. The Fmoc removal steps were realized using piperidine/DMF (20/80 v/v) solution (15 mL) for 1 minute and performed twice. All washings were done successively with 15 mL of DMF, DCM and DMF after coupling steps and deprotection steps. The peptide was cleaved from the resin with TFA/H₂O/TIS (95/2.5/2.5 v/v/v) mixture (2x1h30), concentrated under reduced pressure, recovered by precipitation in diethyl ether. The powder was dried in the dessicator and obtained with 48% of yield (60 mg, 89% of purity). The crude was analysed by LC-MS and NMR analyses.



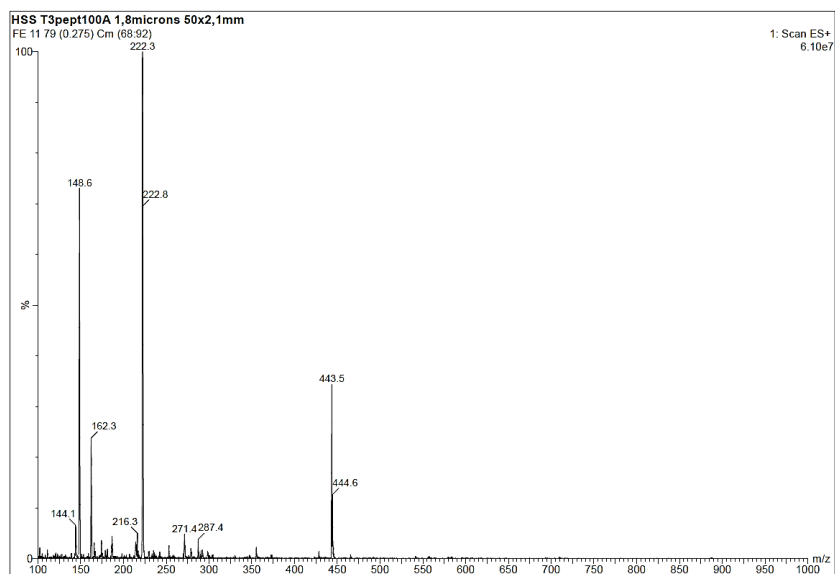


Figure 108 : LC-MS Spectra of H-AhXRR-NH₂ peptide **22**

LC-MS (ESI+): tR = 0.30 min, m/z 443.5 [M+1H]⁺; m/z 222.3 [M+2H]²⁺

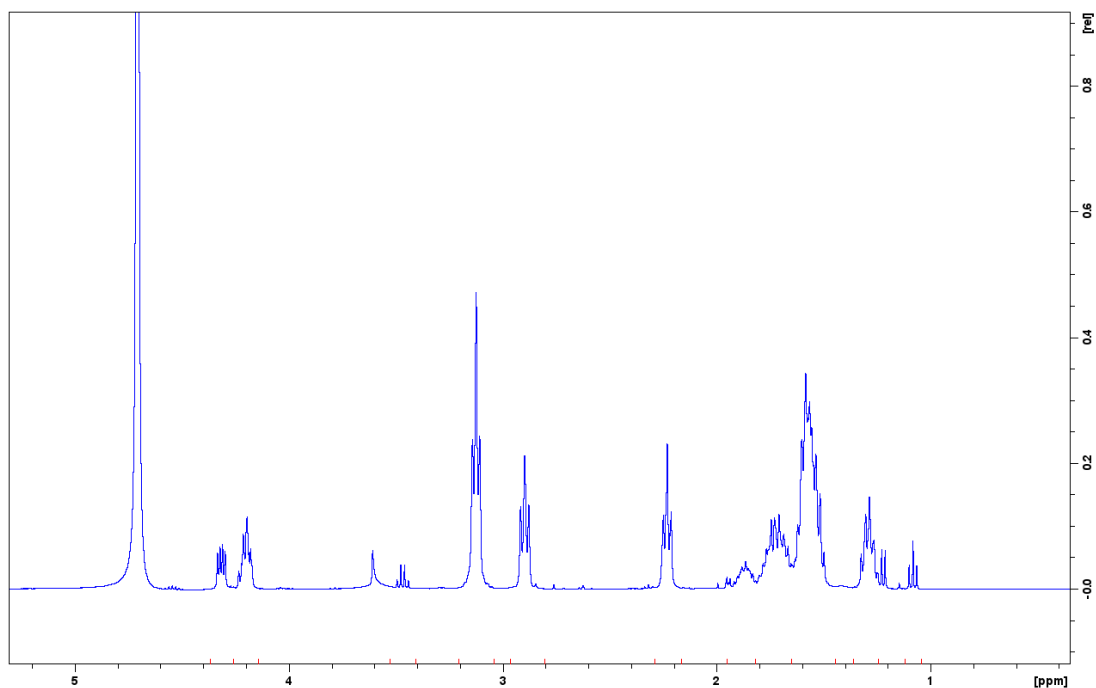


Figure 1059: ^1H NMR Spectrum of H-AhxRR-NH₂ peptide **22** (D₂O, 600 MHz)

H-Ahx-Arg-Arg-NH ₂			
		^1H	^{13}C
Arg	CONH ₂	x	174.2
	CH α	4.41	51.4
	CH ₂ β	1.81-1.97	27.0
	CH ₂ γ	1.68	23.7
	CH ₂ δ	3.22	39.8
	C=N	x	155.8
	C=O	x	173.1
Arg	CH α	4.29	52.7
	CH ₂ β	1.78-1.85	27.3
	CH ₂ γ	1.68	23.7
	CH ₂ δ	3.22	39.8
	C=N	x	155.8
	C=O	x	176.1
Ahx	CH α	2.33	34.0
	CH ₂ β	1.63	24.0
	CH ₂ γ	1.38	24.2
	CH ₂ δ	1.68	25.6
	CH ₂ ϵ	3.00	38.5

Table 30 : Proton and carbons chemical shift assignments of the peptide H-AhxRR-NH₂ **22** (D₂O, 600 MHz)

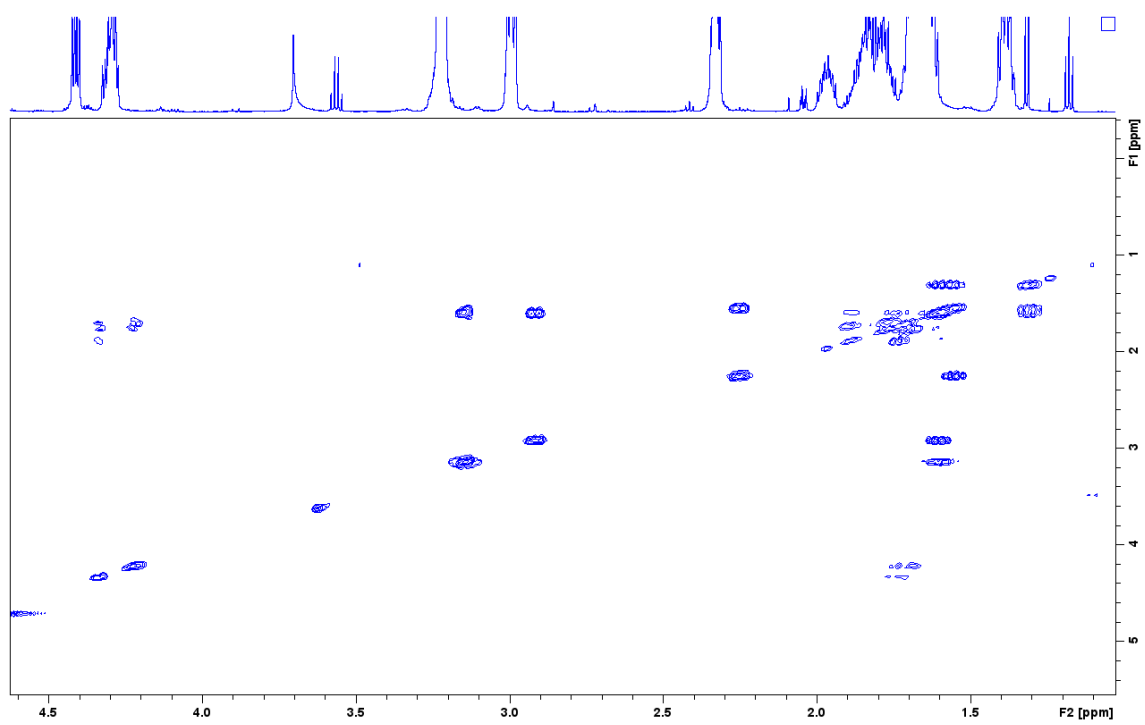


Figure 10610: ^1H - ^1H COSY NMR Spectrum of H-AhXRR-NH₂ peptide **22** (D₂O, 600 MHz)

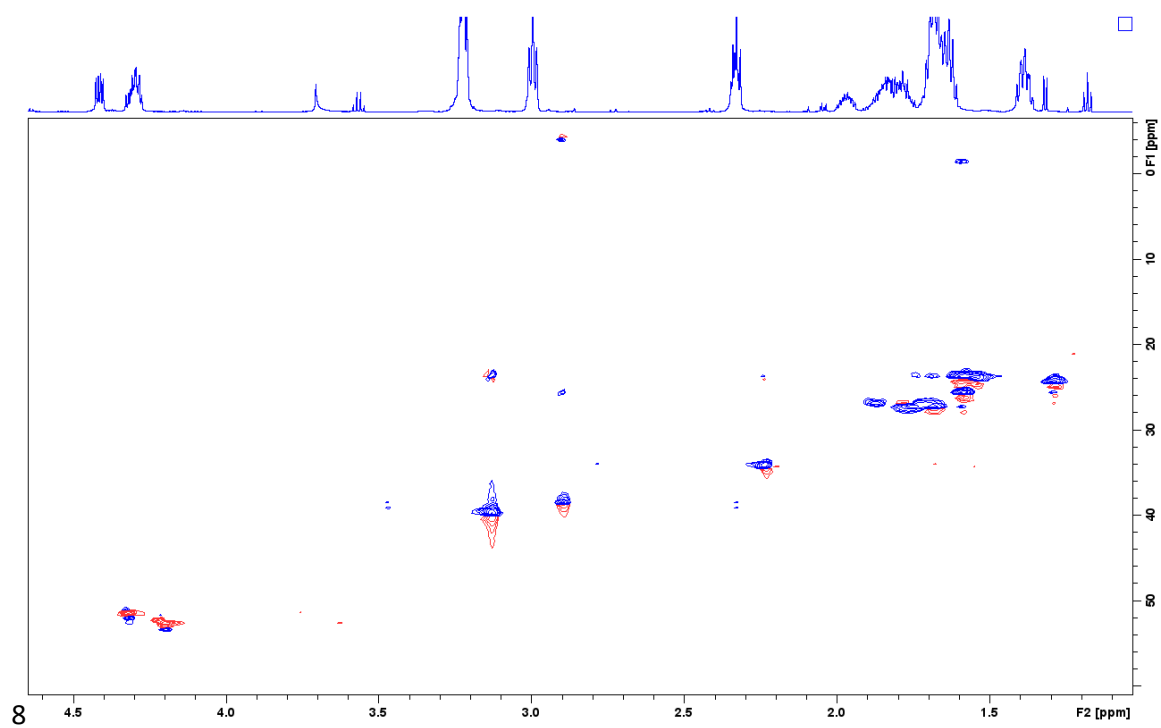


Figure 111: ^{13}C - ^1H HSQC NMR Spectrum of H-AhXRR-NH₂ peptide **22** (D₂O, 600 MHz)

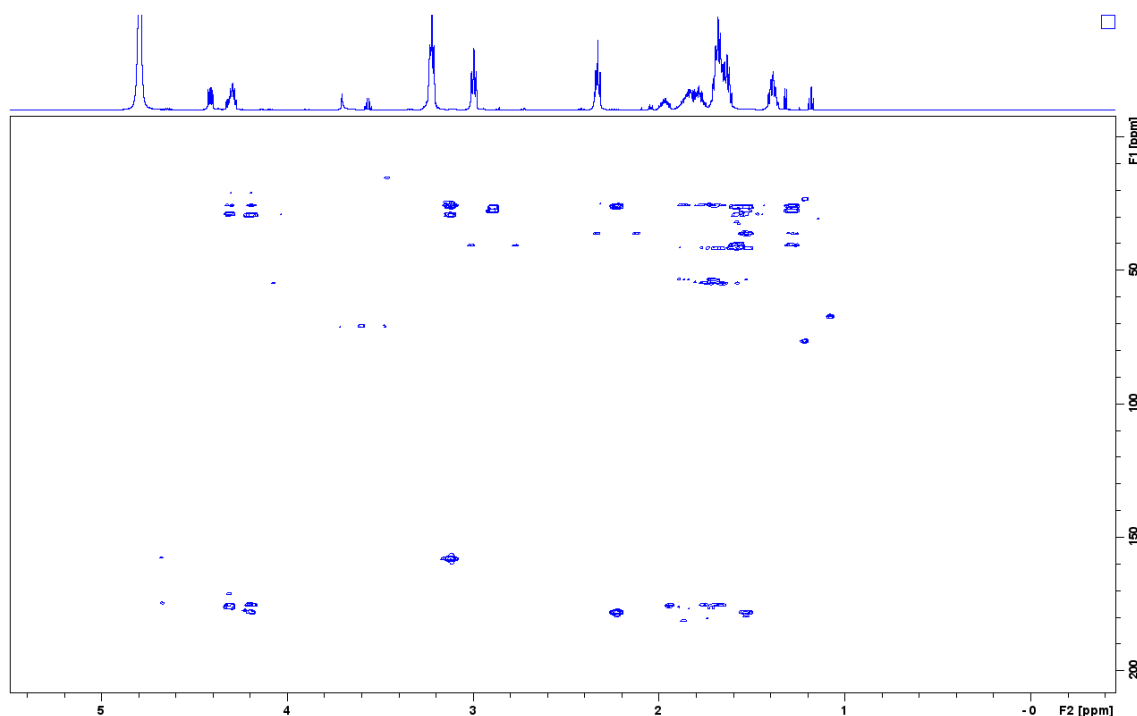
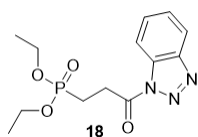


Figure 112: ^{13}C - ^1H HMBC NMR Spectrum of H-AhXRR-NH₂ peptide **22** (D₂O, 600 MHz)

2. Synthesis of PO₃Et₂(PEG3K)-COOH **21**

a. Synthesis of compound **18** : Activation of carboxylic acid via the N-acyl benzotriazole formation



The carboxylic acid of compound **9** was activated with a benzotriazole. For that, the compound **9** (600mg, 2.86mmol) was dissolved in AcOEt (5mL). All reactants were respectively added, benzotriazole (409 mg, 3.43 mmol, 1.2eq), anhydride propylphosphonic (T3P) in 50% of AcOEt (3.3 mL, 1.82 g, 5.71 mmol, 2eq) and pyridine (692 μL , 677.82 mg, 8.58 mmol, 3eq). The solution was stirred at room temperature and monitored by LC-MS. The solution was washed with a solution of NaHSO₄ 1M and extracted three times with water. The organic phase was evaporated under vacuum and an oil was obtained (50% of yield, 445 mg, 83% of purity) and analyzed by LC-MS and ^1H MNR.

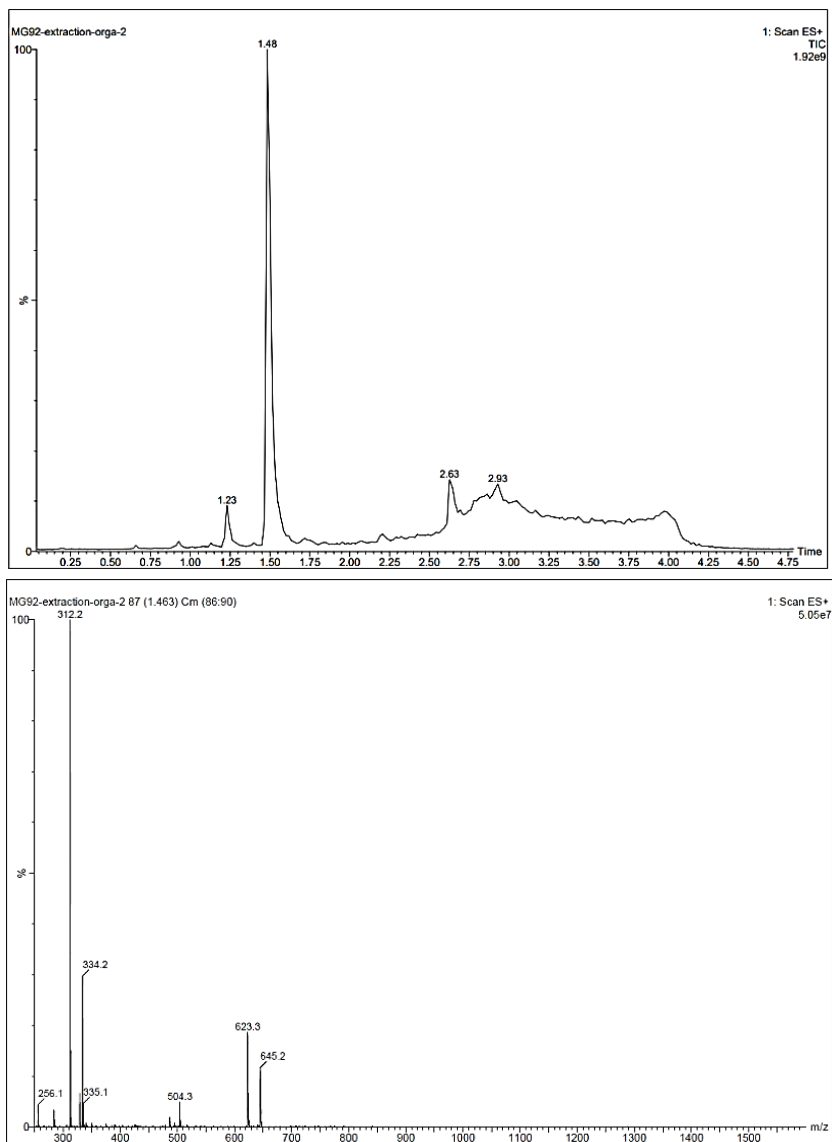


Figure 113: LC-MS Spectra of *N*-acyl benzotriazole **18**

LC-MS (ESI+): tR = 1.48 min, m/z 623.3 [M+H]⁺; 312.2 [M+2H]²⁺

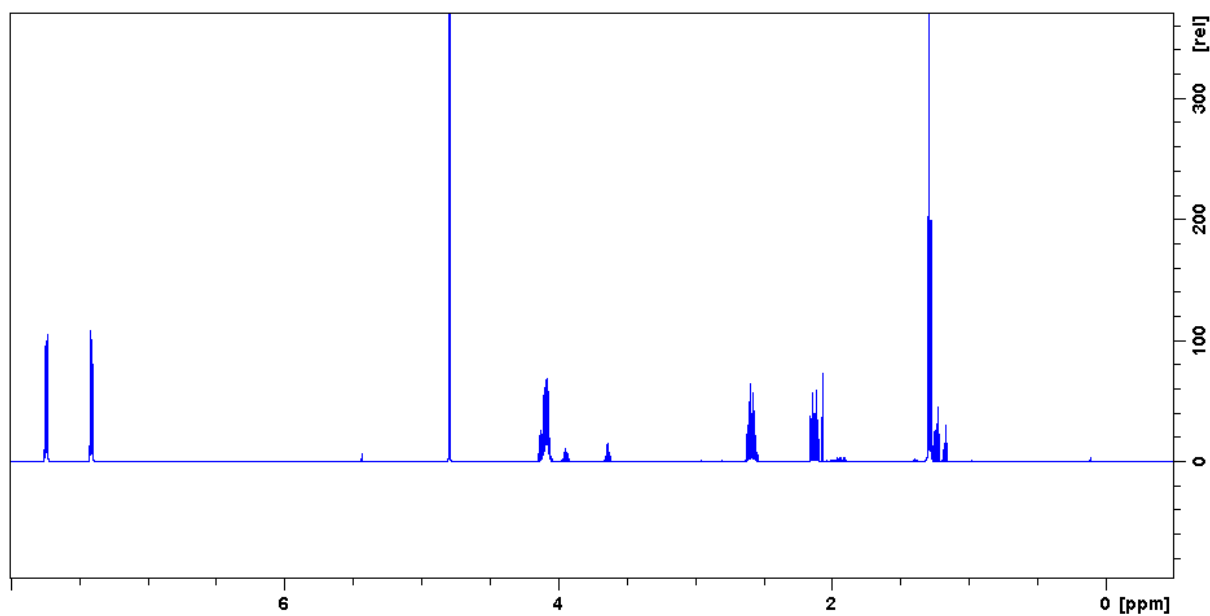


Figure 114: ^1H NMR Spectra of the *N*-acyl benzotriazole **18** (D_2O , 600 MHz)

^1H NMR (600 MHz, D_2O , 298K): δ (ppm) 1.29 (t, 6H, $J = 7.0$ Hz) ; 2.13 (td, 2H, $J = 7.6 / 18.0$ Hz); 2.59 (m, 2H); 4.08 (m, 4H); 7.41 (m, 2H) ; 7.74 (m, 2H).

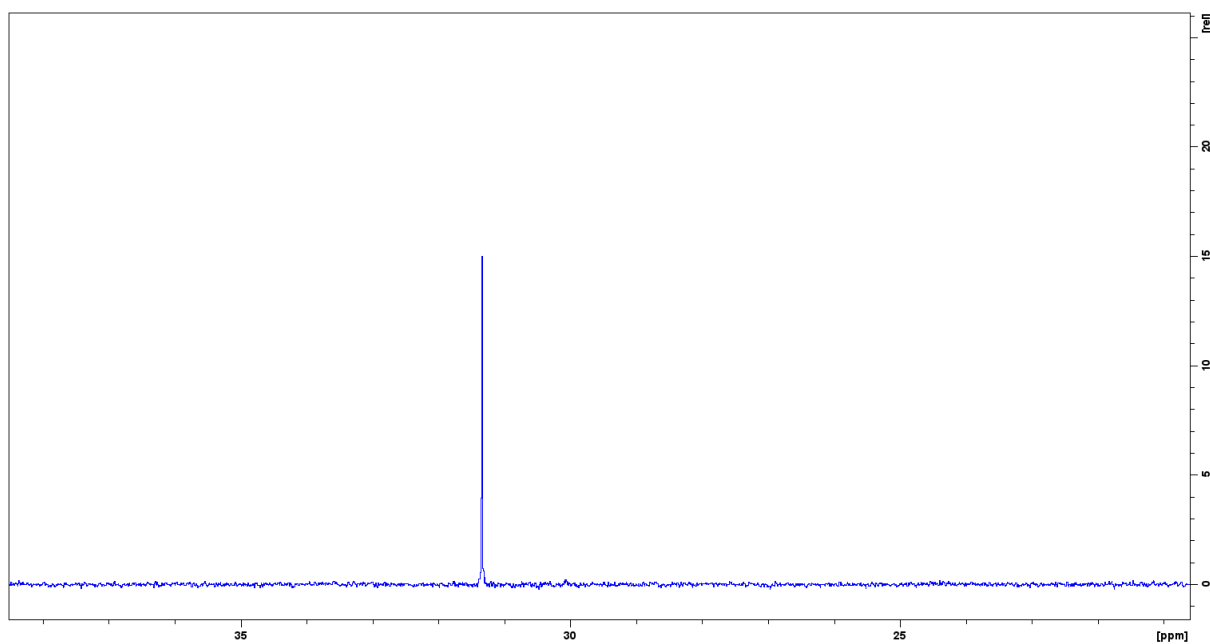
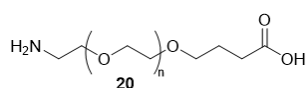


Figure 107: ^{31}P Spectra of the *N*-acyl benzotriazole **18** (D_2O , 202.5 MHz, 34.2ppm)

b. Boc deprotection of BocNH-PEG3K-COOH **19**



The compound BocNH-PEG3K-COOH **19** was solubilized in TFA. The solution was agitated during 1 hour and the Boc deprotected compound NH₂-PEG3K-COOH **20** was retrieved with Et₂O precipitation. The powder obtained was washed several times with Et₂O and dried in the dessicator. The powder was obtained quantitatively and analyzed in ¹H NMR.

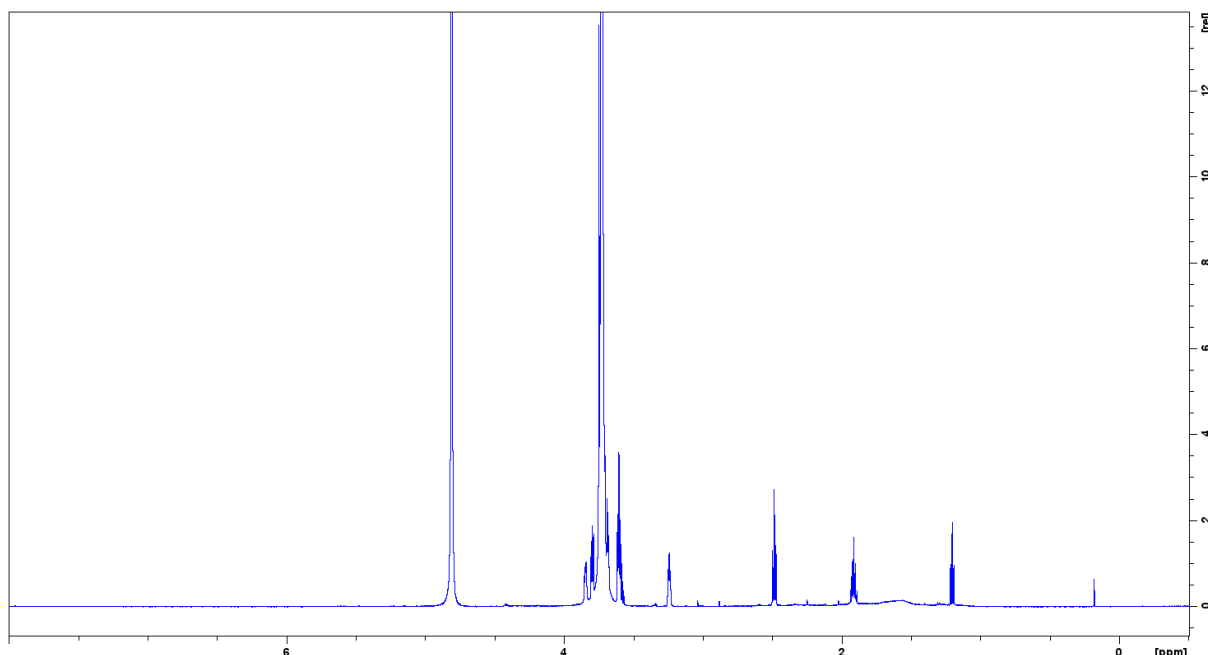
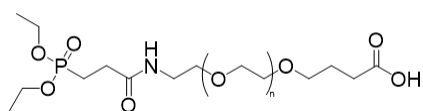


Figure 108 : ¹H NMR Spectra of NH₂-PEG3K-COOH **20** (D₂O, 600 MHz)

¹H NMR (600 MHz, D₂O, 298K): δ (ppm) 1.91 (quint, 2H, J = 6.9 Hz); 2.50 (t, 2H, J = 7.3 Hz) ; 3.24 (br t, 2H, J = 4.9 Hz) ; 3.62 (t, 4H, J = 6.1 Hz) ; 3.68-3.79 (m); 3.81 (m, 2H); 3.86 (m, 2H).

c. N-acyl benzotriazole **18** coupling with the free primary amine of NH₂-PEG3K-COOH **20**

NH₂-PEG3K-COOH **20** (0.59 g, 0.20 mmol) was dissolved in DMF and DIEA (12 0μL, 89.6 mg, 0.29 mmol, 2eq) was added. After five minutes stirring, the N-acyl-benzotriazole **18** (211 mg, 0.68 mmol, 2eq) was added in excess. The solution was stirred at room temperature for one hour and the compound was precipitated with Et₂O and washed several times with AcOEt to remove the excess of N-acyl-benzotriazole **18**. The powder obtained was dried in a dessicator and analyzed by ¹H NMR, ¹³C, ³¹P NMR and 2D experiments (COSY, HSQC and HMBC). Compound **21** was obtained with 100% of yield (629mg).



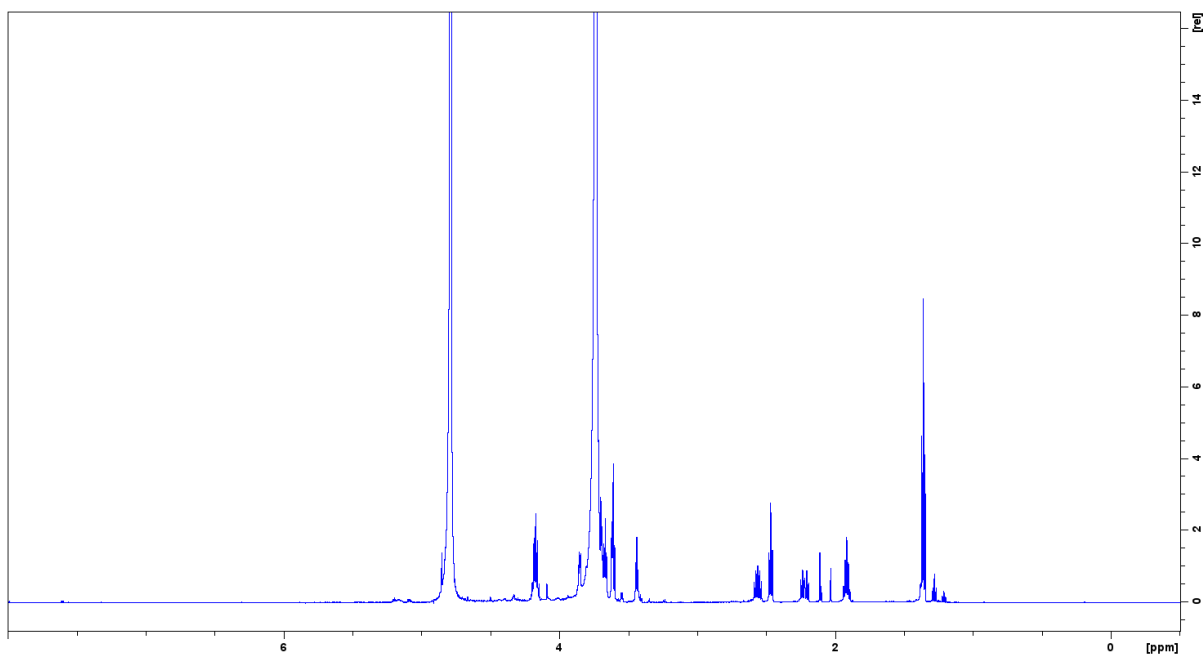


Figure 109 : ^1H NMR Spectrum of $\text{PO}_3\text{Et}_2(\text{PEG3K})\text{-COOH}$ **21** (D_2O , 600 MHz)

^1H NMR (600 MHz, D_2O , 298K): δ (ppm) 1.36 (t, 6H, $J = 7.1$ Hz) ; 1.91 (quint, 2H, $J = 6.9$ Hz) ; 2.23 (ddd, 2H, $J = 7.0, 8.4, 17.9$ Hz) ; 2.47 (t, 2H, $J = 7.3$ Hz) ; 2.56 (ddd, 2H, $J = 7.5, 8.4, 15.5$ Hz) ; 3.44 (t, 2H, $J = 5.5$ Hz) ; 3.61 (t, 2H, $J = 6.4$ Hz) ; 3.67 (t, 2H, $J = 5.4$ Hz) ; 3.70-3.79 (m) ; 3.86 (m, 2H) ; 4.17 (m, 4H).

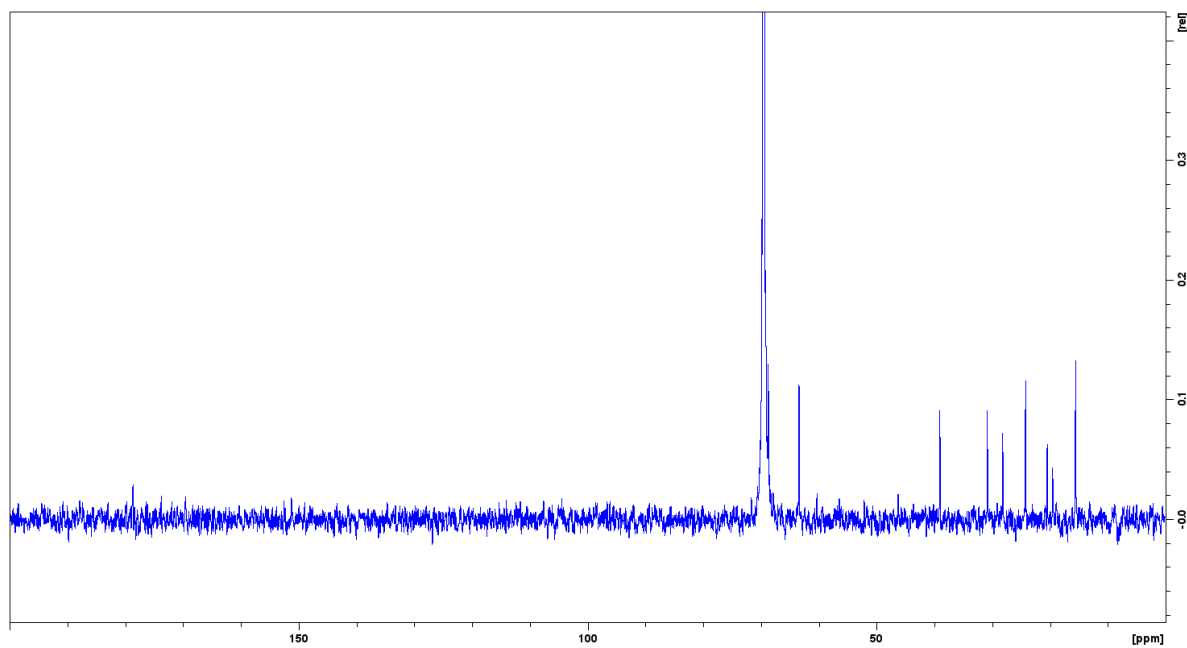


Figure 110: ^{13}C NMR Spectrum of $\text{PO}_3\text{Et}_2(\text{PEG3K})\text{-COOH}$ **21** (D_2O , 600 MHz)

^{13}C NMR (600 MHz, D_2O , 298K): δ (ppm) 15.6 ($2 \times \text{CH}_3$) ; 20.0 (CH_2P , d, $J_{\text{C-P}} = 141.5$ Hz) ; 24.3 (CH_2) ; 28.2 (CH_2) ; 30.9 (CH_2) ; 39.1 (CH_2) ; 63.5 (CH_2) ; 68.8 (CH_2) ; 69.2 (CH_2) ; 69.6 (CH_2 PEG) ; 69.9 (CH_2) ; 173.9 (CO) ; 178.7 ppm (COOH).

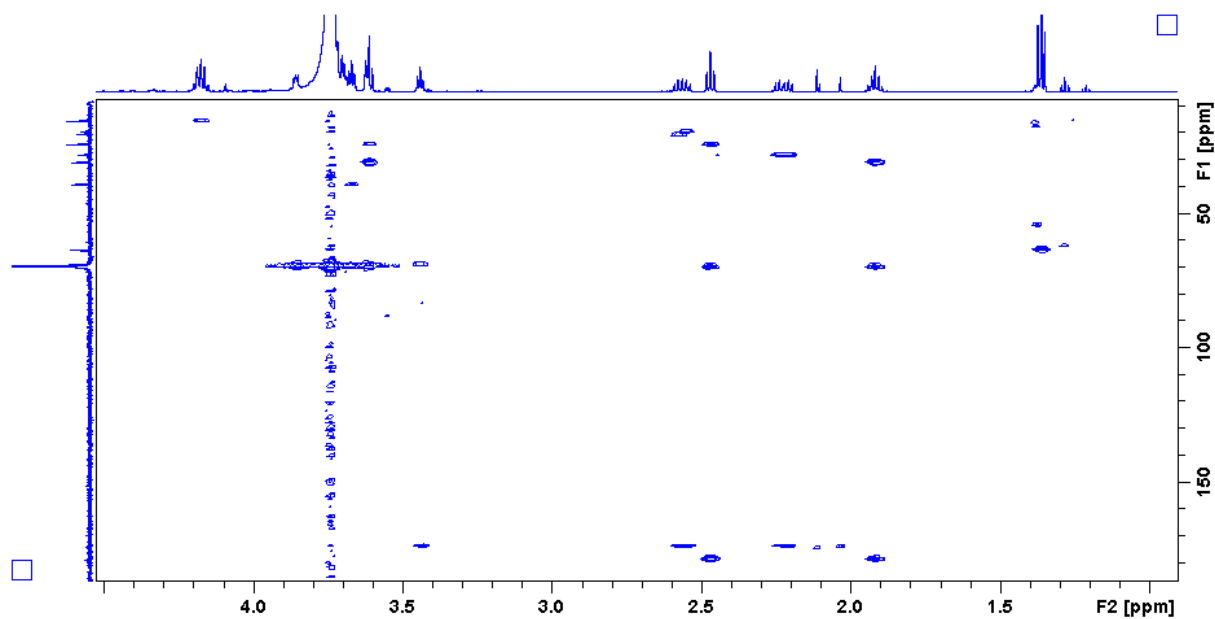


Figure 111 : ^{13}C - ^1H HMBC NMR Spectrum of $\text{PO}_3\text{Et}_2(\text{PEG3K})\text{-COOH}$ **21** (D_2O , 600 MHz)

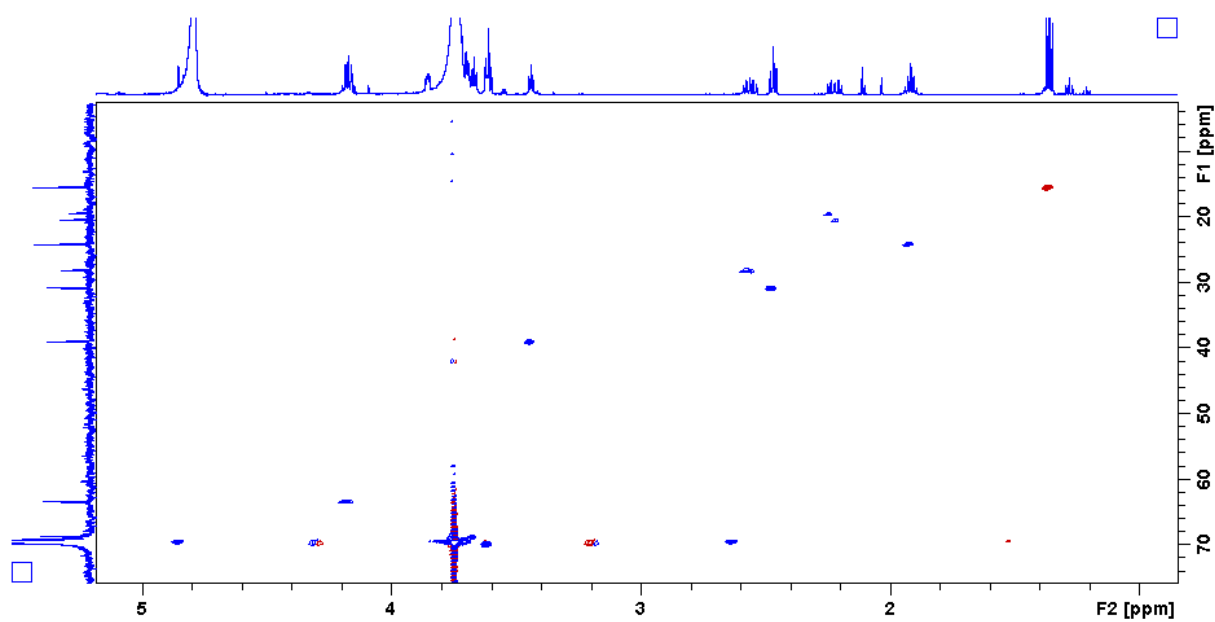


Figure 112 : ^{13}C - ^1H HSQC NMR Spectrum of $\text{PO}_3\text{Et}_2(\text{PEG3K})\text{-COOH}$ **21** (D_2O , 600 MHz)

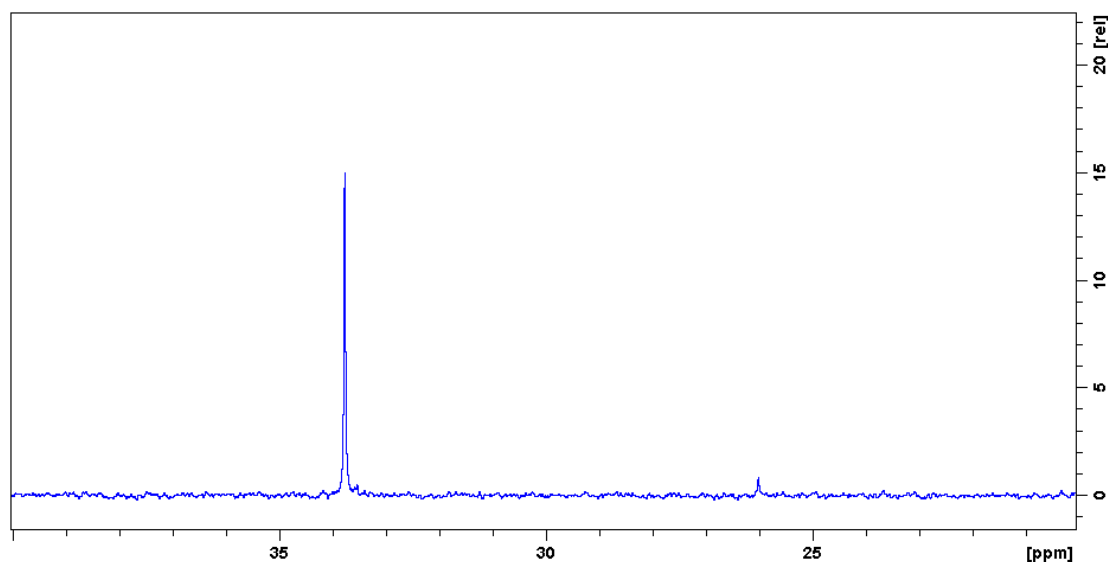


Figure 113: ^{31}P NMR Spectra of $\text{PO}_3\text{Et}_2(\text{PEG3K})\text{-COOH}$ **21** (D_2O , 600 MHz)

3. Synthesis of $P(\text{PEG3K})\text{-Peptide}$ **27**, **28**, **29** and $P(\text{PEG3K})\text{-NEt}_2$ **30**

a. Synthesis of $\text{PO}_3\text{Et}_2(\text{PEG3K})\text{-Peptide}$ **23**, **24**, **25** and synthesis of $\text{PO}_3\text{Et}_2(\text{PEG3K})\text{-NEt}_2$ **26**

$\text{PO}_3\text{Et}_2(\text{PEG3K})\text{-COOH}$ **21** (1eq) was dissolved in DMF, following by the addition of DIEA (2eq) and HATU (1eq). The solution was stirred during 15 minutes. The peptides **1'**, **2'** or NEt_2 was then added with 2eq while peptide **22** was added with 1.1eq. The solution was stirred for one hour at room temperature. The solvent was evaporated and the compounds **23**, **24**, **25** and **26** were retrieved by a precipitation in Et_2O . The powder obtained was washed several times with acetone to remove the excess of peptide or diethylamine. The solvent of the supernatant containing the desired products **23**, **24**, **25** and **26** was evaporated under vacuum and the products were retrieved by a precipitation in Et_2O . A white powder was obtained and analyzed by NMR analysis (Table 31).

Name	n_{engaged} (mmol)	MW ($\text{g}\cdot\text{mol}^{-1}$)	PEGylation rate %	m_{obtained} (mg)	Yield %
26	0.14	3512	100	492	100
23	0.063	3888	96	245	100
24	0.12	4065	100	488	100
25	0.06	3570	82	214	100

Table 31 : Yield and mass obtained (mg) for $\text{PO}_3\text{Et}_2(\text{PEG3K})\text{-NEt}_2$ **26** and $\text{PO}_3\text{Et}_2(\text{PEG3K})\text{-Peptide}$ **23**, **24**, **25**

Characterization of $\text{PO}_3\text{Et}_2(\text{PEG3K})\text{-NEt}_2$ **26**

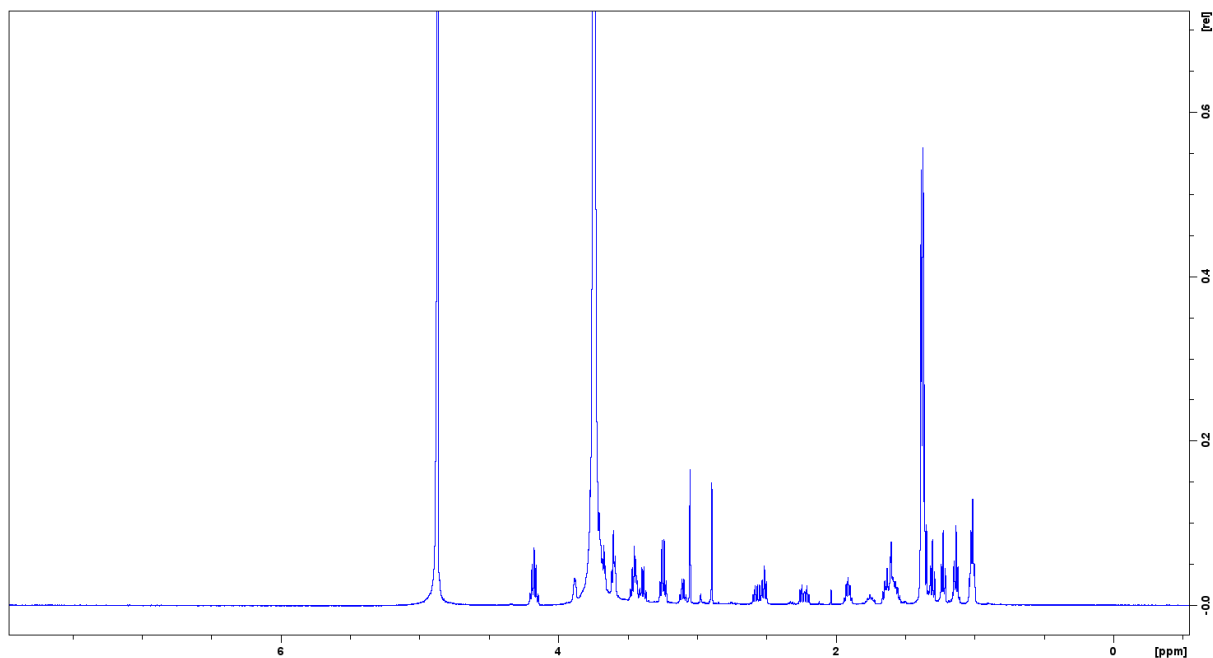
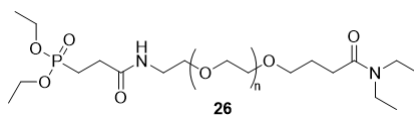


Figure 114 : ^1H NMR Spectrum of $\text{PO}_3\text{Et}_2(\text{PEG3K})\text{-NEt}_2$ **26** (D_2O , 600 MHz)

^1H NMR (D_2O , 600 MHz, 25°C): δ (ppm) 1.14 (t, 3H, $J = 7.2$ Hz) ; 1.23 (t, 3H, $J = 7.2$ Hz) ; 1.36 (m, 6H) ; 1.91 (m, 2H) ; 2.23 (m, 2H) ; 2.52 (t, 2H, $J = 7.5$ Hz) ; 2.57 (m, 2H) ; 3.39 (q, 2H, $J = 7.2$ Hz) ; 3.44 (t, 2H, $J = 5.3$ Hz) ; 3.46 (q, 2H, $J = 7.2$ Hz) ; 3.60 (t, 2H, $J = 6.3$ Hz) ; 3.67 (t, 2H, $J = 5.3$ Hz) ; 3.74 (m, 272H) ; 4.18 (m, 4H)

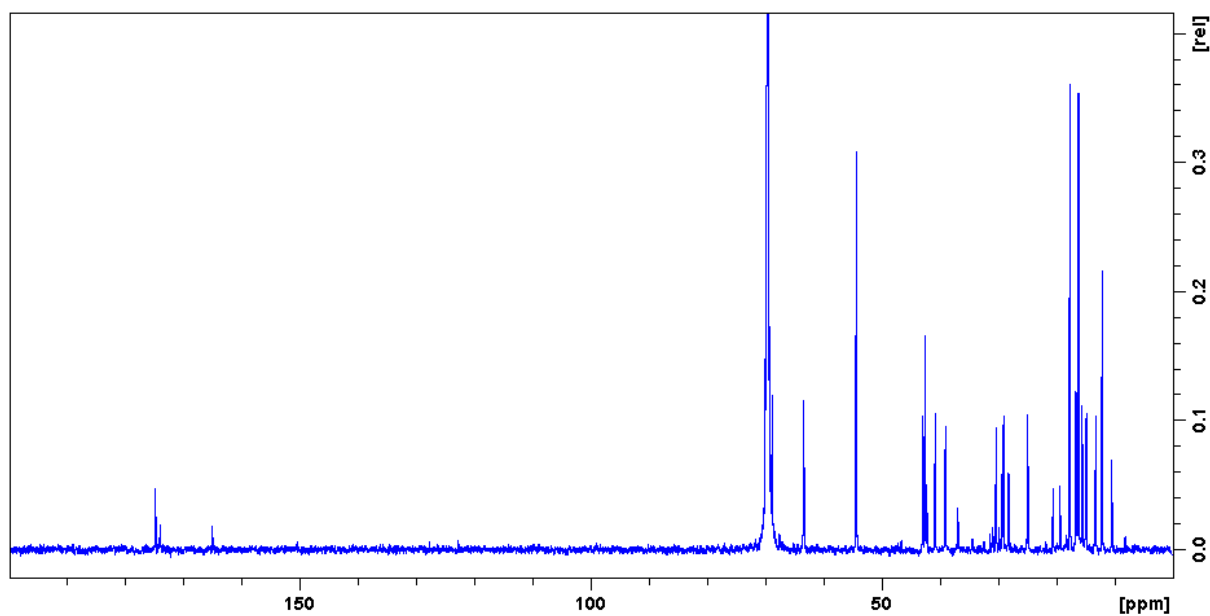


Figure 115: ^{13}C NMR Spectrum of $\text{PO}_3\text{Et}_2(\text{PEG3K})\text{-NEt}_2$ 26 (D_2O , 600 MHz)

^{13}C NMR (D_2O , 600 MHz, 25°C): δ (ppm) 12.2 (CH_3) ; 13.1 (CH_3) ; 15.7 (CH_3) ; 19.9 (CH_2) ; 24.7 (CH_2) ; 28.2 (CH_2) ; 29.0 (CH_2) ; 39.0 (CH_2) ; 40.7 (CH_2) ; 42.9 (CH_2) ; 63.3 (CH_2) ; 68.9 (CH_2) ; 69.6 (CH_2) ; 69.8 (CH_2)

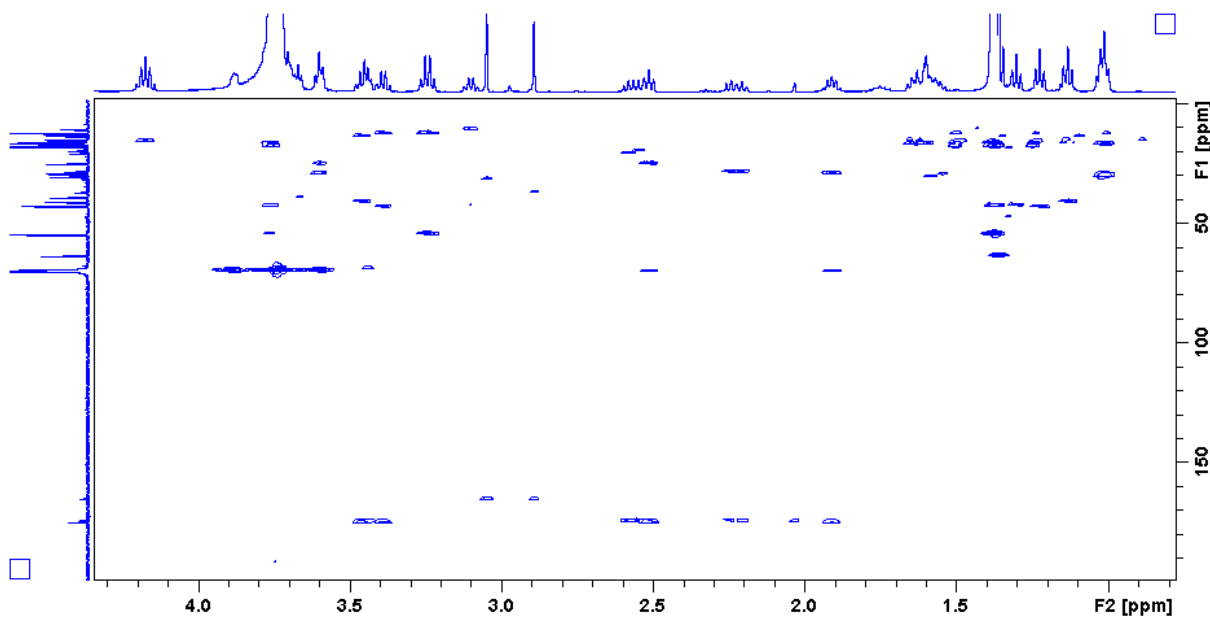


Figure 116: $^{13}\text{C}\text{-}^1\text{H}$ HMBC NMR Spectrum of $\text{PO}_3\text{Et}_2(\text{PEG3K})\text{-NEt}_2$ 26 (D_2O , 600 MHz)

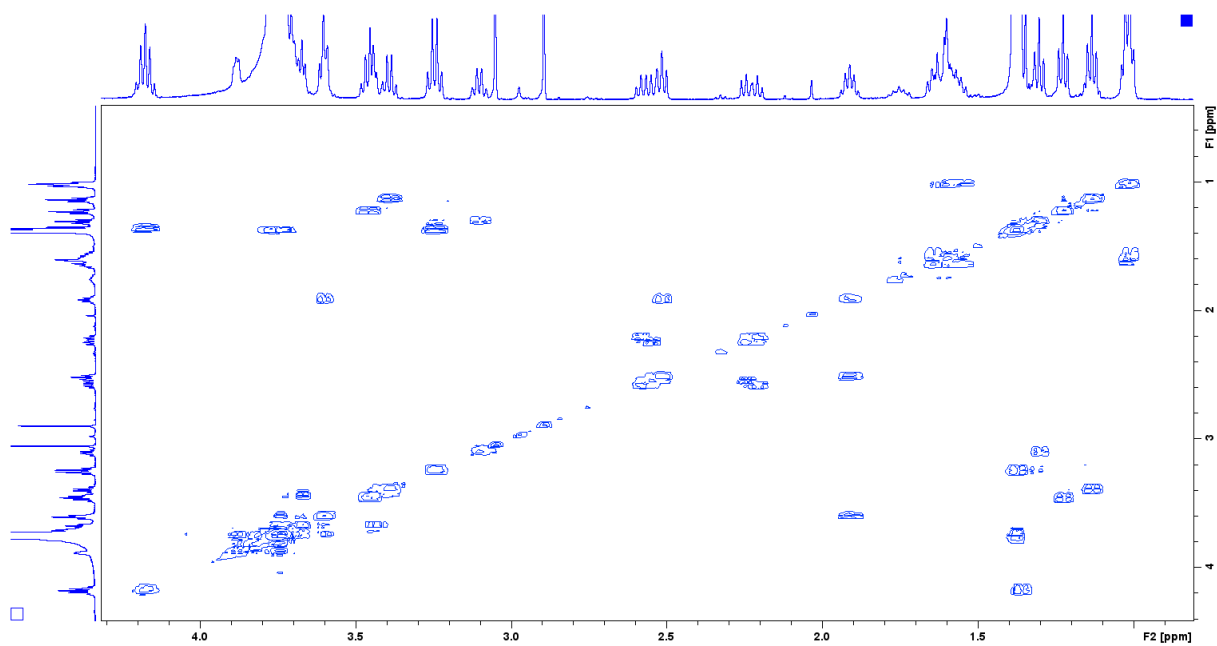


Figure 117: ^1H - ^1H COSY NMR Spectrum of $\text{PO}_3\text{Et}_2(\text{PEG3K})\text{-NEt}_2$ **26** (D_2O , 600 MHz)

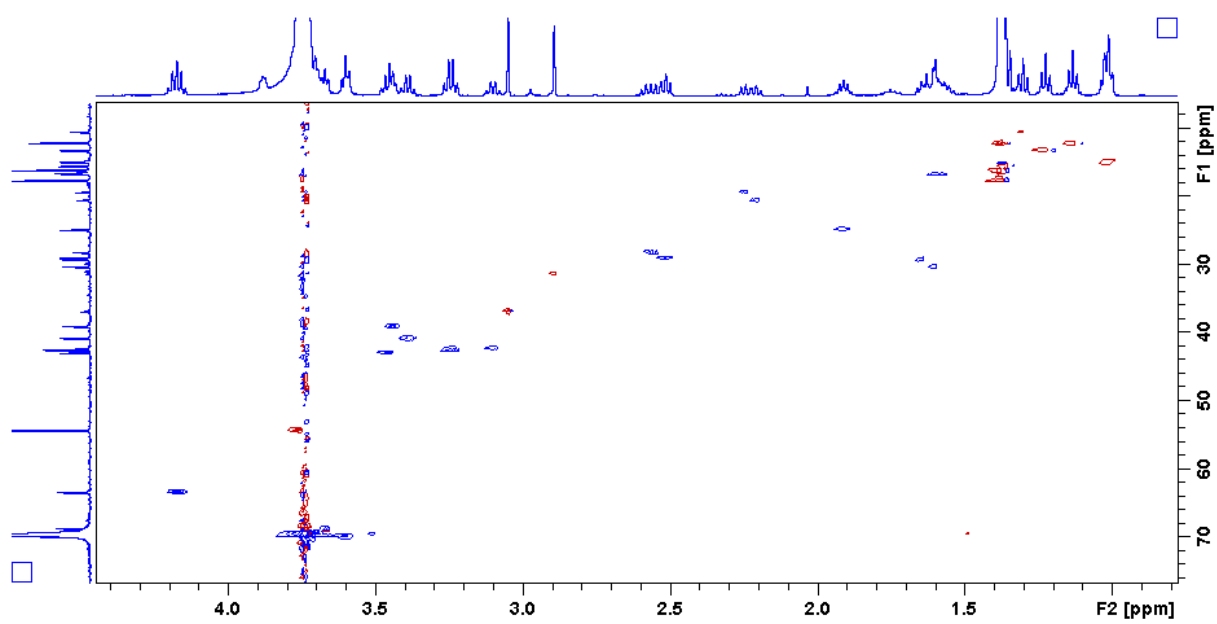


Figure 118: ^{13}C - ^1H HSQC NMR Spectrum of $\text{PO}_3\text{Et}_2(\text{PEG3K})\text{-NEt}_2$ **26** (D_2O , 600 MHz)

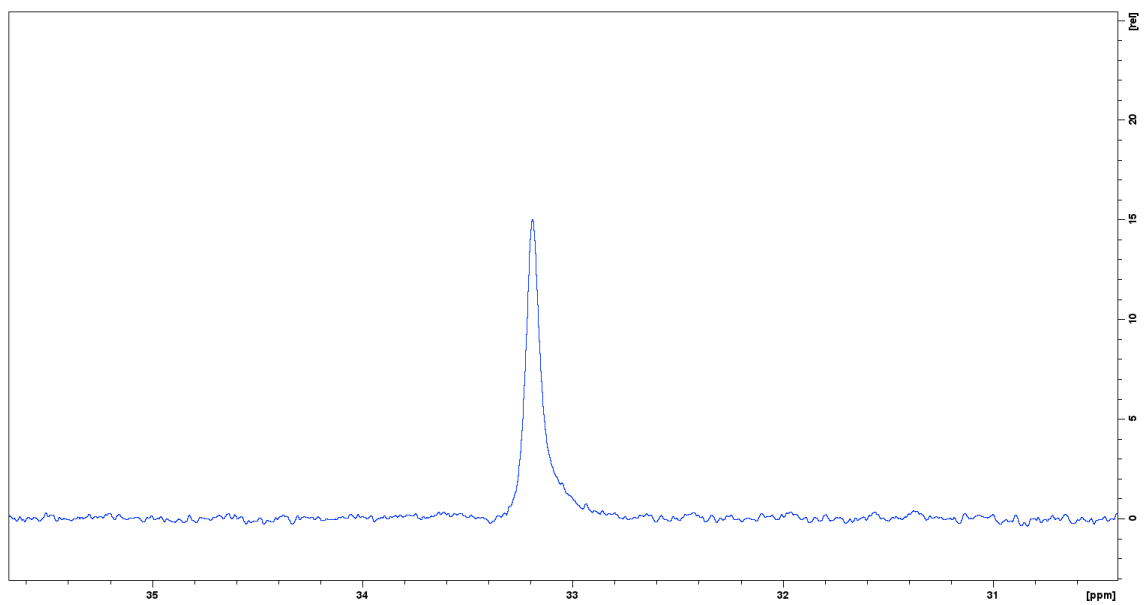


Figure 119: ^{31}P NMR Spectra of $\text{PO}_3\text{Et}_2(\text{PEG3K})\text{-NEt}_2$ **26** (D_2O , 600 MHz, 33.2ppm)

Characterization of PO₃Et₂(PEG3K)-RGD **23**

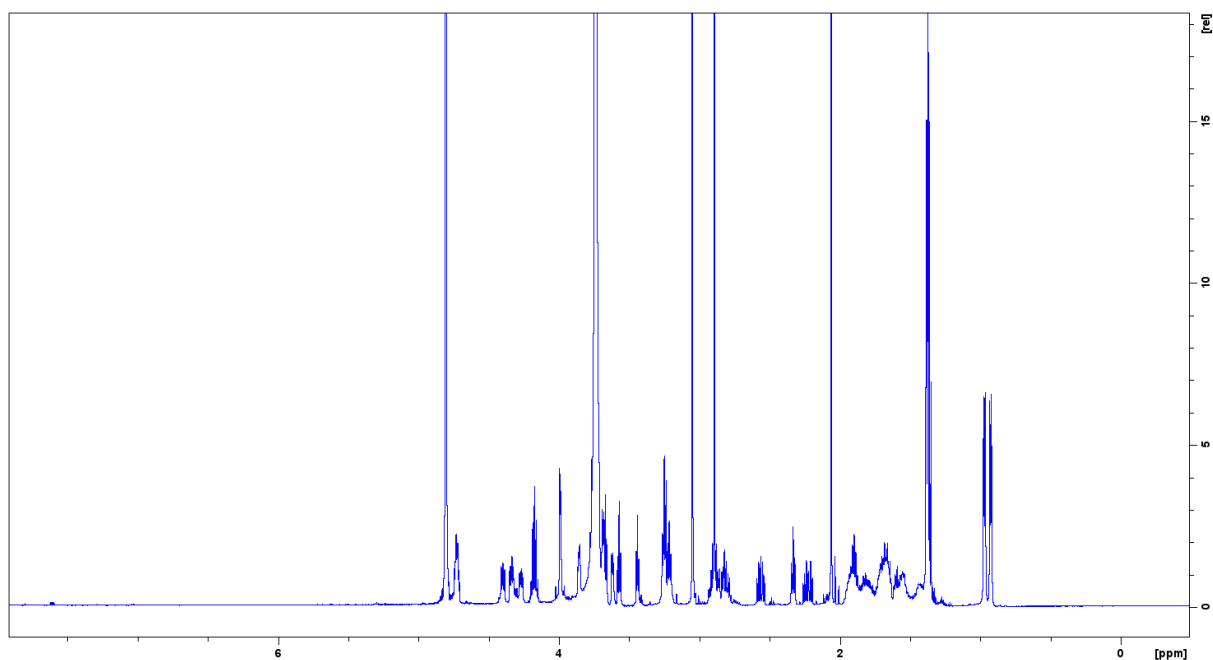
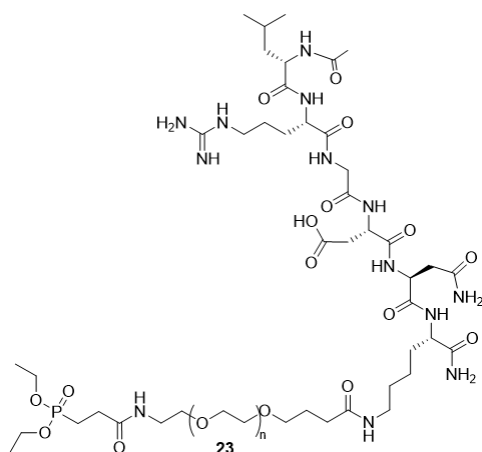


Figure 120 : ¹H NMR Spectrum of PO₃Et₂(PEG3K)-RGD **23** (D₂O, 600 MHz)

¹H NMR (D₂O, 600 MHz, 25°C): δ (ppm) 1.35 (m, 6H) ; 1.88 (t, 2H) ; 2.21 (ddd, 2H, J = 7.0/3.8/17.8 Hz) ; 2.32 (t, 2H, J = 7.5 Hz) ; 2.55 (ddd, 2H, 7.0/8.3/15.5 Hz) ; 3.20 (t, 2H, J = 7.0 Hz) ; 3.43 (t, 2H, J = 5.5 Hz) ; 3.56 (t, 2H, J = 6.5 Hz) ; 3.66 (t, 2H, J = 5.5 Hz) ; 3.74 (m) ; 4.16 (m, 4H)

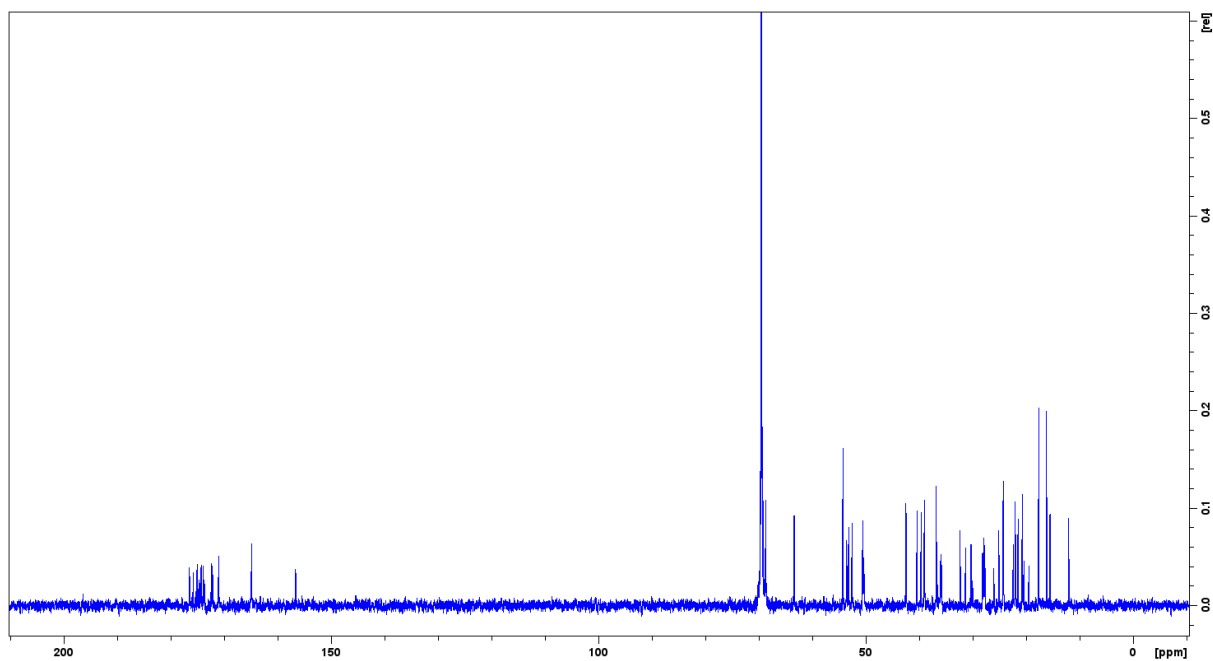


Figure 121 : ^{13}C NMR Spectrum of $\text{PO}_3\text{Et}_2(\text{PEG3K})\text{-RGD 23}$ (D_2O , 600 MHz)

^{13}C NMR (D_2O , 600 MHz, 25°C): δ (ppm) 15.6 (CH_3) ; 20.1 (CH_2) ; 25.2 (CH_2) ; 28.2 (CH_2) ; 32.4 (CH_2) ; 39.1 (CH_2) ; 63.5 (CH_2) ; 68.8 (CH_2) ; 69.6 (CH_2) ; 69.9 (CH_2)

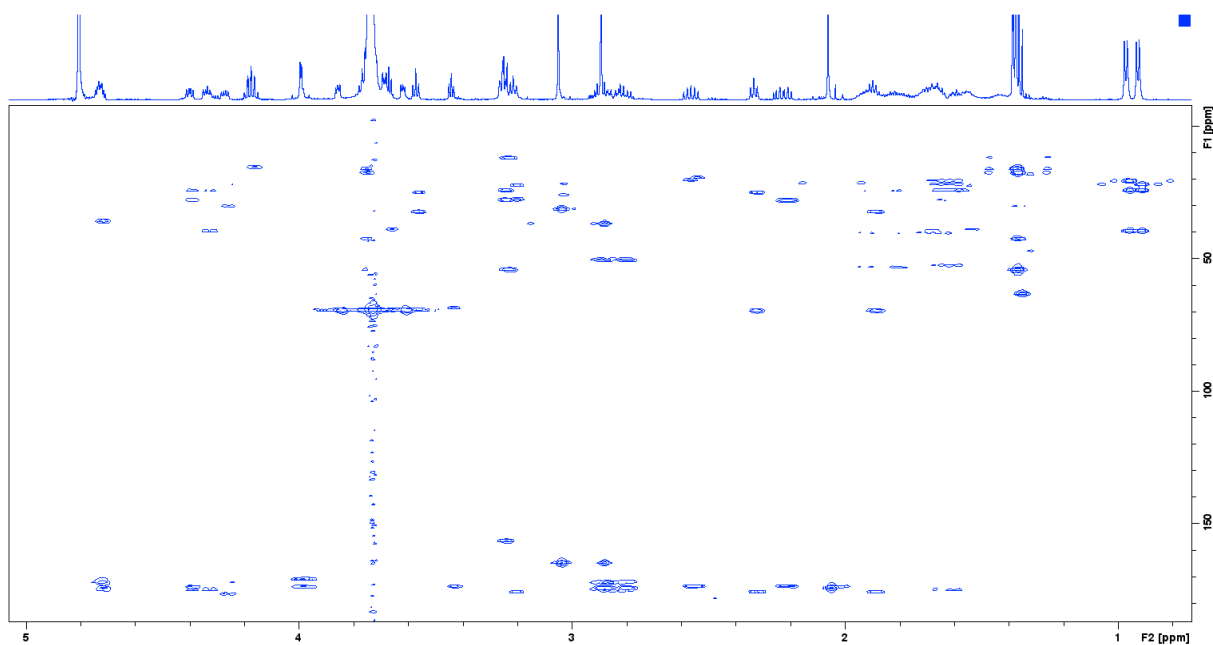


Figure 122: $^{13}\text{C}\text{-}^1\text{H}$ HMBC NMR Spectrum of $\text{PO}_3\text{Et}_2(\text{PEG3K})\text{-RGD 23}$ (D_2O , 600 MHz)

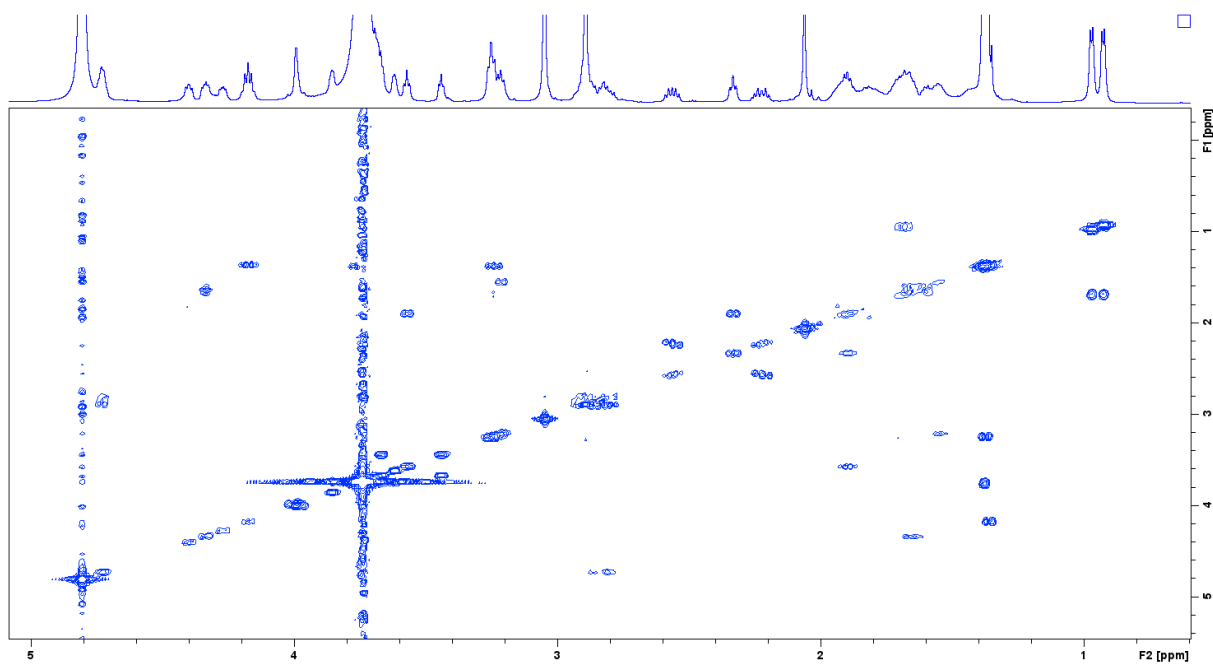


Figure 123: ^1H - ^1H COSY NMR Spectrum of $\text{PO}_3\text{Et}_2(\text{PEG}3\text{K})\text{-RGD } \mathbf{23}$ (D_2O , 600 MHz)

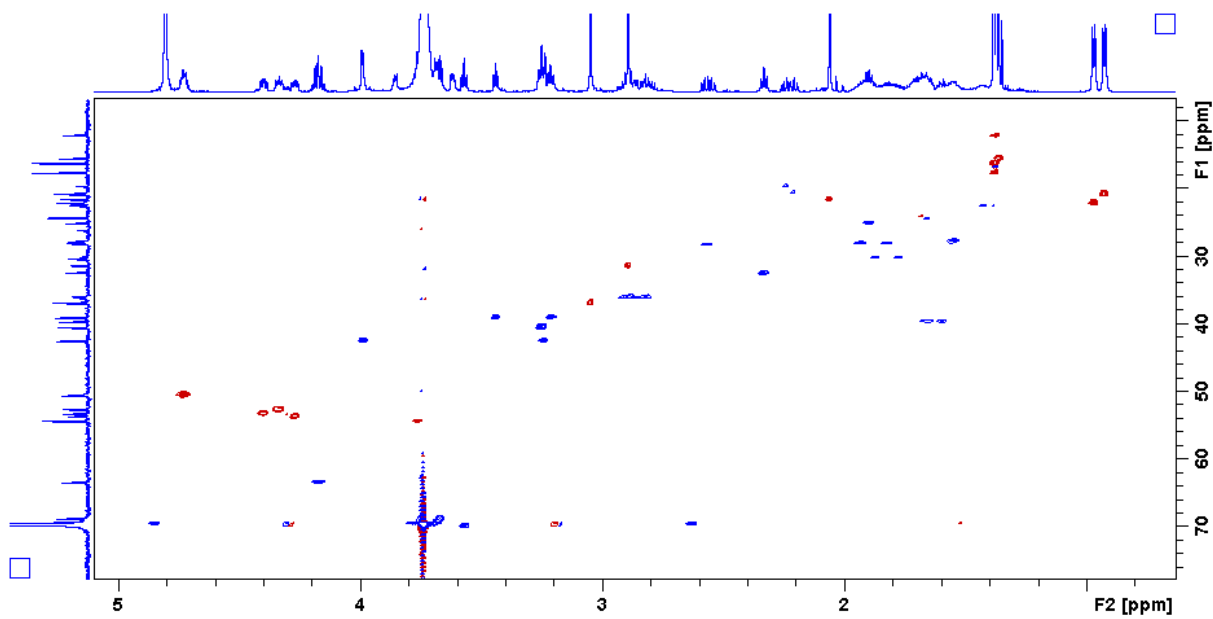


Figure 124: ^{13}C - ^1H HSQC NMR Spectrum of $\text{PO}_3\text{Et}_2(\text{PEG}3\text{K})\text{-RGD } \mathbf{23}$ (D_2O , 600 MHz)

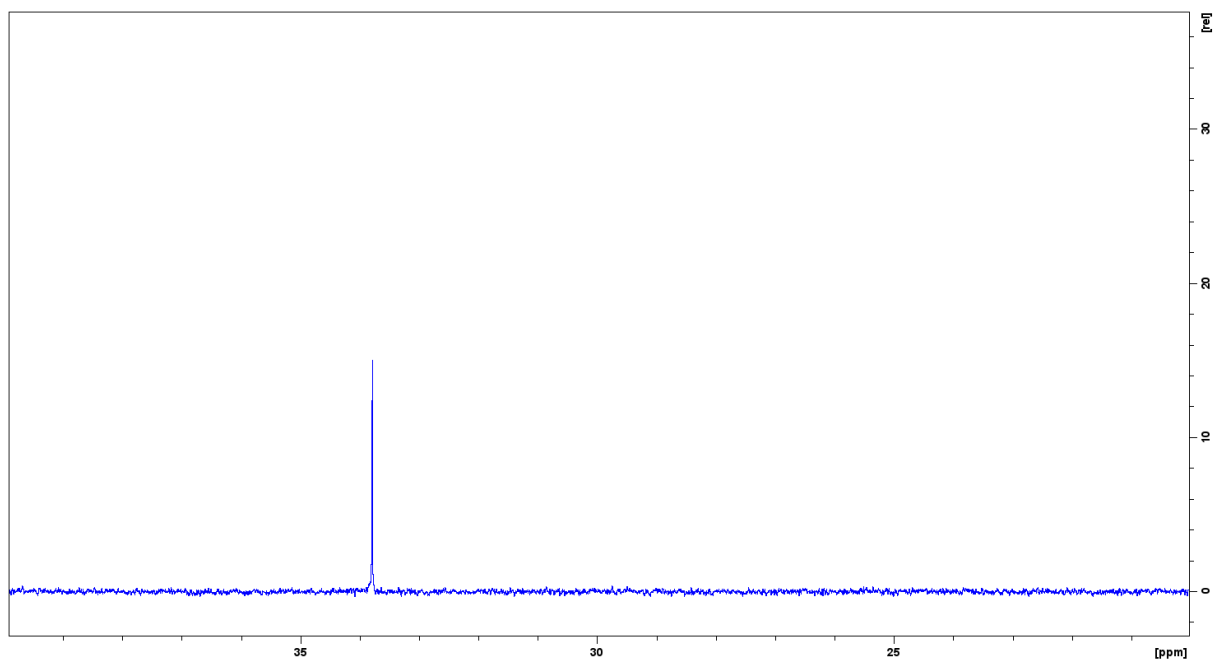
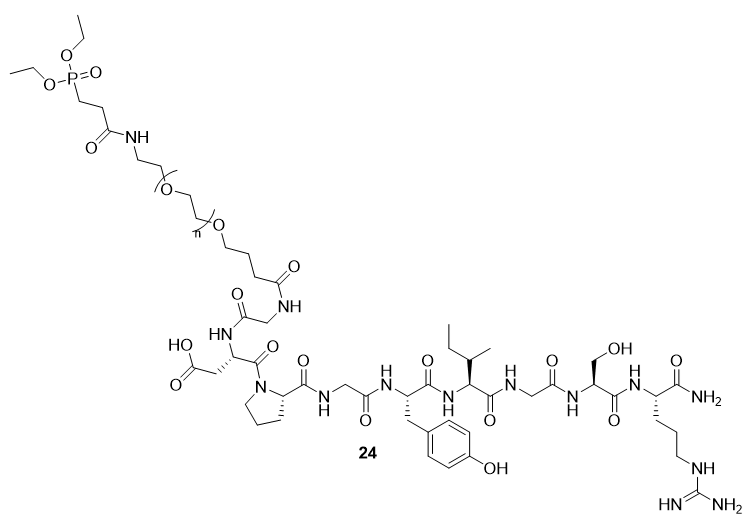


Figure 125: ^{31}P NMR Spectra of $\text{PO}_3\text{Et}_2(\text{PEG}3\text{K})\text{-RGD}$ **23** (D_2O , 600 MHz, 33.8ppm)

Characterization of $\text{PO}_3\text{Et}_2(\text{PEG}3\text{K})\text{-YIGSR}$ **24**



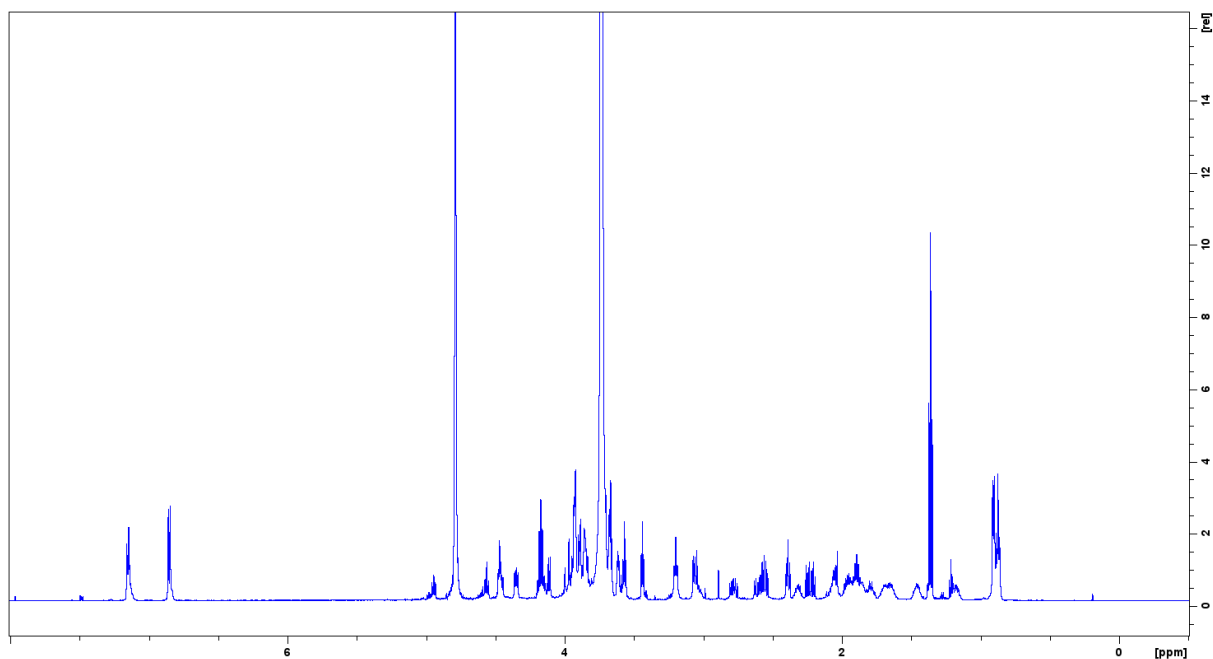


Figure 126 : ^1H NMR Spectrum of $\text{PO}_3\text{Et}_2(\text{PEG3K})\text{-YIGSR 24}$ (D_2O , 600 MHz)

^1H NMR (D_2O , 600 MHz, 25°C): δ (ppm) 1.36 (m, 6H) ; 1.89 (t, 2H) ; 2.22 (ddd, 2H, $J = 7.1/8.3/17.9$ Hz) ; 2.39 (t, 2H, $J = 7.4$ Hz) ; 2.56 (ddd, 2H, $7.1/8.3/15.3$ Hz) ; 3.44 (t, 2H, $J = 5.5$ Hz) ; 3.57 (t, 2H, $J = 6.5$ Hz) ; 3.67 (t, 2H, $J = 6.5$ Hz) ; 3.74 (t, 2H) ; 3.93 (m) ; 4.17 (m, 4H)

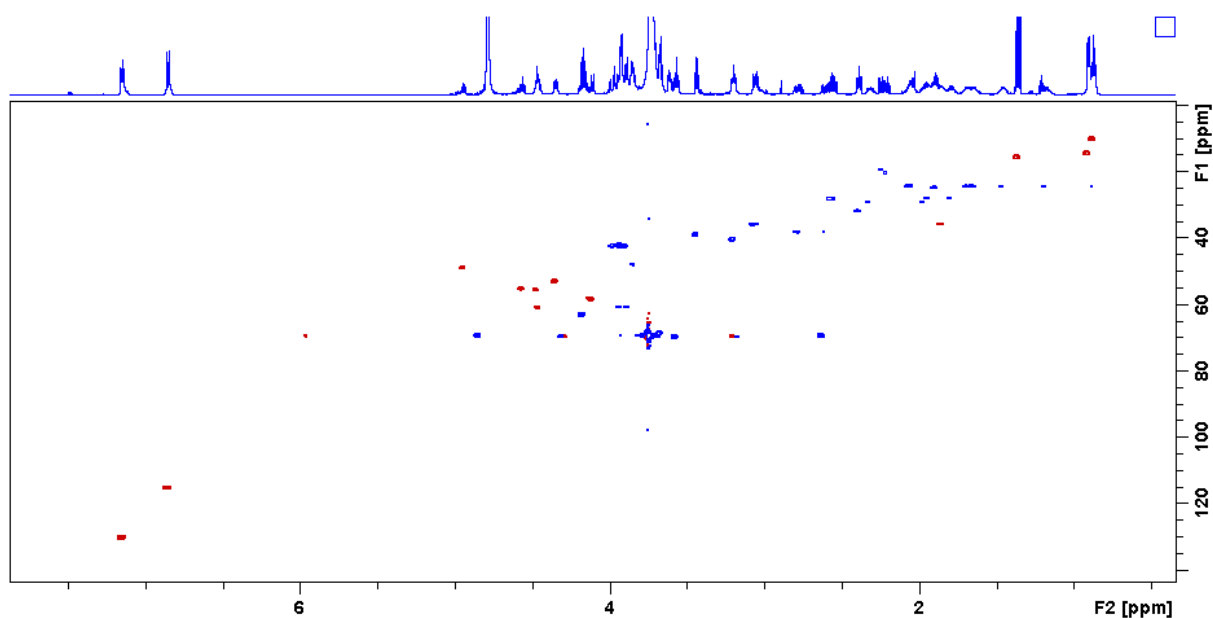


Figure 127: $^{13}\text{C}\text{-}^1\text{H}$ HSQC NMR Spectrum of $\text{PO}_3\text{Et}_2(\text{PEG3K})\text{-YIGSR 24}$ (D_2O , 600 MHz)

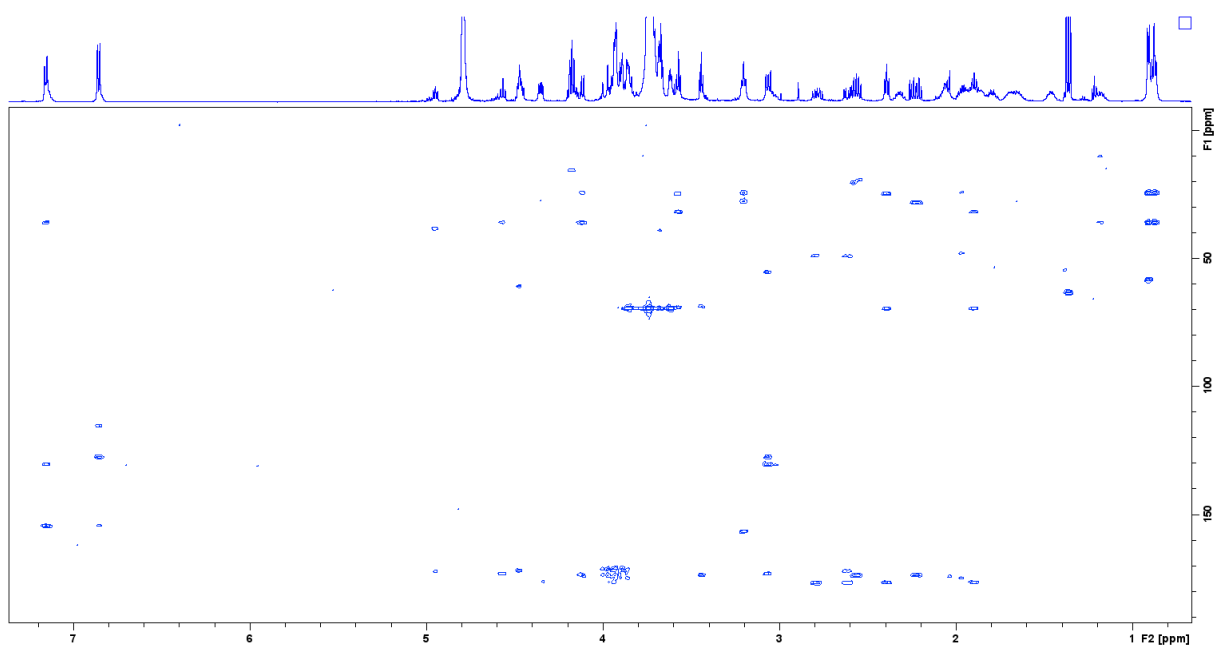


Figure 128: ¹³C-¹H HMBC NMR Spectrum of PO₃Et₂(PEG3K)-YIGSR **24** (D₂O, 600 MHz)

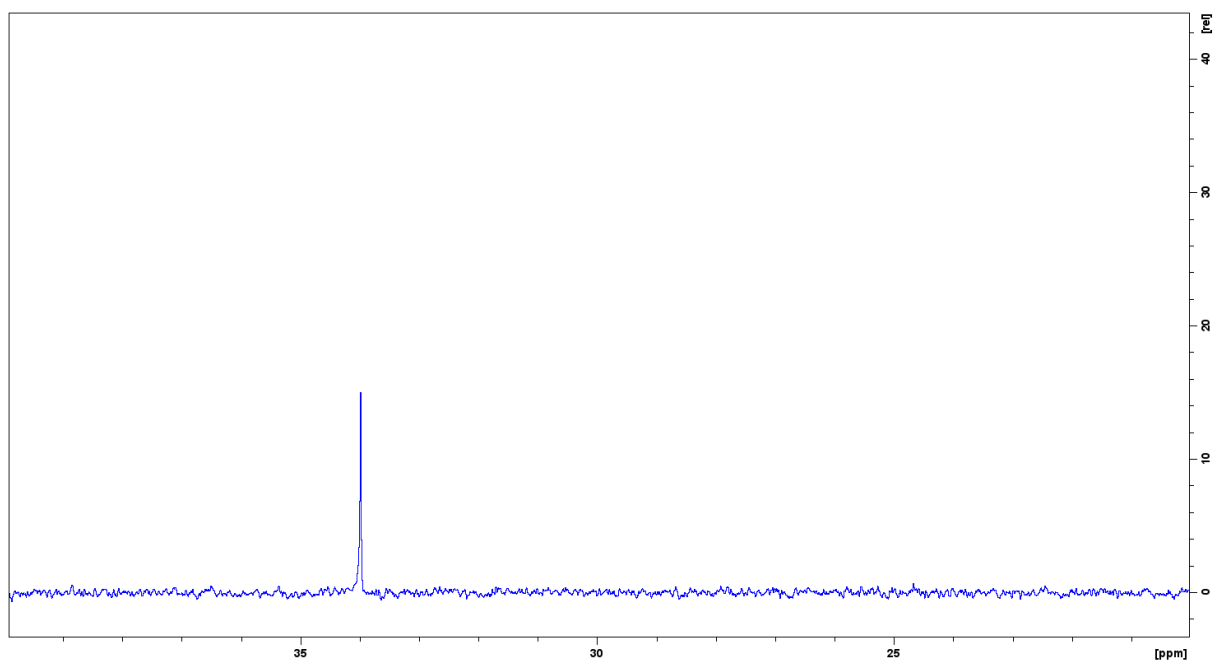


Figure 129: ³¹P NMR Spectra of PO₃Et₂(PEG3K)-YIGSR **24** (D₂O, 500 MHz, 34.0ppm)

Characterization of $\text{PO}_3\text{Et}_2(\text{PEG3K})\text{-AhXRR 25}$

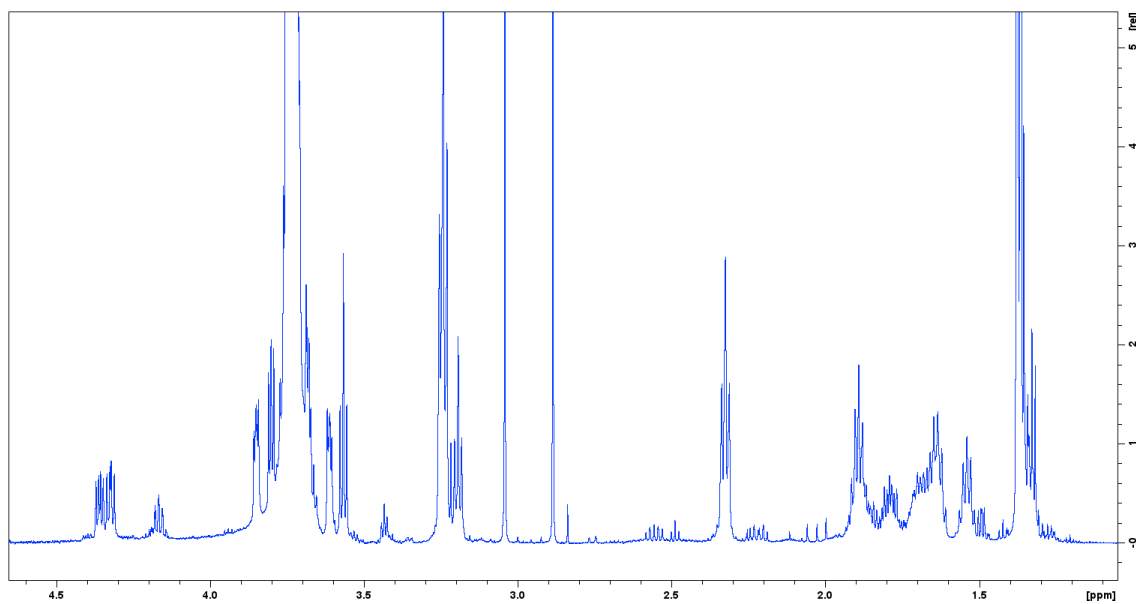
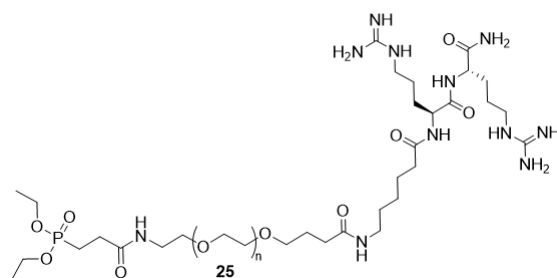


Figure 130: ^1H NMR Spectra of $\text{PO}_3\text{Et}_2(\text{PEG3K})\text{-AhXRR 24}$ (D_2O , 600 MHz)

^1H NMR (D_2O , 600 MHz, 25°C): δ (ppm) 1.36 (m, 6H) ; 1.52 (t, 2H) ; 2.22 (m, 2H, $J = 7.1/8.3/17.9$ Hz) ; 2.39 (m, 2H, $J = 7.4$ Hz) ; 2.56 (m, 2H, 7.1/8.3/15.3 Hz) ; 3.44 (t, 2H, $J = 5.5$ Hz) ; 3.57 (t, 2H, $J = 6.5$ Hz) ; 3.67 (t, 2H, $J = 6.5$ Hz) ; 3.74 (t, 2H) ; 3.93 (m) ; 4.17 (m, 4H)

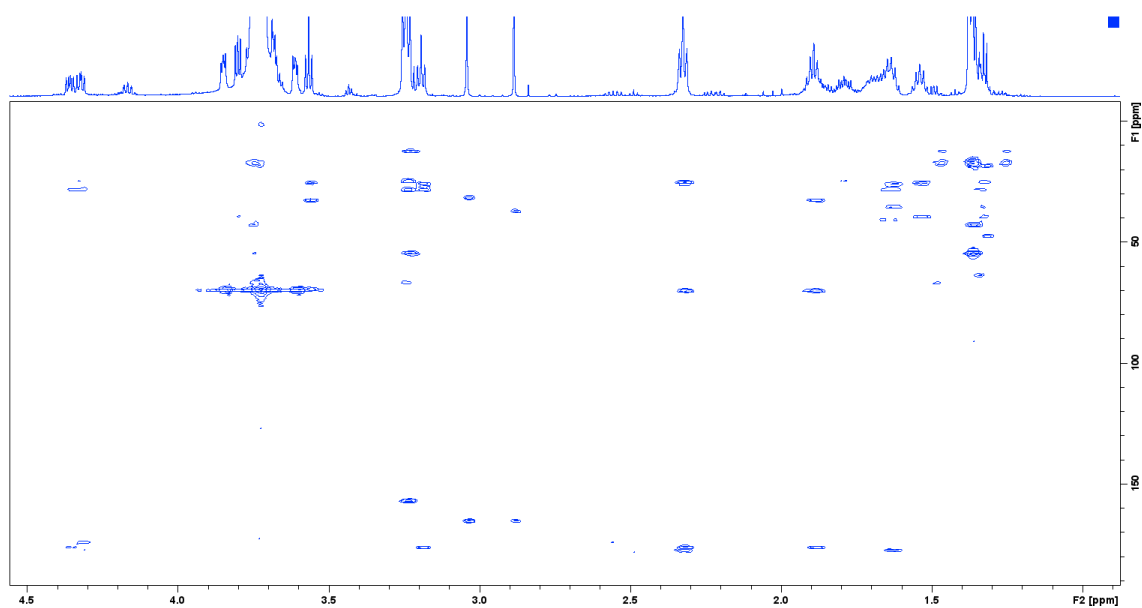


Figure 131 : ^{13}C - ^1H NMR Spectra of $\text{PO}_3\text{Et}_2(\text{PEG3K})\text{-AhXRR 24}$ (D_2O , 600 MHz)

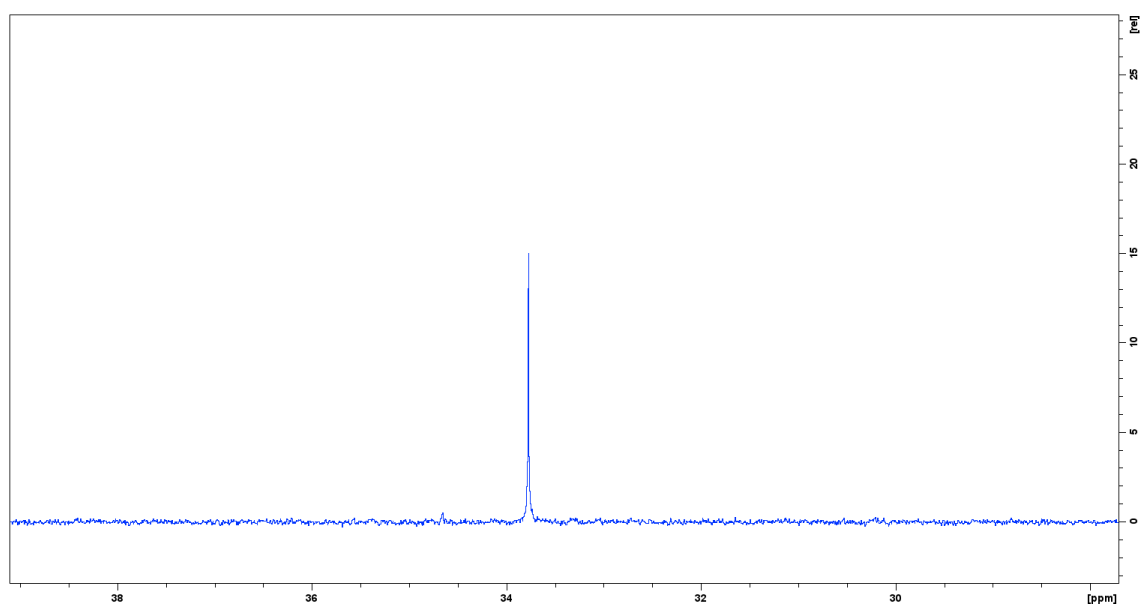


Figure 132: ^{31}P NMR Spectra of $\text{PO}_3\text{Et}_2(\text{PEG3K})\text{-AhXRR 24}$ (D_2O , 600 MHz, 33.8ppm)

4. Dealkylation of compounds **23**, **24**, **25**, **26** by using the McKenna reaction in solution

Previous compounds **23**, **24**, **25** and **26** (250 mg, 0.08 mmol) were dissolved in a minimum of dry dichloromethane. The bromotrimethylsilane (TMSBr) (105 μL , 122 mg, 0.8 mmol, 8eq) was collected under argon with a needle and added to the solution. The mixture was stirred overnight. The solvent was then evaporated. The silylated intermediates were dissolved in methanol during one hour to hydrolyse the silylated group. Finally, the final products were

precipitated in Et₂O and a powder was obtained with 100% of yield. The final product was monitored by ³¹P NMR.

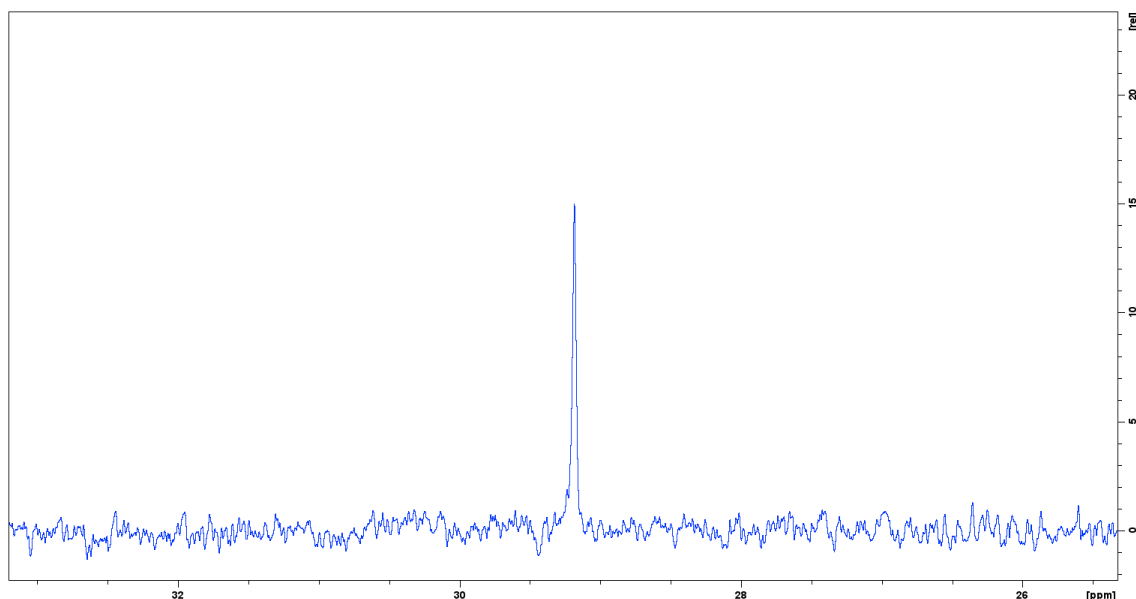


Figure 133 : ³¹P NMR of peptide-based stabilizing agents P(PEG3K)-Peptide **27**, **28**, **29** and of P(PEG3K)-NEt₂ **30** (D₂O, 600 MHz)

E. Synthesis of colloidal nanoparticles surrounded by a mixture of AEP/P(Peptide) 6 and 7

The colloidal suspension was obtained by first mixing the calcium nitrate Ca(NO₃)₂·4H₂O solution (0.395 mmol, 0.53mL) with the stabilizing agents solution (Table 32, 12.5 mL). The molar quantity of the stabilizing agents was divided between AEP and P(Peptide) as reported in Table 32. The pH was then adjusted around 9-10 with ammonia solution. The ammonium hydrogenophosphate (NH₄)₂HPO₄ solution (0.130, 0.53 mL) was added to the mixture and the pH was again adjusted around 9-10 with ammonia solution. The white powder obtained was put in the oven at 100°C for 16 hours. In case of colloidal suspension, a dialysis purification was performed. The colloidal suspension (2.07mL) was introduced in a dialysis membrane with a cut off of about 6-8 kDa before placing in a beaker containing 800 mL of distilled water. The water was changed in the following cycle: 4 hours, 4 hours, 16 hours and 4 hours. If a precipitate was obtained after the maturation time, the solid is recovered after centrifugation and washed several times with water. The white powder obtained is finally lyophilized.

					V=1,016mL		
	R-PO ₃ H ₂ /Ca	AEP	P(RGD)	P(YIGSR)	n _{AEP} (mmol)	n _{P(RGD)} (mmol)	n _{P(YIGSR)} (mmol)
NPs 1	0,5	100	0	/	0,197	/	/
NPs 2	0,5	90	10	/	0,180	0,017	/
NPs 3	0,5	75	25	/	0,147	0,050	/
NPs 4	0,5	50	50	/	0,099	0,099	/
NPs 5	0,5	25	75	/	0,050	0,147	/
NPs 6	0,5	0	100	/	/	0,197	/
NPs 7	0,5	90	/	10	0,180	/	0,017
NPs 8	0,5	75	/	25	0,147	/	0,050
NPs 9	0,5	50	/	50	0,099	/	0,099
NPs 10	0,5	25	/	75	0,050	/	0,147
NPs 11	0,5	0	/	100	/	/	0,197

Table 32 : Summary of the stabilizing agents quantities P(Peptide) 6 or 7 used for the synthesis of NPs 1-11

F. Synthesis of colloidal nanoparticles surrounded by P(PEG3K)-NEt₂ 30/P(PEG3K)-Peptide 27, 28, 29

The colloidal suspension was obtained by first mixing the calcium nitrate Ca(NO₃)₂.4H₂O solution (1.217 mmol, 1.625 mL) with the stabilizing agents solution Table 33 (3.125 mL). The pH was then adjusted around 9-10 with ammonia solution. The ammonium hydrogenophosphate (NH₄)₂HPO₄ solution (0.405, 1.625 mL) was added to the mixture and the pH was again adjusted around 9-10 with ammonia solution. The white powder obtained was put in the oven at 100°C for 16 hours. In case of colloidal suspension a dialysis purification was performed. The colloidal suspension (6.37 mL) was introduced in a dialysis membrane with a cut off of about 12-14 kDa before placing in a beaker containing 800mL of distilled water. The water was changed in the following cycle: 4 hours, 4 hours, 16 hours and 4 hours.

					V=3,125mL				
	R-PO ₃ H ₂ /Ca	P(PEG3K)- NEt ₂	P(PEG3K)- RGD	P(PEG3K)- YIGSR	P(PEG3K)- AhXRR	n _{P(PEG3K)- NEt₂} (mmol)	n _{P(PEG3K)- RGD} (mmol)	n _{P(PEG3K)- YIGSR} (mmol)	n _{P(PEG3K)- AhXRR} (mmol)
NPs 12	0,001	100	/	/	/	0,003	/	/	/
NPs 13	0,005	100	/	/	/	0,006	/	/	/
NPs 14	0,008	100	/	/	/	0,008	/	/	/
NPs 15	0,016	100	/	/	/	0,020	/	/	/
NPs 16	0,032	100	/	/	/	0,039	/	/	/
NPs 17	0,128	100	/	/	/	0,156	/	/	/
NPs 18	0,016	0	100	/	/	/	0,020	/	/
NPs 19	0,016	25	75	/	/	0,005	0,015	/	/
NPs 20	0,016	50	50	/	/	0,010	0,010	/	/
NPs 21	0,016	75	25	/	/	0,015	0,005	/	/
NPs 22	0,016	0	/	100	/	/	/	0,020	/

NPs 23	0,016	25	/	75	/	0,005	/	0,015	/
NPs 24	0,016	50	/	50	/	0,010	/	0,010	/
NPs 25	0,016	75	/	25	/	0,015	/	0,005	/
NPs 26	0,016	0	/	/	100	/	/	/	0,020
NPs 27	0,016	25	/	/	75	0,005	/	/	0,015
NPs 28	0,016	50	/	/	50	0,010	/	/	0,010
NPs 29	0,016	75	/	/	25	0,015	/	/	0,005

Table 33 : Summary of the stabilizing agents quantities P(PEG3K)-NEt₂ and P(PEG3K)-Peptide used for the synthesis of NPs 12-29

II. Experimental section of the Chapter 3

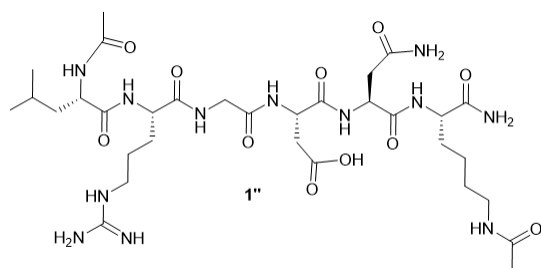
A. Commercial products

Dulbecco's modified eagle's medium (DMEM), minimum essential medium (MEM alpha) and tampon phosphate salin (PBS) were purchased in Gibco 11965092. Fetal bovine serum (FBS) was purchased in R&D systems. Bovine calf serum (BCS) was purchased in ATCC. *P. aeruginosa* and *S. aureus* and lipopolysaccharide (LPS) were purchased in Sigma-Aldrich. Bismaleimido-hexane (BMH) was purchased in Fisher Scientific.

B. Biocompatibility experiments

1. Peptides synthesis for the biological experiments

a. Ac-LRGDNK(Ac)-NH₂ 1''



Synthesis by SPPS was made using the H-Rink Amide ChemMatrix (0.47 mmol.g⁻¹, 1.2 g) resin in DMF. The first to the sixth coupling reactions were performed using Fmoc amino acid (8.80 mL, 5eq) / DIEA (1.52 mL, 10eq) / HATU (8.80 mL, 5eq) mixture for 5 minutes twice with a DMF washing step in between. The Fmoc removal steps were

realized using piperidine/DMF 20/80 v/v solution (15 mL) for 1 minute and performed twice. All washings were done successively with 15mL of DMF, DCM and DMF after coupling steps and deprotection steps. The Alloc protection on the Lysine side chain was removed in DCM with 0.25eq of palladium tetrakis triphenylphosphine followed by 25eq of phenylsilane. The reaction was agitated during 1 hour and performed twice. The solvent was removed and the resin was washed with DCM and DMF (x3). N-Terminal and the chain lateral of the Lysine acetylation were performed with 20% Ac₂O in DMF and DIEA (1%) for 15 minutes twice. The peptide was cleaved from the resin with TFA/H₂O/TIS (95/2.5/2.5, v/v/v) mixture (2x1h30), concentrated under reduced pressure, recovered by precipitation in diethyl ether. The

powder was dried in the dessicator and obtained with 32% of yield (135mg, 98% of purity). The crude was analysed by LC-MS and NMR analyses.

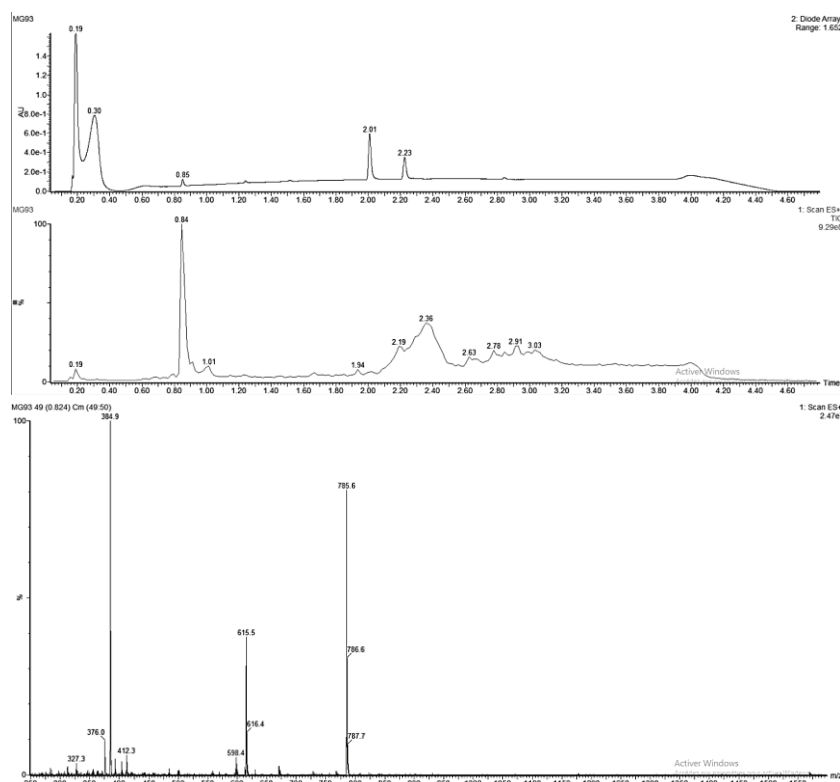
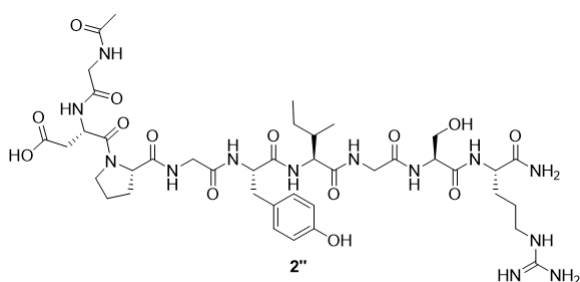


Figure 134 : LC-MS Spectra of peptide Ac-LRGDNK(Ac)-NH₂.1''

LC-MS (ESI+): tR = 0.84 min, m/z 785.6 [M+H]⁺; 384.9 [M+2H]²⁺

b. Ac-GDPGYIGSR-NH₂ 2''



Synthesis by SPPS was made using the H-Rink Amide ChemMatrix (0.47 mmol.g⁻¹, 0.94 g) resin in DMF. The first to the ninth coupling reactions were performed using Fmoc amino acid (5.17 mL, 5eq) / DIEA (889 μL, 10eq) / HATU (5.17 mL, 5eq) mixture for 5 minutes twice with a DMF washing step in between.

The seventh coupling reaction was performed using the Fmoc-Pro-OH (5.17 mL, 5eq) / DIEA (889 μL, 10eq) / HATU (5.17 mL, 5eq) mixture for 15 minutes twice in DMF. The Fmoc removal steps were realized using piperidine/DMF (20/80 v/v) solution (15 mL) for 1 minute and performed twice. All washings were done successively with 15mL of DMF, DCM and DMF after coupling steps and deprotection steps. N-Terminal acetylation was performed with 20% Ac₂O in DMF and DIEA (1%) for 15 minutes twice. The peptide was cleaved from the resin with

TFA/H₂O/TIS, 95/2.5/2.5, v/v/v mixture (2x1h30), concentrated under reduced pressure, recovered by precipitation in diethyl ether. The powder was dried in the dessicator and obtained with 41% of yield (167 mg, 95% of purity). The crude was analysed by LC-MS and NMR analyses.

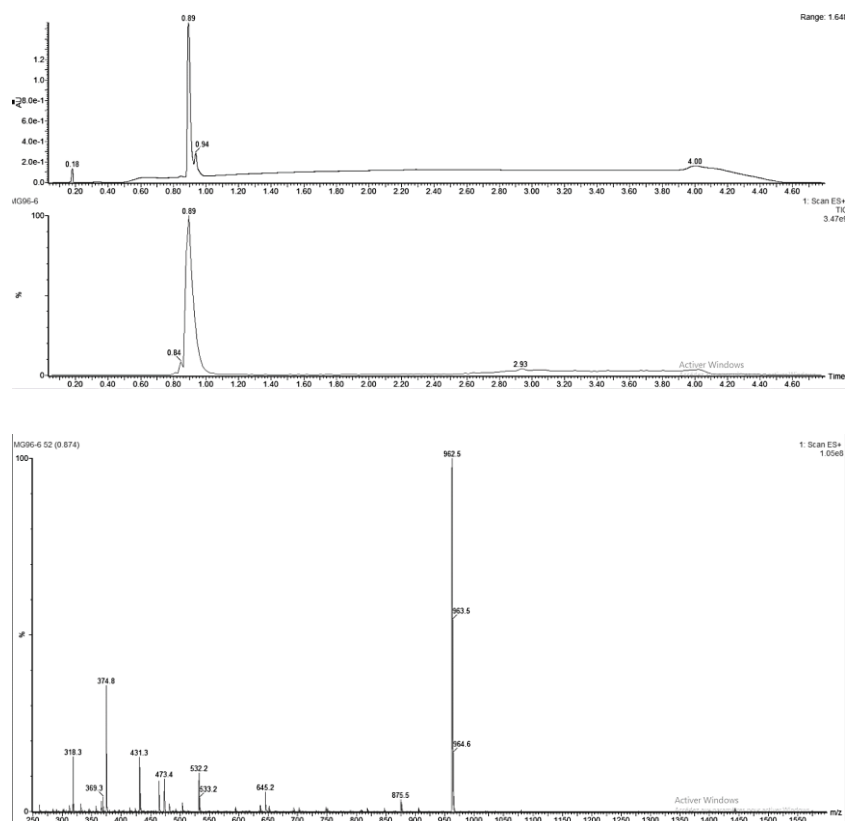


Figure 135 : LC-MS Spectra of peptide Ac-GDPGYIGSR-NH₂.2''

LC-MS (ESI+): tR = 0.89 min, m/z 623.3 [M+H]⁺; 312.2 [M+2H]²⁺

2. *In vitro* biocompatibility assay with MC3T3-E1 osteoblast cells

The MC3T3-E1 cells were passaged at 70-80 % of confluency in T-75 flask with 89% MEM Alpha, 10% Fetal Bovine Serum (FBS) and 1% Penicilin streptomycin as a media.

Three 96-well black-walled plates were prepared:

- First plate : P(PEG3K)-NEt₂ **30** / NPs 15 (Apatite + P(PEG3K)-NEt₂ **30**)
- Second plate : Ac-LRGDNK(Ac)-NH₂ **1'''** / P(PEG3K)-RGD **27** / NPs 18 (Apatite + P(PEG3K)-RGD **27**)
- Third plate : Ac-GDPGYIGSR-NH₂ **2''** / P(PEG3K)-YIGSR **28** / NPs 22 (Apatite + P(PEG3K)-YIGSR **28**)

a. Preparation of the cell culture plate

The 96-well black-walled plates were seeded with 50 μ L of MC3T3-E1 cells in MEM alpha media with 2% of FBS and 1% pen/strep resulting in 19 393 cells / cm^2 . The cell concentration (cells/mL) was measured using an automated cell counter (name machine). The border columns of the 96-well plates were filled with 100 μ L of PBS to avoid dehydration edge effects. For the rest of wells, except for the last second row, cells were seeded with 50 μ L of cells at 19 393 cells / cm^2 . The bottom four wells of the right column were filled with only 50 μ L of media (blank samples) and the most left bottom four wells were only filled with 50 μ L of cells suspended in the media (control samples). The plate was incubated at 37°C for 4 hours to allow the attachment of cells to the bottom of the wells.

b. Preparation of the drug master plate

During the incubation time, the drug master plate (also in a 96-well plate) was prepared using serial dilution of the compounds. For NPs with P(PEG3K)-RGD **27** corona (NPs 18), the range of doses tested were 2.25 mM to 0.07 mM with 1:2 dilutions between wells. For NPs stabilized with P(PEG3K)-YIGSR **28** (NPs 22), the range of doses tested was from 1.91 mM to 0.06 mM. For NPs stabilized with P(PEG3K)-NEt₂ **30** (NPs 15), the range of doses tested was from 2.76 mM to 0.09 mM. For that, 70 μ L of media with 2% of FBS was added to the wells expect to the second-last column from the right. Then, 140 μ L of of the highest concentration of the compound studied was added to the second-last column from the right and serially diluted from the right to the left of the plate to obtain finally 70 μ L in each of the drug master plate wells.

c. Addition of compounds to the cell culture plate

After 4 hours of incubation in the cell culture plate, the cells were checked with the microscope. Then, 50 μ L of each concentration prepared in the drug master plate was gently transferred in the same order to the cell cultured plate. The final plate was incubated at 37°C during 44 hours to allow adequate exposure to the product. The cells were checked in the microscope after 24 hours and 44 hours and pictures of each wells were taken to observe the evolution.

d. Assessing cell viability with the CellTiterBlue assay

For the CellTiterBlue assay, 20 μ L of thawed CellTiterBlue was added to each of the wells and then the plate was incubated for 2 hours. The plate was then taken out the incubator and the fluorescence was recorded at 560 nm/590 nm with a fluorimeter (name machine).

3. *In vitro* biocompatibility assay using NIH/3T3 fibroblast cells

The NIH/3T3 cells were grown up to 70-80 % of confluency in T-75 flask with 89% DMEM, 10% Calf Bovine Serum (BCS) and 1% Penicillin streptomycin as a media.

Three 96-well black-walled plates were prepared. Each experiment was done in 3 replicates:

- First plate : P(PEG3K)-NEt₂ **30** / NPs 15 (Apatite + P(PEG3K)-NEt₂ **30**)
- Second plate : Ac-LRGDNK(Ac)-NH₂ **1''** / P(PEG3K)-RGD **27** / NPs 18 (Apatite + P(PEG3K)-RGD **27**)
- Third plate : Ac-GDPGYIGSR-NH₂ **2''** / P(PEG3K)-YIGSR **28** / NPs 22 (Apatite + P(PEG3K)-YIGSR **28**)

a. Preparation of the cell culture plate

The 96-well black-walled plates were seeded with 50 μ L of NIH/3T3 cells in DMEM media with 2% of BCS and with 19 393 cells /cm² as cell density. The cell concentration (cells/mL) was measured with an automated cell counter (nom de la machine). The border columns of the 96-well plates that did not contain cells were filled with 100 μ L of PBS to avoid dehydration artifacts. For the rest of wells, except for the last second row, cells were seeded with 50 μ L of cells resulting in 19 393 cells /cm². The bottom four wells of the right column was filled with only 50 μ L of media (blank samples) and the most left bottom four wells was only filled with 50 μ L of cells suspended in the media (control samples). The plate was incubated at 37°C for 4 hours to allow the attachment of cells to the bottom of the wells.

b. Preparation of the drug master plate

During the incubation time, the drug master plate (96-well plate) was prepared with through serial dilution of the compounds. For NPs with P(PEG3K)-RGD **27** corona (NPs 18), the range of doses tested were 2.25mM to 0.07mM with 1:2 dilutions between wells. For NPs stabilized with P(PEG3K)-YIGSR **28** (NPs 22), the range of doses tested was from 1.91 mM to 0.06 mM. For NPs stabilized with P(PEG3K)-NEt₂ **30** (NPs 15), the range of doses tested was from 2.76 mM to 0.09 mM. For that, 70 μ L of media with 2% of BCS was added to the wells expect to the second-last column from the right. Then, 140 μ L of of the highest concentration of the compound studied was added to the second-last column from the right and serially diluted from the right to the left of the plate to obtain finally 70 μ L in each wells.

c. Addition of compounds to the cells culture plate

After 4 hours of the incubation time for the cell culture plate, 50 μ L of each of the volumes prepared in the drug master plate were gently transferred in the same order to the cell cultured plate. The plate was incubated at 37°C during 44 hours to allow adequate exposure

to the drug. The cells were checked in the microscope after 24 hours and 44 hours and pictures of each wells were taken to observe changes to cell viability.

d. Cell viability assay

CellTiterBlue (20 μ L) was added to each well and then the plate was incubated for 2 hours. The plate was taken out the incubator and the fluorescence was recorded at 560 nm/590 nm with a fluorimeter plate reader (name machine).

C. In vitro CellTiter Blue method proliferation assay with NIH/3T3 fibroblast cells

The NIH/3T3 cells were grew up to 70-80 % of confluency in T-75 flask with 89% DMEM, 10% Calf Bovine Serum (BCS) and 1% Penicilin streptomycin as a media.

The compounds NPs 15 (Apatite + P(PEG3K)-NEt₂ **30**), NPs 18 (Apatite + P(PEG3K)-RGD **27**, and NPs 22 (Apatite + P(PEG3K)-YIGSR **28**) were added in the same 96 black wells plate with respectively 1.38 mM, 1.13 mM and 0.96 mM as concentration. One plate was prepared for each days of reading (day 1, day 3, day 5 and day 7) four identical plates were prepared.

1. Preparation of the cell culture plate

The 96-well plates with black walls were seeded with the NIH/3T3 cells (15 000 cells /cm²) in media with 2% of BCS and 1% pen/strep. The cell concentration was measured with an automated cell counting machine. The border columns of the 96-well plates were filled with 100 μ L of PBS to avoid dehydration artifacts. For the rest of wells, except for the last second row, cells were seeded with 50 μ L of cells suspension at the correct density, 15 000 cells /cm². The bottom four wells of the right column was filled with only 50 μ L of media (blank samples) and the most left bottom four wells was only filled with 50 μ L of cells suspended in the media (control samples). The plate was incubated at 37°C for 1, 3, 5 or 7 days to allow the attachment of cells to the bottom of the wells.

2. Preparation of the drug master plate

During the incubation time, the drug master plates (96-well plates) were prepared with the test compounds at a variety of concentrations using serial dilution. For that, 70 μ L of media with 2% of BCS was added to the wells located in the second-last column from the right. Then, 140 μ L of the desired concentration of the compounds studied was added to the second-last column from the right and serially diluted from the right to the left of the plate to obtain finally 70 μ L in each wells.

3. Addition of compounds in the cell culture plate

After 4 hours of the incubation time for the cell culture plate, the cells were checked with the microscope. Then, 50 μL of each volume prepared in the drug master plate was gently transferred in the same order to the cell cultured plate. The final plate was incubated at 37°C during 1, 3, 5 and 7 days to allow adequate exposure to the drug. The cells were checked in the microscope after 24 hours and 44 hours and pictures of each wells were taken to observe the evolution.

4. Proliferation Assay using CellTiterBlue

At 1,3,5 and 7 days, CellTiterBlue (20 μL) was added to each of the wells and the plate was incubated for 2 hours. The plate was then taken out the incubator and the fluorescence was recorded at 560 nm/590 nm with (name machine).

D. In vitro scratch assay against NIH/3T3 fibroblast cells

Based on the proliferation experiments, the compounds NPs 18 and NPs 22 were tested for scratch assay with a concentration of 1.13 mM and 0.96 mM, respectively. All compounds were tested on the same plate and triplicates were realized. The NIH/3T3 cells were cultured below 70-80 % confluency in T-75 flask with 89% DMEM, 10% Calf Bovine Serum (BCS) and 1% Penicilin streptomycin as a media.

1. Preparation of the cells culture plate

The border of the plate were filled with 100 μL of PBS to avoid dehydration artifacts. The NIH/3T3 cells in the media with 10% of BCS were seeded at 40 000 cells/ cm^2 to the 96 well plate. The plate was incubated at 37°C for 24 hours to full confluency.

2. In Vitro scratch assay procedure

Upon NIH/3T3 confluency a strip of cells were removed by scratching the middle of each sample well using the p10 pipette tip (10 microliter tip). This step was done before removing the media. After inducing the scratch, a washing steps were necessary. The wounds were washed twice with PBS to remove any cell debris and soften the wound edges. Then, the products NPs 18 and NPs 22 were added at the desired concentration in a media with 2% of BCS. 200 μL was added into each well.

3. Scratch observations on the microscope

The closure of the different created wounds were examined periodically at specific time intervals (0, 24 and 48 hours) using a phase contrast light microscope (Nikon) with a 40x objective and SPOT digital camera.

E. Antibacterial experiments

1. MIC determination

a. Preparation of the inoculum (*S. aureus* and *P. aeruginosa*)

5 mL of *S. aureus* and *P. aeruginosa* bacterial suspensions (10⁸ CFU/mL) in Tryptone-salt were prepared from a bacterial agar culture. Transmitted light (TL) at 620 nm is measured with a spectrophotometer and must reach 75% TL (Absorbance = 0.130) for *S. aureus* and 80% TL (Absorbance = 0.10) for *P. aeruginosa*. Once the bacterial suspension is prepared, 100 µL of it is taken and diluted in 10 mL of BMH CX2 to form the inoculum for the preparation of the plate at approximately 10⁶ CFU/mL.

b. Plate preparation

For the antibacterial experiments a 96 wells plate was used. One compound was tested P(PEG3K)-AhXRR **29**. The range of doses tested was 0.032 mM to 0.000062 mM with 1:2 dilutions between wells. The first column (negative control) was filled with 100 µL of the product tested at 0.032 mM and 100 µL of BMH CX2. The last column (positive control) was filled with the inoculum and 100 µL of sterilized water. The columns 2 to 11 were filled with 100 µL of inoculum and the columns 3 to 11 were filled with sterilized water. 100 µL of the product tested was added with the highest concentration (0.032 mM) to the column 2. Successive dilutions were performed by taking 100 µL from column 2 to put in column 3 and so on until column 11. The plate was then incubated for 24 hours at 37°C.

c. Plate reading

The 96-well plates were read by eye through comparison with the positive and negative controls.

E. Fibroblast membrane mobility experiments

The in vitro experiments on membrane mobility were carried out as follows: fibroblasts were introduced in 4 T75 flasks (10 000 cells/cm²) and incubated for 4 days. 100 µL of Dioll (ci = 100 µM in DMSO) were added to obtain a final concentration of 1 µM in a volume of 10

ml, followed by 24 h of incubation. Then the NPs were added (1000 μ L, leading to a concentration of 0.2 mg/mL in the flask):

- P(YIGSR): mass = 17.85 mg \rightarrow add 9 ml de PBS (sterile) (cf = 2mg/mL) \rightarrow sonication 2 x 7 min for homogenization
- P(RGD) : masse=11.12 mg \rightarrow add 6 ml de PBS (sterile) (cf = 2 mg/mL) \rightarrow sonication 2 x 7min for homogenization
- AEP (reference colloidal NPs): ci =10 mg/ml (cf = 2 mg/ml or 1 mL NPs and 4 ml PBS) \rightarrow sonication 2 x 7min for homogenization

The media were then incubated for 1 night. Cells were then detached with trypsin, then culture medium was added to stop the action of trypsin. A first centrifugation step was carried out for 5 min at 1200 rpm, then the medium was eliminated and the system was washed with PBS. A second centrifugation step was run in the same conditions. The remaining PBS-based supernatant was finally removed and replaced by 2 ml of fresh PBS solution. The cells were counted by spectroscopy and the sample was transferred in an Eppendorf tube with 1mL PBS. The absorbance at 390 nm of the sample was read and dilution was achieved with PBS until obtaining an absorbance of 0.08. By spectrofluorimetry, the emission spectrum was recorded with emission and excitation slits fixed at 2.5 nm. The emission spectra were then recorded from 400 to 600 nm at 37°C and using an excitation wavelength of 390nm. The intensities (I) of fluorescence at 444 nm and 490 nm were in particular determined, respectively corresponding to the gel (rigid) state and liquid crystal (fluid) state of the Dioll probe, allowing for the calculation of the GP factor as:

$$GP = \frac{(I_{440}-I_{490})}{(I_{440}+I_{490})}$$

The more GP is high, the more rigid the membrane. A control is performed with the cells alone to determine the reference value of GP relative to "normal" cell membrane mobility.

References

1. Hughes, J. M. & Rakovan, J. The Crystal Structure of Apatite, $\text{Ca}_5(\text{PO}_4)_3(\text{F},\text{OH},\text{Cl})$. *Rev. Mineral. Geochem.* **48**, 1–12 (2002).
2. Ciobanu, C. S., Massuyeau, F., Constantin, L. V. & Predoi, D. Structural and physical properties of antibacterial Ag-doped nano-hydroxyapatite synthesized at 100°C. *Nanoscale Res. Lett.* **6**, 613 (2011).
3. Arcos, D. & Vallet-Regí, M. Substituted hydroxyapatite coatings of bone implants. *J. Mater. Chem. B* **8**, 1781–1800 (2020).
4. Kolmas, J., Groszyk, E. & Kwiatkowska-Różycka, D. Substituted Hydroxyapatites with Antibacterial Properties. *BioMed Res. Int.* **2014**, 1–15 (2014).
5. Gómez-Morales, J., Lafisco, M., Delgado-López, J. M., Sarda, S. & Drouet, C. Progress on the preparation of nanocrystalline apatites and surface characterization: Overview of fundamental and applied aspects. *Prog. Cryst. Growth Charact. Mater.* **59**, 1–46 (2013).
6. Legros, R., Balmain, N. & Bonel, G. Age-related changes in mineral of rat and bovine cortical bone. *Calcif. Tissue Int.* **41**, 137–144 (1987).
7. Von Euw, S. *et al.* Bone mineral: new insights into its chemical composition. *Sci. Rep.* **9**, 8456 (2019).
8. Drouet, C. A comprehensive guide to experimental and predicted thermodynamic properties of phosphate apatite minerals in view of applicative purposes. *J. Chem. Thermodyn.* **81**, 143–159 (2015).
9. Choimet, M., Tourrette, A., Marsan, O., Rasso, G. & Drouet, C. Bio-inspired apatite particles limit skin penetration of drugs for dermatology applications. *Acta Biomater.* **111**, 418–428 (2020).
10. Vandecandelaere, N., Rey, C. & Drouet, C. Biomimetic apatite-based biomaterials: on the critical impact of synthesis and post-synthesis parameters. *J. Mater. Sci. Mater. Med.* **23**, 2593–2606 (2012).

11. Drouet, C. *et al.* Apatites biomimétiques - Des biominéraux aux analogues de synthèse pour le biomédical. *Technol. Bioméd.* (2018) doi:10.51257/a-v1-in227.
12. Rey, C. *et al.* Characterization of Calcium Phosphates Using Vibrational Spectroscopies. in *Advances in Calcium Phosphate Biomaterials* (ed. Ben-Nissan, B.) 229–266 (Springer, 2014). doi:10.1007/978-3-642-53980-0_8.
13. Wilson, J. W. L., Werness, P. G. & Smith, L. H. Inhibitors of Crystal Growth of Hydroxyapatite: A Constant Composition Approach. *J. Urol.* **134**, 1255–1258 (1985).
14. Okada, M. & Matsumoto, T. Synthesis and modification of apatite nanoparticles for use in dental and medical applications. *Jpn. Dent. Sci. Rev.* **51**, 85–95 (2015).
15. Trakhtenberg, I. Sh. *et al.* Effect of mechanical activation on the morphology and structure of hydroxyapatite. *Inorg. Mater.* **47**, 45–50 (2011).
16. Omori, Y., Okada, M., Takeda, S. & Matsumoto, N. Fabrication of dispersible calcium phosphate nanocrystals via a modified Pechini method under non-stoichiometric conditions. *Mater. Sci. Eng. C* **42**, 562–568 (2014).
17. Kumar, R., Cheang, P. & Khor, K. A. RF plasma processing of ultra-[®]ne hydroxyapatite powders. *J. Mater. Process. Technol.* **7** (2001).
18. Bouyer, E., Gitzhofer, F. & Boulos, M. I. Suspension plasma spraying for hydroxyapatite powder preparation by RF plasma. *IEEE Trans. Plasma Sci.* **25**, 1066–1072 (1997).
19. Xu, J. L. *et al.* Preparation and characterization of nano-sized hydroxyapatite powders produced in a radio frequency (rf) thermal plasma. *Mater. Sci. Eng. A* **374**, 101–108 (2004).
20. Shi, H. B., Zhong, H., Liu, Y., Gu, J. Y. & Yang, C. S. Effect of Precipitation Method on Stoichiometry and Morphology of Hydroxyapatite Nanoparticles. *Key Eng. Mater.* **330–332**, 271–274 (2007).
21. Mobasherpour, I., Heshajin, M. S., Kazemzadeh, A. & Zakeri, M. Synthesis of nanocrystalline hydroxyapatite by using precipitation method. *J. Alloys Compd.* **430**, 330–333 (2007).

22. Noviyanti, A. R. *et al.* A novel hydrothermal synthesis of nanohydroxyapatite from eggshell-calcium-oxide precursors. *Heliyon* **6**, e03655 (2020).
23. Chaudhry, A. A. *et al.* Instant nano-hydroxyapatite: a continuous and rapid hydrothermal synthesis. *Chem. Commun.* 2286 (2006) doi:10.1039/b518102j.
24. Ruffini, A., Sprio, S., Preti, L. & Tampieri, A. Synthesis of Nanostructured Hydroxyapatite via Controlled Hydrothermal Route. in *Biomaterial-supported Tissue Reconstruction or Regeneration* (eds. Barbeck, M., Jung, O., Smeets, R. & Koržinskas, T.) (IntechOpen, 2019). doi:10.5772/intechopen.85091.
25. Hassan, M. N., Mahmoud, M. M., El-Fattah, A. A. & Kandil, S. Microwave-assisted preparation of Nano-hydroxyapatite for bone substitutes. *Ceram. Int.* **42**, 3725–3744 (2016).
26. Ben-Arfa, B. A. E., Salvado, I. M. M., Ferreira, J. M. F. & Pullar, R. C. Novel route for rapid sol-gel synthesis of hydroxyapatite, avoiding ageing and using fast drying with a 50-fold to 200-fold reduction in process time. *Mater. Sci. Eng. C* **70**, 796–804 (2017).
27. Kim, I.-S. & Kumta, P. N. Sol-gel synthesis and characterization of nanostructured hydroxyapatite powder. *Mater. Sci. Eng. B* **111**, 232–236 (2004).
28. Wu, Y. & Bose, S. Nanocrystalline Hydroxyapatite: Micelle Templated Synthesis and Characterization. *Langmuir* **21**, 3232–3234 (2005).
29. Ye, F., Guo, H., Zhang, H. & He, X. Polymeric micelle-templated synthesis of hydroxyapatite hollow nanoparticles for a drug delivery system. *Acta Biomater.* **6**, 2212–2218 (2010).
30. Bose, S. & Saha, S. K. Synthesis and Characterization of Hydroxyapatite Nanopowders by Emulsion Technique. *Chem. Mater.* **15**, 4464–4469 (2003).
31. Cox, S. Synthesis Method of Hydroxyapatite. 11.
32. Iafisco, M. *et al.* The growth mechanism of apatite nanocrystals assisted by citrate: relevance to bone biomineralization. *CrystEngComm* **17**, 507–511 (2015).
33. Delgado-López, J. M. *et al.* Crystallization of bioinspired citrate-functionalized nanoapatite with tailored carbonate content. *Acta Biomater.* **8**, 3491–3499 (2012).

34. Al-Kattan, A., Santran, V., Dufour, P., Dexpert-Ghys, J. & Drouet, C. Novel contributions on luminescent apatite-based colloids intended for medical imaging. *J. Biomater. Appl.* **28**, 697–707 (2014).
35. Al-kattan, A., Dufour, P. & Drouet, C. Purification of biomimetic apatite-based hybrid colloids intended for biomedical applications: A dialysis study. *Colloids Surf. B Biointerfaces* **82**, 378–384 (2011).
36. Drouet, C., Vandecandelaere, N. & Rey, C. Synthesis and post-treatments of biomimetic apatites: How working conditions may configure final physico-chemical features. *MATEC Web Conf.* **7**, 04008 (2013).
37. Al-Kattan, A. Développement de nano-systèmes hybrides à base d'apatites biomimétiques en vue d'applications biomédicales en cancérologie. 243.
38. Al-Kattan, A., Dufour, P., Dexpert-Ghys, J. & Drouet, C. Preparation and Physicochemical Characteristics of Luminescent Apatite-Based Colloids. *J. Phys. Chem. C* **114**, 2918–2924 (2010).
39. CIRIMAT Carnot Institute & Drouet, C. Biomimetic Apatite-Based Functional Nanoparticles as Promising Newcomers in Nanomedicine: Overview of 10 Years of Initiatory Research. *Intern. Med. Prim. Healthc.* **1**, 1–9 (2015).
40. Iafisco, M. *et al.* Biocompatible antimicrobial colistin loaded calcium phosphate nanoparticles for the counteraction of biofilm formation in cystic fibrosis related infections. *J. Inorg. Biochem.* **230**, 111751 (2022).
41. Miragoli, M. *et al.* Inhalation of peptide-loaded nanoparticles improves heart failure. *Sci. Transl. Med.* **10**, eaan6205 (2018).
42. Tourbin, M., Al-Kattan, A. & Drouet, C. Study on the stability of suspensions based on biomimetic apatites aimed at biomedical applications. *Powder Technol.* **255**, 17–22 (2014).
43. Maëla, C. Particules colloïdales multifonctionnalisées pour la vectorisation d'un principe actif : vers une nouvelle formulation pour la dermatologie. 266.

44. Choimet, M., Tourrette, A., Marsan, O., Rasse, G. & Drouet, C. Bio-inspired apatite particles limit skin penetration of drugs for dermatology applications. *Acta Biomater.* **111**, 418–428 (2020).
45. Pizzoccaro, M.-A. *et al.* Adsorption of benzoxaboroles on hydroxyapatite phases. *Acta Biomater.* **41**, 342–350 (2016).
46. Michelot, A. *et al.* Spectroscopic characterisation of hydroxyapatite and nanocrystalline apatite with grafted aminopropyltriethoxysilane: nature of silane–surface interaction. *J. Mater. Sci.* **50**, 5746–5757 (2015).
47. Oulguidoum, A., Bouyarmene, H., Laghzizil, A., Nunzi, J.-M. & Saoiabi, A. Development of sulfonate-functionalized hydroxyapatite nanoparticles for cadmium removal from aqueous solutions. *Colloid Interface Sci. Commun.* **30**, 100178 (2019).
48. Sarda, S. *et al.* Adsorption of tranexamic acid on hydroxyapatite: Toward the development of biomaterials with local hemostatic activity. *Mater. Sci. Eng. C* **66**, 1–7 (2016).
49. El Rhilassi, A., Mourabet, M., Bennani-Ziatni, M., El Hamri, R. & Taitai, A. Interaction of some essential amino acids with synthesized poorly crystalline hydroxyapatite. *J. Saudi Chem. Soc.* **20**, S632–S640 (2016).
50. Pascaud, P. *et al.* Adsorption on apatitic calcium phosphates for drug delivery: interaction with bisphosphonate molecules. *J. Mater. Sci. Mater. Med.* **25**, 2373–2381 (2014).
51. Pascaud, P., Gras, P., Coppel, Y., Rey, C. & Sarda, S. Interaction between a Bisphosphonate, Tiludronate, and Biomimetic Nanocrystalline Apatites. *Langmuir* **29**, 2224–2232 (2013).
52. Hammami, K., Feki, H. E., Marsan, O. & Drouet, C. Adsorption of nucleotides on biomimetic apatite: The case of adenosine 5' monophosphate (AMP). *Appl. Surf. Sci.* **353**, 165–172 (2015).
53. Hammami, K., El-Feki, H., Marsan, O. & Drouet, C. Adsorption of nucleotides on biomimetic apatite: The case of adenosine 5' triphosphate (ATP). *Appl. Surf. Sci.* **360**, 979–988 (2016).
54. Choimet, M., Tourrette, A. & Drouet, C. Adsorption of nucleotides on biomimetic apatite: The case of cytidine 5' monophosphate (CMP). *J. Colloid Interface Sci.* **456**, 132–137 (2015).

55. Tahereh Fatemian & Ezharul Chowdhury. Cytotoxicity Enhancement in Breast Cancer Cells with Carbonate Apatite-Facilitated Intracellular Delivery of Anti-Cancer Drugs. *Toxics* **6**, 12 (2018).
56. Allen, T. M. & Cullis, P. R. Drug Delivery Systems: Entering the Mainstream. *Science* **303**, 1818–1822 (2004).
57. Wawrezynieck, A., Péan, J.-M., Wüthrich, P. & Benoit, J.-P. Biodisponibilité et vecteurs particuliers pour la voie orale. *médecine/sciences* **24**, 659–664 (2008).
58. Olusanya, T., Haj Ahmad, R., Ibegbu, D., Smith, J. & Elkordy, A. Liposomal Drug Delivery Systems and Anticancer Drugs. *Molecules* **23**, 907 (2018).
59. Hossain, S. *et al.* Fabrication and Intracellular Delivery of Doxorubicin/Carbonate Apatite Nanocomposites: Effect on Growth Retardation of Established Colon Tumor. *PLoS ONE* **8**, e60428 (2013).
60. Guo, J., Bourre, L., Soden, D. M., O’Sullivan, G. C. & O’Driscoll, C. Can non-viral technologies knockdown the barriers to siRNA delivery and achieve the next generation of cancer therapeutics? *Biotechnol. Adv.* **29**, 402–417 (2011).
61. Islam, R. A. *et al.* Carbonate Apatite and Hydroxyapatite Formulated with Minimal Ingredients to Deliver siRNA into Breast Cancer Cells In Vitro and In Vivo. *J. Funct. Biomater.* **11**, 63 (2020).
62. Kamaruzman, N., Tiash, S., Ashaie, M. & Chowdhury, E. siRNAs Targeting Growth Factor Receptor and Anti-Apoptotic Genes Synergistically Kill Breast Cancer Cells through Inhibition of MAPK and PI-3 Kinase Pathways. *Biomedicines* **6**, 73 (2018).
63. Hossain, S. *et al.* Carbonate apatite-facilitated intracellularly delivered siRNA for efficient knockdown of functional genes. *J. Controlled Release* **147**, 101–108 (2010).
64. Chowdhury, E. H., Li, Chu, & Kunnath. Reversing multidrug resistance in breast cancer cells by silencing ABC transporter genes with nanoparticle-facilitated delivery of target siRNAs. *Int. J. Nanomedicine* 2473 (2012) doi:10.2147/IJN.S30500.
65. Chua, M. *et al.* Carbonate apatite-facilitated intracellular delivery of c-ROS1 small interfering RNA sensitises MCF-7 breast cancer cells to cisplatin and paclitaxel. *OA Cancer* **1**, (2013).

66. Iafisco, M. *et al.* Conjugation of hydroxyapatite nanocrystals with human immunoglobulin G for nanomedical applications. *Colloids Surf. B Biointerfaces* **90**, 1–7 (2012).
67. Iafisco, M. *et al.* Cell Surface Receptor Targeted Biomimetic Apatite Nanocrystals for Cancer Therapy. *Small* **9**, 3834–3844 (2013).
68. Oltolina, F. *et al.* Monoclonal antibody-targeted fluorescein-5- isothiocyanate-labelled biomimetic nanoapatites: A promising fluorescent probe for imaging applications. 6.
69. Sarda, S. *et al.* Interaction of Folic Acid with Nanocrystalline Apatites and Extension to Methotrexate (Antifolate) in View of Anticancer Applications. *Langmuir* **34**, 12036–12048 (2018).
70. Pallotta, V., D'Amici, G. M., D'Alessandro, A., Rossetti, R. & Zolla, L. Red blood cell processing for cryopreservation: from fresh blood to deglycerolization. *Blood Cells. Mol. Dis.* **48**, 226–232 (2012).
71. Deller, R. C., Vathish, M., Mitchell, D. A. & Gibson, M. I. Synthetic polymers enable non-vitreous cellular cryopreservation by reducing ice crystal growth during thawing. *Nat. Commun.* **5**, 3244 (2014).
72. Pellerin-Mendes, C., Million, L., Marchand-Arvier, M., Labrude, P. & Vigneron, C. In Vitro Study of the Protective Effect of Trehalose and Dextran during Freezing of Human Red Blood Cells in Liquid Nitrogen. *Cryobiology* **35**, 173–186 (1997).
73. Lynch, A. L. *et al.* Biopolymer mediated trehalose uptake for enhanced erythrocyte cryosurvival. *Biomaterials* **31**, 6096–6103 (2010).
74. Holovati, J. L., Gyongyossy-Issa, M. I. C. & Acker, J. P. Effects of trehalose-loaded liposomes on red blood cell response to freezing and post-thaw membrane quality. *Cryobiology* **58**, 75–83 (2009).
75. Stefanic, M. *et al.* Apatite nanoparticles strongly improve red blood cell cryopreservation by mediating trehalose delivery via enhanced membrane permeation. *Biomaterials* **140**, 138–149 (2017).

76. Weber, C. G. *et al.* Enzyme-functionalized biomimetic apatites: concept and perspectives in view of innovative medical approaches. *J. Mater. Sci. Mater. Med.* **25**, 595–606 (2014).
77. Lebugle, A., Pellé, F., Charvillat, C., Rousselot, I. & Chane-Ching, J. Y. Colloidal and monocrystalline Ln³⁺ doped apatite calcium phosphate as biocompatible fluorescent probes. *Chem. Commun.* 606 (2006) doi:10.1039/b515164c.
78. Mondéjar, S. P., Kovtun, A. & Epple, M. Lanthanide-doped calcium phosphate nanoparticles with high internal crystallinity and with a shell of DNA as fluorescent probes in cell experiments. *J. Mater. Chem.* **17**, 4153 (2007).
79. Demchenko, A. P. Photobleaching of organic fluorophores: quantitative characterization, mechanisms, protection*. *Methods Appl. Fluoresc.* **8**, 022001 (2020).
80. Gómez-Morales, J. *et al.* Luminescent biomimetic citrate-coated europium-doped carbonated apatite nanoparticles for use in bioimaging: physico-chemistry and cytocompatibility. *RSC Adv.* **8**, 2385–2397 (2018).
81. Gómez-Morales, J. *et al.* Luminescent Citrate-Functionalized Terbium-Substituted Carbonated Apatite Nanomaterials: Structural Aspects, Sensitized Luminescence, Cytocompatibility, and Cell Uptake Imaging. *Nanomaterials* **12**, 1257 (2022).
82. Chowdhury, E. H. *et al.* pH-sensing nano-crystals of carbonate apatite: Effects on intracellular delivery and release of DNA for efficient expression into mammalian cells. *Gene* **376**, 87–94 (2006).
83. Zohra, F. T., Chowdhury, E. H. & Akaike, T. High performance mRNA transfection through carbonate apatite-cationic liposome conjugates. *Biomaterials* **30**, 4006–4013 (2009).
84. Revilla-López, G. *et al.* Modeling biominerals formed by apatites and DNA. *Biointerphases* **8**, 10 (2013).
85. Welzel, T., Radtke, I., Meyer-Zaika, W., Heumann, R. & Epple, M. Transfection of cells with custom-made calcium phosphate nanoparticles coated with DNA. *J. Mater. Chem.* **14**, 2213 (2004).

86. Han, Y., Wang, X., Dai, H. & Li, S. Nanosize and Surface Charge Effects of Hydroxyapatite Nanoparticles on Red Blood Cell Suspensions. *ACS Appl. Mater. Interfaces* **4**, 4616–4622 (2012).
87. Lara-Ochoa, S., Ortega-Lara, W. & Guerrero-Beltrán, C. E. Hydroxyapatite Nanoparticles in Drug Delivery: Physicochemistry and Applications. *Pharmaceutics* **13**, 1642 (2021).
88. Subramaniam, T., Fauzi, M. B., Lokanathan, Y. & Law, J. X. The Role of Calcium in Wound Healing. *Int. J. Mol. Sci.* **22**, 6486 (2021).
89. Yu, J., Su, H., Wei, S., Chen, F. & Liu, C. Calcium content mediated hemostasis of calcium-modified oxidized microporous starch. *J. Biomater. Sci. Polym. Ed.* **29**, 1716–1728 (2018).
90. Xu, Q., Deng, H., Li, X. & Quan, Z.-S. Application of Amino Acids in the Structural Modification of Natural Products: A Review. *Front. Chem.* **9**, 650569 (2021).
91. Wu, G. Amino acids: metabolism, functions, and nutrition. *Amino Acids* **37**, 1–17 (2009).
92. Behrendt, R., White, P. & Offer, J. Advances in Fmoc solid-phase peptide synthesis. *J. Pept. Sci.* **22**, 4–27 (2016).
93. Merrifield, R. B. Solid Phase Peptide Synthesis. I. The Synthesis of a Tetrapeptide. *J. Am. Chem. Soc.* **85**, 2149–2154 (1963).
94. Pires, D. A. T., Bemquerer, M. P. & do Nascimento, C. J. Some Mechanistic Aspects on Fmoc Solid Phase Peptide Synthesis. *Int. J. Pept. Res. Ther.* **20**, 53–69 (2014).
95. Amblard, M., Fehrentz, J.-A., Martinez, J. & Subra, G. Fundamentals of Modern Peptide Synthesis. in *Peptide Synthesis and Applications* (ed. Howl, J.) 3–24 (Humana Press, 2005). doi:10.1385/1-59259-877-3:003.
96. Merrifield - 1963 - Solid Phase Peptide Synthesis. I. The Synthesis.pdf.
97. Moss, J. A. Guide for Resin and Linker Selection in Solid-Phase Peptide Synthesis. *Curr. Protoc. Protein Sci.* **40**, (2005).
98. Thieriet, N. Use of Alloc-amino Acids in Solid-Phase Peptide Synthesis. Tandem Deprotection-Coupling Reactions Using Neutral Conditions. 4.

99. Isidro-Llobet, A., Álvarez, M. & Albericio, F. Amino Acid-Protecting Groups. *Chem. Rev.* **109**, 2455–2504 (2009).
100. Fuller, W. D., Goodman, M., Naider, F. R. & Zhu, Y.-F. Urethane-protected α -amino acid N-carboxyanhydrides and peptide synthesis. *Biopolymers* **40**, 183–205 (1996).
101. Al-Warhi, T. I., Al-Hazimi, H. M. A. & El-Faham, A. Recent development in peptide coupling reagents. *J. Saudi Chem. Soc.* **16**, 97–116 (2012).
102. Vrettos, E. I. Unveiling and tackling guanidinium peptide coupling reagent side reactions towards the development of peptide-drug conjugates. *RSC Adv.* **8** (2017).
103. Introduction to Peptide Synthesis.pdf.
104. Bouladjine, A., Al-Kattan, A., Dufour, P. & Drouet, C. New Advances in Nanocrystalline Apatite Colloids Intended for Cellular Drug Delivery. *Langmuir* **25**, 12256–12265 (2009).
105. Graf, J. *et al.* A Pentapeptide from the Laminin B1 Chain Mediates Cell Adhesion and Binds the 67 000 Laminin Receptor. **5**.
106. Xu, J. Synthetic Methods of Phosphonopeptides. *Molecules* **25**, 5894 (2020).
107. Błażewska, K. M. McKenna Reaction—Which Oxygen Attacks Bromotrimethylsilane? *J. Org. Chem.* **79**, 408–412 (2014).
108. Justyna, K., Małolepsza, J., Kusy, D., Maniukiewicz, W. & Błażewska, K. M. The McKenna reaction – avoiding side reactions in phosphonate deprotection. *Beilstein J. Org. Chem.* **16**, 1436–1446 (2020).
109. Sevrain, C. M., Berchel, M., Couthon, H. & Jaffrès, P.-A. Phosphonic acid: preparation and applications. *Beilstein J. Org. Chem.* **13**, 2186–2213 (2017).
110. Gutierrez, A. J., Prisbe, E. J. & Rohloff, J. C. DEALKYLATION OF PHOSPHONATE ESTERS WITH CHLOROTRIMETHYLSILANE. *Nucleosides Nucleotides Nucleic Acids* **20**, 1299–1302 (2001).
111. Houghton, S. R., Melton, J., Fortunak, J., Brown Ripin, D. H. & Boddy, C. N. Rapid, mild method for phosphonate diester hydrolysis: development of a one-pot synthesis of tenofovir disoproxil fumarate from tenofovir diethyl ester. *Tetrahedron* **66**, 8137–8144 (2010).

112. Choimet, M. Nanomedicine: Interaction of biomimetic apatite colloidal nanoparticles with human blood components. 8 (2016).
113. Grunenwald, A. *et al.* Revisiting carbonate quantification in apatite (bio)minerals: a validated FTIR methodology. *J. Archaeol. Sci.* **49**, 134 (2014).
114. effects of an RGD peptide wound healing in vivo.pdf.
115. Boateng, S. Y. *et al.* RGD and YIGSR synthetic peptides facilitate cellular adhesion identical to that of laminin and fibronectin but alter the physiology of neonatal cardiac myocytes. *Am. J. Physiol.-Cell Physiol.* **288**, C30–C38 (2005).
116. Kahraman, E., Demirci, E. A., Tanyolaç, Z. G. & Karaman, O. RGD Peptid Dizisinin in vitro Yara İyileşme Modelinde Kullanım Etkinliğinin Belirlenmesi The efficacy of using RGD Peptide Sequence on in vitro Wound Healing. 3.
117. Lu, Y.-A. & Felix, A. M. Pegylated peptides III. Solid-phase synthesis with pegylating reagents of varying molecular weight: synthesis of multiply pegylated peptides. *React. Polym.* **22**, 221–229 (1994).
118. Laconde, G., Amblard, M. & Martinez, J. A simple and versatile method to synthesize N-acyl-benzotriazoles. *Tetrahedron Lett.* **60**, 341–343 (2019).
119. Choimet, M., Tourrette, A., Marsan, O., Rassu, G. & Drouet, C. Bio-inspired apatite particles limit skin penetration of drugs for dermatology applications. *Acta Biomater.* **111**, 418–428 (2020).
120. Adumeau, L. *et al.* Impact of surface grafting density of PEG macromolecules on dually fluorescent silica nanoparticles used for the in vivo imaging of subcutaneous tumors. *Biochim. Biophys. Acta BBA - Gen. Subj.* **1861**, 1587–1596 (2017).
121. Garcia, S. D. Les Hydroxyapatites, un système basique atypique modulable par la synthèse: vers l'identification des sites actifs. 281.

122. Von Euw, S. *et al.* Amorphous surface layer versus transient amorphous precursor phase in bone – A case study investigated by solid-state NMR spectroscopy. *Acta Biomater.* **59**, 351–360 (2017).
123. Boateng *et al.* - 2005 - RGD and YIGSR synthetic peptides facilitate cellul.pdf.
124. Battistini, L., Bugatti, K., Sartori, A., Curti, C. & Zanardi, F. RGD Peptide-Drug Conjugates as Effective Dual Targeting Platforms: Recent Advances. *Eur. J. Org. Chem.* **2021**, 2506–2528 (2021).
125. Leider, M. On the Weight of the Skin**From the New York Skin and Cancer Unit, Department of Dermatology and Syphilology (Marion B. Sulzberger, M.D. Director) and the Post Graduate Medical School of the New York University-Bellevue Medical Center. *J. Invest. Dermatol.* **12**, 187–191 (1949).
126. Wilkinson, H. N. & Hardman, M. J. Wound healing: cellular mechanisms and pathological outcomes. *Open Biol.* **10**, 200223 (2020).
127. Brown, M. S., Ashley, B. & Koh, A. Wearable Technology for Chronic Wound Monitoring: Current Dressings, Advancements, and Future Prospects. *Front. Bioeng. Biotechnol.* **6**, 47 (2018).
128. Nicks, B. A., Ayello, E. A., Woo, K., Nitzki-George, D. & Sibbald, R. G. Acute wound management: revisiting the approach to assessment, irrigation, and closure considerations. *Int. J. Emerg. Med.* **3**, 399–407 (2010).
129. Rapp, L. M. Physiological changes in tissues denervated by spinal cord injury tissues and possible effects on wound healing. *Int. Wound J.* **5**, 435–444 (2008).
130. Zhao, R., Liang, H., Clarke, E., Jackson, C. & Xue, M. Inflammation in Chronic Wounds. *Int. J. Mol. Sci.* **17**, 2085 (2016).
131. Mathieu, S. Etude des mécanismes d'adhérence et d'activation des plaquettes sanguines appliquée à l'identification de nouvelles cibles anti-thrombotiques plus sûres. 280 (2012).
132. HEMOSTASE 2005-2006.pdf.

133. Stupin, V. *et al.* The Effect of Inflammation on the Healing Process of Acute Skin Wounds Under the Treatment of Wounds with Injections in Rats. *J. Exp. Pharmacol.* **Volume 12**, 409–422 (2020).
134. Frykberg, R. G. & Banks, J. Challenges in the Treatment of Chronic Wounds. *Adv. Wound Care* **4**, 560–582 (2015).
135. Montanari, T., Pošćić, N. & Colitti, M. Factors involved in white-to-brown adipose tissue conversion and in thermogenesis: a review: Factors involved in WAT browning. *Obes. Rev.* **18**, 495–513 (2017).
136. Baranoski, S. A Myriad of Challenging Decisions. **23**, 11 (2005).
137. Reinke, J. M. & Sorg, H. Wound Repair and Regeneration. *Eur. Surg. Res.* **49**, 35–43 (2012).
138. Lazaro, J. L. *et al.* Elevated levels of matrix metalloproteinases and chronic wound healing: an updated review of clinical evidence. *J. Wound Care* **25**, 277–287 (2016).
139. Wound Infection in Clinical Practice.: An International Consensus. *Int. Wound J.* **5**, iii–11 (2008).
140. Sen, C. K. *et al.* Human skin wounds: A major and snowballing threat to public health and the economy. *Wound Repair Regen.* **17**, 763–771 (2009).
141. Siddiqui, A. R. & Bernstein, J. M. Chronic wound infection: Facts and controversies. *Clin. Dermatol.* **28**, 519–526 (2010).
142. Tandara, A. A. & Mustoe, T. A. Oxygen in Wound Healing? More than a Nutrient. *World J. Surg.* **28**, 294–300 (2004).
143. The Edge Effect Current Therapeutic.pdf.
144. Vincent, A. M., Russell, J. W., Low, P. & Feldman, E. L. Oxidative Stress in the Pathogenesis of Diabetic Neuropathy. *Endocr. Rev.* **25**, 612–628 (2004).
145. Consensus Development Conference on.pdf.
146. Shrivastava, R. Clinical evidence to demonstrate that simultaneous growth of epithelial and fibroblast cells is essential for deep wound healing. *Diabetes Res. Clin. Pract.* **92**, 92–99 (2011).

147. Schneider, L. A., Korber, A., Grabbe, S. & Dissemond, J. Influence of pH on wound-healing: a new perspective for wound-therapy? *Arch. Dermatol. Res.* **298**, 413–420 (2007).
148. Yang, X. *et al.* Antibacterial and anti-biofouling coating on hydroxyapatite surface based on peptide-modified tannic acid. *Colloids Surf. B Biointerfaces* **160**, 136–143 (2017).
149. Nikfarjam, N. *et al.* Antimicrobial Ionic Liquid-Based Materials for Biomedical Applications. *Adv. Funct. Mater.* **31**, 2104148 (2021).
150. Gupta, P., Singh, H. S., Shukla, V. K., Nath, G. & Bhartiya, S. K. Bacteriophage Therapy of Chronic Nonhealing Wound: Clinical Study. *Int. J. Low. Extrem. Wounds* **18**, 171–175 (2019).
151. Kazemzadeh-Narbat, M. *et al.* Antimicrobial peptides on calcium phosphate-coated titanium for the prevention of implant-associated infections. *Biomaterials* **31**, 9519–9526 (2010).
152. Rima, M. *et al.* Antimicrobial Peptides: A Potent Alternative to Antibiotics. *Antibiotics* **10**, 1095 (2021).
153. Larsen, M. J. & Nyvad, B. Enamel Erosion by Some Soft Drinks and Orange Juices Relative to Their pH, Buffering Effect and Contents of Calcium Phosphate. *Caries Res.* **33**, 81–87 (1999).
154. Nikonam M., R., Sadrnezhad, S. K. & Vahdati Khaki, J. Effect of Cu²⁺ ion on Biological Performance of Nanostructured Fluorapatite Doped with Copper. *Sci. Iran.* **0**, 0–0 (2017).
155. Lansdown, A. B. G., Mirastschijski, U., Stubbs, N., Scanlon, E. & Ågren, M. S. Zinc in wound healing: Theoretical, experimental, and clinical aspects. *Wound Repair Regen.* **15**, 2–16 (2007).
156. Pierschbacher, M. D. & Ruoslahti, E. Cell attachment activity of fibronectin can be duplicated by small synthetic fragments of the molecule. *Nature* **309**, 30–33 (1984).
157. Massia, S. P. & Hubbell, J. A. An RGD Spacing of 440 nm Is Sufficient for Integrin $\alpha_5\beta_3$ -mediated Fibroblast Spreading and 140 nm for Focal Contact and Stress Fiber Formation. *J. Cell Biol.* **114**, 12 (1991).
158. Integrins Bidirectional.pdf.
159. Margadant, C., Charafeddine, R. A. & Sonnenberg, A. Unique and redundant functions of integrins in the epidermis. *FASEB J.* **24**, 4133–4152 (2010).

160. Kim, Y.-Y. *et al.* Laminin peptide YIGSR enhances epidermal development of skin equivalents. *J. Tissue Viability* **27**, 117–121 (2018).
161. Yoon, J. H. *et al.* Laminin peptide YIGSR induces collagen synthesis in Hs27 human dermal fibroblasts. *Biochem. Biophys. Res. Commun.* **428**, 416–421 (2012).
162. Battistini, L., Bugatti, K., Sartori, A., Curti, C. & Zanardi, F. RGD Peptide-Drug Conjugates as Effective Dual Targeting Platforms: Recent Advances. *Eur. J. Org. Chem.* **2021**, 2506–2528 (2021).
163. Yussof, S. J. Mohd., Omar, E., Pai, D. R. & Sood, S. Cellular events and biomarkers of wound healing. *Indian J. Plast. Surg.* **45**, 220–228 (2012).
164. Bernard, F. X., Barrault, C., Juchaux, F., Laurensou, C. & Apert, L. Stimulation of the proliferation of human dermal fibroblasts *in vitro* by a lipidocolloid dressing. *J. Wound Care* **14**, 215–220 (2005).
165. Eming, S. A., Wynn, T. A. & Martin, P. Inflammation and metabolism in tissue repair and regeneration. *Science* **356**, 1026–1030 (2017).
166. Li, X.-J. *et al.* Lipopolysaccharide Stimulated the Migration of NIH3T3 Cells Through a Positive Feedback Between β -Catenin and COX-2. *Front. Pharmacol.* **9**, 1487 (2018).
167. effects of an RGD peptide wound healing in vivo.pdf.
168. CellTiter Blue Cell Viability Assay TB317.pdf.
169. Cheng Kuhn 2007 Nanoparticles Cisplatin.pdf.
170. Pinese, C. *et al.* Simple and Specific Grafting of Antibacterial Peptides on Silicone Catheters. *Adv. Healthc. Mater.* **5**, 3067–3073 (2016).
171. Abawi, A. *et al.* Monomethyl Auristatin E Grafted-Liposomes to Target Prostate Tumor Cell Lines. *Int. J. Mol. Sci.* **22**, 4103 (2021).
172. Laurdan and Prodan as Polarity-Sensitive Fluorescent Membrane Probes | SpringerLink. <https://link.springer.com/article/10.1023/A:1020528716621>.

173. Lagarrigue, P. *et al.* Poly(d,l-lactide)-Grafted Bioactive Glass Nanoparticles: From Nanobricks to Freeze-Cast Scaffolds for Bone Substitution. *ACS Appl. Nano Mater.* (2022)
doi:10.1021/acsanm.2c00313.
174. Brinkmann, A., Edén, M. & Levitt, M. H. Synchronous helical pulse sequences in magic-angle spinning nuclear magnetic resonance: Double quantum recoupling of multiple-spin systems. *J. Chem. Phys.* **112**, 8539–8554 (2000).